

## **Modification of Graphitic Carbon Nitride (g-C<sub>3</sub>N<sub>4</sub>) for photocatalytic redox reactions**

Adeem Ghaffar Rana

Vollständiger Abdruck der von der TUM School of Life Sciences der Technischen  
Universität München zur Erlangung eines  
Doktors der Ingenieurwissenschaften (Dr.-Ing)  
genehmigten Dissertation.

Vorsitz: Prof. Dr. Stephan Schrettl

Prüfer\*innen der Dissertation:

1. Prof. Dr. Mirjana Minceva
2. Prof. Dr. Reinhard Schomäcker

Die Dissertation wurde am 01.09.2022 bei der Technischen Universität München  
eingereicht und durch die TUM School of Life Sciences am 28.11.2022  
angenommen.

## Acknowledgments

I am deeply grateful to Prof. Mirjana Minceva for her supervision and guidance during this thesis and her kindness, openness, and availability for research and emotional support during my time as the chair. I would also like to thank Prof. Dr. Reinhard Schomäcker for his role as an examiner.

I am thankful to the Higher Education Commission of Pakistan and DAAD for giving me the scholarship and opportunity to do my Ph.D. at the Technical University of Munich (TUM), Germany. I am thankful to the University of Engineering and Technology (UET), Lahore, Department of chemical, polymer, and composite materials engineering, and Dr. Tanveer Iqbal for their support and study leave for this duration. I thank Prof. Joaquim Luis Faria and Dr. Eliana da Silva for the pleasant three-month research stay at the Laboratory of Separation and Reaction Engineering - Laboratory of Catalysis and Materials (LSRE-LCM) at the University of Porto, Portugal.

I am thankful to Dr. Michael and Dr. Minoo from TU Berlin and Dr. Zahid Hussain from Catalytic Research Center, TU Munich, for the collaborative work, which resulted in published journal articles and is part of the thesis. I would also like to thank Dr. Manuel Hoegerl for taking the time out of his busy schedule to share his valuable insights and perspectives with me through the TUM Mentoring program. A special thanks to Dr. Sharad for his support throughout the journey.

A big thank you goes out to my Biothermodynamics colleagues for their support. Special thanks to Ahmad, Andreas, Simon, Raena, Vlad, Melanie, Bene, Vanessa, Sahar, and Caren for their constant emotional and technical support. A special thanks to Anja and Yasmine for their kind support from the first day for bureaucratic/visa issues and Heinrich's support in the lab. I am also grateful to have had the opportunity to supervise my student, Nikki Hammond, Mahnoor, and Isabelle Abbas.

I am indebted to my dear friends Saqib and Aamir for their support throughout my journey. A special thanks to Sumaira Saleem for her invaluable advices, support, and encouragement throughout my Ph.D. To them and all the other beautiful people who cheered me on, brought growth and color to my life, and helped me maintain my equilibrium during this rollercoaster ride of the last five years: You are wicked awesome, and I cherish every one of you.

Lastly, I would like to thank my parents, sister, brothers, and family for their endless love and support throughout my endeavors, big and small, near and far.



This page is intentionally left blank.

## Abstract

Photocatalysis has gained much attention for redox reactions, for instance, towards energy generation and wastewater treatment. Evidently, several photocatalysts can already use the UV part of the solar spectrum. However, utilizing the visible part of the spectrum is still challenging. Materials like graphitic carbon nitride (g-C<sub>3</sub>N<sub>4</sub>) are visible light active and absorb the visible portion of light due to their lower bandgap energy. Still, the stacked structure, high recombination rate, and low surface areas are key issues that are responsible for a low photocatalytic activity. Exfoliation and doping are a few techniques that can improve the morphology and surface properties of the material. The current thesis presents the synthesis strategies of bulk- and exfoliated g-C<sub>3</sub>N<sub>4</sub>, their derived nanocomposites, and their doped derivatives towards environmental and energy applications. Briefly, it systematically comprises the following research findings:

The effects of exfoliation and operating parameters, i.e., catalyst concentration, pollutant concentration, pH, and oxygen concentration, on the photodegradation of phenolic compounds were studied. The exfoliated g-C<sub>3</sub>N<sub>4</sub> was prepared from bulk g-C<sub>3</sub>N<sub>4</sub>, while the bulk g-C<sub>3</sub>N<sub>4</sub> was synthesized from melamine using the thermal decomposition method. The exfoliated g-C<sub>3</sub>N<sub>4</sub> was characterized for chemical, optical, and surface properties using X-ray powder diffraction (XRD), X-ray photoelectron spectroscopy (XPS), Photoluminescence spectroscopy (PL), Fourier transform infrared spectroscopy (FTIR), Brunauer–Emmett–Teller (BET), and Scanning- and Transmission electron microscopy (SEM, TEM) techniques. The exfoliated g-C<sub>3</sub>N<sub>4</sub> was highly porous with a nanosheet morphology and a high surface area of 170 m<sup>2</sup>/g. The photocatalytic performance of the bulk and exfoliated g-C<sub>3</sub>N<sub>4</sub> catalysts were evaluated for the degradation of phenol and other phenolic compounds (catechol, m-cresol, and xylenol) under the influence of two lamps, namely, a xenon and light-emitting diodes (LED) lamp. The efficiency of synthesized g-C<sub>3</sub>N<sub>4</sub> was better under the influence of an LED lamp at a wavelength of 430 nm. Moreover, response surface methodology (RSM) involving a Box–Benken design (BBD) was employed to analyze the photocatalytic degradation of phenol using exfoliated g-C<sub>3</sub>N<sub>4</sub> and an LED lamp. The influence and interactions between three parameters, namely, catalyst concentration, pollutant concentration, and solution pH, were examined and modeled to derive an empirical regression quadratic model.

Furthermore, the effects of non-metal doping on the photodegradation of two endocrine-disrupting hormones: 17β-estradiol (E2) and 17α-ethinylestradiol (EE2), were studied. Non-metallic doped g-C<sub>3</sub>N<sub>4</sub> was synthesized via the decomposition of acid-treated melamine. Acetic acid, sulfuric acid, and phosphoric acid were used to dope oxygen, sulfur, and phosphorous. Adsorption and photocatalytic degradation kinetics were studied and fitted with different kinetic models. The pseudo-second-order kinetic model fitted the adsorption kinetics, whereas the

photocatalytic degradation followed the exponential decay model. Among the three doped catalysts, the sulfur-doped g-C<sub>3</sub>N<sub>4</sub> demonstrated the highest activity by completely removing the hormone pollutant in the shortest time.

Finally, the effects of non-noble metals (Ni, Co, and Cu), and the synthesis method of loaded exfoliated g-C<sub>3</sub>N<sub>4</sub> on the hydrogen production efficiency in water splitting, were studied. Among the three types of loaded exfoliated g-C<sub>3</sub>N<sub>4</sub>, the one loaded with nickel showed the highest performance towards hydrogen production. Subsequently, nickel-loaded exfoliated g-C<sub>3</sub>N<sub>4</sub> was synthesized using three synthesis methods, namely, colloidal, incipient wet impregnation, and precipitation deposition methods. The photoactivity for hydrogen evolution of the synthesized catalysts was evaluated using triethanolamine (TEOA) as a sacrificial agent, using a xenon lamp, with a cut-off filter at wavelengths above 395 nm. Nickel-loaded exfoliated g-C<sub>3</sub>N<sub>4</sub>, synthesized via the colloidal method, performed the best towards hydrogen production from water splitting.

## Kurzzusammenfassung

Die Nutzung von Photokatalyse für Redoxreaktionen hat in jüngster Zeit viel Aufmerksamkeit erlangt, beispielsweise zur Energieerzeugung und Abwasserbehandlung. Mehrere Photokatalysatoren können bereits den UV-Teil des Sonnenspektrums nutzen. Die Nutzung des sichtbaren Teils des Spektrums ist jedoch immer noch eine Herausforderung. Materialien wie graphitisches Kohlenstoffnitrid ( $g\text{-C}_3\text{N}_4$ ) sind im sichtbaren Licht aktiv und absorbieren diesen Anteil des Lichts aufgrund ihrer geringeren Bandlückenenergie. Dennoch sind deren Schichtstruktur, die hohe Rekombinationsrate und die geringen Oberflächen Schlüsselfaktoren, die für eine geringe photokatalytische Aktivität verantwortlich sind. Exfoliation und Dotierung sind einige Techniken, die die Morphologie und Oberflächeneigenschaften des Materials verbessern können. Die vorliegende Dissertation präsentiert die Synthesestrategien von Bulk- und exfoliertem  $g\text{-C}_3\text{N}_4$ , daraus abgeleiteten Nanokompositen und ihren dotierten Derivaten für Umwelt- und Energieanwendungen. Sie umfasst systematisch die folgenden Forschungsergebnisse:

Die Wirkungen der Exfoliation und der Betriebsparameter, d. h. Katalysatorkonzentration, Schadstoffkonzentration, pH-Wert und Sauerstoffkonzentration, auf den Photoabbau von Phenolverbindungen wurden untersucht. Das exfolierte  $g\text{-C}_3\text{N}_4$  wurde aus Bulk- $g\text{-C}_3\text{N}_4$  hergestellt, das Bulk- $g\text{-C}_3\text{N}_4$  aus Melamin unter Verwendung des thermischen Zersetzungsverfahrens. Das exfolierte  $g\text{-C}_3\text{N}_4$  wurde auf chemische, optische und Oberflächeneigenschaften unter Verwendung von Röntgenpulverbeugung (XRD), Röntgenphotoelektronenspektroskopie (XPS), Photolumineszenzspektroskopie (PL), Fourier-Transformations-Infrarotspektroskopie (FTIR), Brunauer–Emmett-Teller (BET) und Scanning- und Transmissionselektronenmikroskopie (SEM, TEM)-Techniken charakterisiert. Das exfolierte  $g\text{-C}_3\text{N}_4$  war hochporös mit einer Nanoblatt-Morphologie und einer großen Oberfläche von  $170\text{ m}^2/\text{g}$ . Die photokatalytische Leistung der Bulk- und exfolierten  $g\text{-C}_3\text{N}_4$ -Katalysatoren wurde für den Abbau von Phenol und anderen phenolischen Verbindungen (Catechin, m-Cresol und Xylenol) unter dem Einfluss von zwei Lampen, einer Xenon- und einer Leuchtdiode (LED-Lampe, untersucht. Die Effizienz von synthetisiertem  $g\text{-C}_3\text{N}_4$  war unter einer LED-Lampe bei einer Wellenlänge von 430 nm besser. Darüber hinaus wurde die Response Surface Methodology (RSM) mit einem Box-Benken-Design (BBD) eingesetzt, um den photokatalytischen Abbau von Phenol unter Verwendung von exfoliertem  $g\text{-C}_3\text{N}_4$  und einer LED-Lampe zu analysieren. Der Einfluss und die Wechselwirkungen zwischen den drei Parametern Katalysatorkonzentration, Schadstoffkonzentration und pH-Wert der Lösung wurden untersucht und modelliert, um ein empirisches quadratisches Regressionsmodell abzuleiten.

Darüber hinaus wurden die Auswirkungen von Nichtmetalldoping auf den Photoabbau von zwei endokrin wirksamen Hormonen untersucht:  $17\beta$ -Estradiol (E2) und  $17\alpha$ -Ethinylestradiol (EE2). Nichtmetallisch dotiertes  $g\text{-C}_3\text{N}_4$  wurde durch Zersetzung von säurebehandeltem Melamin synthetisiert. Essigsäure, Schwefelsäure und Phosphorsäure wurden verwendet, um Sauerstoff, Schwefel und Phosphor zu dotieren. Die Kinetik der Adsorption und des photokatalytischen Abbaus wurde untersucht und mit verschiedenen kinetischen Modellen angepasst. Das kinetische Modell pseudo-zweiter Ordnung passte zur Adsorptionskinetik, während der photokatalytische Abbau dem exponentiellen Zerfallsmodell folgte. Unter den drei dotierten Katalysatoren zeigte das mit Schwefel dotierte  $g\text{-C}_3\text{N}_4$  die höchste Aktivität, es entfernte die Hormonschadstoffe in kürzester Zeit vollständig.

Schließlich wurden die Auswirkungen von Nichtedelmetallen (Ni, Co und Cu) und das Syntheseverfahren von beladenem exfoliertem  $g\text{-C}_3\text{N}_4$  auf die Effizienz der Wasserstoffproduktion bei der Wasserspaltung untersucht. Unter den drei Typen von beladenem exfoliertem  $g\text{-C}_3\text{N}_4$  zeigte das mit Nickel beladene die höchste Leistung in Bezug auf die Wasserstoffproduktion. Anschließend wurde nickelbeladenes exfoliertes  $g\text{-C}_3\text{N}_4$  unter Verwendung von drei Syntheseverfahren synthetisiert, und zwar mit kolloidaler Methode, beginnender Nassimprägnierung und Niederschlagsabscheidungsverfahren. Die Photoaktivität für die Wasserstoffentwicklung der synthetisierten Katalysatoren wurde unter Verwendung von Triethanolamin (TEOA) als Elektronendonator und einer Xenonlampe mit einem Sperrfilter bei Wellenlängen über 395 nm bewertet. Nickelbeladenes exfoliertes  $g\text{-C}_3\text{N}_4$ , das über die kolloidale Methode synthetisiert wurde, schnitt am besten bei der Wasserstoffproduktion durch Wasserspaltung ab.

## Table of Contents

Acknowledgments .....	I
Abstract .....	III
Kurzzusammenfassung .....	V
1 Introduction .....	1
2 Theoretical and technological background.....	6
2.1 Photocatalysis .....	6
2.2 Working principle and mechanism of photocatalysis.....	7
2.3 Applications of photocatalysis .....	9
2.3.1 Oxidation pollutant degradation .....	9
2.3.2 Hydrogen (H <sub>2</sub> ) evolution reduction reaction.....	10
2.4 Photocatalysts and their properties .....	11
2.5 Graphitic carbon nitride .....	11
3 Methodology.....	15
3.1 g-C <sub>3</sub> N <sub>4</sub> synthesis methods.....	15
3.2 Characterization methods.....	15
3.2.1 Powder X-ray diffraction (PXRD) .....	16
3.2.2 N <sub>2</sub> physisorption measurements (BET) .....	16
3.2.3 Fourier-transform infrared spectroscopy (FTIR) .....	17
3.2.4 X-Ray photoelectron spectroscopy (XPS).....	17
3.2.5 UV-visible spectroscopy (UV-Vis) .....	17
3.2.6 Transmission electron microscopy (TEM) and Energy dispersive X-ray spectroscopy (EDX).....	17
3.2.7 Scanning electron microscopy (SEM) .....	18
3.3 Analytical methods .....	18
3.3.1 High-performance liquid chromatography (HPLC).....	18
3.4 Mathematical methods .....	18
3.4.1 Response surface methodology.....	18
4 Results .....	20
4.1 Paper I: Efficient Advanced Oxidation Process (AOP) for photocatalytic contaminant degradation using exfoliated Metal-Free Graphitic Carbon Nitride and Visible Light-Emitting Diodes .....	21
4.2 Paper II: Synthesis of highly active doped graphitic carbon nitride using acid-functionalized precursor for efficient adsorption and photodegradation of endocrine-disrupting compounds.....	40
4.3 Paper III: Impact of co-catalysts (Ni, Co, Cu) and synthesis method on the photocatalytic activity of exfoliated graphitic carbon nitride for hydrogen production .....	53

4.4	Paper IV: Analysis of photocatalytic degradation of phenol with exfoliated Graphitic Carbon Nitride and Light-Emitting Diodes Using Response Surface Methodology .....	68
5	Overall discussion .....	85
5.1	Impact of g-C <sub>3</sub> N <sub>4</sub> modifications on its photocatalytic activity.....	85
5.2	Influence of operating conditions on the performance of g-C <sub>3</sub> N <sub>4</sub> .....	87
5.3	Selection of photocatalytic reaction operating parameters by response surface methodology .....	89
6	Conclusion .....	91
7	Outlook.....	93
8	References.....	94
	Appendix .....	106
	Supplementary Information of all papers.....	107
	List of abbreviations and symbols .....	123

# 1 Introduction

In recent years, pertaining to the perpetual industrial and economic developments, there are emerging energy and environmental challenges, which necessitate urgent attention, including sustainable and rapid solutions. Industrialization and increasing population are assumed to be the predominant causes behind energy and environmental crises [1-3]. Majority of the global energy demand is fulfilled via the employment of non-renewable sources (petrol, diesel, coal, etc.), which are constantly diminishing with each passing day. In addition, during the past few decades, increased consumption of non-renewable fossil fuels to meet the rising energy demand, as well as different types of hazardous wastes in industrial wastewater streams, has led to severe environmental issues, such as global warming and climate change [4, 5]. As of today, the most critical challenges are countering pollution affected by wastewater eliminated from different industries, discovering, and inventing green and sustainable energy sources, and tackling global warming. These represent a handful of fundamental challenges for both developed and under-developed economies [6-10].

The industries discharge harmful pollutants into wastewater streams, which are potentially harmful to humans, aquatic life, and living organisms, and can adversely affect several physiological organs, including the liver, kidney, brain, and the nervous system [11-17]. Water quality may deteriorate with associated health risks towards humans due to organic pollutants, even at low concentrations [18, 19]. Phenols represent a severe type of organic pollutant. Petrochemicals, aluminum, steel, oil refinery, chemical, paint, resin, cosmetic, and automobile production industries can discharge phenolic compounds into the environment through their wastewater streams [20, 21]. Pharmaceutical pollutants are another type of organic pollutant, which are classified as emerging due to their toxicity and persistency in affecting the ecosystem and environment, as well as their widespread presence in marine waters and drinking water [22]. Pharmaceutical pollutants persist typically at low concentrations, and their prolonged presence in the system can adversely affect the environment, including possessing a similar potential to act as endocrine disrupters [23-27]. As of today, several traditional methods have been employed towards the purification of water, such as flocculation [28], precipitation [29], coagulation [30], adsorption [24], filtration, sedimentation, reverse osmosis [24], chlorination [31], biological treatment [32], among others. Nevertheless, these purification techniques are not completely efficient and present a handful of intrinsic shortcomings, including not being cost-effective, being time-consuming, and producing toxic by-products with heavy sludge [12, 33]. While conventional wastewater treatment plants (WWTPs) can remove the pollutants, they cannot degrade them since these plants are not designed accordingly [12, 14, 34-37].

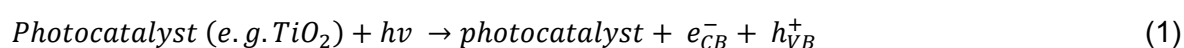
Traditional energy resources are constantly depleting due to overconsumption. Subsequently, renewable and green energy sources must be explored to counter and resolve the energy



crisis, including minimizing environmental pollution [38, 39]. Contextually, solar energy is a viable natural energy source, and the amount of solar energy reaching the surface of the earth yearly is much higher than human consumption [40, 41]. The conversion of solar energy to chemical energy via chemical reactions represents a potential way of producing renewable energy. Inspired by the natural photosynthesis of green plants, which convert solar energy to chemical energy in the form of carbohydrates or hydrogen, artificial photosynthesis (photocatalysis) is touted to be a prospective technology for converting solar energy to chemical energy [42-44]. Ever since Fujishima and Honda [45] discovered water photolysis on TiO<sub>2</sub> electrodes in 1972, photocatalysis has received tremendous attention and has been developed rapidly in recent decades due to its promising applications in renewable energy production [46, 47].

During the last few decades, semiconductor photocatalysis has gained much attention as a possible solution to overcome the problems of water pollution and energy. Photocatalysis, which generates green energy, has effectively removed the difficult micropollutants produced otherwise via conventional techniques. In contrast to the traditional oxidation processes, photocatalysis demonstrates significant benefits. Photocatalysis is an attractive, eco-friendly, and promising technique for removing pollutants, as it is economical, non-toxic, safe, and renewable. In the photocatalytic process, sunlight can be utilized as an energy source. The selection, design, and modification of the catalyst in artificial photosynthesis have attracted significant scientific interest worldwide in harvesting this energy. Degradation of pollutants can completely degrade the stable organic pollutants to CO<sub>2</sub> and H<sub>2</sub>O. This process can work efficiently under ambient conditions without excess oxygen. The photocatalysis process is cheaper and produces less waste than conventional processes [48]. Production of hydrogen from water and fuel from CO<sub>2</sub> reduction is an effective use of photocatalysis for green energy production.

Electron-hole pairs carry out the initiation process in semiconductor photocatalysis after bandgap excitation. When a photoactive material is irradiated by a light source with energy equal to or greater than the bandgap energy of the material, the valence band electrons absorb that energy and move to the conduction band (CB), leaving a positive hole in the valence band (VB):



The excited electrons ( $e_{CB}^-$ ) and holes ( $h_{VB}^+$ ) produced after excitation can recombine, leading to no reaction, thereby decreasing the overall efficiency of the process. Migration of electrons and holes to the surface of the semiconductor without recombination is necessary for a reaction to occur. These can participate in oxidation and reduction reactions with adsorbed species, such as water, oxygen, and other organic or inorganic species.

For photocatalytic degradation of pollutants, which is an oxidation reaction, valence band holes are vital as they induce the oxidation degradation reaction of the contaminants. These holes can directly oxidize the contaminants. However, in most cases, they react with water to form hydroxyl radicals ( $\bullet\text{OH}$ ), which can completely convert the pollutants into  $\text{CO}_2$ ,  $\text{H}_2\text{O}$ , etc. [7-9]. On the other hand, photocatalytic water splitting is a reduction reaction. In this case, reducing conduction band electrons is more critical, inducing water reduction for hydrogen production. Different sacrificial agents (methanol, phenol, glycerol, TEOA) are used for water splitting reactions. The conduction band level must be more negative than the total hydrogen production level, and  $E_H = -1.23$  V Normal Hydrogen Electrode (NHE) redox potential of the overall reaction for hydrogen production to start [49-52].

A large number of semiconductor photocatalysts has been investigated so far for the degradation of different pollutants, such as  $\text{ZnO}$  [53, 54],  $g\text{-C}_3\text{N}_4$  [55, 56],  $\text{WO}_3$  [57, 58],  $\text{Fe}_2\text{O}_3$  [59],  $\text{CdSe}$  [60], and  $\text{SrTiO}_3$  [61]. The fundamental aspects of a good photocatalyst are that they must be: 1) active in the light range, 2) chemically stable, 3) non-toxic, and 4) cheap and easily available [43].  $\text{TiO}_2$  is the most widely used catalyst. However,  $\text{TiO}_2$  is active under UV irradiation due to the high bandgap, which is only 5% of the solar spectrum. Due to this reason, visible light photocatalysis has attracted researchers to develop novel visible light active materials, in order to fully harvest the solar spectrum. Various modifications have been carried out to  $\text{TiO}_2$  to reduce its bandgap and tune it to become functional in the visible range of light. Besides  $\text{TiO}_2$ , many novel materials absorb photons in the visible light range, for instance,  $g\text{-C}_3\text{N}_4$ .

$g\text{-C}_3\text{N}_4$  is a recently reported, attractive, metal-free polymeric semiconductor consisting of heptazine networks, which has attracted much attention attributing to its wide range of applications [62].  $g\text{-C}_3\text{N}_4$  possesses excellent thermal and chemical stability, along with electronic and optical properties. Additionally, it is straightforward to synthesize, which is beneficial for large-scale synthesis, and it has visible light absorption at around 430 nm with a suitable bandgap of 2.7 eV [63, 64]. It has recently been used for oxidation and reduction applications, for instance,  $\text{CO}_2$  reduction,  $\text{H}_2$  reduction, and degradation of organic pollutants [65-69].

Most photocatalysts are primarily active under UV irradiation ( $\lambda < 385$  or bandgap  $< 3.0$  eV), which corresponds to only a small portion of the solar light. Particularly,  $\text{TiO}_2$  is one semiconductor, which is majorly active in the UV range, due to its high bandgap energy of 3.0 - 3.2 eV. This high bandgap prevents the material from using the visible portion of the solar light. Recently, different techniques have been employed to modify the semiconductor materials to shift the bandgap in the visible range and make these materials capable of using

the visible light ( $\lambda = 400\text{-}700\text{ nm}$ ). These techniques include doping, templating, exfoliation, sensitization, and composite formation with small bandgap materials [70, 71].

Metal ion doping has been majorly used and studied to enhance photocatalytic activity under light irradiation. Recently, considerable efforts have been directed towards visible light photocatalysis by metal-doped materials, as many of these doped materials have shown absorption in the visible light range. This visible light absorption is due to the excitation of electrons of metals doped on the semiconductor material to the conduction band. Different metal/transition metals (platinum, nickel, ruthenium, copper, and iron) and rare earth metals (lanthanum, cerium, and ytterbium) have been studied as a dopant for visible light photocatalysis. However, metal ion dopants may also serve as a recombination center, resulting in decreased photocatalytic activities [72, 73].

Non-metallic doping is also a research area, which has been extensively explored for visible light active semiconductor materials. Non-metallic elements, namely nitrogen (N), sulfur (S), and carbon (C), are some elements that have been tested. Doping aims to narrow the bandgap and bring the photocatalytic activity to the visible light region. Unlike metal ions, non-metallic dopants replace lattice oxygen, and are less likely to form recombination centers [74, 75].

Besides the elements involved in doping, the impact of the physical structure of the catalyst has also been studied. The clay minerals are layered materials that were the first to be artificially exfoliated. Subsequently, this process of exfoliation was applied to various layered structures. Novoselov and Geim [76] successfully achieved the exfoliation of graphene via mechanical exfoliation, which facilitated original research focusing on different nanosheet-based materials. There are several ways of carrying out exfoliation: chemical, ultrasonic, and thermal [76, 77].

Sensitization involves coupling a small bandgap to a high bandgap material, in order to utilize the visible light range. In sensitization with organic dyes, dye molecule electrons excited by the visible light can be injected into the CB of the semiconductor, in order to initiate the catalytic reactions. In composite photocatalysts, the CB electrons photo-generated from a small bandgap semiconductor by absorbing visible light, can move into the CB of a large bandgap semiconductor. In contrast, the photo-generated holes are trapped in a small bandgap semiconductor [78].

The objective of the current thesis is to study the effects of various physical and chemical modifications on the structural, optical, surface, and morphological characteristics, as well as the efficiency of the  $g\text{-C}_3\text{N}_4$  in catalyzing redox reactions, i.e., pollutant degradation (oxidation reaction), and hydrogen production from water (reduction reaction). In addition, the photocatalytic reaction using the response surface methodology will be analyzed and studied.

Finally, the influence of light source and catalyst synthesis method on the photocatalytic activity of g-C<sub>3</sub>N<sub>4</sub> will be investigated.

This thesis consists of 7 chapters. The first three chapters are related to the introduction, theoretical and technological background, and the methodology used to conduct the research. Chapter 4 documents the results presented as four peer-reviewed published papers, including a summary of each paper.

- 1) The first paper reported the efficient degradation of phenol using metal-free bulk and exfoliated g-C<sub>3</sub>N<sub>4</sub> utilizing visible light from a LED and a xenon lamp.
- 2) The second paper assessed the non-metallic (sulfur, phosphorous, and oxygen) doped g-C<sub>3</sub>N<sub>4</sub> for efficient adsorption and photodegradation of endocrine-disrupting compounds.
- 3) The third paper studied the impacts of co-catalysts (Ni, Co, Cu) and the synthesis method on the photocatalytic activity of exfoliated g-C<sub>3</sub>N<sub>4</sub> for hydrogen production.
- 4) The fourth paper analyzed and modeled the photocatalytic degradation of phenol with exfoliated g-C<sub>3</sub>N<sub>4</sub> and LED using the response surface methodology

A thorough discussion and conclusion on the findings of the papers and a comprehensive analysis of the thesis topic are given in chapters 5 and 6. In chapter 7, the outlook for future work is presented.

## 2 Theoretical and technological background

### 2.1 Photocatalysis

According to the IUPAC (International Union of Pure and Applied Chemistry), catalyst is "a substance that increases the rate of a reaction without modifying the overall standard Gibbs energy change in the reaction." The essential characteristic of a catalyst is to modify reaction rate without being consumed during the process, and hence to be able to be reused in subsequent reactions. Catalysis is one of the most vital phenomena in nature and chemistry [79]. The number of exposed surface atoms need to be specified for a valid comparison of the catalytic activity. Thus a convenient way to express catalytic activity is by employing a turnover number (TON) equal to the number of reactant molecules converted per minute per catalytic site for given reaction conditions [80].

According to the IUPAC, photocatalysis is defined as a "change in the rate of a chemical reaction or its initiation under the action of ultraviolet, visible or infrared radiation in the presence of a substance—the photocatalyst—that absorbs light and is involved in the chemical transformation of the reaction partners." The term photocatalyst consists of 'photo' related to the light, and 'catalyst' related to the material, which absorbs that light. When light with a high energy wavelength interacts with a photocatalyst, the light gets absorbed, and electrons move from the valence- to the conduction band. These electrons can be removed more easily for the chemical transformation of the reactants, and this transformation is called a photocatalytic reaction. The process utilizing these photocatalysts is called photocatalysis, also known as semiconductor photocatalysis, due to the semiconducting nature of the material [81, 82]. The photocatalyst does not undergo any chemical change during and after the reaction. Photocatalysis replicates a similar approach to the natural process of photosynthesis (Fig 1). In this process, the sunlight is absorbed by chlorophyll in plants and produces starch and oxygen from carbon dioxide and water. The photocatalysis process is also known as artificial photosynthesis. [83]. 'Photokatalyse' and 'photokatalytisch' appeared probably for the first time in the textbook 'Photochemie', published by Plotnikov in 1910 [84].

There can be two categories of photocatalytic reactions based on the reactants and the reaction phase.

- 1) Homogeneous photocatalysis in which both reactants and photocatalysts are in the same phase.
- 2) Heterogeneous photocatalysis in which reactants and photocatalysts are in different phases.

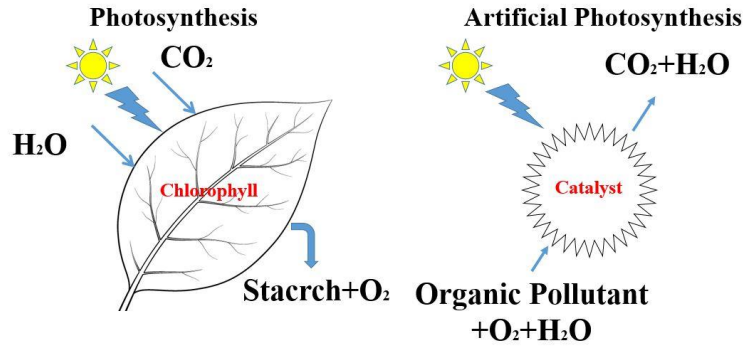


Figure 1: Natural and artificial photosynthesis

The energy band gap is essential in semiconductor photocatalysis, and there are two energy bands, i.e., the valence band and the conduction band. The valence band is the energy band that comprises valence electrons present in the outermost shell of an atomic structure. When provided with sufficient energy, these valence electrons change into free electrons and move to the conduction band, harnessing conductivity. A conduction band is an energy band that consists of free electrons responsible for the conduction of electrons. The electrons moving out from the valence band leave behind the holes in the valence band. The energy difference between the conduction- and the valence band is known as the bandgap ( $E_g$ ). Depending on the bandgap, the materials are classified into three basic categories (see Figure 2):

- metal or conductor: bandgap  $< 1$  eV
- semiconductor: bandgap between 1 and 3.5 eV
- insulator: bandgap  $> 5.0$  eV

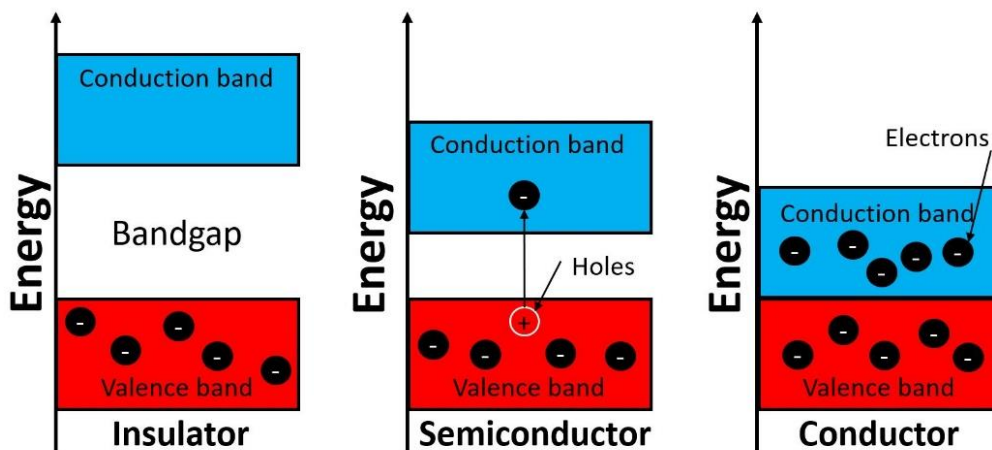


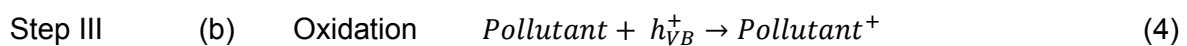
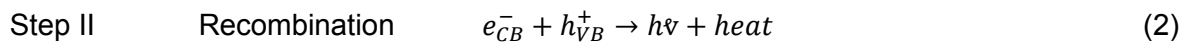
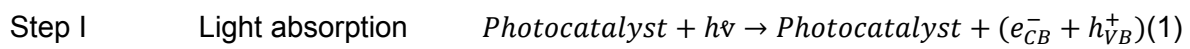
Figure 2: Bandgaps of different types of materials

## 2.2 Working principle and mechanism of photocatalysis

The main working principle governing photocatalysis, as shown in Figure 3 [85], is usually described via the following five-step [86] process:

1. transfer of the reactant to the surface of the photocatalyst.
2. adsorption of the reactant on the surface.
3. photonic activation and decomposition of adsorbed molecules.
4. reaction desorption of products.
5. removal of reaction products from the surface of the photocatalyst.

When a semiconductor material is irradiated with an equal or a higher energy light relative to its bandgap, absorption of photons by photocatalyst from light generates electron-hole pairs. Due to the absorption of photon energy by electrons, the electrons move from the valance- to the conduction band, generating holes in the valance band [87]. These electrons and holes carry out the oxidation and reduction reactions of the molecules adsorbed on the surface of the catalyst. One of the significant drawbacks of the photocatalytic process is the surface and volume recombination of the electron and holes, reducing the reaction rate, releasing the energy, and as a result, decreasing the overall efficiency of the process [88]. These electron-hole pairs may recombine, and the electrons ( $e_{CB}^-$ ) and holes ( $h_{VB}^+$ ), which do not recombine, may participate in oxidation and reduction reactions with the pollutants [83, 89-92]. The photocatalysis mechanism is a complex phenomenon, and the steps involved are explained here and summarized below in equations (1-4):



The reduction potential of electrons in the conduction band, and the oxidation potential of holes in the valance band, are the limiting factors. The bandgap energy of semiconductor materials, and the charge transfer rate, are the critical parameters for photocatalysis [93, 94].

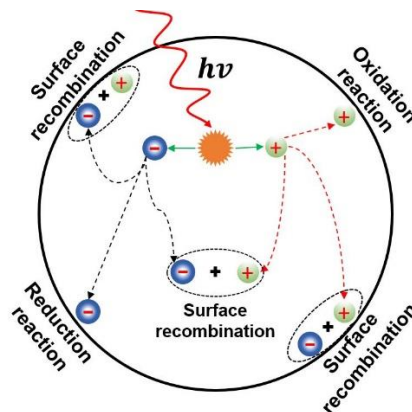


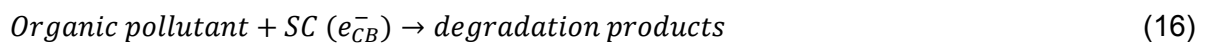
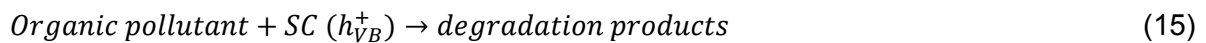
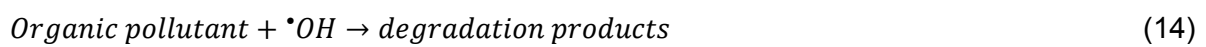
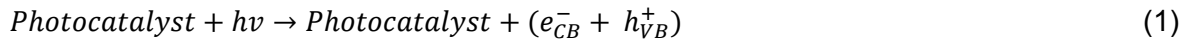
Figure 3: Photoexcitation, de-excitation, and surface recombination on the surface of the catalyst: a representative schematic of the process [85]

## 2.3 Applications of photocatalysis

Several applications, for instance, the production of hydrogen (H<sub>2</sub>), carbon dioxide (CO<sub>2</sub>) reduction, degradation of organic waste, and production of benzaldehyde, were investigated [50, 95, 96]. These applications can be categorized into either oxidation (pollutant degradation) reactions, or reduction (CO<sub>2</sub> reduction and water splitting) reactions [50, 96]. Photoreduction can also be used to reduce metal doping on the surface of the support materials, i.e., platinum, nickel, and copper [97]. Since the key focus of this thesis concerns the reduction and oxidation applications, the photocatalytic mechanisms of these two are described here.

### 2.3.1 Oxidation pollutant degradation

Persistent organic pollutants can be degraded and removed even at very low concentrations, assisted via semiconductor photocatalysis [48, 83, 98]. As discussed earlier, the holes produced in the valence band embody the active species in oxidation reactions. These holes also possess strong oxidation properties, or they react with H<sub>2</sub>O to produce hydroxyl radicals (<sup>•</sup>OH), which are also potent oxidants with an oxidation potential of 2.8 eV (NHE). The generated hydroxyl radicals may attack the adsorbed pollutants either at the surface or in the solution, leading to the synthesis of CO<sub>2</sub> and H<sub>2</sub>O via the degradation of the pollutants. The mechanism of oxidation reactions is extensively discussed in the literature [48, 98, 99] and is only briefly explained here.





Eq. 1 represents the absorption of light by photocatalyst, and the generation of electrons and holes. Eqs. 5 and 6 represent the reactive oxygen species (ROS) generation using electrons and holes, and Eqs. 14, 15, and 16 represent the reaction using these electrons and holes. Several oxidants ( $\cdot OH$ ,  $H_2O_2$ ) can be responsible for the mineralization of the pollutant.

### 2.3.2 Hydrogen (H<sub>2</sub>) evolution reduction reaction

The fuel generation from water and CO<sub>2</sub>, using solar light and artificial photosynthesis, is one of the promising ways of producing H<sub>2</sub>, syngas, and hydrocarbons, as sustainable energy and chemical feedstock [100]. Hydrogen is one of the essential alternative energy sources to fossil fuels. The dissociation of the water molecule to yield hydrogen and oxygen occurs according to the equation [101]:



This reaction has gained a lot of interest, since it can provide clean H<sub>2</sub> from a cost-effective and environmentally abundant raw material, which is water. The major problem is that water is very stable and would require a 2500 K temperature to dissociate at atmospheric pressure. The photochemical dissociation provides a feasible alternative, as photons can provide energy to react. However, the photocatalyst only reduces the energy barrier and allows the water dissociation reaction to occur [101]. For an actual photocatalytic water splitting, the conduction band energy must be negative enough compared to NHE, in order to generate photoexcited electrons that can reduce water [102, 103].



Redox potential (also known as oxidation/reduction potential) is a measure of the tendency of a chemical species to acquire electrons (Eq. 20) from or lose electrons (Eq. 21) to an electrode, and thereby be reduced or oxidized, respectively. The redox potential for the overall reaction at pH = 7 is  $E_H = -1.23$  V (NHE) with an overall  $\Delta G^\circ = 237$  kJ/mol. Most of the catalysts display poor activity for hydrogen production under visible light, due to low redox potential, high recombination rate, and absence of charge separation. Although, with the addition of a co-catalyst and a hole scavenger, the electrons and holes should be rapidly captured by the co-catalysts for efficient separation and transfer of photo-generated charges, and participation in the reduction reactions on the surface, which is critically important for photocatalytic water splitting [104].

## 2.4 Photocatalysts and their properties

An efficient photocatalyst must possess several common features for any catalyst, such as high surface area and low recombination rate. In addition, a photocatalyst should combine the properties of the semiconductor with other desirable properties, as listed in Table 1.

Table 1: Desirable properties of a photocatalyst [105].

Desired property	Benefits of the property
High surface area	Small particle size can help achieve high surface area, which can result in high adsorption of pollutants
Single site structure	Crystallinity helps toward the single sites and enhances homogeneity
Light absorption	Bandgap engineering increases the light absorption and results in higher efficiency
Efficient charge separation	Low recombination is the result of the efficient charge separation and directs the reaction in a specific direction
Long lifetime of charge separation	The addition of co-catalysts increases the lifetime of the charges and, as a result, the possibility of chemical reactions
Selectivity towards a single product	Adequate co-catalysts can increase the selectivity of the reaction and enhance the efficiency of the chemical process

## 2.5 Graphitic carbon nitride

g-C<sub>3</sub>N<sub>4</sub> is a recently reported, promising, metal-free polymeric semiconductor, consisting of heptazine networks. It has attracted much attention due to its wide range of applications, as well as optical and surface properties [62]. g-C<sub>3</sub>N<sub>4</sub> is generally synthesized using nitrogen-rich precursors, such as melamine, urea, thiourea, or cyanamide, via thermal decomposition, forming two-dimensional tri-s-triazine sheets [106]. There are numerous additional semiconductor materials reported in the literature, such as, titanium dioxide (TiO<sub>2</sub>) [96] and zinc oxide (ZnO) [107], which are photoactive, and possess favorable characteristics for carrying out the reaction. These semiconductor materials also suffer from certain limitations, for instance, a high recombination rate and bandgap. The high bandgap (3.3–3.5 eV) materials can absorb the UV portion of the sunlight, representing only 5% of the whole spectrum. The high recombination rate of electrons and holes leads to the lower efficiency of the process [108-111]. A bandgap comparison, corresponding to different semiconductor materials, is shown in Figure 4. The materials with a bandgap exceeding 3 eV are generally active in the UV range, while those with a bandgap below 2.6 eV can be activated by visible light. g-C<sub>3</sub>N<sub>4</sub> possesses a bandgap in the range of 2.4-2.7 eV, making it photoactive in the visible range. g-

$C_3N_4$  demonstrates noteworthy thermal and chemical stability, along with electronic and optical properties. It is also straightforward to synthesize, which is beneficial for a large-scale synthesis, and absorbs light in the visible range at around 430 nm, with a suitable bandgap of 2.7 eV [63, 64]. It has recently been used for oxidation and reduction applications, for instance,  $CO_2$  reduction,  $H_2$  reduction, and degradation of organic pollutants [65-69].

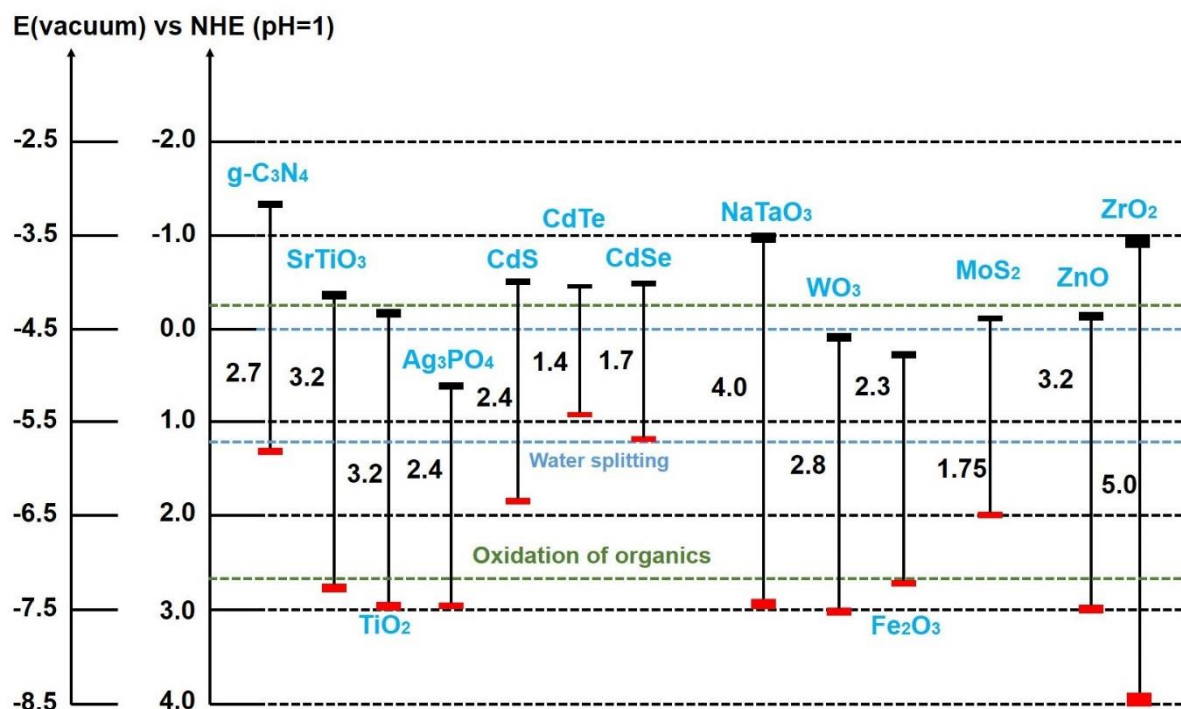


Figure 4: Bandgap energy of different semiconductors [83]

Bulk materials are 3D materials that differ from modified nanomaterials based on several features, such as porosity, surface area, morphology, and optical properties. While the surface area influences the adsorption capacity, the quantum confinement effects influence the electrical and optical properties of the materials [112]. The modifications in bulk materials enhance the properties of the material, and can enhance charge transfer, light absorption, and material adsorption, resulting in a better efficiency of the photocatalytic process. Nanostructured  $g-C_3N_4$ , i.e., nanoparticles, nanotubes, and nanosheets, have recently attracted much attention [113-115]. In its current state-of-the-art, the reported  $g-C_3N_4$  in literature is divided into the following categories, based on its geometric dimension: 0-dimensional  $g-C_3N_4$  ( $g-C_3N_4$  quantum dots); 1-dimensional  $g-C_3N_4$  ( $g-C_3N_4$  tubes); 2-dimensional  $g-C_3N_4$  ( $g-C_3N_4$  nanosheets); and 3-dimensional  $g-C_3N_4$  (nanoporous  $g-C_3N_4$  microspheres) [116].

The dimensions of carbon materials bear a crucial impact on the photoelectric properties of the material [117-119]. The basic properties of different dimensional materials are shown in Table 2, and the morphology is displayed in Figure 5.

Table 2: Basic properties of different carbon materials based on varied dimensions

Dimension	Representative material	Basic property
0D	Fullerene, carbon quantum dots	Nonlinear optical property, low density
1D	Carbon nanotube (CNT), carbon nanowires	Good conductivity, hydrogen storage capacity, diathermancy
2D	Graphene, graphdiyne	High specific surface area, electronic transmission capacity
3D	Carbon sphere, carbon shell, porous carbon	High specific surface area, designability, multihole

0-dimensional materials, like quantum dots, are of great interest in photocatalysis. A thermal etching process is used for synthesizing the g-C<sub>3</sub>N<sub>4</sub> quantum dots. The 0-D quantum dots are synthesized using the hydrothermal treatment of 1D g-C<sub>3</sub>N<sub>4</sub>. These quantum dots are stable under ambient conditions and are photoactive even in a long-wavelength light (705-862 nm) [120-122]. The 1D functional nanocarbon materials, used for modification of g-C<sub>3</sub>N<sub>4</sub>, are mainly carbon nanotubes (CNTs) with different nanofibers (CNFs) [123]. Recently, there has been a lot of interest in 1D nanostructures due to their morphology and characteristics [124-126]. The 1D nanorods exhibit high surface area and excellent optical properties. Nanorods are produced from 2D materials by rolling up nanosheets due to exfoliation and regrowth. A large-scale synthesis of g-C<sub>3</sub>N<sub>4</sub> nanorods, using thermolysis of molecular precursors under heat treatment, was demonstrated by Zhihong and co-workers [127]. 2D materials are sheet-like, and showcase superior surface, morphological, and optical properties. These materials typically possess a high surface area, decent crystallinity, excellent light absorption, and improved charge separation. 2D g-C<sub>3</sub>N<sub>4</sub> nanosheets were synthesized by Ping and co-workers using a direct thermal-oxidative "etching" of bulk g-C<sub>3</sub>N<sub>4</sub> under air [128]. In this cost-effective, rapid, and scalable synthesis method, the hydrogen bonds in the structure were removed by thermal treatment, and the thickness of the bulk g-C<sub>3</sub>N<sub>4</sub> was reduced. Besides thermal exfoliation, certain additional strategies have been employed to synthesize the 2D g-C<sub>3</sub>N<sub>4</sub> nanosheets, using liquid exfoliation with water, methanol, or isopropanol as solvents [129, 130]. 3D nanomaterials provide the opportunity to design novel and efficient photocatalyst systems. For instance, hierarchical 3D nanoporous g-C<sub>3</sub>N<sub>4</sub> was synthesized using a solvothermal method without any template [131, 132]. In this work, 2D and 3D g-C<sub>3</sub>N<sub>4</sub> were synthesized and used for different applications.

### Heterogeneous Nanostructured Materials with Different Morphologies

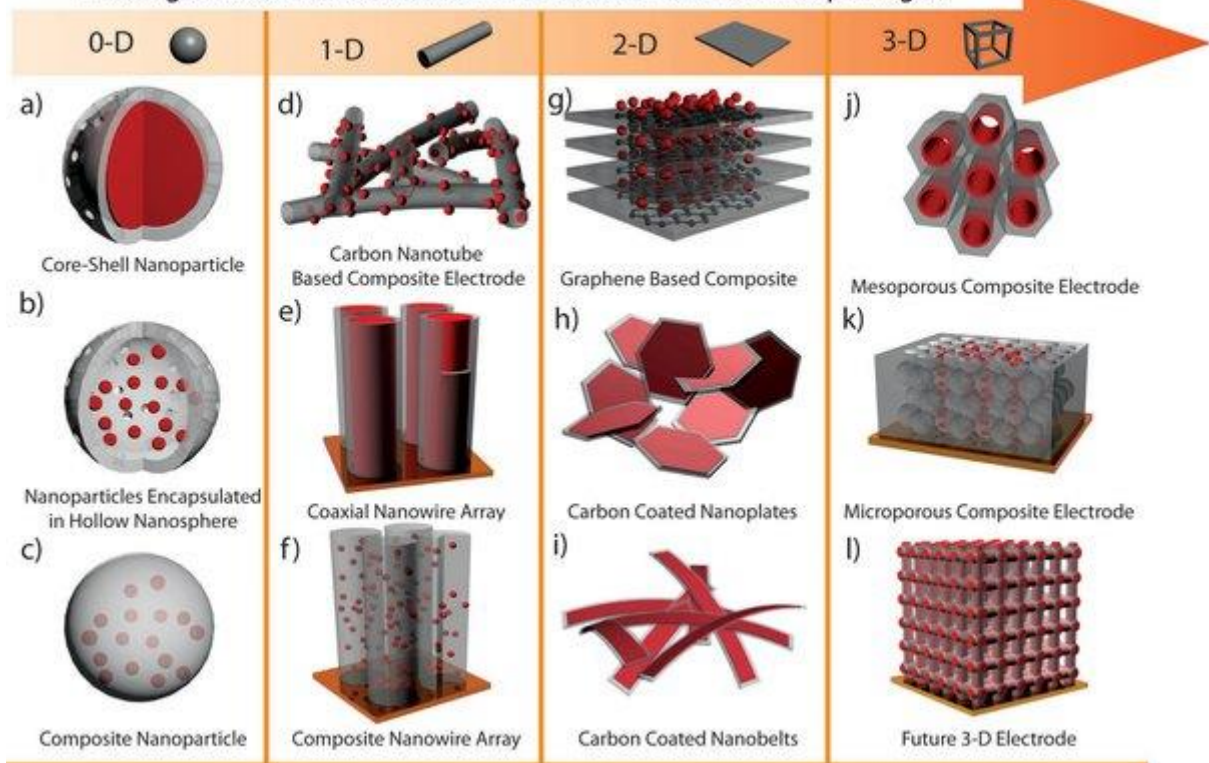


Figure 5: Schematic of heterogeneous nanostructures based on 0D (a), 1D (b), 2D (c) and 3D (d) structure [133]

### 3 Methodology

This chapter briefly presents the synthesis procedures of bulk and modified g-C<sub>3</sub>N<sub>4</sub>, characterizations, and analytical methodologies. The key characterization techniques used to study the properties of the synthesized material, and instruments used for these characterizations, are discussed below. The application methodologies were already discussed in the papers.

#### 3.1 g-C<sub>3</sub>N<sub>4</sub> synthesis methods

g-C<sub>3</sub>N<sub>4</sub> used in this work was synthesized using different synthesis methods. These synthesis methods are explained in detail in the respective papers and briefly summarized in Table 3 below.

Table 3: Synthesis procedure for bulk, exfoliated and modified g-C<sub>3</sub>N<sub>4</sub>

Material	Precursor	Temperature
Bulk g-C <sub>3</sub> N <sub>4</sub>	Melamine	450 °C and 550 °C
Exfoliated g-C <sub>3</sub> N <sub>4</sub>	Bulk g-C <sub>3</sub> N <sub>4</sub>	500 °C
Metal loaded g-C <sub>3</sub> N <sub>4</sub>	Metal salt and exfoliated g-C <sub>3</sub> N <sub>4</sub>	80 °C
Non-metal doped g-C <sub>3</sub> N <sub>4</sub>	Acid-functionalized melamine	450 °C and 550 °C
g-C <sub>3</sub> N <sub>4</sub> composite	Exfoliated g-C <sub>3</sub> N <sub>4</sub> and TiO <sub>2</sub>	Room temperature

#### 3.2 Characterization methods

The morphological, structural, chemical, optical, and surface properties of the catalyst synthesized in this work are summarized in Figure 6. Morphology was studied using scanning (SEM) and transmission (TEM) electron microscopy. XPS, XRD, and FTIR were used for studying chemical and structural properties. Ultraviolet-visible spectroscopy (UV-Vis) and PL were used for characterizing the optical properties. Surface properties were studied using BET and zeta potential techniques.

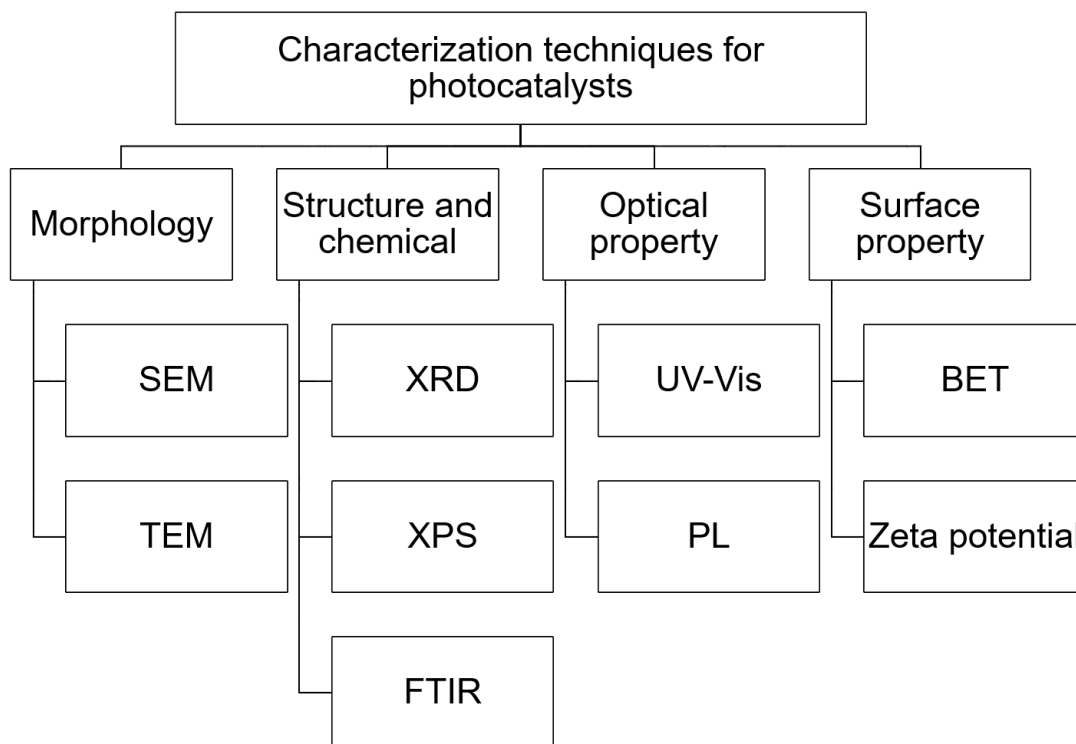


Figure 6: Different characterization techniques for photocatalysts

### 3.2.1 Powder X-ray diffraction (PXRD)

The PXRD technique identifies the crystalline structures of the material. X-ray radiations are used to generate a diffraction pattern interpreted in the angular position  $2\theta$  and the intensity of the diffracted X-rays to determine the inter-lattice spacing  $d$ . In this work, the PXRD measurements were performed to confirm the crystalline structures of bulk  $g\text{-C}_3\text{N}_4$ , exfoliated  $g\text{-C}_3\text{N}_4$ , and doped  $g\text{-C}_3\text{N}_4$  using the PXRD instrument (Cu  $K\alpha$  radiation,  $1.54 \text{ \AA}$  at 40 kV, 40 mA). Mostly, the PXRD patterns were recorded in the  $2\theta$  range from  $10^\circ$  to  $90^\circ$ .

### 3.2.2 $\text{N}_2$ physisorption measurements (BET)

The BET method determines the physical adsorption of gas molecules on the surface of the material, to measure the specific surface area. The analysis is performed by the physisorption of  $\text{N}_2$  gas at the boiling point (77K). The BET isotherms represent the number of  $\text{N}_2$  gas molecules adsorbed and desorbed on the material surface within a relative pressure range of 0 to 1. This work measured surface properties, such as specific surface area, micro/mesopore volumes, and pore size distribution (PSD) of  $g\text{-C}_3\text{N}_4$  and its derivatives. The measurements were carried out on an autosorb @iQ-MP/XR (Nova 4200e), Quantachrome instrument (Germany) apparatus equipped with a micropore port ( $1 \times 10^{-5}$  bar) via the conventional volumetric technique. Before the surface area analysis, the samples were degassed at  $120^\circ\text{C}$  for 3 hours under a vacuum.

### **3.2.3 Fourier-transform infrared spectroscopy (FTIR)**

The FTIR spectroscopy identifies functional groups in solid, liquid, or gaseous materials. The incident radiations are transmitted and absorbed through the material. The absorbed/transmitted energies of IR are interpreted by the Fourier transform function and displayed in a spectrum. The peaks in a spectrum represent the IR active vibrational modes (fingerprints) such as stretching, bending, twisting, or oscillating chemical bonds [134]. In this work, the FTIR spectra of the g-C<sub>3</sub>N<sub>4</sub> and its derivatives were recorded in the range of 4000-400 cm<sup>-1</sup> on a Spectrum Two FT-IR Spectrometer (PerkinElmer, Switzerland) with a universal ATR (UATR Two) cell equipped with a ZnSe single crystal.

### **3.2.4 X-Ray photoelectron spectroscopy (XPS)**

XPS is a spectroscopic technique that determines chemical states, elemental composition, overall electronic structure, and density of the electronic states of the materials. Typically, the sample is irradiated with an x-ray under ultra-high vacuum conditions, to gather information about the atomic concentrations, chemical states, and electronic configuration of the element. Elements show peaks at specific binding energies, representing the electronic configuration, such as, 1s, 2s, 2p, 2s, and 3d [135, 136]. In this work, the surface chemical analyses of g-C<sub>3</sub>N<sub>4</sub> and its derivatives were obtained by Thermo Scientific (Waltham, MA, USA) K Alpha and X-ray Photoelectron Spectrometer. All samples were analyzed using a micro-focused, monochromated Al K  $\alpha$  X-ray source (1486.68 eV: 400  $\mu$ m spot size). The analyzer had a pass energy of 200 eV (survey) and 50 eV (high-resolution spectra), respectively.

### **3.2.5 UV-visible spectroscopy (UV-Vis)**

UV spectroscopy or UV-visible spectrophotometry refers to absorption or reflectance spectroscopy in part of the ultraviolet and the full, adjacent visible regions of the electromagnetic spectrum. Generally, it is used to calculate the energy bandgap of the material between the valence band (the highest occupied molecular orbital, HOMO) and the conduction band (the lowest unoccupied molecular orbital, LUMO). The UV-Vis spectrophotometer measures the intensity of incident light before and after passing through the sample, and the difference in energy is used to calculate the energy bandgap. The UV-Vis spectra are plotted as the intensity of the absorbed light as a function of the light wavelength. This work recorded the UV-Vis absorption spectra of g-C<sub>3</sub>N<sub>4</sub> and its derivatives using a UV-3600 Plus (Shimadzu, Kyoto, Japan) spectrometer. A medium scan speed, using a 20-slit width with three external detectors in the 200–800 nm range, was used, and Tauc plots calculated the energy bandgaps.

### **3.2.6 Transmission electron microscopy (TEM) and Energy dispersive X-ray spectroscopy (EDX)**

TEM uses electrons transmitted through the sample to create an image of the sample. Electrostatic and electromagnetic lenses are used to control the trajectory of the generated



electrons. The incident beams passing through the sample produce the electrons, which generate the image of the material. TEM can study the growth of layers, composition, and defects in semiconductors. High-resolution TEM can analyze quantum wells, wires, and quality, shape, size, and density of the dots. The EDX is studied to quantify and identify the elements present in the material [137, 138]. In this work, high-resolution TEM images were recorded using JEM 1400 plus (JEOL, Akishima, Japan) microscope (LaB6 filament) using Quantifoil S7/2 (2 nm carbon film) grids and a CCD camera (Ruby) at 120 kV.

### **3.2.7 Scanning electron microscopy (SEM)**

SEM is used to investigate the morphology and surface topography of the materials. An electron beam is generated from an electron gun, accelerating between the cathode and the anode, by applying a certain voltage. The condenser and the objective lens are used to demagnify the electron beam, thereby generating a sharp image. SEM can provide morphological information, such as shape, size, and surface texture of the sample. This work recorded SEM images using an SEM-type microscope operated at an acceleration voltage of 10 kV, and a probe current of 15 Pa [139, 140].

## **3.3 Analytical methods**

### **3.3.1 High-performance liquid chromatography (HPLC)**

The concentrations of phenol and hormones (17 $\beta$ -estradiol and 17 $\alpha$ -ethinylestradiol) were analyzed using a Prominence 3.4.1 High-performance liquid chromatography (HPLC) system, (Shimadzu, Japan) comprising a binary pump (LC-20AB), a SIL-20A autosampler, a DGU-20A3 degasser, and an SPD-M20A diode-array detector. The analysis was conducted with a Phenomenex (C18, 150 mm  $\times$  4.6 mm, 3  $\mu$ m) column at a fixed flow rate of 0.8 mL/min, using water (A) and acetonitrile (B) as a mobile phase. Phenol and xylenol were analyzed at a wavelength of 270 nm, catechol at 277 nm, and m-cresol at 273 nm. 17 $\beta$ -estradiol and 17 $\alpha$ -ethinylestradiol were analyzed at a wavelength of 205 nm. The intermediates of the hormone degradation were identified using LC-MS. The following MS conditions were used: dual ion source (DUIS),  $m/z$  range 50-500, negative ionization mode, nebulizing gas flow 2 L min<sup>-1</sup>, drying gas flow 15 L min<sup>-1</sup>, DL temperature 300 °C, heat block temperature 500 °C.

## **3.4 Mathematical methods**

### **3.4.1 Response surface methodology**

The mathematical technique used in this work is the RSM, an optimization technique commonly used for experimental design data and an efficient system analysis [141-143]. It uses mathematics and statistics to study and analyze the influence of the experimental parameters (independent) on the response of the system (dependent). It helps predict the effects of individual experimental operating parameters and their interactions on a response variable. Design of experiment (DoE) uses a systematic technique to vary all parameters

simultaneously, and RSM evaluates the influence of these parameters [144, 145]. DoE uses a systematic approach for the experimental design, which mostly requires fewer experiments, thus reducing the time required to analyze the system, in addition to being more economical. For designing experiments, CCD [146] and BBD [142, 143] are most commonly used. Since BBD requires fewer experiments than CCD [146], it was selected as a preferred design approach [56].

## 4 Results

This section contains the outcomes of four investigations published within the framework of this thesis and reprinted with permission from respective journals. In Paper I (Section 4.1), the exfoliated g-C<sub>3</sub>N<sub>4</sub> was synthesized and tested for photocatalytic degradation of phenol in aqueous solutions using two lamps. In Paper II (Section 4.2), non-metallic (O, S, and P) functionalization of melamine was performed to synthesize doped g-C<sub>3</sub>N<sub>4</sub> and tested for adsorption and photocatalytic degradation of hormones. Paper III (Section 4.3) compares different methods for synthesizing non-noble metal-based g-C<sub>3</sub>N<sub>4</sub> for photocatalytic water splitting. Finally, in Paper IV (Section 4.4), the Response surface methodology (RSM), involving a Box–Benken design (BBD), was employed to analyze the photocatalytic degradation of phenol using exfoliated g-C<sub>3</sub>N<sub>4</sub> and LED (wavelength = 430 nm).

#### **4.1 Paper I: Efficient Advanced Oxidation Process (AOP) for photocatalytic contaminant degradation using exfoliated Metal-Free Graphitic Carbon Nitride and Visible Light-Emitting Diodes**

Adeem Ghaffar Rana, Mino Tasbihi, Michael Schwarze, and Mirjana Minceva

Catalysts 11 (6), 662 (<https://doi.org/10.3390/catal11060662>)

**Author contribution:** The thesis author conceptualized the paper's idea, performed the experiments, and characterized the catalysts (excluding XRD). He evaluated and interpreted the experimental results and wrote the manuscript draft.

##### **Summary:**

Polluted water is grossly harmful towards humans and the ecosystem, with phenol being the major pollutant from pharmaceutical, textile, pesticide, and petrochemical industries. Several conventional technologies, commonly used to remove phenolic pollutants, practically are not able to remove these pollutants completely. The small pollutant molecules are difficult to remove, and waste is produced during the utilization of these conventional technologies. Photocatalysis provides the opportunity to completely degrade the pollutant to smaller, but not harmful molecules. Conventional photocatalysts ( $\text{TiO}_2$ ,  $\text{ZnO}$ ) are only active in the UV range, so  $\text{g-C}_3\text{N}_4$ , which is active in the visible range, was chosen for this study. A xenon lamp and LED lamp provide the opportunity to irradiate the visible light in a full spectrum of wavelength, and at a specific single wavelength, respectively. The aim of Paper I was to study the photocatalytic advanced oxidation process using metal-free graphitic carbon nitride, under the influence of a single wavelength visible light LED lamp, in order to remove phenol. Individual lamps were previously used for photocatalytic degradation. However, this work was the first to conduct a comparative study between a LED- and a xenon lamp. This work studied the effects of exfoliation on the property, structure, and catalytic activity of  $\text{g-C}_3\text{N}_4$ . In addition, it assessed the influence of different operating parameters on the photocatalytic performance of the catalysts, including evaluating their re-usability. The exfoliated metal-free  $\text{g-C}_3\text{N}_4$  was tested for other phenolic compounds as well.

This paper synthesized the bulk and exfoliated  $\text{g-C}_3\text{N}_4$  using melamine via the thermal decomposition method, and the  $\text{TiO}_2$  and  $\text{g-C}_3\text{N}_4$  composites. A comparative (two lamps) and parametric (catalyst concentration, pollutant concentration, pH, and oxygen concentration) study was conducted. Bulk  $\text{g-C}_3\text{N}_4$  was exfoliated thermally, which helped to improve the material's surface area from 11 to 170  $\text{m}^2/\text{g}$ , aggregated 3D morphology to nanosheets, and photocatalytic activity. A glass jacketed reactor with a working capacity of 225 ml, with the immersion lamp of 1 cm away from the reaction medium, was used for experimentation. The experiments showed that the exfoliated material performed better than the bulk material under the LED light. Exfoliated  $\text{g-C}_3\text{N}_4$  degraded the phenol (20 ppm) entirely, while bulk  $\text{g-C}_3\text{N}_4$

degraded only 40% of the pollutant in 90 mins. The effects of catalyst and pollutant concentrations were studied, showing that an increased catalyst amount increases the efficiency, while showing a contrasting relationship with an increased pollutant quantity. Acidic pH favored the reaction due to the positive charge on the surface, as the positive surface attracted the negatively charged molecules. Finally, the effect of oxygen on the degradation efficiency was studied. In the presence and absence of external oxygen, the efficiency was 100% and 40% for 20 ppm phenol, respectively. Oxygen plays a vital role in trapping the photoinduced electron produced by the photo-activation of catalysts. Reutilization tests confirmed that the catalyst is stable and can be used for at least 3 cycles. The catalyst was also tested for other phenolic compounds (catechol, m-cresol, and xylenol), which proved equally effective for their removal.

This work concluded that the exfoliated g-C<sub>3</sub>N<sub>4</sub> effectively degrades the phenolic compound in water using a single wavelength (430 nm) LED lamp. Exfoliation improves the surface area and activity, eventually producing an excellent performance to degrade these pollutants.

## Article

# Efficient Advanced Oxidation Process (AOP) for Photocatalytic Contaminant Degradation Using Exfoliated Metal-Free Graphitic Carbon Nitride and Visible Light-Emitting Diodes

Adeem Ghaffar Rana <sup>1,2</sup> , Minoo Tasbihi <sup>3</sup> , Michael Schwarze <sup>3</sup> and Mirjana Minceva <sup>1,\*</sup> 

- <sup>1</sup> Biothermodynamics, TUM School of Life Sciences Weihenstephan, Technical University of Munich, Maximus-von-Imhof-Forum 2, 85354 Freising, Germany; adeem.rana@tum.de
- <sup>2</sup> Department of Chemical, Polymer and Composite Materials Engineering, University of Engineering and Technology (UET), Lahore 39161, Pakistan
- <sup>3</sup> Department of Chemistry, Technische Universität Berlin, Str. des 17. Juni 124, 10623 Berlin, Germany; minoo.tasbihi@tu-berlin.de (M.T.); michael.schwarze@tu-berlin.de (M.S.)
- \* Correspondence: mirjana.minceva@tum.de; Tel.: +49-8161-71-6170

**Abstract:** The photocatalytic performance of metal-free graphitic carbon nitride ( $g\text{-C}_3\text{N}_4$ ) was examined using visible light-emitting diodes (LEDs). A comparative and parametric study was conducted using the photocatalytic degradation of phenol as a model reaction. The  $g\text{-C}_3\text{N}_4$  photocatalyst was synthesized from melamine using thermal condensation, followed by a thermal exfoliation that increases the catalyst surface area from 11 to 170  $\text{m}^2/\text{g}$ . Different characterization techniques, namely X-ray powder diffraction, X-ray photoelectron spectroscopy, nitrogen adsorption using the Brunauer–Emmett–Teller method, ultraviolet-visible (UV–vis) spectroscopy, transmission electron microscopy, photoluminescence spectroscopy (PL), and zeta potential analysis, were used to characterize the photocatalyst. A comparison of the photodegradation experiments conducted with a full-spectrum xenon lamp and a custom-made single-wavelength LED immersion lamp showed that the photocatalyst performance was better with the LED immersion lamp. Furthermore, a comparison of the performance of exfoliated and bulk  $g\text{-C}_3\text{N}_4$  revealed that exfoliated  $g\text{-C}_3\text{N}_4$  completely degraded the pollutant in 90 min, whereas only 25% was degraded with bulk  $g\text{-C}_3\text{N}_4$  in 180 min because the exfoliated  $g\text{-C}_3\text{N}_4$  enhances the availability of active sites, which promotes the degradation of phenol. Experiments conducted at different pH have shown that acidic pH favors the degradation process. The exfoliated  $g\text{-C}_3\text{N}_4$  has shown high photocatalytic performance in the photodegradation of other phenolic compounds, such as catechol, m-cresol, and xylenol, as well.

**Keywords:**  $g\text{-C}_3\text{N}_4$ ; photocatalysis; LEDs; wastewater treatment; phenol



**Citation:** Rana, A.G.; Tasbihi, M.; Schwarze, M.; Minceva, M. Efficient Advanced Oxidation Process (AOP) for Photocatalytic Contaminant Degradation Using Exfoliated Metal-Free Graphitic Carbon Nitride and Visible Light-Emitting Diodes. *Catalysts* **2021**, *11*, 662. <https://doi.org/10.3390/catal11060662>

Academic Editor: Raúl Molina

Received: 29 April 2021

Accepted: 21 May 2021

Published: 23 May 2021

**Publisher's Note:** MDPI stays neutral with regard to jurisdictional claims in published maps and institutional affiliations.



**Copyright:** © 2021 by the authors. Licensee MDPI, Basel, Switzerland. This article is an open access article distributed under the terms and conditions of the Creative Commons Attribution (CC BY) license (<https://creativecommons.org/licenses/by/4.0/>).

## 1. Introduction

Phenol and its chemical derivatives are widely used in pharmaceutical, textile, pesticide, and petrochemical industries; therefore, they are characteristic pollutants in the effluent from these industries. Polluted water is harmful to human health and the ecosystem [1,2]. In this context, several efforts have been made to completely remove phenolic contaminants from wastewater using conventional methods, including adsorption [3,4], distillation [5], biological treatments [6], and chemical oxidation [7]; however, these techniques have their demerits. Heterogeneous photocatalysis has proven to be an effective and feasible method for removing organic contaminants, producing  $\text{CO}_2$  and mineral salts as byproducts [8]. Many research efforts have been devoted to the development of advanced oxidation processes (AOPs) using ultraviolet (UV) and visible light [9]. Sunlight has limitless energy, which can be used for the activation of photocatalysts; however, it has a wide wavelength range. In this regard, visible light-emitting diodes (LEDs) offer the selectivity and flexibility of a specific wavelength, the possibility of designing the reactor, and cost-efficiency for achieving controlled irradiation [10,11].

Many semiconductor materials reported in the literature, for example, titanium dioxide (TiO<sub>2</sub>) [12] and zinc oxide (ZnO) [13], are promising because of their availability, nontoxicity, and photostability. However, there are numerous drawbacks associated with these materials, such as (i) a high bandgap energy (3.3–3.5 eV), which limits their utilization to only the UV region of sunlight, i.e., 4% of the solar energy, and (ii) a high rate of recombination of electrons and holes, which is detrimental to the efficiency of the material [14–17].

Graphitic carbon nitride (g-C<sub>3</sub>N<sub>4</sub>) is a recently reported polymeric semiconductor consisting of heptazine networks, which has attracted much attention because of its wide range of photocatalytic applications [11]. It exhibits chemical and thermal stability along with promising optical and electronic semiconductor properties. The additional advantages of g-C<sub>3</sub>N<sub>4</sub> are its easy synthesis and suitable band gap (2.7 eV) [18,19] for the efficient use of solar light approximately 430 nm with sufficient energy to conduct oxidation and reduction applications, for example, H<sub>2</sub> production, CO<sub>2</sub> reduction, and degradation of organic pollutants [20–24].

Generally, g-C<sub>3</sub>N<sub>4</sub> can be synthesized via thermal decomposition of nitrogen-rich precursors, such as melamine, urea, thiourea, cyanamide, or dicyanamide, which results in the formation of two-dimensional tri-s-triazine sheets [25]. The main bottleneck limiting the practical application of pristine g-C<sub>3</sub>N<sub>4</sub> is the fast electron-hole recombination in the excited state, which results in a limited activity because of a low surface area [15]. In the design of photocatalysts, different strategies have been used to improve the surface area, such as templating, doping, or exfoliation [26]. Among these strategies, thermal exfoliation has attracted particular attention as a fast, easy, and efficient method to produce thin-layered g-C<sub>3</sub>N<sub>4</sub> of high quality. During the heating process of this procedure, oxygen-containing functional groups of g-C<sub>3</sub>N<sub>4</sub> decompose and generate large amounts of gas, creating sufficient pressure to overcome van der Waals interactions and further expand the layers to form porous frameworks [10]. More importantly, thermal exfoliation has been demonstrated as a convenient way to enhance the surface area, to introduce pores, and to tune the texture of the material [26].

In photocatalytic contaminant degradation, very reactive species are formed during irradiation that decomposes the contaminant, in the ideal case to CO<sub>2</sub> and water. The basic principle of conventional AOP involves the production of hydroxyl radicals (HO•) as reactive molecules, which can be generated from hydrogen peroxide (H<sub>2</sub>O<sub>2</sub>). Meanwhile, as a difference to conventional AOPs, the proposed mechanism of the photocatalytic degradation of organic pollutants using metal-free g-C<sub>3</sub>N<sub>4</sub> suggests the in situ production of reactive oxygen species via oxygen reduction so that no further auxiliaries are required [10,27].

The main objective of the present study was to carry out a comparative study between an LED and a xenon immersion lamp using exfoliated g-C<sub>3</sub>N<sub>4</sub>. Although LEDs have found their way into photocatalysis for water splitting [28] or contaminant degradation [10], comparative reports between light sources are rare. This is, to the best of our knowledge, the first comparative report of its kind for exfoliated g-C<sub>3</sub>N<sub>4</sub> using two different lamps. Using exfoliated g-C<sub>3</sub>N<sub>4</sub>, an LED immersion lamp, and phenol as a model pollutant, the effect of process parameters, such as pH, catalyst concentration, pollutant concentration, air flow, and exfoliation on the performance of the catalyst, was evaluated. The study was extended to the photodegradation of other phenolic compounds, including m-cresol, catechol, and xylenol.

## 2. Results and Discussion

### 2.1. Photocatalyst Characterization

The morphology of bulk and exfoliated g-C<sub>3</sub>N<sub>4</sub> was analyzed by TEM. Figure 1 presents the selected micrographs. The structure of bulk g-C<sub>3</sub>N<sub>4</sub> shows continuous and closed stacks with irregular aggregates. After the exfoliation, the material transformed into a thin nanosheet. The layer thickness was reduced, and the large layer split into a small nanosheet

because of exfoliation [15,29]. It can be inferred from these results that the exfoliation enabled the formation of porous nanosheets with increased specific surface area in g-C<sub>3</sub>N<sub>4</sub> [30].

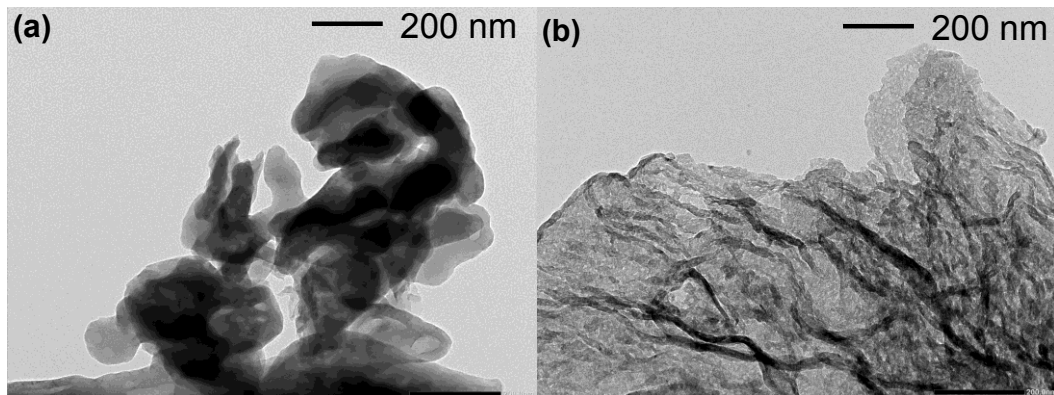


**Figure 1.** Transmission electron microscopy images of bulk (a) and exfoliated (b) graphitic carbon nitride (g-C<sub>3</sub>N<sub>4</sub>).

Specific surface areas were measured to reveal any change in the structural features of carbon nitride before and after the exfoliation. The surface area of exfoliated g-C<sub>3</sub>N<sub>4</sub> was significantly higher than that of bulk g-C<sub>3</sub>N<sub>4</sub> (170 and 11 m<sup>2</sup>/g, respectively), and the pore size distribution was also increased for the former, according to the TEM results. Hydrogen bonding and van der Waals forces were the main interactions contributing to the stacking between g-C<sub>3</sub>N<sub>4</sub> layers, and their removal caused the exfoliation into thinner layers. This process led to an increase in the surface area of the material.

Figure 2 shows the N<sub>2</sub> adsorption-desorption isotherms and BJH pore size distributions of bulk and exfoliated g-C<sub>3</sub>N<sub>4</sub>. Both samples show a hysteresis loop of type IV, suggesting the existence of a large number of pores. These characteristic curves for mesoporous materials stem from the difference in the curvatures of the meniscus during adsorption and desorption with a capillary condensation. The pore size distribution curves of both materials show a maximum at a radius of 1.9 nm, which means that the materials were mesoporous [31,32].

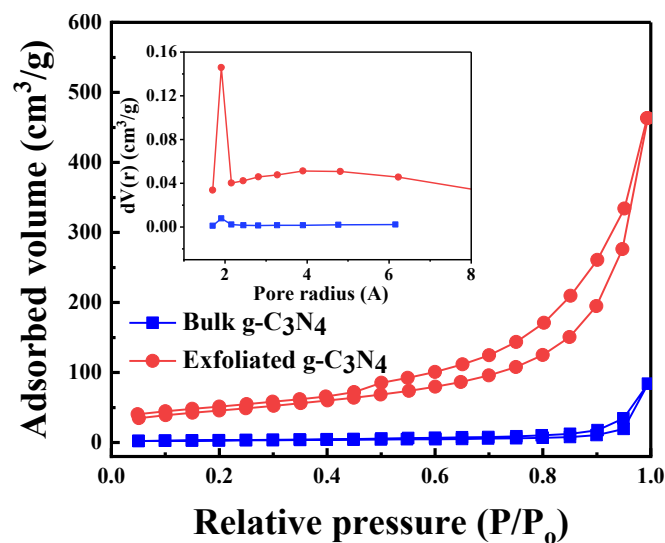


**Figure 2.** N<sub>2</sub> adsorption-desorption isotherms of bulk and exfoliated g-C<sub>3</sub>N<sub>4</sub>. The inset shows the corresponding Barrett–Joyner–Halenda pore size distribution curves of the samples.

To study the optical properties, bulk and exfoliated g-C<sub>3</sub>N<sub>4</sub> were characterized using UV–vis and PL spectroscopy. Figure 3a presents the PL spectra of bulk and exfoliated



g-C<sub>3</sub>N<sub>4</sub>. For the bulk g-C<sub>3</sub>N<sub>4</sub> catalyst, a strong PL emission band is observed at 458 nm, resulting from the direct interband electron-hole recombination. A second weaker emission band observed at approximately 525 nm can be attributed to the radiative recombination of charge carriers captured by traps (structural defects) [15,33]. The spectrum of exfoliated g-C<sub>3</sub>N<sub>4</sub> shows a blue shift, an increase in intensity, and a strong PL emission band at 436 nm. The blue shift of both bandgap and PL spectrum is most likely due to the quantum confinement effect, with the conduction and valence band shifting in opposite directions. Another possible reason is the reduction in conjugation length caused by the ultrathin structure of exfoliated g-C<sub>3</sub>N<sub>4</sub> [34–36].

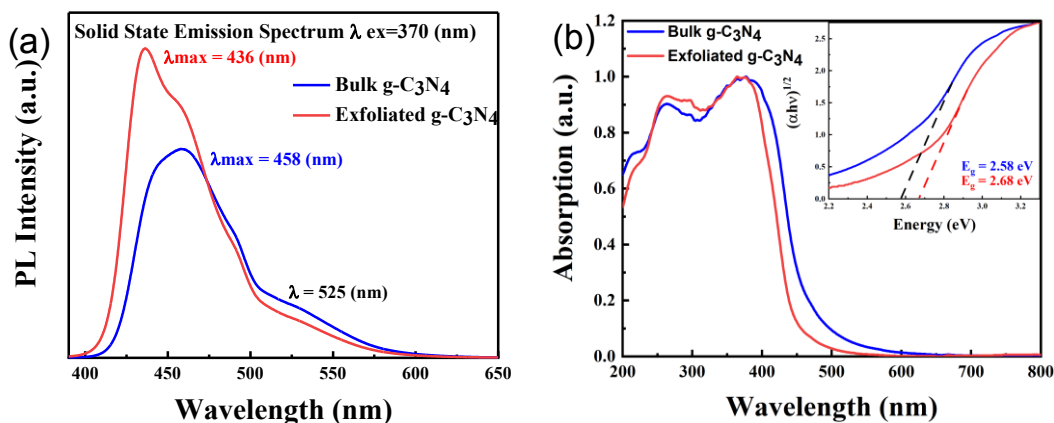


**Figure 3.** Photoluminescence spectra (a) Ultraviolet-visible absorption spectra (b) of bulk and exfoliated g-C<sub>3</sub>N<sub>4</sub>; the inset of (b) shows the Tauc plots.

Figure 3b shows the UV-vis absorption spectra and their respective Tauc plots (inset) of both materials. The absorption edges of exfoliated and bulk g-C<sub>3</sub>N<sub>4</sub> were estimated at 440 and 460 nm, respectively, indicating visible light response and a blue shift in the absorption edge from bulk to exfoliated g-C<sub>3</sub>N<sub>4</sub>. The general tauc plot equation used for band gap calculation is as follows:

$$(\alpha h\nu)^n = A(h\nu - E_g) \quad (1)$$

Here,  $\alpha$  is the absorption coefficient,  $h\nu$  is the incident photon energy,  $A$  is the constant,  $E_g$  is the band and  $n$  is the nature of transition. A standard value of  $n$  equal to  $1/2$  is preferable for graphitic g-C<sub>3</sub>N<sub>4</sub>, which is ideal for an indirect bandgap semiconductor. In Tauc plot method,  $h\nu$  is plotted on  $x$ -axis against  $(\alpha h\nu)^n$  on  $y$ -axis. Then, by extrapolating the linear part of the curve to a point where it intersects the  $x$ -axis is the optical band gap energy of the material. A slight increase in the bandgap of bulk g-C<sub>3</sub>N<sub>4</sub> from 2.58 to 2.68 eV was observed after the exfoliation [31,37], which can be attributed to the quantum confinement effect [34,36].

The chemical state and composition of bulk and exfoliated g-C<sub>3</sub>N<sub>4</sub> were analyzed by XPS, and the spectra corresponding to N1s and C1s are presented in Figure 4. The C1s spectra (Figure 4 a,b) of the samples show two strong peaks at 287.8 and 284.7 eV and two weak peaks at 286.2 and 293.5 eV. The weak peak at 293.5 eV corresponds to the  $\pi$  electron delocalization in C<sub>3</sub>N<sub>4</sub> heterocycles, and that at 286.2 eV is attributable to amino functional groups (C-NH<sub>2</sub>) bonded to the surface of g-C<sub>3</sub>N<sub>4</sub>. Meanwhile, the two strong peaks can be attributed to standard carbon bonds (C-C) and sp<sup>2</sup>-hybridized carbon (N-C=N) in triazine rings [26,38,39]. As can be seen in Figure 4 (c,d), the N1s spectra of the samples show several peaks. The strong peak at 397.8 eV corresponds to sp<sup>2</sup> nitrogen bonded to carbon (C-N-C) of triazine rings. The peaks of medium intensity at 399.1 and 400.1 eV can be attributed to the presence of tertiary N in N-(C)<sub>3</sub> units and amino functional groups (NH<sub>2</sub> or NH). The weak peak observed at 403.5 eV can be assigned to positive charge localization in the cyano group and heterocycles and/or NO<sub>2</sub> terminal groups [15,40–42]. As shown

in Figure 4, the binding energy of C1s and N1s core electrons does not shift significantly, which suggests that the chemical states of both carbon and nitrogen in the exfoliated are the same as in the bulk  $g\text{-C}_3\text{N}_4$  [43].

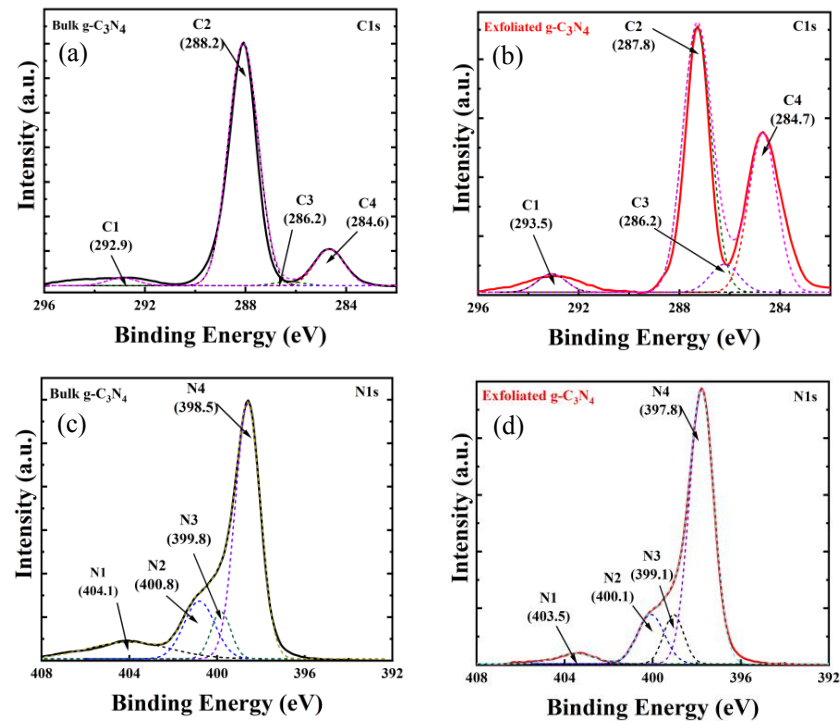


Figure 4. X-ray photoelectron spectra of bulk (a,c) and exfoliated (b,d)  $g\text{-C}_3\text{N}_4$  (C1s and N1s).

The catalysts were then subjected to XRD analysis to examine the phase structures of  $g\text{-C}_3\text{N}_4$  powders. As can be seen in Figure 5, the patterns of both bulk and exfoliated materials show a strong peak at  $2\theta = 27.2^\circ$  and a weaker peak at  $2\theta = 13^\circ$ . The strong peak can be indexed to the (002) plane, which is a characteristic interlayer stacking peak of aromatic  $g\text{-C}_3\text{N}_4$  systems. Moreover, the weak peak, which can be assigned to the (100) crystal plane, is attributable to repeated units of tri-*s*-triazine [15,34]. The decrease in the intensity of the diffraction peaks for the treated materials indicates a modification of the interlayer structures [44,45].

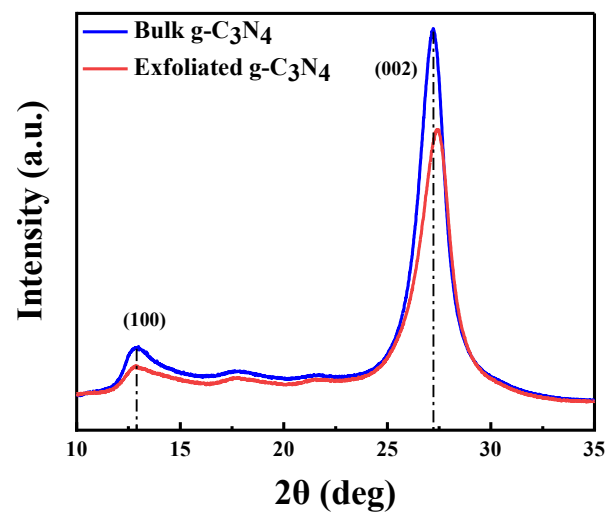
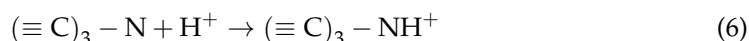
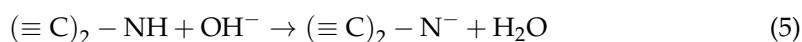
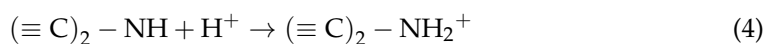
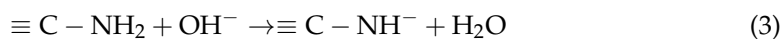


Figure 5. X-ray diffraction patterns of bulk and exfoliated  $g\text{-C}_3\text{N}_4$ .

The pH had a significant effect on the zeta potential of exfoliated g-C<sub>3</sub>N<sub>4</sub>. This effect was studied, and the results are shown in supplementary Figure S2. The possible ionization of primary, secondary, and tertiary amine groups on the surface of g-C<sub>3</sub>N<sub>4</sub> can be described by the following equations [46]:



Supplementary Figure S3 shows that the material surface is negatively charged in basic (pH = 10) and natural solutions (pH = 6.5) and positively charged at acidic pH (pH = 3), which is in accordance with Equations (2)–(6). The excess of protons H<sup>+</sup> in the system changes the overall charge on the surface to positive [46,47].

The bulk g-C<sub>3</sub>N<sub>4</sub> synthesized has less surface area and aggregate like structure which is converted to nanosheets and there is an increase in the surface area as the result of exfoliation. The base characteristics of g-C<sub>3</sub>N<sub>4</sub> remained the same, e.g., chemical structure and functional groups.

## 2.2. Photocatalytic Degradation of Phenol

The photocatalytic activity of the synthesized materials was studied using phenol as a model compound. The effect of the exfoliation process, light source, catalyst and pollutant concentration, pH, and dissolved oxygen on the photodegradation of phenol was studied in detail. The photolysis experiments were carried out without catalyst. All other experiments were carried out with water, phenol and catalyst reaction mixture. The homogeneous dispersion of the catalyst was ensured by sonicating the reaction mixture (water solution of phenol and catalyst), followed by stirring for 30 min in the dark. The photolysis experiments were conducted only under the influence of light without any catalyst. The reaction starts as soon as the light is turned on, before that there is only adsorption process.

### 2.2.1. Effect of Exfoliation

The photodegradation of phenol (initial concentration of 20 ppm) using 0.5 g/L bulk or exfoliated g-C<sub>3</sub>N<sub>4</sub> was evaluated, and the results are displayed and compared in Figure 6a. The photolysis of phenol curve is presented, it shows that in presence of light and without catalyst there is almost no degradation. Bulk g-C<sub>3</sub>N<sub>4</sub> showed approximately 40% phenol degradation after 180 min, whereas complete phenol degradation was achieved in 90 min of reaction time with exfoliated g-C<sub>3</sub>N<sub>4</sub>. As the bandgap of both materials is similar, the better photo efficiency of exfoliated g-C<sub>3</sub>N<sub>4</sub> is most likely due to its higher surface area, which provides more available active sites compared with bulk g-C<sub>3</sub>N<sub>4</sub>. The obtained results are in accordance with the results reported by Babu, Bathula et al. and Ding, Wang et al. [48,49]. Due to its better photoefficiency, exfoliated g-C<sub>3</sub>N<sub>4</sub> was used for further experiments.

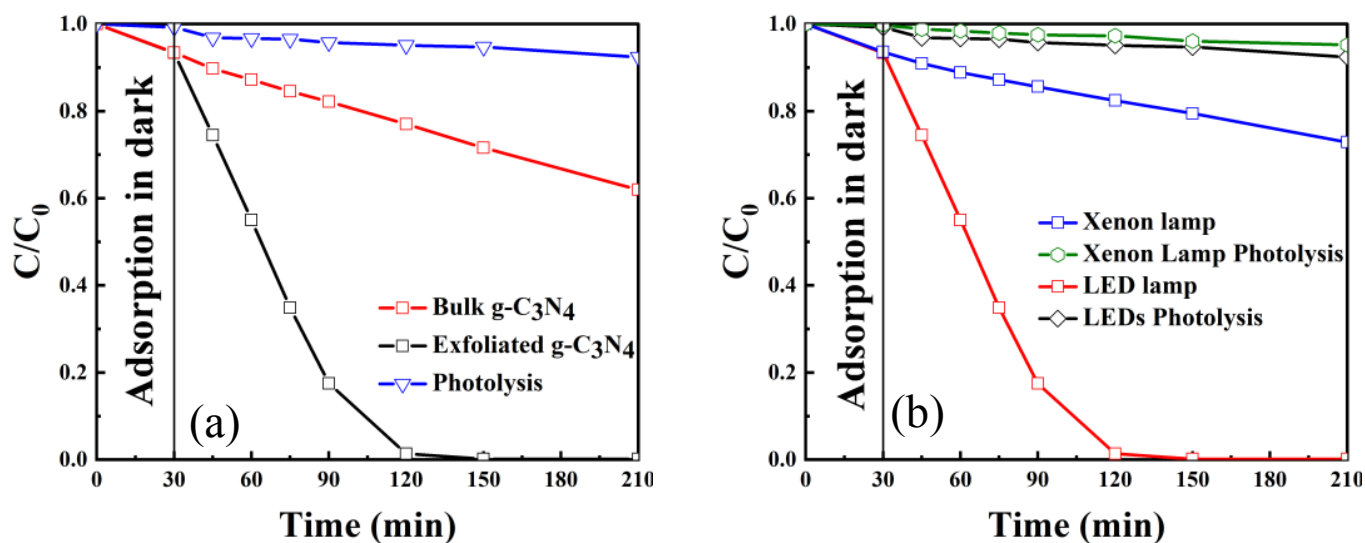


**Figure 6.** Phenol degradation with (a) bulk and exfoliated  $g-C_3N_4$  (b) as a function of the light source;  $C_0 = 20$  ppm, airflow = 50 mL/min, catalyst concentration = 0.5 g/L, pH = natural.

### 2.2.2. Effect of the Light Source

To study the effect of light on the photodegradation of phenol, two light sources were used, namely, a full-spectrum xenon lamp and a single-wavelength LED lamp. Figure 6b presents the performance of exfoliated  $g-C_3N_4$  using the two different light sources. Experiments performed with both light source in the absence of a catalyst have shown no degradation of phenol. In this study, we used a custom-made immersion lamp with six LEDs of 430 nm because that was the maximum excitation wavelength of exfoliated  $g-C_3N_4$  according to the PL spectra (Figure 3). A significant difference between the photodegradation using the two lamps was observed; namely, approx. 100% of phenol degradation was achieved within 90 min of reaction time using the LED lamp, whereas only 20% of degradation was achieved with the xenon lamp after 180 min. The faster reaction with the LED lamp is attributable to the higher availability of electrons at the maximum excitation wavelength. Therefore, exfoliated  $g-C_3N_4$  and the LED lamp were selected for further experiments. The photocatalytic results of both lamps are compared to the photolysis as well to show that the degradation is due to the presence of a catalyst.

### 2.2.3. Effect of Catalyst Amount

The amount of catalyst was optimized to avoid using an excess of the catalyst and to enhance the efficiency of the degradation process. The amount of exfoliated  $g-C_3N_4$  was varied from 0.1 to 1.5 g/L. Figure 7a shows the obtained phenol degradation curves. The degradation of phenol was negligible in the absence of the catalyst, and no significant improvement was achieved for catalyst concentrations below 0.5 g/L. By contrast, phenol was completely degraded in 90 min of reaction time for all the amounts above 0.5 g/L. Further increase in the catalyst amount resulted in a decrease in efficiency because of hindered light absorption and light scattering. Therefore, a catalyst concentration of 0.5 g/L was selected for further studies.

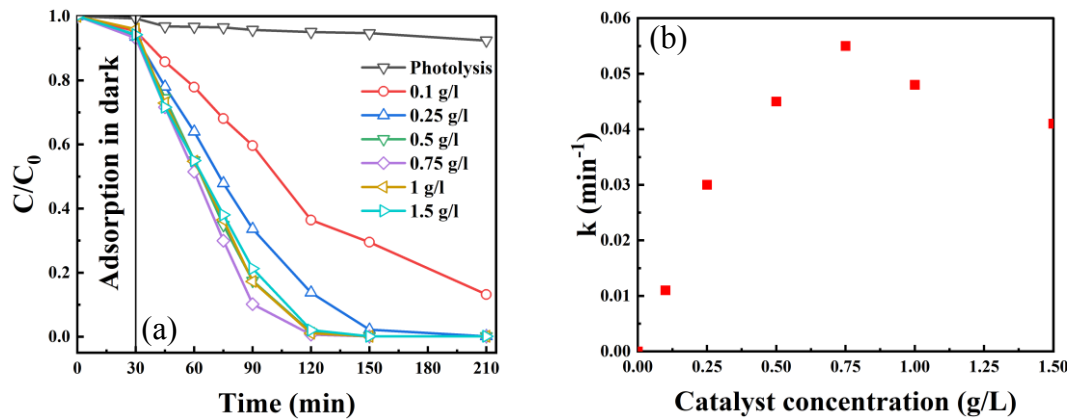


**Figure 7.** (a) Photodegradation curves of phenol concentration (b) reaction rate constant as a function of the catalyst concentration;  $C_0 = 20$  ppm, airflow = 50 mL/min, pH = natural, light source = LEDs, Catalyst = exfoliated  $g\text{-C}_3\text{N}_4$ .

The photodegradation curves followed the exponential decay model and were fitted to obtain the reaction rate constant ( $k$ ) [50,51] as follows:

$$\frac{C}{C_0} = e^{-kt} \quad (7)$$

The highest rate constant of  $0.055 \text{ min}^{-1}$  was obtained for a concentration of 0.75 g/L (Figure 7b), whereas lower and similar values were found for 0.5 and 1 g/L, respectively. This decrease in the rate constant can be attributed to the increase in the catalyst amount hindering the absorption of light.

#### 2.2.4. Effect of Pollutant Concentration

Figure 8a displays the phenol degradation curves obtained for different concentrations of phenol in an aqueous solution (20, 40, 60, 80, and 100 ppm) and the same amount of exfoliated  $g\text{-C}_3\text{N}_4$ . The overall efficiency of the process decreased as the pollutant concentration increased, which could be due to the excessive amount of pollutants covering the surface, with the concomitant decrease in photon absorption and the number of available active sites [52]. The dependence of the removal efficiency on initial phenol concentration was also studied and reported in terms of rate of reaction, expressed by the reaction rate constant. As shown in Figure 8b, and similar to data reported in the literature [53], the rate decreases with increasing initial phenol concentration.

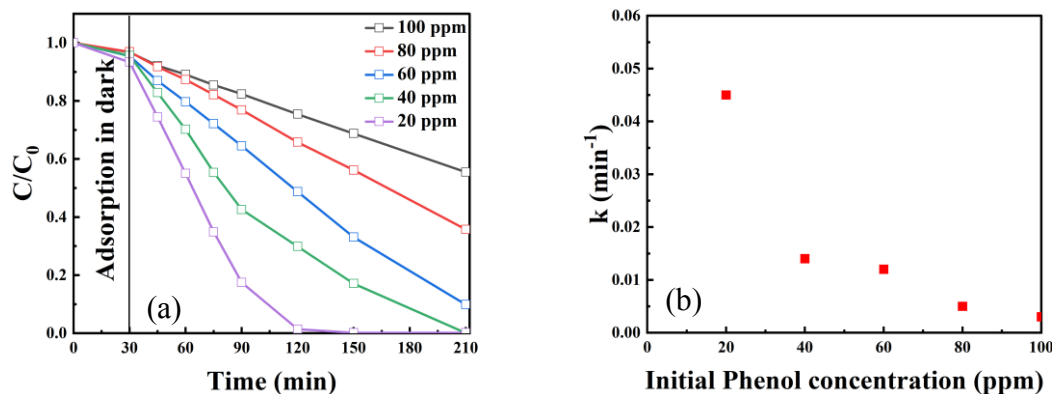


**Figure 8.** (a) Photodegradation curves of phenol as a function of the initial concentration; (b) reaction rate constant as a function of the initial phenol concentration airflow = 50 mL/min, catalyst = 0.5 g/L, pH = natural, light source = LEDs, Catalyst = exfoliated  $g\text{-C}_3\text{N}_4$ .

### 2.2.5. Effect of Initial pH

Figure 9 shows the influence of pH on phenol degradation. The photodegradation efficiency of phenol at acidic pH (2–5) was better than at basic pH (9–12). Almost 97% of phenol degradation was achieved in 60 min of reaction time at acidic pH compared with 100% for natural pH in 90 min and 80% at basic pH in 180 min, a similar pH dependency was shown in the literature [47,54]. The reason for this trend is that the catalyst surface is positively charged at acidic pH (see Figure S3), which enhances the adsorption of negatively charged molecules, e.g.,  $\text{OH}^-$ , from the suspension compared with the negatively charged surface at basic pH. Hence, high pH is not favorable for the photodegradation of phenol [55,56].

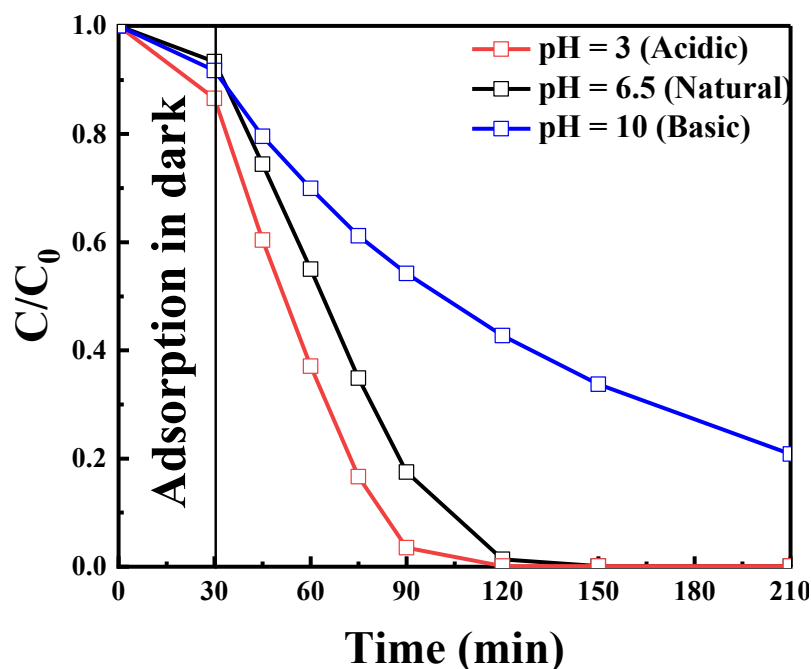


**Figure 9.** Photodegradation curves of phenol as a function of pH;  $C_0 = 20$  ppm, airflow = 50 mL/min, catalyst = 0.5 g/L, light source = LEDs, Catalyst = exfoliated  $g\text{-C}_3\text{N}_4$ .

### 2.2.6. Effect of Dissolved Oxygen

The influence of dissolved oxygen on the degradation of phenol was studied by conducting experiments with and without an external airflow. As can be seen in Figure 10, in both cases, the degradation curves show the same trend for the first 15 min. After that, in the absence of airflow, the phenol degradation slows down, probably because of the consumption of all dissolved oxygen in the aqueous solution, and no change in the degradation is observed after the first 30 min. During the reaction in the absence of air, the system is closed and there is much less overhead space above the reaction medium in the reactor for enough air to carry out the reaction. By contrast, complete degradation is observed under an airflow within 90 min of reaction time because of the presence of extra oxygen to perform the reaction [54]. Oxygen plays an important role in trapping the photoinduced electron produced by the photoactivation of catalysts, consequently reducing the possibility of electron/hole ( $e^-/h^+$ ) recombination as well. [57,58]. The mechanisms proposed in Equations (8–12) are for activation of catalyst by light and formation of  $\text{H}_2\text{O}_2$ . In several studies, the authors suggested that the catalyst is activated with light ( $h\nu$ ) which originates the electron/hole ( $e^-/h^+$ ) pairs [10,57,58].  $\text{H}_2\text{O}_2$  is formed during the process by the utilization of the electrons produced and oxygen present in the system. Then,  $\text{H}_2\text{O}_2$  and  $\text{O}_2$  are reduced to  $\text{OH}^-$  and superoxide radical  $\text{O}_2^-$  which are used in the degradation of organic pollutants.

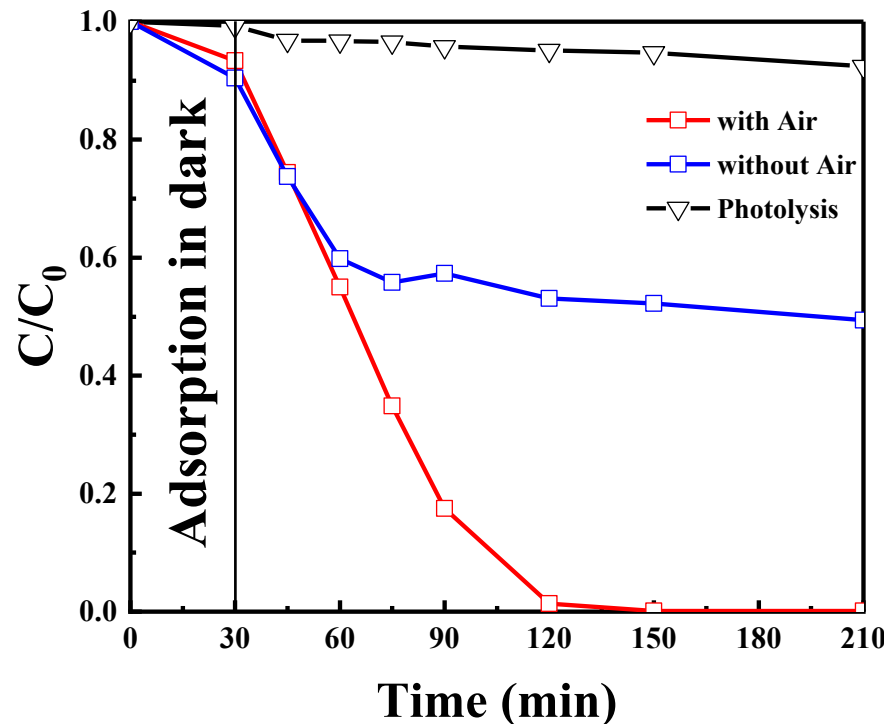
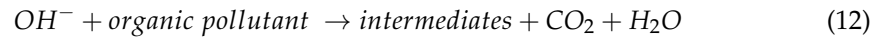
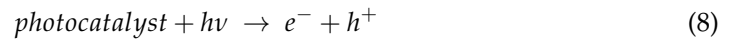


**Figure 10.** Photodegradation curves of phenol in the absence or presence of an airflow;  $C_0 = 20$  ppm, airflow = 50 mL/min, catalyst = 0.5 g/L, pH = natural, light source = LEDs, Catalyst = exfoliated  $g-C_3N_4$ .

### 2.2.7. Effect of $TiO_2$ and its Composite

Titanium oxide ( $TiO_2$ ) is one of the most prominent and widely used semiconductor photocatalysts. The performance of  $g-C_3N_4$  was compared with that of  $TiO_2$  and a composite of both materials, i.e., exfoliated  $g-C_3N_4:TiO_2$  (1:1). Figure 11 shows the phenol degradation curves obtained under the same operating conditions. Exfoliated  $g-C_3N_4$  afforded complete phenol degradation in 90 min of reaction time,  $TiO_2$  showed 50% degradation in 180 min, and complete degradation was also obtained with the composite in 150 min. The better performance of exfoliated  $g-C_3N_4$  can be attributed to the same excitation wavelength of exfoliated  $g-C_3N_4$  and the LED lamp (430 nm), whereas the maximum absorption of  $TiO_2$  lies in the range of 190–400 nm [59]. Consequently, the addition of exfoliated  $g-C_3N_4$  to  $TiO_2$  enhanced its performance under visible light irradiation.



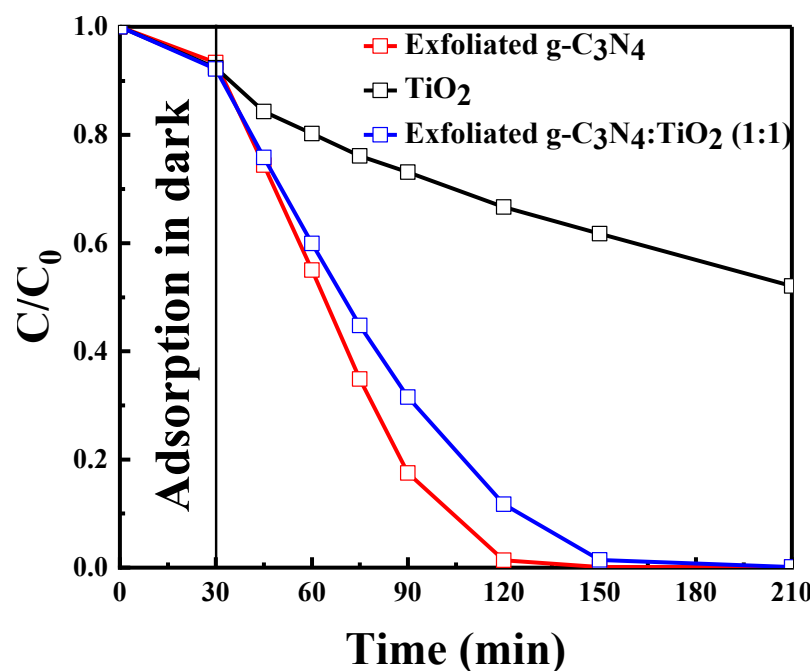


**Figure 11.** Phenol degradation with exfoliated  $g\text{-C}_3\text{N}_4$ ,  $\text{TiO}_2$ , and a  $g\text{-C}_3\text{N}_4\text{:TiO}_2$  composite;  $C_0 = 20$  ppm, airflow = 50 mL/min, catalyst = 0.5 g/L, pH = natural, light source = LEDs, Catalyst = exfoliated  $g\text{-C}_3\text{N}_4$ .

#### 2.2.8. Catalyst Reutilization Tests

The reusability of exfoliated  $g\text{-C}_3\text{N}_4$  was demonstrated by performing three cycles of phenol degradation after subjecting the catalyst to thorough washing and drying at 120 °C for 12 h. The degradation efficiency of the catalyst remained unchanged for at least three cycles (supplementary Figure S3), and the complete degradation of phenol was achieved within 3 h. It can be concluded that the material remained stable for at least three cycles while maintaining its photocatalytic activity.

#### 2.2.9. Photocatalytic Efficiency for the Degradation of a Mixture of Organic Pollutants

Three additional phenolic compounds commonly found in oil refinery wastewater [60], namely, *m*-cresol, catechol, and xylol, (chemical structures in supplementary Table S1) were chosen to further study the photocatalytic degradation performance of exfoliated  $g\text{-C}_3\text{N}_4$ . Figure 12 shows the photodegradation curves for each organic pollutant in single-compound aqueous solutions. Xylol was completely degraded in approximately 60 min, phenol and *m*-cresol in 120 min, and catechol in 150 min of reaction time. In the photocatalytic reactions of aromatic compounds, the degradation is considered to be initiated by an electrophilic attack of the “holes” produced by exfoliated  $g\text{-C}_3\text{N}_4$  to the benzene ring. Hydroxyl (–OH) and alkyl (e.g., –CH<sub>3</sub>) groups are generally known to increase the electron density of the aromatic ring, making it more susceptible to undergo an electrophilic attack at its *ortho* and *para* positions. Compared with phenol, catechol was more difficult to degrade. Even though catechol has two –OH groups, their *ortho* orientation reduces the number of distinct carbon atoms that are prone to undergo electrophilic substitution [10,61]. The *meta* orientation of the –CH<sub>3</sub> and –OH groups in *m*-cresol is favorable to a facile attack on the aromatic ring in three distinct positions, providing *m*-cresol with a higher reactivity compared with phenol. Having the highest number of activating substituents (–OH and 2 × –CH<sub>3</sub>), the aromatic ring of xylol degraded the fastest among the four studied phenolic compounds.



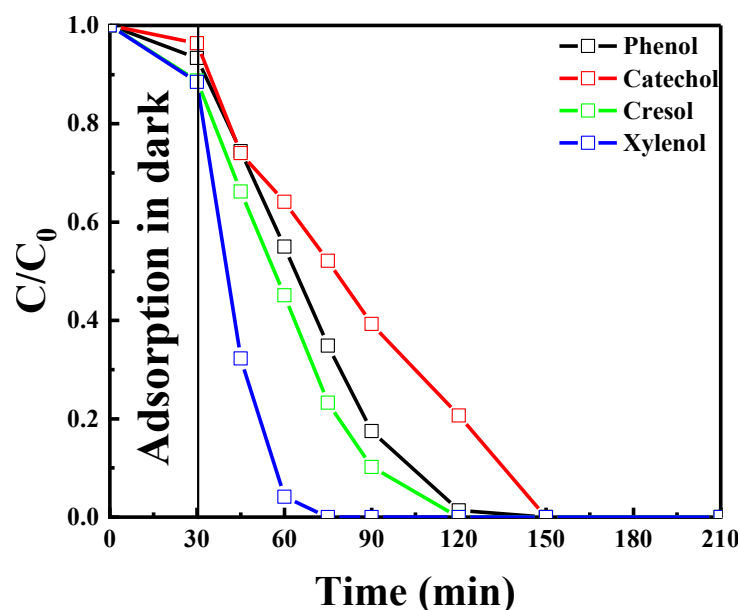


**Figure 12.** Degradation profile of (a) individual pollutants (20 ppm) and (b) a mixture of 20 ppm of each pollutant;  $C_0 = 20$  ppm, airflow = 50 mL/min, catalyst = 0.5 g/L, pH = natural, light source = LEDs, Catalyst = exfoliated  $g-C_3N_4$ .

### 3. Materials and Methods

#### 3.1. Chemicals and Materials

Melamine ( $C_3H_6N_6$ , 99%), *m*-cresol ( $CH_3C_6H_4(OH)$ , 99%), and catechol ( $C_6H_4(OH)_2$ , 99%) (Alfa Aesar); phenol ( $C_6H_5OH$ , 99%) (Merck); xylenol (2,6-dimethylphenol) ( $(CH_3)_2C_6H_3OH$ , 99%) and titanium oxide ( $TiO_2$ ) (Acros); hydrochloric acid (HCl), sodium hydroxide (NaOH) (VWR); acetonitrile ( $C_2H_3N$ , 99.99%) and ultrapure water for high-performance liquid chromatography (HPLC) (Sigma Aldrich) were used as received without any pretreatment.

#### 3.2. Synthesis and Characterization of the Catalysts

Bulk  $g-C_3N_4$  was prepared by thermal decomposition of melamine. The precursor (melamine) 5g was placed in a closed crucible in a muffle furnace (Carbolite, GPC 1200) under a static air atmosphere; 2.6 g  $g-C_3N_4$  were produced which corresponds to a yield of 52%. A heating ramp of  $2\text{ }^\circ\text{C min}^{-1}$  was programmed up to  $450\text{ }^\circ\text{C}$ , and this temperature was maintained for 2 h. Next, the temperature was increased up to  $550\text{ }^\circ\text{C}$  using a heating ramp of  $2\text{ }^\circ\text{C min}^{-1}$  and then maintained for 4 h. After cooling down naturally, the material was crushed to powder using a mortar and pestle, rinsed with ultrapure water, filtered, and dried overnight at  $80\text{ }^\circ\text{C}$  [15]. The exfoliation of the prepared catalyst was performed by placing the catalyst in an open crucible inside a muffle furnace for 2 h at  $500\text{ }^\circ\text{C}$  using a heating ramp of  $2\text{ }^\circ\text{C min}^{-1}$ . The  $g-C_3N_4$  material obtained after exfoliation is referred to hereafter as exfoliated  $g-C_3N_4$ . Two catalysts, namely, bulk  $g-C_3N_4$  and exfoliated  $g-C_3N_4$ , were characterized and tested in photodegradation experiments. The molecular structure of the  $g-C_3N_4$  is presented in supplementary materials (Figure S4). Additionally, the performances of commercial  $TiO_2$  and its composite with  $g-C_3N_4$  ( $TiO_2:g-C_3N_4$ ), which were prepared in this study, were examined and compared with that of exfoliated  $g-C_3N_4$ . Briefly, an equal amount of exfoliated  $g-C_3N_4$  and commercial  $TiO_2$  were mixed separately in methanol and sonicated, then the two mixtures were mixed and again sonicated for 6 h. Later the mixture was centrifuged and the solid was dried overnight at  $80\text{ }^\circ\text{C}$ .

Brunauer–Emmett–Teller (BET) surface area, pore-volume, and pore size distribution were determined using an autosorb<sup>®</sup>iQ-MP/XR (Nova 4200e), Quantachrome instrument (Germany). The samples were degassed at  $120\text{ }^\circ\text{C}$  for 3 h before the analysis. The surface area of the catalyst was calculated from  $N_2$  adsorption-desorption isotherms at  $-196\text{ }^\circ\text{C}$ .

The Barrett–Joyner–Halenda (BJH) method was used to determine the micropore volume. UV–vis absorption spectra were recorded using a UV-3600 Plus (Shimadzu, Kyoto, Japan) spectrometer with medium scan speed using a 20 slit width with three external detectors in the range of 200–800 nm. Solid-state photoluminescence (PL) spectra were obtained using an FP-8300 (Jasco, Hachioji-shi, Japan) spectrofluorometer with a 150 W xenon lamp as a light source. The measurements were performed using both excitation and emission bandwidth fixed at 2.5 and 5 nm, respectively, with low sensitivity. The excitation wavelength was set at 370 nm, and the emission was measured in the range of 380–700 nm. A ZEN5600 Zetasizer Nano (Malvern, UK) instrument was used to measure the zeta potential of the synthesized materials, which was determined using phenol and catalyst aqueous suspensions at acidic, basic, and natural pH. Hydrochloric acid and sodium hydroxide were used to adjust the pH of the suspensions. To investigate the crystalline phases of the synthesized catalysts, X-ray diffraction (XRD) analysis was conducted with a Mini Flex 600C (Rigaku, Tokyo, Japan) diffractometer using  $\text{CuK}\alpha$  radiation at a voltage of 40 kV, a current of 15 mA, and a spin speed of 80 rpm in the range between  $3^\circ$  and  $60^\circ$  with a step size of  $0.0075^\circ$ . Transmission electron microscopy (TEM) images were obtained using a JEM 1400 plus (JEOL, Akishima, Japan) microscope (LaB<sub>6</sub> filament) using Quantifoil S7/2 (2 nm carbon film) grids and a CCD camera (Ruby) at 120 kV. X-ray photoelectron spectroscopy (XPS) was conducted using a Thermo Scientific (Waltham, MA, USA) K Alpha and X-ray Photoelectron Spectrometer. All samples were analyzed using a micro-focused, monochromated Al K  $\alpha$  X-ray source (1486.68 eV; 400  $\mu\text{m}$  spot size). The analyzer had pass energy of 200 eV (survey), and 50 eV (high-resolution spectra), respectively. To prevent any localized charge buildup during analysis the K-alpha +ve charge compensation system was employed at all measurements. The samples were mounted on conductive carbon tape the resulting spectra analyzed using the Avantage software from Thermo Scientific.

### 3.3. Photocatalytic Experimentation

The photocatalytic experiments were conducted in a jacketed glass reactor (Peschl Ultraviolet GmbH) with a maximum working capacity of 225 mL, under a custom-made LED immersion lamp comprising 6 LEDs (each of 10 W) with maximum emission at 430 nm and UV-visible light irradiation using a 150 W full-spectrum (200 nm to 800nm) xenon lamp. The reactor was placed in a safety cabinet (Supplementary Figure S1).

The homogeneous dispersion of the catalyst was ensured by sonicating the reaction mixture (water solution of phenol and catalyst), followed by stirring for 30 min in the dark under a continuous airflow to maintain the adsorption-desorption equilibrium. The photolysis experiments were conducted only under the influence of light without any catalyst. In a typical experiment, the initial concentration of phenol was kept at 20 ppm, and the catalyst concentration was varied from 0.1 to 1.5 g/L in a 225 mL phenol solution. Samples (1 mL) were collected periodically from the reaction mixture for the determination of the concentration of phenol. After centrifugation and filtration, the samples were analyzed by HPLC. Experiments were also conducted to study the effect of process parameters, including pH, catalyst concentration, pollutant concentration, air, and exfoliation, on the performance of the catalysts. Experiments with other phenolic compounds, such as *m*-cresol, catechol, and xylenol, were conducted using 0.5 g/L catalysts and 20 ppm pollutant concentration at natural pH. The catalysts exhibited reusability properties, which were established by performing three cycles of reutilization test. The catalysts were tested for reutilization after thorough washing with water and drying at 120 °C for 12 h. The percentage of degradation efficiency was determined using the following Equation (13):

$$\text{Degradation Efficiency} = \frac{C_0 - C}{C_0} \times 100 \quad (13)$$

where,  $C_0$  (mg/L) and  $C$  (mg/L) are the initial phenol concentration and the residual phenol concentration in the solution at an irradiation time  $t$ , respectively. The rate of the reaction of the experiments were calculated using Equation (7), the rate is determined

for the time of the reaction in which either the lights are on and reaction is taking place or there is change in the concentration of the pollutant.  $C/C_0$  was plotted against time and the exponential model (Equation (7)) was fitted to the data, and the slope of the curve is the rate constant “ $k$ ” of the single reaction. Different reaction rate constants were plotted in Figures 7b and 8b. The concentration of phenol was analyzed using a Prominence HPLC system (Shimadzu, Japan) comprising a binary pump (LC-20AB), a SIL-20A autosampler, a DGU-20A3 degasser, and an SPD-M20A diode-array detector. The analysis was conducted with a Phenomenex (C18, 150 mm  $\times$  4.6 mm, 3  $\mu$ m) column at a fixed flow rate of 0.8 mL/min, using water (A) and acetonitrile (B) as a mobile phase with the following gradient: 15% B followed by 60% B in 7 min and back to 15% B in 8 min (injection 5  $\mu$ L; UV 254 nm). Phenol and xylenol were analyzed at a maximum absorption wavelength ( $\lambda_{\max}$ ) of 270 nm, catechol at 277 nm, and *m*-cresol at 273 nm.

#### 4. Conclusions

In this study, g-C<sub>3</sub>N<sub>4</sub> was synthesized using melamine as a precursor and exfoliated. The morphology, structure, and optical and surface properties of the material were characterized using TEM, XRD, XPS, PL, and BET. The chemical structure of g-C<sub>3</sub>N<sub>4</sub> was confirmed by its characteristic peaks in the FTIR and XPS spectra, and its phases were identified by XRD. The zeta potential was measured at different pH values, which confirmed that surface charges of g-C<sub>3</sub>N<sub>4</sub> particles are caused by different surface groups. Phenol was used as a model pollutant to study the influence of process parameters on photocatalytic degradation. It was found that the exfoliation significantly improves the optical (absorption) and surface properties (surface area, porosity) of bulk g-C<sub>3</sub>N<sub>4</sub>, resulting in enhanced photocatalytic performance in comparison with that of non-exfoliated g-C<sub>3</sub>N<sub>4</sub>. The use of a visible light single-wavelength LED lamp as an irradiation source improves the photocatalytic degradation of phenol compared with a full-spectrum xenon lamp. The degradation rate increases with the catalyst concentration, whereas it decreases in the presence of the excess amount of pollutants (i.e., phenol). Moreover, it was shown that an acidic environment is favorable for the photocatalytic degradation of phenol. Dissolved oxygen proved to be an important factor in the degradation of phenol since only 50% of the degradation was achieved in the absence of oxygen. A comparison between g-C<sub>3</sub>N<sub>4</sub> and TiO<sub>2</sub> showed that the performance of the former in the degradation of phenol under visible light irradiation is better. Furthermore, TiO<sub>2</sub> performance improves with the addition of g-C<sub>3</sub>N<sub>4</sub>. The versatility of exfoliated g-C<sub>3</sub>N<sub>4</sub> was demonstrated in the degradation of other phenolic pollutants individually and in a mixture. Furthermore, exfoliated g-C<sub>3</sub>N<sub>4</sub> proved to be a stable catalyst that can be recycled and reused without any loss of activity.

**Supplementary Materials:** The following are available online at <https://www.mdpi.com/article/10.3390/catal11060662/s1>, Figure S1 Photocatalytic reactor setup, Figure S2 Zeta potential of exfoliated g-C<sub>3</sub>N<sub>4</sub> as a function of the pH value of the suspension, Figure S3 Phenol degradation conversion for the reutilized catalyst; C<sub>0</sub> = 20 ppm, airflow = 50 mL/min, catalyst = 0.5 g/L, pH = natural, Table S1 Chemical structures of the pollutants used.

**Author Contributions:** Conceptualization, A.G.R.; Formal analysis, A.G.R. and M.T.; Investigation, A.G.R. and M.T.; Methodology, A.G.R.; Resources, M.M.; Supervision, M.M.; Validation, A.G.R.; Visualization, A.G.R.; Writing original draft, A.G.R.; Writing review and editing, M.S. and M.M. All authors have read and agreed to the published version of the manuscript.

**Funding:** This research received no external funding.

**Acknowledgments:** Adeem Ghaffar Rana acknowledges the financial support from the Higher Education Commission, Pakistan, and Deutscher Akademischer Austauschdienst (DAAD), Germany.

**Conflicts of Interest:** The authors declare no conflict of interest.

## References

1. Dewidar, H.; Nosier, S.; El-Shazly, A. Photocatalytic degradation of phenol solution using Zinc Oxide/UV. *J. Chem. Heal. Saf.* **2018**, *25*, 2–11. [[CrossRef](#)]
2. Zarin, S.; Aslam, Z.; Zahir, A.; Kamal, M.S.; Rana, A.G.; Ahmad, W.; Ahmed, S. Synthesis of bimetallic/carbon nanocomposite and its application for phenol removal. *J. Iran. Chem. Soc.* **2018**, *15*, 2689–2701. [[CrossRef](#)]
3. Hararah, M.A.; Ibrahim, K.A.; Al-Muhtaseb, A.H.; Yousef, R.I.; Abu-Surrah, A.; Qatatsheh, A. Removal of phenol from aqueous solutions by adsorption onto polymeric adsorbents. *J. Appl. Polym. Sci.* **2010**, *117*, 1908–1913. [[CrossRef](#)]
4. Aslam, Z.; Qaiser, M.; Ali, R.; Abbas, A.; Ihsanullah; Zarin, S. Al<sub>2</sub>O<sub>3</sub>/MnO<sub>2</sub>/CNTs nanocomposite: Synthesis, characterization and phenol adsorption. *Full Nanotub. Carbon Nanostruct.* **2019**, *27*, 591–600. [[CrossRef](#)]
5. Shen, W.; Ge, Q.; Gu, K.; Nie, Y.; Jiao, L.; Zhu, Z.; Fang, Y. Stable Organic Titanium Catalysts and Reactive Distillation Used for the Transesterification of Dimethyl Carbonate with Phenol. *Chem. Eng. Technol.* **2020**, *43*, 2359–2364. [[CrossRef](#)]
6. Huang, C.-H.; Liou, R.-M.; Chen, S.-H.; Hung, M.-Y.; Lai, C.-L.; Lai, J.-Y. Microbial degradation of phenol in a modified three-stage airlift packing-bed reactor. *Water Environ. Res.* **2010**, *82*, 249–258. [[CrossRef](#)] [[PubMed](#)]
7. Yavuz, Y.; Koparal, A.S.; Ögütveren, Ü.B. Phenol Removal through Chemical Oxidation using Fenton Reagent. *Chem. Eng. Technol.* **2007**, *30*, 583–586. [[CrossRef](#)]
8. Tasbihi, M.; Acharjya, A.; Thomas, A.; Reli, M.; Ambrožová, N.; Kočci, K.; Schomäcker, R. Photocatalytic CO<sub>2</sub> Reduction by Mesoporous Polymeric Carbon Nitride Photocatalysts. *J. Nanosci. Nanotechnol.* **2018**, *18*, 5636–5644. [[CrossRef](#)]
9. Chowdhury, P.; Nag, S.; Ray, A.K. Degradation of Phenolic Compounds Through UV and Visible- Light-Driven Photocatalysis: Technical and Economic Aspects. In *Phenolic Compounds—Natural Sources, Importance and Applications*; IntechOpen: London, UK, 2017.
10. Torres-Pinto, A.; Sampaio, M.J.; Silva, C.G.; Faria, J.L.; Silva, A.M. Metal-free carbon nitride photocatalysis with in situ hydrogen peroxide generation for the degradation of aromatic compounds. *Appl. Catal. B Environ.* **2019**, *252*, 128–137. [[CrossRef](#)]
11. Kumar, S.; Karthikeyan, S.; Lee, A.F. g-C<sub>3</sub>N<sub>4</sub>-Based Nanomaterials for Visible Light-Driven Photocatalysis. *Catalysts* **2018**, *8*, 74. [[CrossRef](#)]
12. Rana, A.G.; Ahmad, W.; Al-Matar, A.; Shawabkeh, R.; Aslam, Z. Synthesis and characterization of Cu–Zn/TiO<sub>2</sub> for the photocatalytic conversion of CO<sub>2</sub> to methane. *Environ. Technol.* **2016**, *38*, 1085–1092. [[CrossRef](#)] [[PubMed](#)]
13. Rosli, N.I.M.; Lam, S.-M.; Sin, J.-C.; Satoshi, I.; Mohamed, A.R. Photocatalytic Performance of ZnO/g-C<sub>3</sub>N<sub>4</sub> for Removal of Phenol under Simulated Sunlight Irradiation. *J. Environ. Eng.* **2018**, *144*, 04017091. [[CrossRef](#)]
14. Moradi, V.; Ahmed, F.; Jun, M.B.; Blackburn, A.; Herring, R.A. Acid-treated Fe-doped TiO<sub>2</sub> as a high performance photocatalyst used for degradation of phenol under visible light irradiation. *J. Environ. Sci.* **2019**, *83*, 183–194. [[CrossRef](#)] [[PubMed](#)]
15. Lima, M.J.; Silva, A.M.; Silva, C.G.; Faria, J.L. Graphitic carbon nitride modified by thermal, chemical and mechanical processes as metal-free photocatalyst for the selective synthesis of benzaldehyde from benzyl alcohol. *J. Catal.* **2017**, *353*, 44–53. [[CrossRef](#)]
16. Nobijari, L.A.; Schwarze, M.; Tasbihi, M. Photocatalytic Degradation of Phenol Using Photodeposited Pt Nanoparticles on Titania. *J. Nanosci. Nanotechnol.* **2020**, *20*, 1056–1065. [[CrossRef](#)]
17. Al-Kandari, H.; Abdullah, A.M.; Ahmad, Y.H.; AlQaradawi, S.Y.; Mohamed, A.M. An efficient eco advanced oxidation process for phenol mineralization using a 2D/3D nanocomposite photocatalyst and visible light irradiations. *Sci. Rep.* **2017**, *7*, 9898. [[CrossRef](#)]
18. Ren, H.-T.; Jia, S.-Y.; Wu, Y.; Wu, S.-H.; Zhang, T.-H.; Han, X. Improved Photochemical Reactivities of Ag<sub>2</sub>O/g-C<sub>3</sub>N<sub>4</sub> in Phenol Degradation under UV and Visible Light. *Ind. Eng. Chem. Res.* **2014**, *53*, 17645–17653. [[CrossRef](#)]
19. Lee, S.C.; Lintang, H.O.; Yuliati, L. A Urea Precursor to Synthesize Carbon Nitride with Mesoporosity for Enhanced Activity in the Photocatalytic Removal of Phenol. *Chem. Asian J.* **2012**, *7*, 2139–2144. [[CrossRef](#)]
20. Hu, J.-Y.; Tian, K.; Jiang, H. Improvement of phenol photodegradation efficiency by a combined g-C<sub>3</sub>N<sub>4</sub>/Fe(III)/persulfate system. *Chemosphere* **2016**, *148*, 34–40. [[CrossRef](#)]
21. Deng, P.; Gan, M.; Zhang, X.; Li, Z.; Hou, Y. Non-noble-metal Ni nanoparticles modified N-doped g-C<sub>3</sub>N<sub>4</sub> for efficient photocatalytic hydrogen evolution. *Int. J. Hydrogen Energy* **2019**, *44*, 30084–30092. [[CrossRef](#)]
22. Huang, Z.; Li, F.; Chen, B.; Lu, T.; Yuan, Y.; Yuan, G. Well-dispersed g-C<sub>3</sub>N<sub>4</sub> nanophases in mesoporous silica channels and their catalytic activity for carbon dioxide activation and conversion. *Appl. Catal. B Environ.* **2013**, *136–137*, 269–277. [[CrossRef](#)]
23. Sharma, M.; Vaidya, S.; Ganguli, A.K. Enhanced photocatalytic activity of g-C<sub>3</sub>N<sub>4</sub>-TiO<sub>2</sub> nanocomposites for degradation of Rhodamine B dye. *J. Photochem. Photobiol. A Chem.* **2017**, *335*, 287–293. [[CrossRef](#)]
24. Hernández-Uresti, D.; Vázquez, A.; Sanchez-Martinez, D.; Obregón, S. Performance of the polymeric g-C<sub>3</sub>N<sub>4</sub> photocatalyst through the degradation of pharmaceutical pollutants under UV–vis irradiation. *J. Photochem. Photobiol. A Chem.* **2016**, *324*, 47–52. [[CrossRef](#)]
25. Zheng, Q.; Durkin, D.P.; Elenewski, J.E.; Sun, Y.; Banek, N.A.; Hua, L.; Chen, H.; Wagner, M.J.; Zhang, W.; Shuai, D. Visible-Light-Responsive Graphitic Carbon Nitride: Rational Design and Photocatalytic Applications for Water Treatment. *Environ. Sci. Technol.* **2016**, *50*, 12938–12948. [[CrossRef](#)] [[PubMed](#)]
26. Yuan, Y.-J.; Shen, Z.; Wu, S.; Su, Y.; Pei, L.; Ji, Z.; Ding, M.; Bai, W.; Chen, Y.; Yu, Z.-T.; et al. Liquid exfoliation of g-C<sub>3</sub>N<sub>4</sub> nanosheets to construct 2D-2D MoS<sub>2</sub>/g-C<sub>3</sub>N<sub>4</sub> photocatalyst for enhanced photocatalytic H<sub>2</sub> production activity. *Appl. Catal. B Environ.* **2019**, *246*, 120–128. [[CrossRef](#)]

27. Dang, T.T.T.; Le, S.T.T.; Channei, D.; Khanitchaidecha, W.; Nakaruk, A. Photodegradation mechanisms of phenol in the photocatalytic process. *Res. Chem. Intermed.* **2016**, *42*, 5961–5974. [[CrossRef](#)]
28. Benisti, I.; Shaik, F.; Xing, Z.; Ben-Refael, A.; Amirav, L.; Paz, Y. The effect of Pt cocatalyst on the performance and transient IR spectrum of photocatalytic g-C<sub>3</sub>N<sub>4</sub> nanospheres. *Appl. Surf. Sci.* **2021**, *542*, 148432. [[CrossRef](#)]
29. Yang, Y.; Lei, W.; Xu, Y.; Zhou, T.; Xia, M.; Hao, Q. Determination of trace uric acid in serum using porous graphitic carbon nitride (g-C<sub>3</sub>N<sub>4</sub>) as a fluorescent probe. *Microchim. Acta* **2017**, *185*, 39. [[CrossRef](#)]
30. Dong, F.; Wang, Z.; Sun, Y.; Ho, W.-K.; Zhang, H. Engineering the nanoarchitecture and texture of polymeric carbon nitride semiconductor for enhanced visible light photocatalytic activity. *J. Colloid Interface Sci.* **2013**, *401*, 70–79. [[CrossRef](#)]
31. Papailias, I.; Giannakopoulou, T.; Todorova, N.; Demotikali, D.; Vaimakis, T.; Trapalis, C. Effect of processing temperature on structure and photocatalytic properties of g-C<sub>3</sub>N<sub>4</sub>. *Appl. Surf. Sci.* **2015**, *358*, 278–286. [[CrossRef](#)]
32. Djoko, S.Y.T.; Bashiri, H.; Njoyim, E.T.; Arabamiri, M.; Djepang, S.; Tamo, A.K.; Laminsi, S.; Tasbihi, M.; Schwarze, M.; Schomäcker, R.; et al. Urea and green tea like precursors for the preparation of g-C<sub>3</sub>N<sub>4</sub> based carbon nanomaterials (CNMs) composites as photocatalysts for photodegradation of pollutants under UV light irradiation. *J. Photochem. Photobiol. A Chem.* **2020**, *398*, 112596. [[CrossRef](#)]
33. Stroyuk, A.L.; Panasiuk, Y.V.; Raevskaya, A.E.; Kuchmy, S.Y. Spectral and Luminescent Characteristics of Products from Exfoliation of Graphitic Carbon Nitride Produced at Various Temperatures. *Theor. Exp. Chem.* **2015**, *51*, 243–251. [[CrossRef](#)]
34. Jiang, J.; Ou-Yang, L.; Zhu, L.; Zheng, A.; Zou, J.; Yi, X.; Tang, H. Dependence of electronic structure of g-C<sub>3</sub>N<sub>4</sub> on the layer number of its nanosheets: A study by Raman spectroscopy coupled with first-principles calculations. *Carbon* **2014**, *80*, 213–221. [[CrossRef](#)]
35. Zhang, X.; Xie, X.; Wang, H.; Zhang, J.; Pan, B.; Xie, Y. Enhanced Photoresponsive Ultrathin Graphitic-Phase C<sub>3</sub>N<sub>4</sub> Nanosheets for Bioimaging. *J. Am. Chem. Soc.* **2013**, *135*, 18–21. [[CrossRef](#)]
36. Ma, Y.; Liu, E.; Hu, X.; Tang, C.; Wan, J.; Li, J.; Fan, J. A simple process to prepare few-layer g-C<sub>3</sub>N<sub>4</sub> nanosheets with enhanced photocatalytic activities. *Appl. Surf. Sci.* **2015**, *358*, 246–251. [[CrossRef](#)]
37. Yu, B.; Meng, F.; Khan, M.W.; Qin, R.; Liu, X. Facile synthesis of AgNPs modified TiO<sub>2</sub>@g-C<sub>3</sub>N<sub>4</sub> heterojunction composites with enhanced photocatalytic activity under simulated sunlight. *Mater. Res. Bull.* **2020**, *121*, 110641. [[CrossRef](#)]
38. Muñoz-Batista, M.J.; Rodríguez-Padrón, D.; Puente-Santiago, A.R.; Kubacka, A.; Luque, R.; Fernández-García, M. Sunlight-Driven Hydrogen Production Using an Annular Flow Photoreactor and g-C<sub>3</sub>N<sub>4</sub>-Based Catalysts. *ChemPhotoChem* **2018**, *2*, 870–877. [[CrossRef](#)]
39. Yuan, X.; Zhou, C.; Jin, Y.; Jing, Q.; Yang, Y.; Shen, X.; Tang, Q.; Mu, Y.; Du, A.-K. Facile synthesis of 3D porous thermally exfoliated g-C<sub>3</sub>N<sub>4</sub> nanosheet with enhanced photocatalytic degradation of organic dye. *J. Colloid Interface Sci.* **2016**, *468*, 211–219. [[CrossRef](#)]
40. Xu, J.; Zhang, L.; Shi, R.; Zhu, Y. Chemical exfoliation of graphitic carbon nitride for efficient heterogeneous photocatalysis. *J. Mater. Chem. A* **2013**, *1*, 14766–14772. [[CrossRef](#)]
41. Li, Y.; Wang, M.-Q.; Bao, S.-J.; Lu, S.; Xu, M.; Long, D.; Pu, S. Tuning and thermal exfoliation graphene-like carbon nitride nanosheets for superior photocatalytic activity. *Ceram. Int.* **2016**, *42*, 18521–18528. [[CrossRef](#)]
42. Yang, L.; Liu, X.; Liu, Z.; Wang, C.; Liu, G.; Li, Q.; Feng, X. Enhanced photocatalytic activity of g-C<sub>3</sub>N<sub>4</sub> 2D nanosheets through thermal exfoliation using dicyandiamide as precursor. *Ceram. Int.* **2018**, *44*, 20613–20619. [[CrossRef](#)]
43. Niu, P.; Zhang, L.; Liu, G.; Cheng, H.-M. Graphene-Like Carbon Nitride Nanosheets for Improved Photocatalytic Activities. *Adv. Funct. Mater.* **2012**, *22*, 4763–4770. [[CrossRef](#)]
44. Wang, J.; Guo, P.; Dou, M.; Cheng, Y.; Jönsson, P.G.; Zhao, Z. Visible light-driven g-C<sub>3</sub>N<sub>4</sub>/m-Ag<sub>2</sub>Mo<sub>2</sub>O<sub>7</sub> composite photocatalysts: Synthesis, enhanced activity and photocatalytic mechanism. *RSC Adv.* **2014**, *4*, 51008–51015. [[CrossRef](#)]
45. Wang, Y.; Yang, W.; Chen, X.; Wang, J.; Zhu, Y. Photocatalytic activity enhancement of core-shell structure g-C<sub>3</sub>N<sub>4</sub>@TiO<sub>2</sub> via controlled ultrathin g-C<sub>3</sub>N<sub>4</sub> layer. *Appl. Catal. B Environ.* **2018**, *220*, 337–347. [[CrossRef](#)]
46. Zhu, B.; Xia, P.; Ho, W.; Yu, J. Isoelectric point and adsorption activity of porous g-C<sub>3</sub>N<sub>4</sub>. *Appl. Surf. Sci.* **2015**, *344*, 188–195. [[CrossRef](#)]
47. Dong, S.; Zeng, Z.; Cai, W.; Zhou, Z.; Dou, C.; Liu, H.; Xia, J. The zeta potentials of g-C<sub>3</sub>N<sub>4</sub> nanoparticles: Effect of electrolyte, ionic strength, pH, and humic acid. *J. Nanoparticle Res.* **2019**, *21*, 233. [[CrossRef](#)]
48. Babu, B.; Shim, J.; Kadam, A.; Yoo, K. Modification of porous g-C<sub>3</sub>N<sub>4</sub> nanosheets for enhanced photocatalytic activity: In-situ synthesis and optimization of NH<sub>4</sub>Cl quantity. *Catal. Commun.* **2019**, *124*, 123–127. [[CrossRef](#)]
49. Ding, W.; Liu, S.; He, Z. One-step synthesis of graphitic carbon nitride nanosheets for efficient catalysis of phenol removal under visible light. *Chin. J. Catal.* **2017**, *38*, 1711–1718. [[CrossRef](#)]
50. Sampaio, M.J.; Silva, C.G.; Silva, A.M.T.; Faria, J.L. Kinetic modelling for the photocatalytic degradation of phenol by using TiO<sub>2</sub>-coated glass raschig rings under simulated solar light. *J. Chem. Technol. Biotechnol.* **2014**, *91*, 346–352. [[CrossRef](#)]
51. Herrmann, J.-M. Titania-based true heterogeneous photocatalysis. *Environ. Sci. Pollut. Res.* **2012**, *19*, 3655–3665. [[CrossRef](#)] [[PubMed](#)]
52. Pattnaik, S.P.; Behera, A.; Martha, S.; Acharya, R.; Parida, K. Facile synthesis of exfoliated graphitic carbon nitride for photocatalytic degradation of ciprofloxacin under solar irradiation. *J. Mater. Sci.* **2019**, *54*, 5726–5742. [[CrossRef](#)]
53. Daneshvar, N.; Rabbani, M.; Modirshahla, N.; Behnajady, M. Kinetic modeling of photocatalytic degradation of Acid Red 27 in UV/TiO<sub>2</sub> process. *J. Photochem. Photobiol. A Chem.* **2004**, *168*, 39–45. [[CrossRef](#)]



54. Lam, S.-M.; Sin, J.-C.; Mohamed, A.R. Parameter effect on photocatalytic degradation of phenol using TiO<sub>2</sub>-P<sub>25</sub>/activated carbon (AC). *Korean J. Chem. Eng.* **2010**, *27*, 1109–1116. [[CrossRef](#)]
55. Malekshoar, G.; Pal, K.; He, Q.; Yu, A.; Ray, A.K. Enhanced Solar Photocatalytic Degradation of Phenol with Coupled Graphene-Based Titanium Dioxide and Zinc Oxide. *Ind. Eng. Chem. Res.* **2014**, *53*, 18824–18832. [[CrossRef](#)]
56. Benhebal, H.; Chaib, M.; Salmon, T.; Geens, J.; Leonard, A.; Lambert, S.D.; Crine, M.; Heinrichs, B. Photocatalytic degradation of phenol and benzoic acid using zinc oxide powders prepared by the sol–gel process. *Alex. Eng. J.* **2013**, *52*, 517–523. [[CrossRef](#)]
57. Tseng, D.-H.; Juang, L.-C.; Huang, H.-H. Effect of Oxygen and Hydrogen Peroxide on the Photocatalytic Degradation of Monochlorobenzene in Aqueous Suspension. *Int. J. Photoenergy* **2012**, *2012*, 328526. [[CrossRef](#)]
58. Escobar, J.A.P.; Moctezuma, E.; Rosales, B.S. Heterojunctions for Photocatalytic Wastewater Treatment: Positive Holes, Hydroxyl Radicals and Activation Mechanism under UV and Visible Light. *Int. J. Chem. React. Eng.* **2020**, *18*. [[CrossRef](#)]
59. Riaz, N.; Bustam, M.A.; Chong, F.K.; Man, Z.B.; Khan, M.S.; Shariff, A.M. Photocatalytic Degradation of DIPA Using Bimetallic Cu-Ni/TiO<sub>2</sub> Photocatalyst under Visible Light Irradiation. *Sci. World J.* **2014**, *2014*, 342020. [[CrossRef](#)]
60. Al Hashemi, W.; Maraqa, M.; Rao, M.; Hossain, M. Characterization and removal of phenolic compounds from condensate-oil refinery wastewater. *Desalination Water Treat.* **2015**, *54*, 660–671. [[CrossRef](#)]
61. Graham Solomons, T.W.; Fryhle, C.B. *Organic Chemistry*, 10th ed.; Wiley: Hoboken, NJ, USA, 2011; p. 1164S.

## 4.2 Paper II: Synthesis of highly active doped graphitic carbon nitride using acid-functionalized precursor for efficient adsorption and photodegradation of endocrine-disrupting compounds

Adeem Ghaffar Rana, Mian Zahid Hussain, Nikki Hammond, Simon Vlad Luca, Roland A. Fischer, Mirjana Minceva

ChemistrySelect 7(32) (10.1002/slct.202201909)

**Author contribution:** The thesis author conceptualized the paper's idea, performed part of the experiments, and characterized the catalysts (excluding XRD and SEM). He evaluated and interpreted the experimental results and wrote the manuscript draft.

### Summary

Endocrine-disrupting compounds (EDCs) embody one of the most persistent water pollutants affecting human and aquatic life. There is a need to develop a system or a material to remove these compounds from the water completely. g-C<sub>3</sub>N<sub>4</sub> provides a viable and cheap alternative compared to the conventional photocatalysts (TiO<sub>2</sub>, ZnO), and is also active in the visible range. Due to the low surface area, high bandgap, and high recombination rate, there is a need to alter g-C<sub>3</sub>N<sub>4</sub> to ensure a better catalytic activity. Paper II aims to study the effects of non-metallic doping, using an acid-functionalized precursor, on the photocatalytic performance of g-C<sub>3</sub>N<sub>4</sub>. The photocatalytic degradation was studied using a single wavelength (430 nm) visible light LED lamp and removal, using adsorption in the dark. This work synthesized a highly active, doped g-C<sub>3</sub>N<sub>4</sub> via a single-step strategy, in order to remove hormones using adsorption and photooxidation.

In this paper, the non-metallic doped g-C<sub>3</sub>N<sub>4</sub> catalysts were synthesized using sulfuric-, phosphoric-, and acetic acid-treated melamine, for sulfur (S), phosphorous (P), and oxygen (O) doping, respectively. This method provides a rapid, one-step synthesis for doping g-C<sub>3</sub>N<sub>4</sub> compared to the conventional method, saving time and energy. Metal doping can be environmentally unfavorable and incur high costs. In contrast, non-metallic doping can be economical, which can alter the interlayer distance to help modify the surface area, and the bandgap of the materials. The efficient adsorption and photocatalytic degradation of E2 and EE2, by non-metallic doped g-C<sub>3</sub>N<sub>4</sub>, were studied. The synthesized catalysts were characterized for surface, optical, and chemical properties using XPS, BET, UV-Vis, and XRD techniques. The sulfur-doped g-C<sub>3</sub>N<sub>4</sub> showed a narrow energy bandgap and a high surface area. Due to these attributes, the sulfur-doped g-C<sub>3</sub>N<sub>4</sub> performed better than the other catalysts synthesized in this work. Hormone adsorption using sulfur-doped g-C<sub>3</sub>N<sub>4</sub> was carried out in the dark. The glass jacketed reactor, with a working volume of 120 mL, and an immersion LED lamp, were used for experimentation. Only 63% of E2 (5ppm) was removed after 60 minutes due to adsorption, and the rest was degraded entirely with photocatalysis in only 45 minutes for 0.1 g/L of the catalyst. The kinetic data of E2 adsorption was fitted with three different adsorption

models: pseudo-first-order, pseudo-second-order, and the Elovich kinetic model. The pseudo-second-order kinetic model fitted the adsorption kinetics of E2 well, and photocatalytic degradation followed the exponential decay model. The intermediates produced during the photocatalytic reactions were identified using LC-MC, showing that the E2 has been degraded to smaller, less toxic molecules. The stability of the catalyst was also studied by performing the re-usability test of the catalyst.

It is concluded in this work that sulfur doping of g-C<sub>3</sub>N<sub>4</sub>, using acid-treated melamine, modified its energy bandgap, and helped increase the surface area. The change in the bandgap and the surface area, compared to the non-doped bulk g-C<sub>3</sub>N<sub>4</sub>, resulted in an enhanced photocatalytic activity to degrade the endocrine-disrupting compounds from water.



# Synthesis of Highly Active Doped Graphitic Carbon Nitride using Acid-Functionalized Precursors for Efficient Adsorption and Photodegradation of Endocrine-Disrupting Compounds

Adeem Ghaffar Rana,<sup>[a, b]</sup> Mian Zahid Hussain,<sup>[c]</sup> Nikki Hammond,<sup>[a]</sup> Simon Vlad Luca,<sup>[a]</sup> Roland A. Fischer,<sup>[c]</sup> and Mirjana Minceva<sup>\*[a]</sup>

A highly active non-metallic doped bulk graphitic carbon nitride ( $g\text{-C}_3\text{N}_4$ ) was synthesized via acid-functionalized melamine decomposition. Specifically, melamine was treated with acetic acid, sulfuric acid, and phosphoric acid to obtain oxygen, sulfur, and phosphorus-doped  $g\text{-C}_3\text{N}_4$  derivatives. Sulfur-doped  $g\text{-C}_3\text{N}_4$  exhibited remarkable photocatalytic activity to degrade two environmentally harmful hormones,  $17\beta$ -estradiol, and  $17\alpha$ -ethinylestradiol, due to its narrow energy bandgap and high surface area. The hormones were removed entirely in 30–

45 min by adsorption in the dark, followed by photodegradation under visible light (430 nm). Furthermore, the pseudo-second-order kinetic model fitted the adsorption kinetics well, and photocatalytic degradation followed the exponential decay model. LC–MS identified the intermediate products for the photodegradation of  $17\beta$ -estradiol (E2). This study provides a simple one-step method to synthesize highly reactive metal-free doped bulk  $g\text{-C}_3\text{N}_4$  photocatalysts to remove harmful water pollutants.

## Introduction

Pollution caused by endocrine-disrupting compounds (EDCs) is a persistent challenge in water treatment.<sup>[1]</sup> EDCs pose a health hazard to humans and animals and are a growing environmental concern.<sup>[2]</sup> These compounds can interfere with the hormone balance in humans and animals and adversely affect reproduction, sexual development, stress response, and the body's overall chemical equilibrium.<sup>[3]</sup> Exposure to EDCs can even lead to several human cancers.<sup>[4]</sup> EDCs disrupt the normal endocrine function by interacting with hormone receptors and mimicking natural estrogens' physiological function.<sup>[5]</sup> Among EDCs, which include both natural and synthetic compounds,<sup>[3]</sup>  $17\beta$ -estradiol (E2) and  $17\alpha$ -ethinylestradiol (EE2) are the most harmful and persistent natural estrogens.<sup>[4]</sup> E2 is a natural

hormone in women and is associated with the reproductive system; on the other hand, EE2 is a synthetic hormone produced from natural E2 and used as the active ingredient in some oral contraceptives. Even at low concentrations (ng/L), E2 and EE2 have a solid estrogenic effect.<sup>[1]</sup> E2 primarily enters the water systems via human and animal urine; however, the intake of products such as birth control pharmaceuticals and other hormonal products used in the dairy industry can cause an increase in its prevalence as a pollutant in water.<sup>[6]</sup> E2 is resistant to typical sewage treatment procedures and frequently gets released back into the water from where it can enter drinking and surface water.<sup>[7]</sup> Given the threats that E2 and EE2 pose to human health,<sup>[3]</sup> a need exists to develop effective treatment processes to remove these compounds from water systems.

Advanced oxidation processes (AOPs) are alternative solutions to removing organic pollutants like E2 from aqueous media.<sup>[4]</sup> Although AOP systems rely on various reaction means and methods, they all share the common characteristic of producing  $\bullet\text{OH}$  radicals. The reactivity of  $\bullet\text{OH}$  radicals toward organic molecules, combined with their limited selectivity, renders them beneficial oxidants for wastewater treatment.<sup>[8]</sup> Indeed,  $\bullet\text{OH}$  radicals have been observed to play a vital role in removing and degrading toxic wastewater contaminants into benign species.<sup>[9]</sup> Among the various AOP processes, photocatalysis is one of the promising approaches to wastewater treatment, as it is cost-effective, highly efficient, and exhibits low toxicity.<sup>[2]</sup>

The reaction kinetics of photocatalysis is affected by multiple factors, including the catalyst's appropriate energy bandgap and surface properties, the incident light's wavelength, and the target compound's chemical properties.<sup>[1]</sup> Although a wide variety of catalytic materials exist that can be used in photo-

[a] A. Ghaffar Rana, N. Hammond, Dr. S. Vlad Luca, Prof. Dr. M. Minceva  
Biothermodynamics, TUM School of Life Sciences  
Technical University of Munich  
Maximus-von-Imhof-Forum 2,  
Freising 85354, Germany  
E-mail: Mirjana.minceva@tum.de

[b] A. Ghaffar Rana  
Department of Chemical, Polymer, and Composite Materials Engineering  
University of Engineering and Technology (UET)  
Lahore 39161, Pakistan

[c] Dr. M. Zahid Hussain, Prof. Dr. R. A. Fischer  
Department of Chemistry and Catalysis Research Center  
Technical University of Munich  
Garching 85748, Germany

Supporting information for this article is available on the WWW under <https://doi.org/10.1002/slct.202201909>

© 2022 The Authors. ChemistrySelect published by Wiley-VCH GmbH. This is an open access article under the terms of the Creative Commons Attribution License, which permits use, distribution and reproduction in any medium, provided the original work is properly cited.

catalysis, graphitic carbon nitride ( $g\text{-C}_3\text{N}_4$ ) has emerged as one of the most promising materials for photocatalytic applications in both environmental and energy-producing processes.<sup>[10]</sup>  $g\text{-C}_3\text{N}_4$  is a non-toxic polymeric semiconductor exhibiting high chemical and thermal stability.<sup>[11]</sup> This semiconductor can easily be synthesized from compounds such as melamine and urea via the thermal decomposition of nitrogen-rich precursors under appropriate reaction conditions. The main drawback of  $g\text{-C}_3\text{N}_4$  is its limited photocatalytic activity resulting from its low surface area.<sup>[11]</sup> Some techniques like exfoliation improve the surface area and performance but need additional heat. Metal doping has become a popular approach to improving the photocatalytic performance of  $g\text{-C}_3\text{N}_4$ ,<sup>[10]</sup> however, using metals can be costly and environmentally unfriendly, and it may cause the catalyst to become toxic. Therefore, developing alternative strategies for increasing the photocatalytic activity of  $g\text{-C}_3\text{N}_4$  is a crucial research goal.

This study aims to enhance the activity of  $g\text{-C}_3\text{N}_4$  in removing harmful estrogenic compounds from water systems without adding metals to the catalytic system. To achieve this goal, melamine was functionalized with non-metallic elements such as sulfur (S), oxygen (O), and phosphorus (P) to obtain the synthesized doped  $g\text{-C}_3\text{N}_4$  species. The activity of the doped catalysts was tested for degradation of  $17\beta$ -estradiol and  $17\alpha$ -ethinylestradiol in an aqueous solution using adsorption in dark and photodegradation in a stirred glass reactor under irradiation with an immersion LED lamp. The extent of EDC photodegradation was determined by analyzing the concentration of the hormones in the water solution at regular time intervals using high-performance liquid chromatography (HPLC) technology.

## Results and Discussion

### Photocatalyst characterization

The crystalline structures of the undoped  $g\text{-C}_3\text{N}_4$  (BCN) and S, O, and P doped  $g\text{-C}_3\text{N}_4$  (SBCN, OBCN, and PBCN) samples synthesized after decomposition of acid-treated melamine

were determined based on the powder X-ray diffraction (PXRD) patterns reported in Figure 1a. BCN, OBCN, and SBCN catalysts exhibited the characteristic peaks of  $g\text{-C}_3\text{N}_4$  at about  $2\theta$  of  $27.3^\circ$  and  $2\theta$  of  $13.1^\circ$ . From the (002) plane, the high-intensity peak is due to the typical interlayer stacking of conjugated aromatic systems like  $g\text{-C}_3\text{N}_4$ . Moreover, a minor peak due to the (100) plane is ascribed to repeated units of tri-s-triazine.<sup>[11–12]</sup> The PXRD peak intensities of BCN and OBCN are almost the same, while in the case of SBCN, the peak intensity is slightly lower. Although no peaks due to phosphorus were observed in PBCN, the intensity of the  $g\text{-C}_3\text{N}_4$  PXRD characteristic peaks has decreased, indicating the reduction in the crystallinity of this material. Indeed, the presence of large amounts of phosphorus in the catalyst can be assumed to cause an enhancement of layer spacing.<sup>[13]</sup> During the poly-condensation of acid-treated precursors, the loss of lattice C or N centers leads to a change in the crystalline structure, which inhibits the growth of  $g\text{-C}_3\text{N}_4$  crystals.<sup>[13–14]</sup> In addition, the PXRD patterns of PBCN comprised (see inset in Figure 1a) an extremely broad (002) peak, and the relative intensities of both peaks massively decreased compared to BCN. This broad peak is due to the significant phosphorus content, indicating that the growth of  $g\text{-C}_3\text{N}_4$  crystals is inhibited by introducing phosphoric acid.<sup>[14]</sup>

The FTIR spectra were recorded to determine the prepared samples' doping extent. The FTIR spectra of the doped and undoped  $g\text{-C}_3\text{N}_4$  samples are presented in Figure 1b. The peaks observed between  $1650$  and  $1242\text{ cm}^{-1}$  can be attributed to the stretching vibration modes of the C–N bond and the aromatic C=N heterocyclic species in repeated units of tri-s-triazine.<sup>[12,15]</sup> Additionally, the sharp peak appearing at  $813\text{ cm}^{-1}$  in the spectra of BCN, OBCN, and SBCN is due to the breathing mode of the s-triazine ring system. Still, this peak was almost absent in the FTIR spectrum of PBCN, which indicates that tri-s-triazine in this catalyst undergoes a drastic modification.

On the contrary, the broad-band visible in the  $3100$ – $3500\text{ cm}^{-1}$  wavenumber range in the spectra of all four catalysts can be attributed to the vibration modes of the OH group from adsorbed water molecules and the stretching vibrations of N–H bonds from residual amino groups. In the

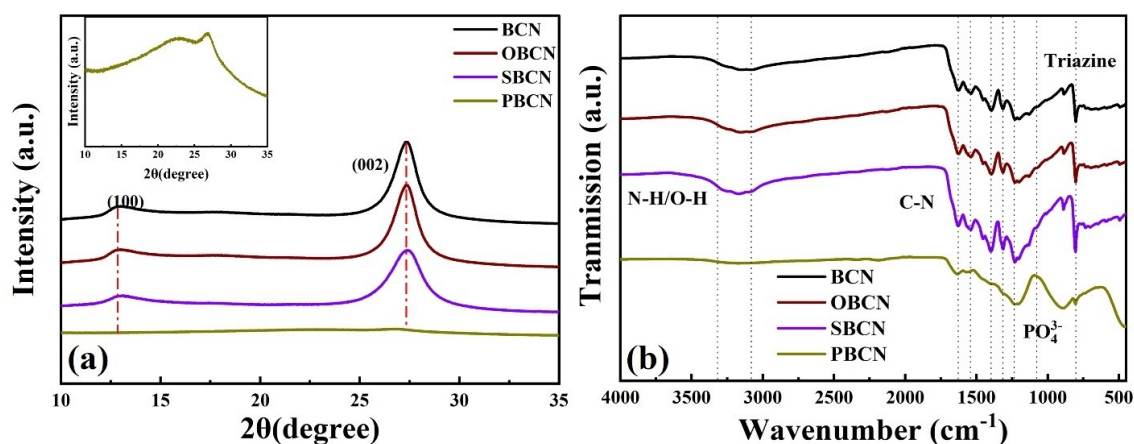


Figure 1. (a) PXRD and (b) FTIR spectra of BCN and doped OBCN, SBCN, and PBCN.

PBCN spectrum, a broad peak between 1250 and 800  $\text{cm}^{-1}$  was identified due to the vibration modes of  $\text{PO}_4^{3-}$  groups.<sup>[16]</sup> Also, the intensity of the spectra of PBCN is low compared to BCN. This observation can be ascribed to a modification in the chemical structure of tri-s-triazine due to the presence of P in the catalyst, and this result was in good agreement with PXRD data (Figure 1a). In the SBCN spectrum, no prominent peaks attributable to moieties containing S were observed, probably due to the low sulfur content in the structure of this species.<sup>[15]</sup> The BCN and OBCN have shown similar FTIR spectra. The results of the further characterization performed in this work are graphically presented only for the doped  $\text{g-C}_3\text{N}_4$  catalysts. The complete characterization results of undoped  $\text{g-C}_3\text{N}_4$  are presented in our previous work.<sup>[11]</sup>

The chemical composition of the OBCN, SBCN, and PBCN samples was investigated using X-ray photoelectron spectroscopy (XPS). Notable, the XPS elemental survey spectra of the samples (Figure S1) confirmed the presence of C, N, and O in all samples. The C/N ratio in PBCN is lower than in OBCN and SBCN; P in PBCN is 21.32 atomic % pointing to the possible reason behind the observed reduction in C and N contents in the sample. Remarkably, S present in SBCN is only 0.16 atomic %. This observation is because  $\text{CH}_3\text{COOH}$  and  $\text{H}_2\text{SO}_4$  were removed during the heating and sublimation of melamine. However, phosphorous is not entirely removed from the  $\text{g-C}_3\text{N}_4$  structure as  $\text{PO}_4^{3-}$  cannot be decomposed entirely at melamine's decomposition temperature (550  $^\circ\text{C}$ ).<sup>[17]</sup>

The C 1s and N 1s XPS spectra were recorded to investigate the interaction between C and N atoms. The deconvoluted C 1s XPS spectra of the doped samples (Figure 2a) exhibited two strong peaks appearing at 285 and 288 eV, which can be assigned to the standard (C–C) carbon bonds and  $\text{sp}^2$  hybridized carbon (N–C=N) in triazine rings.<sup>[11,18]</sup> Two low-intensity peaks observed at 286 and 289 eV can be assigned to the amino-functional groups (C–NH<sub>2</sub>) and the carboxyl group (O–C=O) bound to the surface of  $\text{g-C}_3\text{N}_4$ , respectively.<sup>[11,18a,19]</sup> In the case of PBCN, the intensities of C 1s peaks were substantially lower than their counterparts observed for SBCN and OBCN, which indicates that the C atoms might have been replaced by P atoms in the chemical structure of  $\text{g-C}_3\text{N}_4$ .<sup>[20]</sup> The deconvoluted N 1s spectra (Figure 2b) exhibited three prominent peaks at around 398.4, 400.2, and 401.2 eV for OBCN and SBCN with varying intensities. The strong peak at 397.8 eV corresponds to the triazine rings'  $\text{sp}^2$  hybridized nitrogen atom bound to carbon (C–N=C). The other two peaks of medium intensity appearing at 400.2 and 401.2 eV can be assigned to the presence of tertiary N in N–(C)<sub>3</sub> units and amino functional groups (NH<sub>2</sub> or NH), respectively.<sup>[11,18,20]</sup>

The O 1s spectrum of OBCN reported in Figure 2c includes peaks at 532.7 and 535.7 eV, corresponding to the O–C–N/C–O bonds and adsorbed moisture, respectively.<sup>[21]</sup> Notably, deconvolution of the S 2p spectrum of SBCN reported in Figure 2d indicated the presence of three peaks at 163.9, 165.1, and 168.9 eV. The peak at 163.9 eV can be assigned to the C–S bond formed due to the substitution of lattice nitrogen with

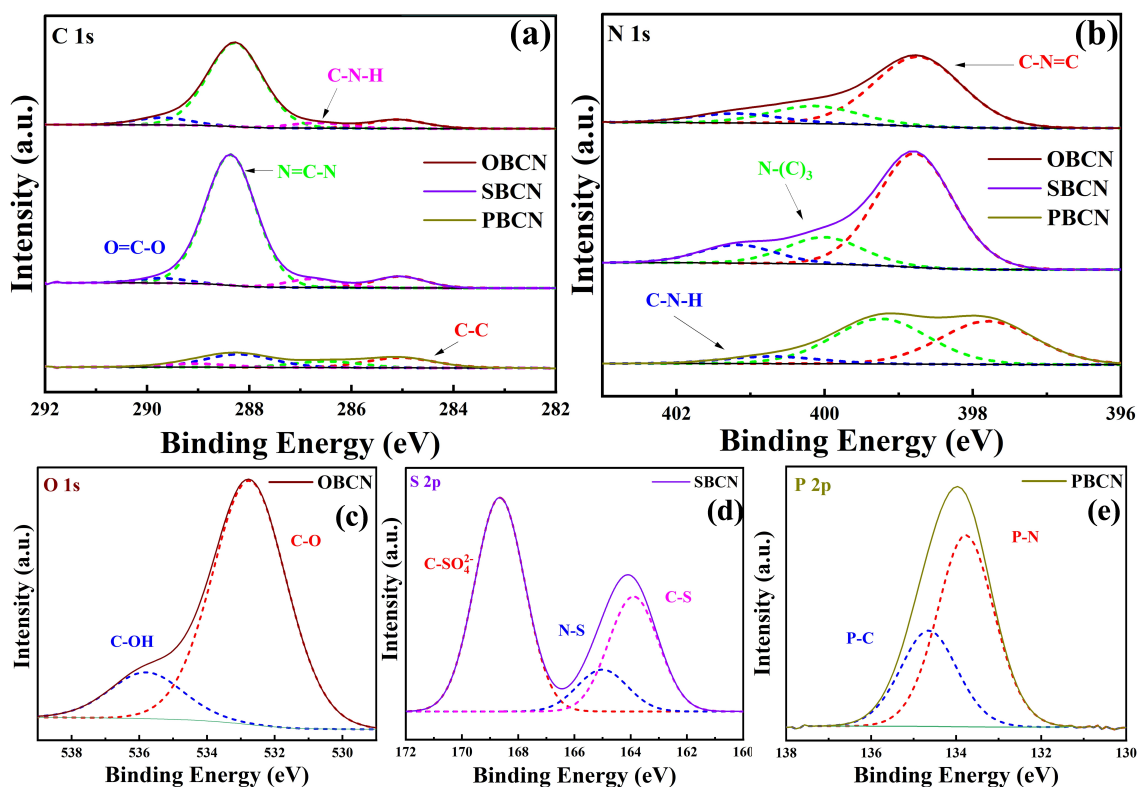


Figure 2. High resolution deconvoluted XPS spectra of (a) C 1s (b) N 1s (c) O 1s (d) S 2p, and (e) P 2p for catalysts OBCN, SBCN, and PBCN.

sulfur. The weakest peak was at 165.4 eV, which was regarded due to N–S bonds resulting from replacing lattice carbon with sulfur. The most substantial peak was centered at 169.3 eV, indicating that  $\text{SO}_4^{2-}$  was present in SBCN.<sup>[15,22]</sup> The P 2p spectrum of PBCN (reported in Figure 2e) includes peaks at 133.6 and 132.8 eV, attributed to P–C and P–N bonds, respectively.<sup>[17,23]</sup>

The BET surface area and pore size distribution of the undoped and doped  $\text{g-C}_3\text{N}_4$  samples were determined from their  $\text{N}_2$  adsorption/desorption isotherms. In general, a high surface area can provide more active sites for the reactants, resulting in the high efficiency of the catalytic process. As can be seen from the data reported in Figure 3, the curves obtained for the OBCN, SBCN, and PBCN samples are type IV isotherms with H3 hysteresis loops. These curves are characteristic of mesoporous materials, and they stem from the difference in the curvatures of the meniscus during adsorption and desorption with a capillary condensation. The pore radius ranges between (1.5 and 4.5 nm), which confirms the presence of mesopore in the structure. The values for the BET surface area of BCN, OBCN, SBCN, and PBCN were calculated to be 11, 11, 46.9, and 38  $\text{m}^2/\text{g}$ , respectively. As presented in our previous work, the undoped  $\text{g-C}_3\text{N}_4$  has shown a similar

adsorption-desorption isotherm, hysteresis loop, and pore size distribution to doped  $\text{g-C}_3\text{N}_4$  and BET surface area of 10  $\text{m}^2/\text{g}$ .<sup>[11]</sup> As expected, BCN and OBCN have similar surface areas. Indeed, the surface area of SBCN and PBCN was manifold higher than that of the non-doped catalyst (BCN). Hence a superior catalytic performance could be expected for the SBCN and PBCN compared to BCN and OBCN due to the availability of active sites for substrate adsorption and photoreaction. The Scanning electron microscopy image of the SBCN sample is reported in Figure 3d. It shows that the sulfur-doped  $\text{g-C}_3\text{N}_4$  exhibits a stacked structure.

UV-vis absorption spectra were recorded to gather evidence on the optical absorption and calculate the energy bandgaps of the doped  $\text{g-C}_3\text{N}_4$ . The absorption spectra of OBCN, SBCN, and PBCN samples are reported in Figure 4a, and their Tauc plots are reported in Figure 4b. All three catalysts exhibited absorption in the visible region, and the absorption edge of OBCN was observed at around 473 nm. However, the spectra of SBCN and PBCN exhibited a blue shift for this absorption to 462 and 440 nm compared to OBCN, respectively. The energy bandgaps of the synthesized catalysts were calculated from their respective Tauc plots.<sup>[11]</sup> As can be seen from Figure 4b, the energy bandgaps were 2.48, 2.53, and 2.65 eV for OBCN,

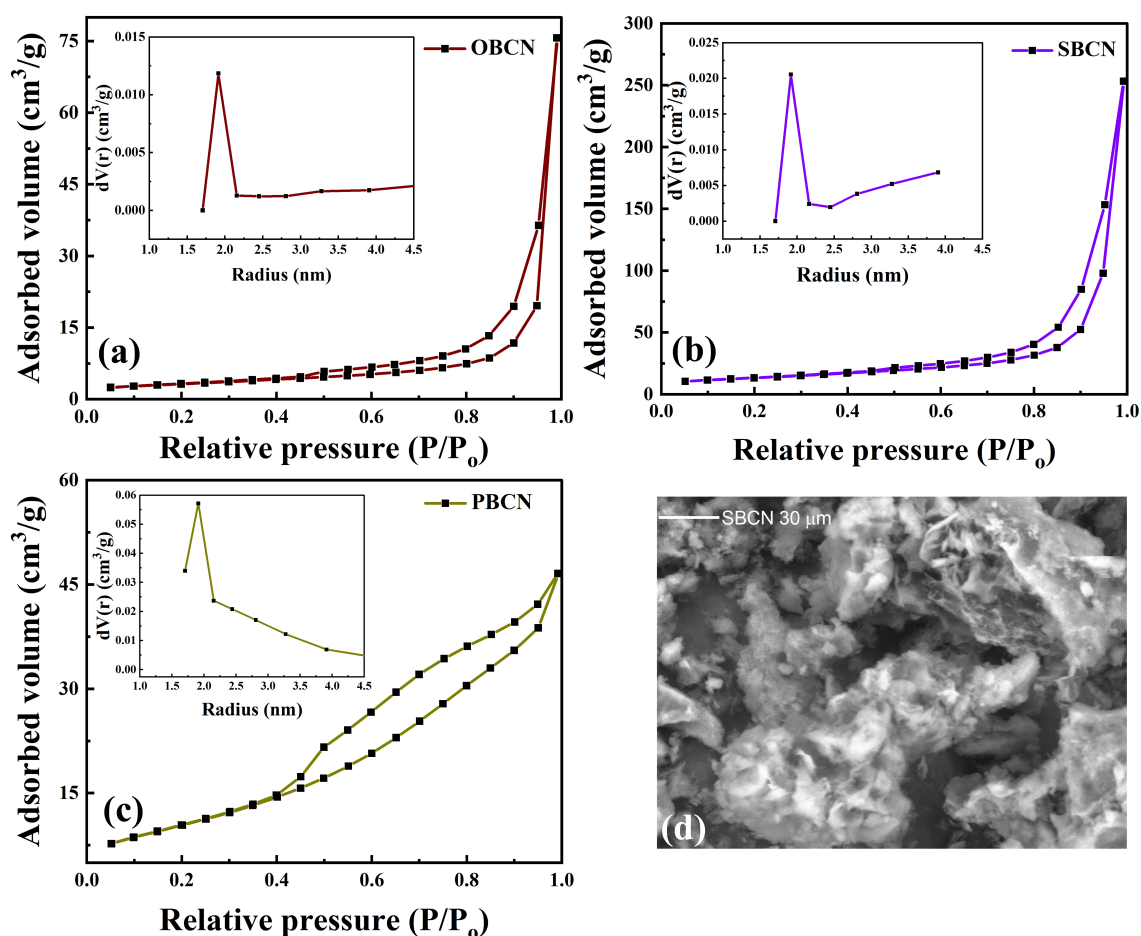


Figure 3. BET surface area and particle size distribution (shown in inset) of (a) OBCN, (b) SBCN, and (c) PBCN; (d) SEM image of the SBCN catalyst.



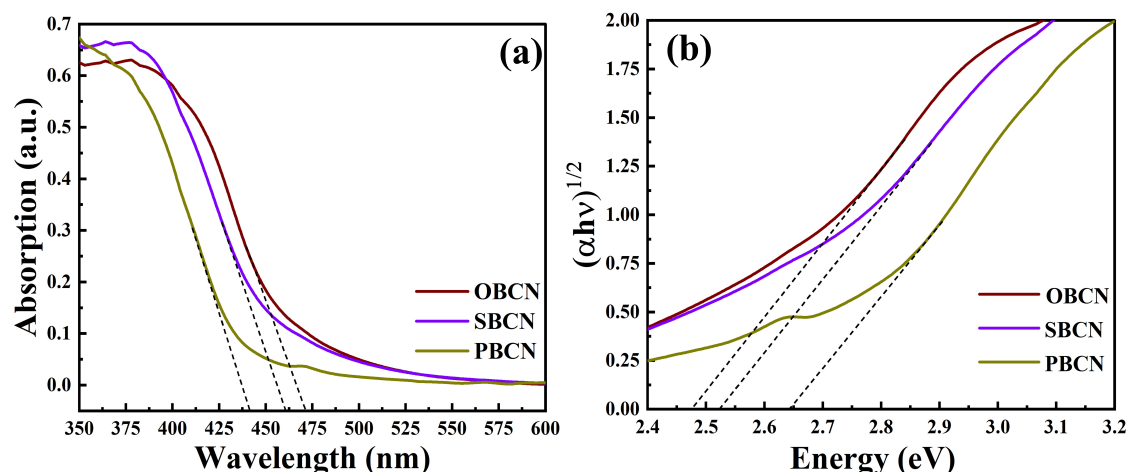


Figure 4. (a) UV-vis absorption spectra and (b) Tauc plots of OBCN, SBCN, and PBCN.

SBCN, and PBCN, respectively. In our previous published study, the bandgap of undoped bulk  $g\text{-C}_3\text{N}_4$  was determined to have a value of 2.58 eV.<sup>[11]</sup> The narrow bandgap of OBCN and SBCN compared to bulk  $g\text{-C}_3\text{N}_4$  can be ascribed to the incident light reflections in the structure, which increase the effective path length for light absorption. Meanwhile, a small amount of S and O can affect the electronic structure of  $g\text{-C}_3\text{N}_4$  to narrow the bandgap.<sup>[24]</sup> In the case of PBCN, the bandgap is wider than undoped bulk  $g\text{-C}_3\text{N}_4$  because of the high amount of P present in the structure. A large amount of impurity present in the structure can affect the electronic structure of the catalyst in such a way that it shows a blue shift and a large bandgap.<sup>[25]</sup> The  $\text{H}_3\text{PO}_4$  in melamine does not undergo complete decomposition during the heating and sublimation of melamine, so a large amount of P is present in the structure of the catalyst.<sup>[17,26]</sup>

#### Adsorption and photocatalytic performance of the catalysts

As described in the experimental section, the hormone adsorption experiments were performed in the dark. The results of the kinetics study of  $17\beta$ -estradiol adsorption are reported in Figure 5. All three photocatalysts, OBCN, SBCN, and PBCN, exhibited similar adsorption patterns; for simplicity, only the data collected for SBCN are reported here as a representative case for all studied catalysts. The adsorption kinetics curve of  $17\beta$ -estradiol is presented in Figure 5a. As shown in Figure 5a, predominantly adsorption took place in the first 5 min of the contact between  $17\beta$ -estradiol and the photocatalyst. After 15 min, there was only a minor change in the hormone concentration in the solution. Namely, after 60 min, 63% of the  $17\beta$ -estradiol was removed, while after 180 min, 66% (not shown in Figure 5a). The fast adsorption in the first 5 min can be associated with the hydrophobicity of  $17\beta$ -estradiol (octanol/water partitioning coefficient,  $\log K_{ow}$  of 4.01).<sup>[27]</sup>

Three different kinetic models were used to analyze the adsorption data: pseudo-first-order (Eq. (4)), pseudo-second-order (Eq. (5)), and Elovich kinetic model (Eq. (6)). A comparison

of the experimental and calculated data is presented in Figure 5 (b–d). The fitted model parameters are summarized in Table S1. The pseudo-second-order kinetic model showed the highest correlation coefficient value ( $R^2 = 0.999$ ) for the adsorption of  $17\beta$ -estradiol on SBCN, demonstrating that it is the best fitting model for this system. According to this model, the equilibrium adsorption capacity ( $q_e$ ) is  $17\beta$ -estradiol on SBCN 33.38 mg/g. Elovich's kinetic model exhibited a higher  $R^2$  (0.904) value than the pseudo-first-order (0.471) model.<sup>[27d]</sup>

The photocatalytic performance of synthesized photocatalysts for hormone degradation was investigated. First, a photolysis experiment was conducted without a catalyst (Figure 6a) to determine whether these hormones undergo self-degradation in visible light. There was almost negligible degradation during the photolysis reaction. All other experiments were performed in the presence of the catalysts. The homogeneous dispersion of the catalyst was ensured by sonicating the reaction mixture (i.e., the mixture comprising the water solution of the hormones and the catalyst) and by stirring it for 15 min (an optimal time chosen after initial adsorption experiments) in the dark. The reaction time starts as soon as the light is turned on; only an adsorption process takes place up to that moment.

As shown from the data reported in Figure 6a, the sulfur-doped SBCN sample demonstrated the highest adsorption and photodegradation with almost complete removal of  $17\beta$ -estradiol in 45 min; over the same period, 86% removal was achieved with BCN, 88% with OBCN, and 64% with PBCN. From this amount, 63%, 59%, 57%, and 55% of  $17\beta$ -estradiol were removed by adsorption on SBCN, BCN, OBCN, and PBCN, respectively. For BCN and OBCN, a relatively lower surface area limits the adsorption and, subsequently, the photodegradation of the  $17\beta$ -estradiol. BCN and OBCN have shown almost the same activity because of the similar nature confirmed by XRD, BET, and FTIR. Notably, PBCN exhibited negligible photodegradation, and with this catalyst, the  $17\beta$ -estradiol was removed primarily by adsorption. The observed poor perform-

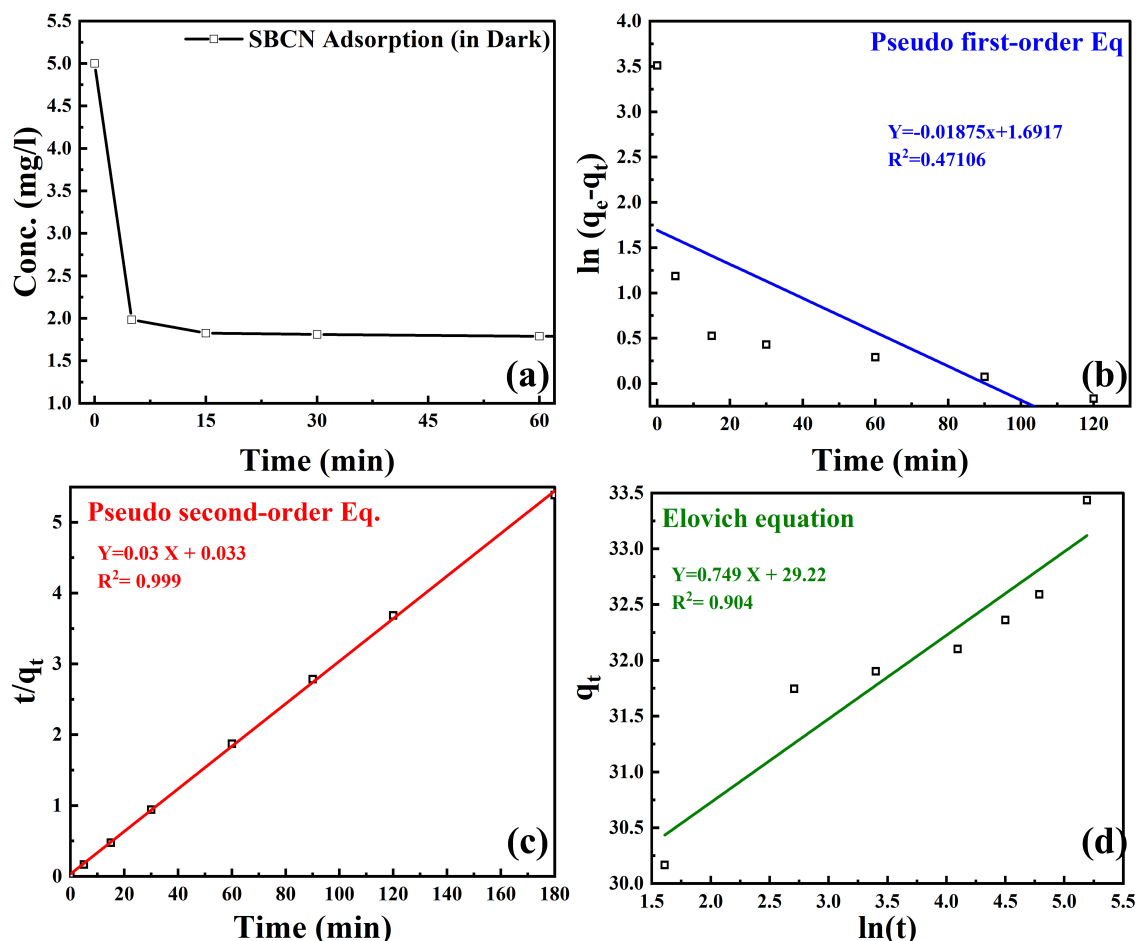


**Figure 5.** (a) Adsorption kinetics of 17β-estradiol with 0.1 g/L SBCN and 5 mg/L pollutant concentration; (b) pseudo-first-order model, (c) pseudo-second-order model, and (d) Elovich model, pH 7, temperature 25 °C.

ance of PBCN may have to do with the fact that P atoms had replaced the structural C and N atoms, and there is a large amount of residual  $\text{PO}_4^{3-}$  species in the catalyst, which suppressed catalytic activity.

Different amounts of catalyst were used further to investigate the kinetics of the photocatalytic degradation reaction. For this study, SBCN was selected as the best performing catalyst, and its concentration in a 17β-estradiol aqueous solution varied between 0.05 and 0.2 g/L. The 17β-estradiol removal curves are presented in Figure 6b. The photocatalytic degradation efficiency increases with the amount of catalyst because the number of active sites increases with the increase of the catalyst.<sup>[11]</sup> However, it should be noted that complete 17β-estradiol removal was achieved in 45 min with 0.1 and 0.2 g/L of SBCN catalyst.

In the following, adsorption followed by photodegradation was also carried out for 17α-ethinylestradiol with the 0.1 g/L SBCN catalyst. As can be seen from Figure 6c, the 17α-ethinylestradiol was also entirely degraded and removed from water in 45 min. Notably, the photodegradation of 17α-ethinylestradiol was even faster than that of 17β-estradiol. This observation is due to the presence of unsaturated triple bonds

in 17α-ethinylestradiol, which readily undergo oxidation to produce less harmful products. This study can provide an initial base, but optimizing the amount of catalyst should be performed to save the cost for other hormonal pollutants selected. The chemical structures of both compounds are reported in Table S2.

The photodegradation curves reported in Figure 6 were well-fitted by an exponential decay model, and by fitting the said curves with this model, the reaction rate constant ( $k$ ) could be calculated utilizing the following equation (1):

$$\frac{C}{C_0} = e^{-kt} \quad (1)$$

where  $C$  is the concentration of 17β-estradiol at irradiation time  $t$ ,  $C_0$  is the 17β-estradiol concentration after adsorption in this case, i.e., at the beginning of the photocatalytic degradation reaction, and  $k$  is the rate constant. The rate constant  $k$  for SBCN, OBCN, and PBCN were 0.139, 0.046, and 0.008  $\text{min}^{-1}$ , respectively. In detail, the decomposition of  $\text{SO}_4^{2-}$  during the heat treatment of melamine contributed to SBCN acquiring a porous structure, which benefited substrate adsorption and

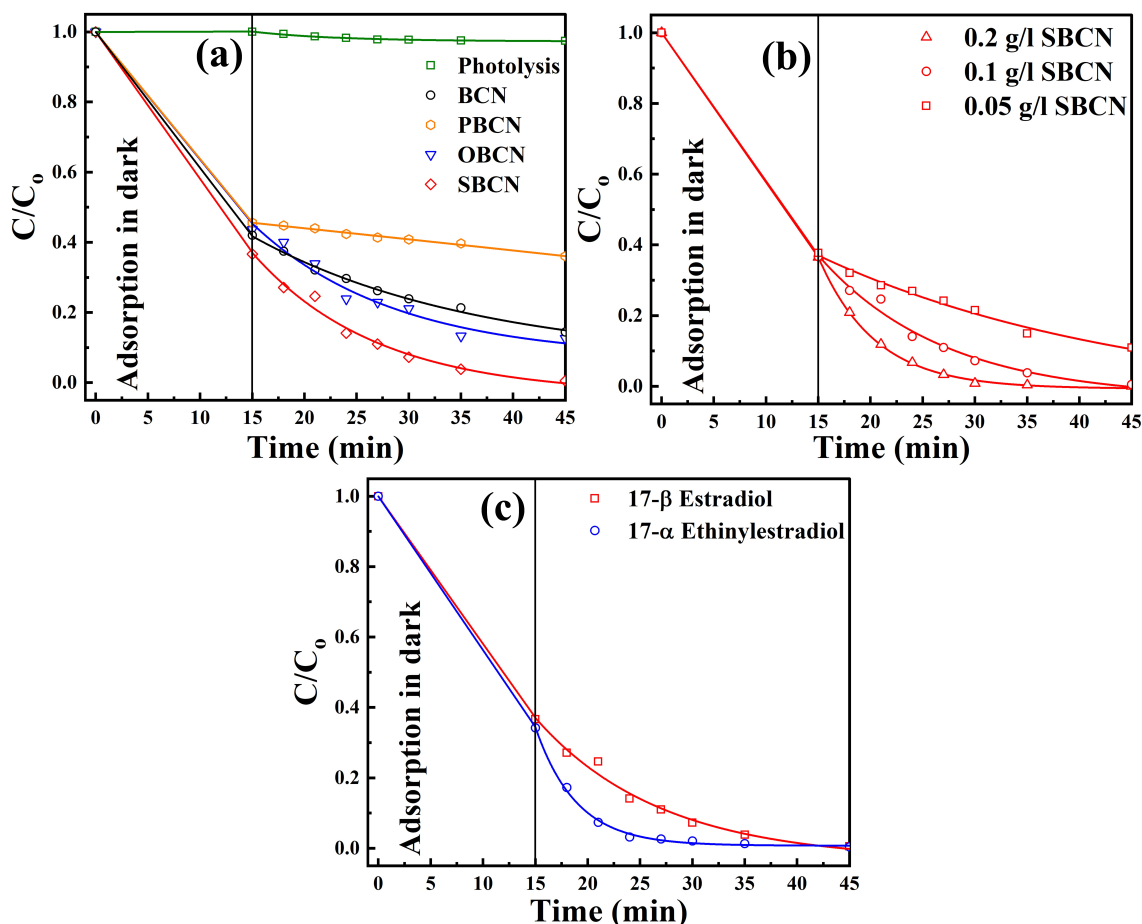


**Figure 6.** Photocatalytic degradation curves of (a) 17 $\beta$ -estradiol with doped g-C<sub>3</sub>N<sub>4</sub> catalysts with a catalyst concentration of 0.1 g/L; (b) 17 $\beta$ -estradiol using different concentrations of SBCN catalyst, and (c) 17 $\beta$ -estradiol and 17 $\alpha$ -ethinylestradiol at 0.1 g/L SBCN.

increased the accessibility of the active catalytic sites. The photodegradation curves for the different amounts of best-performing SBCN reported in Figure 6b fit the exponential decay model. The values for the rate constant  $k$  for the degradation reactions whereby the SBCN concentrations were 0.2, 0.1, and 0.05 g/L were 0.24, 0.139, and 0.042 min<sup>-1</sup>, respectively.

The re-usability of SBCN was demonstrated by performing two cycles of hormone degradation after subjecting the catalyst to thorough washing and drying at 120 °C for 12 h. The degradation efficiency of the catalyst remained unchanged, and the material remained stable for at least two cycles (Supplementary Figure S2).

### Photocatalytic degradation mechanism

The typical mechanism is given in equations (2)–(8). These photo-induced charge carriers and radicals eventually lead to the degradation of pollutants by the reduction and oxidation processes. The primary intermediates and products of E2 were analyzed and identified by LC/MS. The identification results are presented in Table 1. The SBCN can generate electrons  $e^-$  and

holes  $h^+$  in the conduction and valence band when irradiated with light to react with the adsorbed hormones on the surface of the SBCN catalyst. The generated holes can directly oxidize water or hydroxide ions to hydroxyl radical ( $\bullet OH$ ). The oxygen molecules present in the system can accept the electron to produce the superoxide radical ( $\bullet O_2^-$ ). These superoxide radicals can also produce hydroxyl radicals ( $\bullet OH$ ). The generated radicals and holes react with the pollutants to produce intermediates and products.<sup>[11,28]</sup> The presence of these ROS, e.g., hydrogen peroxide using g-C<sub>3</sub>N<sub>4</sub>, was previously confirmed.<sup>[28,29]</sup>

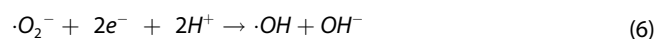
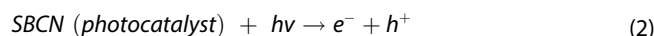


Table 1. Degradation products of E2.

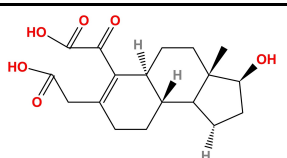
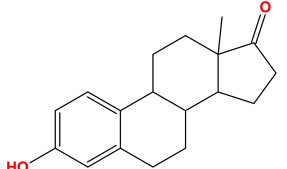
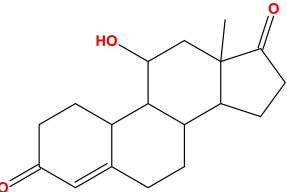
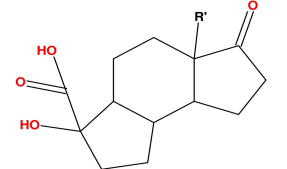
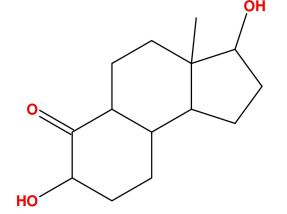
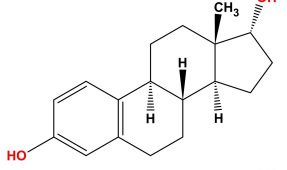
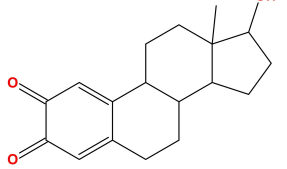
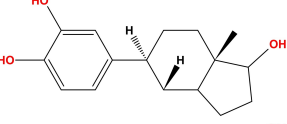
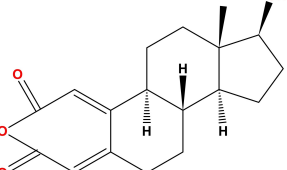
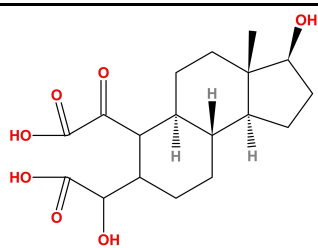
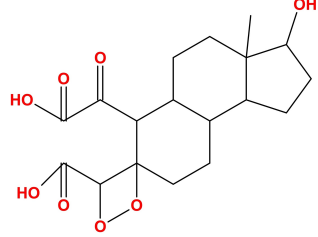
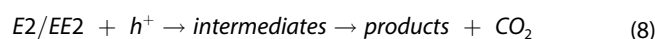
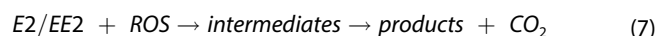
No	Molecular Formula	m/z	Probable structure	Ref
1	C <sub>18</sub> H <sub>24</sub> O <sub>6</sub>	335.11		[28a]
2	C <sub>18</sub> H <sub>22</sub> O <sub>2</sub>	269.14		[30]
3	C <sub>18</sub> H <sub>26</sub> O <sub>3</sub>	288.70		[30]
4	C <sub>14</sub> H <sub>20</sub> O <sub>4</sub>	251.17		[31]
5	C <sub>14</sub> H <sub>22</sub> O <sub>3</sub>	236.91		[30]
6	C <sub>18</sub> H <sub>24</sub> O <sub>2</sub>	271.15		[32]
7	C <sub>18</sub> H <sub>22</sub> O <sub>3</sub>	285.14		[30]
8	C <sub>18</sub> H <sub>24</sub> O <sub>3</sub>	287.13		[28a]
9	C <sub>18</sub> H <sub>22</sub> O <sub>4</sub>	301.16		[32]

Table 1. continued

No	Molecular Formula	m/z	Probable structure	Ref
10	C <sub>18</sub> H <sub>24</sub> O <sub>7</sub>	352.96		[32]
11	C <sub>18</sub> H <sub>24</sub> O <sub>8</sub>	365.69		[30]



The degradation products formed during the photocatalytic experiments determined using the LC-MS method described in the materials and method section are listed in Table 1

## Conclusion

In summary, undoped and nonmetal sulfur, oxygen, and phosphorous doped g-C<sub>3</sub>N<sub>4</sub> (BCN, SBCN, OBCN, and PBCN) were successfully synthesized from untreated and acid-treated melamine. The photocatalytic performance of obtained catalysts was tested to degrade two hormones, namely 17β-estradiol and 17α-ethinylestradiol, under visible light irradiation. PXRD, FTIR, and XPS analyses confirmed the phase and chemical structures of g-C<sub>3</sub>N<sub>4</sub> and its derivatives obtained by doping g-C<sub>3</sub>N<sub>4</sub> with nonmetals. Among the synthesized g-C<sub>3</sub>N<sub>4</sub> derivatives, sulfur-doped g-C<sub>3</sub>N<sub>4</sub> (SBCN) exhibited the highest photocatalytic activity toward the studied hormones due to its higher BET surface area and narrower energy bandgap than the other three catalysts. The hormone adsorption on SBCN was quick due to the hydrophobic nature of these hormones. The adsorption was followed by photodegradation under visible light (430 nm) irradiation. Complete removal of 17β-estradiol was achieved in 45 min, and of 17α-ethinylestradiol was achieved in 30 min. Three kinetic adsorption models were used to fit the experimental data, and the pseudo-second-order model was observed to best represent the adsorption of 17β-estradiol onto SBCN. The proposed mechanism of the ROS generation and intermediate products from pollutant photodegradation are presented. The nonmetal doping of g-C<sub>3</sub>N<sub>4</sub> via acid-treated melamine modified its energy bandgap and helped increase the surface area. As a result, it enhanced the



photocatalytic activity to degrade the endocrine-disrupting compounds from the water.

## Experimental Section

### Reagents and chemicals

Melamine (C<sub>3</sub>H<sub>6</sub>N<sub>6</sub>, 99%) (Alfa Aesar), sulfuric acid (H<sub>2</sub>SO<sub>4</sub>, 96%) (VWR Chemicals), orthophosphoric acid (H<sub>3</sub>PO<sub>4</sub>, 85%) (VWR Chemicals), acetic acid (CH<sub>3</sub>COOH), (VWR Chemicals), acetonitrile (C<sub>2</sub>H<sub>3</sub>N, 99.99%) (Sigma Life Science), 17β-estradiol (C<sub>18</sub>H<sub>24</sub>O<sub>2</sub>, 99%) (Sigma Life Science), 17α-ethinylestradiol (C<sub>20</sub>H<sub>24</sub>O<sub>2</sub>, 99%) (Sigma Life Science), methanol (Sigma Aldrich) and ultrapure water for HPLC (Sigma Aldrich) were used as received without pre-treatment.

### Synthesis of g-C<sub>3</sub>N<sub>4</sub>

g-C<sub>3</sub>N<sub>4</sub> was prepared using the published procedure involving the thermal decomposition of melamine.<sup>[12]</sup> Specifically, a muffle furnace kept under a static air atmosphere was used to synthesize g-C<sub>3</sub>N<sub>4</sub> from melamine (5 g) in a closed crucible. A 2 °C/min heating gradient was set in a two-step heating process until 450 °C was reached; this temperature was then maintained for 2 h. Subsequently, 550 °C was set as the final temperature, with a heating ramp of 2 °C/min; the muffle furnace was kept at the mentioned temperature for 4 h. A roughly 50% yield of bulk g-C<sub>3</sub>N<sub>4</sub> was obtained by conducting this process. The isolated material was allowed to cool down to room temperature naturally; it was then weighed and ground up using a mortar and pestle. The as-prepared g-C<sub>3</sub>N<sub>4</sub> was then washed and filtered; it was subsequently dried overnight in an oven at 80 °C.

### Synthesis of doped g-C<sub>3</sub>N<sub>4</sub>

The non-metallic doped g-C<sub>3</sub>N<sub>4</sub> was prepared by treating melamine with acetic acid, sulfuric acid, and phosphoric acid to achieve oxygen, sulfur, and phosphorous doping. In detail, melamine was mixed with a 2 M solution of the relevant acid. The mixture thus obtained was stirred for 2 h; the mixture was then centrifuged, washed, and filtered to obtain the relevant doped melamine sample. The said sample was thus used to prepare the relevant doped g-C<sub>3</sub>N<sub>4</sub> material via the same procedure implemented to prepare undoped g-C<sub>3</sub>N<sub>4</sub>. The undoped bulk sample was named BCN, and the doped bulk samples were named OBCN, SBCN, and PBCN, which stood for oxygen, sulfur, and phosphorus-doped g-C<sub>3</sub>N<sub>4</sub>, respectively.

### Characterizations of the catalyst

The N<sub>2</sub> sorption isotherms recorded to determine the values of the samples' Brunauer–Emmett–Teller (BET) surface area, pore size distribution, and pore volume were determined using an autosorb <sup>®</sup>iQ-MP/XR (Nova 4200e), Quantachrome instrument (Germany). Sample degassing was performed at 120 °C for 3 h before the analysis. The surface area of the catalyst was calculated from the N<sub>2</sub> sorption isotherms obtained at −196 °C. The Barrett–Joyner–Halenda (BJH) method determined the samples' pore size distribution. A Bruker D8 instrument with Cu Kα radiation (1.54 Å) (40 kV, 40 mA), a spin speed of 40 rpm in the range between 3° and 35°, and a step size of 0.01° was employed to study the crystalline phases of the synthesized catalysts. A Spectrum, Two FTIR Spectrometer (PerkinElmer, Switzerland) with a universal ATR

(UATR Two) cell equipped with a ZnSe single crystal, was used to collect the Fourier-transform infrared (FTIR) spectra of the samples in the 400–4000 cm<sup>−1</sup> wavenumber range. The FTIR spectral measurements were conducted at 4 cm<sup>−1</sup> and 60 scans. X-ray photoelectron spectroscopy (XPS) showed the samples' surface chemical analysis. A Kratos Axis Ultra DLD spectrometer with a monochromated Al Kα X-ray source operating at 168 W (12 mA × 14 kV) was used to collect the data. Step sizes of 1 and 0.1 eV were used for the survey spectra, and high-resolution scans were recorded with pass energies of 160 and 20 eV, respectively. Ultraviolet-visible (UV-vis) absorption spectra were recorded using a UV-3600 Plus spectrometer (Shimadzu, Kyoto, Japan) with medium scan speed using a 20-slit width with three external detectors in the 200–800 nm wavelength range.

### Hormone adsorption and photocatalytic degradation

This study performed two types of experiments: adsorption experiments in the absence of light and photocatalytic degradation in the presence of light. The experiments were carried out in a jacketed glass reactor with a maximum working capacity of 120 mL and placed in a safety cabinet (Peschl Ultraviolet GmbH, Mainz, Germany). SBCN experiments were performed in duplicates to ensure the reproducibility of the results. The irradiation for photocatalytic experiments was done using a custom-made immersion LED lamp comprising five individual LEDs (10 W) with a maximum emission of 430 nm. The photocatalytic reactor setup is shown in Figure S3.

First, only adsorption experiments in the absence of light were performed to evaluate the removal of the hormone by adsorption. The catalyst was suspended in a 5 mg/L hormone aqueous solution prepared from 1000 mg/L stock solution in methanol and stirred for 180 min. Samples were taken at regular time intervals and analyzed with the HPLC. For the adsorption/photocatalytic degradation experiments, the photocatalyst was added to a hormone aqueous solution in the reactor. The reactor was sonicated for 15 min to ensure the catalyst's homogenous dispersion in the solution. Afterward, the solution was stirred for 15 min in the dark under an airflow (50 mL/min). A sample was taken for analysis to determine the hormone concentration of the solution after the adsorption step. Next, the LED lamp was turned on, the photocatalytic reaction was started, and samples were collected at regular intervals. A photolysis experiment was conducted without a catalyst to verify the extent of self-degradation of 17β-estradiol under light irradiation.

The removal efficiency was evaluated by using equation (9):

$$\text{Total removal efficiency (\%)} = \frac{C_0 - C}{C_0} * 100 \quad (9)$$

where C<sub>0</sub> and C represent the pollutant concentrations at the beginning of the experiment (t = 0) and after a specific time interval of t, respectively.

The adsorption kinetics of 17β-estradiol was modeled using pseudo-first-order, pseudo-second-order, and Elovich kinetic models [Eq. (10)–(12)].<sup>[27d]</sup> The following equations were used to fit the adsorption data:

Pseudo-first-order model

$$\ln(q_e - q_t) = \ln q_e - k_1 t \quad (10)$$

Pseudo-second-order model

$$t/q_t = 1/k_2q_e^2 + t/q_e \quad (11)$$

Elovich equation

$$q_t = \left(1/\beta\right)\ln(\alpha\beta) + \left(1/\beta\right)\ln(t) \quad (12)$$

where  $k_1$  and  $k_2$  are the rate constants in  $\text{min}^{-1}$  and  $q_e$  and  $q_t$  are adsorption capacities at equilibrium and at time  $t$  in Eqs. (10) and (11), respectively. Notably, the constants  $\alpha$  and  $\beta$  in Eq. (12) represent the initial adsorption rate ( $\text{mg/g}\cdot\text{min}$ ) and the extent of surface coverage of the adsorbent and the activation energy, respectively.

### Analytical methods

The concentrations of  $17\beta$ -estradiol and  $17\alpha$ -ethinylestradiol were determined using a Prominence HPLC system (Shimadzu, Japan) comprising a binary pump (LC-20AB), a SIL-20 A autosampler, a DGU-20 A3 degasser, an SPD-M20 A diode-array detector and a single quadrupole MS (LCMS-2020). The analysis was conducted employing a Phenomenex (C18, 150 mm  $\times$  4.6 mm, 3  $\mu\text{m}$ ) column at a fixed flow rate of 0.8 mL/min, using 40% acetonitrile in water as the eluent; the run time was 10 min (sample injection volume 10  $\mu\text{L}$ ; detection wavelength 205 nm). The following MS conditions were used: dual ion source (DUIS),  $m/z$  range 50–500, negative ionization mode, nebulizing gas flow 2 L  $\text{min}^{-1}$ , drying gas flow 15 L  $\text{min}^{-1}$ , DL temperature 300  $^\circ\text{C}$ , heat block temperature 500  $^\circ\text{C}$ .

### Supporting Information Summary

Details of the characterization results (Figure S1), stability result (Figure S2), Details of the reactor (Figure S3), fitting data for the adsorption models (Table S1), and chemical structure of E2 and EE2 (Table S2) are provided in supporting information.

### Acknowledgements

Adeem Ghaffar Rana thanks the DAAD, Germany, and Higher Education Commission (HEC), Pakistan. Open Access funding enabled and organized by Projekt DEAL.

### Conflict of Interest

The authors declare no conflict of interest.

### Data Availability Statement

The data that support the findings of this study are available in the supplementary material of this article.

**Keywords:** graphitic carbon nitride · hormones · photocatalysis · water treatment ·  $17\beta$ -estradiol ·  $17\alpha$ -ethinylestradiol

- [1] M. J. Arlos, R. Liang, M. M. Hatat-Fraile, L. M. Bragg, N. Y. Zhou, M. R. Servos, S. A. Andrews, *J. Hazard. Mater.* **2016**, *318*, 541–550.
- [2] L. Li, Y. Long, Y. Chen, S. Wang, L. Wang, S. Zhang, F. Jiang, *Solid State Sci.* **2018**, *83*, 143–151.
- [3] A. R. Upreti, Y. Li, N. Khadgi, S. Naraginti, C. Zhang, *RSC Adv.* **2016**, *6*, 32761–32769.
- [4] V. M. Mboula, V. Héquet, Y. Andrès, Y. Gru, R. Colin, J. M. Doña-Rodríguez, L. M. Pastrana-Martínez, A. M. T. Silva, M. Leleu, A. J. Tindall, S. Mateos, P. Falaras, *Appl. Catal. B* **2015**, *162*, 437–444.
- [5] N. G. Menon, L. George, S. S. V. Tatiparti, S. Mukherji, *J. Environ. Manage.* **2021**, *288*, 112340.
- [6] L. Orozco-Hernandez, L. M. Gomez-Olivan, A. Elizalde-Velazquez, R. Natividad, L. Fabian-Castono, N. SanJuan-Reyes, *Sci. Total Environ.* **2019**, *669*, 955–963.
- [7] J. Mai, W. Sun, L. Xiong, Y. Liu, J. Ni, *Chemosphere* **2008**, *73*, 600–606.
- [8] a) R. Andreozzi, V. Caprio, A. Insola, R. Marotta, *Catal. Today* **1999**, *53*, 51–59; b) A. G. Rana, W. Ahmad, A. Al-Matar, R. Shawabkeh, Z. Aslam, *Environ. Technol.* **2017**, *38*, 1085–1092.
- [9] J. A. Garrido-Cardenas, B. Esteban-Garcia, A. Aguera, J. A. Sanchez-Perez, F. Manzano-Aguilario, *Int. J. Environ. Res. Public Health* **2019**, *17*, 21–39.
- [10] H. Sudrajat, *J. Solid State Chem.* **2018**, *257*, 26–33.
- [11] A. G. Rana, M. Tasbihi, M. Schwarze, M. Minceva, *Catalysts* **2021**, *11*, 662–679.
- [12] A. G. Rana, M. Minceva, *Catalysts* **2021**, *11*, 898–913.
- [13] S. Guo, Y. Tang, Y. Xie, C. Tian, Q. Feng, W. Zhou, B. Jiang, *Appl. Catal. B* **2017**, *218*, 664–671.
- [14] L. Zhang, X. Chen, J. Guan, Y. Jiang, T. Hou, X. Mu, *Mater. Res. Bull.* **2013**, *48*, 3485–3491.
- [15] K. Wang, Q. Li, B. Liu, B. Cheng, W. Ho, J. Yu, *Appl. Catal. B* **2015**, *176–177*, 44–52.
- [16] C.-Y. Kuo, C.-H. Wu, J.-T. Wu, Y.-R. Chen, *React. Kinet. Mech. Catal.* **2014**, *114*, 753–766.
- [17] Y. Zhao, J. Liu, C. Wang, X. Zhang, C. Chen, X. Zhao, J. Li, H. Jin, *J. Power Sources* **2019**, *424*, 176–183.
- [18] a) M. J. Lima, A. M. T. Silva, C. G. Silva, J. L. Faria, *J. Catal.* **2017**, *353*, 44–53; b) X. Yuan, C. Zhou, Y. Jin, Q. Jing, Y. Yang, X. Shen, Q. Tang, Y. Mu, A. K. Du, *J. Colloid Interface Sci.* **2016**, *468*, 211–219; c) M. J. Muñoz-Batista, D. Rodríguez-Padrón, A. R. Puente-Santiago, A. Kubacka, R. Luque, M. Fernández-García, *ChemPhotoChem* **2018**, *2*, 870–877.
- [19] a) M. Arif, G. Yasin, M. Shakeel, X. Fang, R. Gao, S. Ji, D. Yan, *Chem. Asian J.* **2018**, *13*, 1045–1052; b) Y. O. Ibrahim, A. Hezam, T. F. Qahtan, A. H. Al-Aswad, M. A. Gondal, Q. A. Drmash, *Appl. Surf. Sci.* **2020**, *534*, 86–95.
- [20] Z. Liu, X. Zhang, Z. Jiang, H.-S. Chen, P. Yang, *Int. J. Hydrogen Energy* **2019**, *44*, 20042–20055.
- [21] a) L. G. Devi, R. Kavitha, *Mater. Chem. Phys.* **2014**, *143*, 1300–1308; b) H. Xie, Y. Zheng, X. Guo, Y. Liu, Z. Zhang, J. Zhao, W. Zhang, Y. Wang, Y. Huang, *ACS Sustainable Chem. Eng.* **2021**, *9*, 6788–6798; c) D. A. Tran, C. T. Nguyen Pham, T. Nguyen Ngoc, H. Nguyen Phi, Q. T. Hoai Ta, D. H. Truong, V. T. Nguyen, H. H. Luc, L. T. Nguyen, N. N. Dao, S. J. Kim, V. Vo, *J. Phys. Chem. Solids* **2021**, *151*, 26–35; d) F. Wei, Y. Liu, H. Zhao, X. Ren, J. Liu, T. Hasan, L. Chen, Y. Li, B. L. Su, *Nanoscale* **2018**, *10*, 4515–4522; e) Y. Zhang, Z. Chen, J. Li, Z. Lu, X. Wang, *J. Energy Chem.* **2021**, *54*, 36–44.
- [22] a) H. Yan, Y. Chen, S. Xu, *Int. J. Hydrogen Energy* **2012**, *37*, 125–133; b) S. Cao, B. Fan, Y. Feng, H. Chen, F. Jiang, X. Wang, *Chem. Eng. J.* **2018**, *353*, 147–156; c) K. Guan, J. Li, W. Lei, H. Wang, Z. Tong, Q. Jia, H. Zhang, S. Zhang, *J. Mater.* **2021**, *7*, 1131–1142; d) Z. Zhu, Z. Liu, X. Tang, K. Reeti, P. Huo, J. W.-C. Wong, J. Zhao, *Catal. Sci. Technol.* **2021**, *11*, 1725–1736; e) X. Xiao, Y. Wang, Q. Bo, X. Xu, D. Zhang, *Dalton Trans.* **2020**, *49*, 8041–8050; f) N. D. Shcherban, S. M. Filonenko, M. L. Ovcharov, A. M. Mishura, M. A. Skoryk, A. Aho, D. Y. Murzin, *ChemistrySelect* **2016**, *1*, 4987–4993; g) F. Zhao, H. Cheng, Y. Hu, L. Song, Z. Zhang, L. Jiang, L. Qu, *Sci. Rep.* **2014**, *4*, 5882; h) D. Long, L. Wang, H. Cai, X. Rao, Y. Zhang, *Catal. Lett.* **2020**, *150*, 2487–2496.
- [23] a) D. Vashisht, E. Sharma, M. Kaur, A. Vashisht, S. K. Mehta, K. Singh, *Spectrochim. Acta Part A* **2020**, *228*, 117773; b) X. Qin, L. Jing, G. Tian, Y. Qu, Y. Feng, *J. Hazard. Mater.* **2009**, *172*, 1168–1174.
- [24] Q. Fan, J. Liu, Y. Yu, S. Zuo, B. Li, *Appl. Surf. Sci.* **2017**, *391*, 360–368.
- [25] D. Mocatta, G. Cohen, J. Schattner, O. Millo, E. Rabani, U. Banin, *Science* **2011**, *332*, 77–81.
- [26] L. Jiang, X. Yuan, G. Zeng, X. Chen, Z. Wu, J. Liang, J. Zhang, H. Wang, H. Wang, *ACS Sustainable Chem. Eng.* **2017**, *5*, 5831–5841.

- [27] a) E. Nazari, F. Suja, *Rev. Environ. Health* **2016**, *31*, 465–491; b) A. M. E. Khalil, F. A. Memon, T. A. Tabish, D. Salmon, S. Zhang, D. Butler, *Chem. Eng. J.* **2020**, *398*, 461–470; c) J. Ferandin Honorio, M. T. Veit, P. Y. R. Suzaki, P. F. Coldebella, E. Sloboda Rigobello, C. R. G. Tavares, *Environ. Technol.* **2020**, *41*, 1075–1092; d) M. Z. Hussain, Z. Yang, A. M. E. Khalil, S. Hussain, S. U. Awan, Q. Jia, R. A. Fischer, Y. Zhu, Y. Xia, *J. Mater. Sci. Technol.* **2022**, *101*, 49–59.
- [28] a) T. Huang, B. Pan, H. Ji, W. Liu, *Water* **2020**, *12*; b) Y. Long, D. Huang, L. Luo, L. Li, L. Wang, S. Zhang, F. Jiang, *Res. Chem. Intermed.* **2018**, *44*, 7117–7133; c) A. Torres-Pinto, M. J. Sampaio, C. G. Silva, J. L. Faria, A. M. T. Silva, *Appl. Catal. B* **2019**, *252*, 128–137.
- [29] a) S. D. Rojas, N. Espinoza-Villalobos, R. Salazar, N. Escalona, D. Contreras, V. Melin, M. A. Laguna-Bercero, M. Sánchez-Arenillas, E. Vergara, L. Caceres-Jensen, J. Rodriguez-Becerra, L. Barrientos, *J. Photochem. Photobiol. A* **2021**, *421*, 45–56; b) J. Liu, C. Xiong, S. Jiang, X. Wu, S. Song, *Appl. Catal. B* **2019**, *249*, 282–291; c) H. Tan, P. Kong, R. Zhang, M. Gao, M. Liu, X. Gu, W. Liu, Z. Zheng, *Innovation (Camb)* **2021**, *2*, 215–227.
- [30] Y. Liu, H. Guo, Y. Zhang, W. Tang, *RSC Adv.* **2016**, *6*, 79910–79919.
- [31] A. Kumar, A. Kumar, G. Sharma, M. Naushad, R. C. Veses, A. A. Ghfar, F. J. Stadler, M. R. Khan, *New J. Chem.* **2017**, *41*, 10208–10224.
- [32] Y. Chen, L. Sun, Z. Yu, L. Wang, G. Xiang, S. Wan, *Sep. Purif. Technol.* **2015**, *152*, 46–54.

Submitted: May 16, 2022

Accepted: August 4, 2022

### 4.3 Paper III: Impact of co-catalysts (Ni, Co, Cu) and synthesis method on the photocatalytic activity of exfoliated graphitic carbon nitride for hydrogen production

Adeem Ghaffar Rana, Michael Schwarze, Mino Tasbihi, Xavier Sala, Jordi García-Antón, and Mirjana Minceva

Submitted to Nanomaterials

**Author contribution:** The thesis author conceptualized the paper's idea and characterized the catalysts (excluding XRD, SEM, and TEM). He evaluated and interpreted the experimental results and wrote the manuscript draft.

#### Summary

The world is facing the challenge of global warming due to increased industrialization, and unregulated utilization of non-renewable energy sources (petrol, diesel, coal), thereby harnessing energy and environmental issues. There is a need to develop methods for efficient implementation of sustainable and renewable energy sources. Solar light is a renewable source used to store energy in chemical bonds of the fuel. Hydrogen is an alternative renewable energy source that will not cause global warming due to practically zero emission of greenhouse gases. Hence, photocatalytic H<sub>2</sub> production via solar light-driven water splitting, using semiconductor materials that convert solar energy into chemical energy, has assumed to be a promising approach. Consequently, developing a stable, effective, and inexpensive catalyst for the hydrogen evolution reaction (HER), presents a challenging and important research endeavor. g-C<sub>3</sub>N<sub>4</sub> is one of the options available for solar light harvesting due to its photoactivity in the visible range. Due to the limited activity of the bulk g-C<sub>3</sub>N<sub>4</sub>, it has to be modified for better activity using co-catalyst and exfoliation. Paper III aims to study the effects of co-catalyst loading on the photocatalytic performance of the g-C<sub>3</sub>N<sub>4</sub> using visible light. This work studied the photocatalytic activity of exfoliated graphitic carbon nitride (ex-g-CN) for hydrogen production. Catalyst exposure to the medium was also studied for practical applications.

In this paper, exfoliated g-C<sub>3</sub>N<sub>4</sub> was synthesized using melamine. For initial screening, the co-catalysts nickel (Ni), cobalt (Co), and copper (Cu) loaded ex-g-CN were synthesized with the incipient wetness impregnation method. The synthesized catalysts were tested for hydrogen production in a non-commercial, side-irradiated, double-walled, quartz-glass reactor with a maximum volume of 35 mL, using a Xenon lamp with a 395 cut-off filter. Nickel-loaded ex-g-CN performed best for hydrogen production, and was subsequently selected for further studies. Different synthesis methods, namely incipient wetness impregnation, colloidal deposition, and precipitation deposition, were used to synthesize the nickel-loaded ex-g-CN. Different characterization techniques showed that the nickel-loaded ex-g-CN, synthesized via the colloidal method, possesses a higher amount of nanoparticles on the surface than the

other. Nanoparticle presence on the surface of the catalyst could be the cause of its most efficient performance for hydrogen production. Suspended catalyst performance was compared to the immobilized catalyst on the surface of the filter paper. However, the suspended catalyst performed better than the immobilized, indicating that the immobilization process is essential for technical applications. The effect of catalyst concentration on hydrogen production was also studied. The outcomes showed that the amount of hydrogen produced increased with an increase in the catalyst concentration up to a certain threshold quantity, after which it started to decrease due to hindrance in the absorption and scattering of light. The stability of the catalyst was also studied, and results showed that the catalyst remains stable for at least three cycles, producing an identical amount of hydrogen.

It was concluded in this work that the nickel-loaded ex-g-CN, synthesized using the colloidal method, performed the best among all the catalysts. A probable cause could be attributed to the presence of nanoparticles on the surface of ex-g-CN, as detected via TEM and XPS.

## Article

# Influence of Cocatalysts (Ni, Co, and Cu) and Synthesis Method on the Photocatalytic Activity of Exfoliated Graphitic Carbon Nitride for Hydrogen Production

Adeem Ghaffar Rana <sup>1,2</sup>, Michael Schwarze <sup>3,\*</sup>, Mino Tasbihi <sup>3</sup>, Xavier Sala <sup>4</sup>, Jordi García-Antón <sup>4</sup> and Mirjana Minceva <sup>1,\*</sup>

- <sup>1</sup> Biothermodynamics, TUM School of Life Sciences, Technical University of Munich, Maximus-Von-Imhof-Forum 2, 85354 Freising, Germany
- <sup>2</sup> Department of Chemical, Polymer and Composite Materials Engineering, University of Engineering and Technology (UET), Lahore 39161, Pakistan
- <sup>3</sup> Department of Chemistry, Technische Universität Berlin, Straße des 17. Juni 124, 10623 Berlin, Germany
- <sup>4</sup> Departament de Química, Unitat de Química Inorgànica, Universitat Autònoma de Barcelona, 08193 Bellaterra, Barcelona, Spain
- \* Correspondence: michael.schwarze@tu-berlin.de (M.S.); mirjana.minceva@tum.de (M.M.); Tel.: +49-8161716170 (M.M.)

**Abstract:** Exfoliated graphitic carbon nitride (ex-g-CN) was synthesized and loaded with non-noble metals (Ni, Cu, and Co). The synthesized catalysts were tested for hydrogen production using a 300-W Xe lamp equipped with a 395 nm cutoff filter. A noncommercial double-walled quartz-glass reactor irradiated from the side was used with a 1 g/L catalyst in 20 mL of a 10 vol% triethanolamine aqueous solution. For preliminary screening, the metal-loaded ex-g-CN was synthesized using the incipient wetness impregnation method. The highest hydrogen production was observed on the Ni-loaded ex-g-CN, which was selected to assess the impact of the synthesis method on hydrogen production. Ni-loaded ex-g-CN was synthesized using different synthesis methods: incipient wetness impregnation, colloidal deposition, and precipitation deposition. The catalysts were characterized by X-ray powder diffraction, X-ray photoelectron spectroscopy, nitrogen adsorption using the Brunauer–Emmett–Teller method, and transmission electron microscopy. The Ni-loaded ex-g-CN synthesized using the colloidal method performed best with a hydrogen production rate of 43.6  $\mu\text{mol h}^{-1} \text{g}^{-1}$ . By contrast, the catalysts synthesized using the impregnation and precipitation methods were less active, with 28.2 and 10.1  $\mu\text{mol h}^{-1} \text{g}^{-1}$ , respectively. The hydrogen production performance of the suspended catalyst (440  $\mu\text{mol m}^{-2} \text{g}^{-1}$ ) showed to be superior to that of the corresponding immobilized catalyst (236  $\mu\text{mol m}^{-2} \text{g}^{-1}$ ).

**Keywords:** graphitic carbon nitride; water splitting; hydrogen production; nickel; cocatalyst deposition



**Citation:** Rana, A.G.; Schwarze, M.; Tasbihi, M.; Sala, X.; García-Antón, J.; Minceva, M. Influence of Cocatalysts (Ni, Co, and Cu) and Synthesis Method on the Photocatalytic Activity of Exfoliated Graphitic Carbon Nitride for Hydrogen Production. *Nanomaterials* **2022**, *12*, 4006. <https://doi.org/10.3390/nano12224006>

Academic Editor: Joon Ching Juan

Received: 13 July 2022

Accepted: 11 November 2022

Published: 14 November 2022

**Publisher's Note:** MDPI stays neutral with regard to jurisdictional claims in published maps and institutional affiliations.



**Copyright:** © 2022 by the authors. Licensee MDPI, Basel, Switzerland. This article is an open access article distributed under the terms and conditions of the Creative Commons Attribution (CC BY) license (<https://creativecommons.org/licenses/by/4.0/>).

## 1. Introduction

Energy and environmental challenges are emerging with industrial and economic development [1–3]. Industrialization and increasing population are the main reasons behind the energy and environmental crises. Most of the world's energy demand is fulfilled by nonrenewable sources (petrol, diesel, and coal), which are becoming depleted [4,5]. Additionally, during the past few decades, the increased consumption of fossil fuels has led to severe environmental issues, such as global warming and climate change. As a result, researchers are putting more effort into developing renewable energy sources, the only alternative to ensure sustainable development. Solar light, wind, biomass, hydro, and geothermal energy sources are eco-friendly sources of renewable energy [6–9]. Among them, sunlight energy can be stored in the chemical bonds of a fuel (e.g., hydrogen, H<sub>2</sub>) through artificial photosynthesis [4,10–12]. Hydrogen, an alternative renewable energy source, can release considerable energy without emitting greenhouse gases; water is the



only by-product of hydrogen combustion. Hence, photocatalytic H<sub>2</sub> generation through solar light-driven water splitting using semiconductor materials that convert solar energy to chemical energy has become a promising approach [13]. Consequently, the development of a stable, effective, and inexpensive catalyst for the hydrogen evolution reaction (HER) has become a challenging and important research topic [14].

A wide variety of semiconductor-based photocatalysts, such as TiO<sub>2</sub> [15], ZnO [16,17], Bi [18], CdS [19], and g-CN [20], have been investigated in the last few decades. The more conventional (i.e., TiO<sub>2</sub> and ZnO) have advantages and disadvantages regarding stability and nontoxicity [21,22]. Conversely, they typically have large bandgaps and a high rate of electron–hole recombination, which results in low solar-to-fuel efficiency [23]. Among semiconductor materials, graphitic carbon nitride (g-CN) has attracted considerable attention since Wang et al. first reported its use for water splitting [14,24]. g-CN, a visible-light photocatalyst composed of N, C, and H, has attracted interest because of its extensive application in CO<sub>2</sub> reduction [25], pollutant degradation [23], organic synthesis reactions [26], and water splitting [27]. These nitrogen-rich materials are inexpensive, abundant, and easy to synthesize [22,28]. The thermal decomposition of nitrogen-rich precursors, such as melamine, urea, thiourea, cyanamide, or dicyanamide, is used to synthesize g-CN in the form of tri-s-triazine sheets. Moreover, the nontoxic g-CN, which can be activated by visible light because of the low bandgap energy (2.7 eV), possesses chemical, electronic, and thermodynamic stability [22,23,29]. However, the photocatalytic performance of bulk g-CN is low because of the low specific surface area (10 m<sup>2</sup>/g), low availability of active sites, low adsorption and absorption, and rapid recombination of photogenerated electron–hole pairs. Several strategies can be adopted during the photocatalyst design to improve the surface and optical properties of g-CN to overcome these problems. These include metal and nonmetal doping, morphology control, compositing with other semiconductor materials, and exfoliation [22,30]. From these strategies, exfoliation is a fast, efficient, and easy method to improve a given material and its optical properties by increasing its surface area [23]. Moreover, doping can help improve the electronic properties of materials by introducing more electron–hole pairs and minimizing charge recombination [8,22,24,30].

Modifying the catalyst with a cocatalyst enhances the performance of materials significantly. Immobilization of a cocatalyst on the surface of the semiconductor material is one of the efficient and essential methods to accelerate the separation efficiency of electron–hole pairs generated in the process, consequently enhancing the overall photocatalytic performance of the semiconductor material. Therefore, adding cocatalysts enhances hydrogen production in a water-splitting reaction. Noble and non-noble metals can play this role [1,6,13,21,31].

Noble metal cocatalysts typically enhance the kinetics of the reaction at low overpotentials and help induce charge separation from the semiconductor to the cocatalyst [13]. Noble metals, such as platinum (Pt) [32], gold (Au) [33], ruthenium (Ru) [34], silver (Ag) [35], and palladium (Pd) [36], are usually the most common cocatalysts for improving the photocatalytic performance [1]. However, noble metals are scarce, which prevents their practical implementation on a large scale. Hence, researchers are trying to find a cocatalyst that can replace these noble metals, such as non-noble metals, metal oxides, and metal sulfides [21,31]. From all the non-noble metals available for HER, nickel-based cocatalysts have attracted attention because of their low price, stability, and high activity [1].

Recently, Ni metal and Ni-based compounds (Ni<sub>2</sub>P, Ni(OH)<sub>2</sub>, NiN<sub>3</sub>, NiB, NiS, and Ni<sub>3</sub>C) have shown significant HER performance when used as cocatalysts in g-CN-based photocatalytic systems. Ni can play a similar role to noble metals, improving the separation efficiency of electron–hole pairs [1,13]. The cocatalyst loading on the support material can be achieved using diverse synthetic methods. The synthesis methods determine the structure, dispersion, and size distribution of the cocatalyst, which affects the activity of the final hybrid material. In recent years, various methods have been proposed to synthesize supported nanoparticles. However, few studies have compared different synthesis methods

for a given support and a given photocatalytic processes. Therefore, rationally choosing the most suitable method remains a challenge [37].

This study evaluated the effect of non-noble metal (Ni, Cu, and Co) cocatalyst loading on exfoliated g-CN (ex-g-CN) for hydrogen production. The hybrid photocatalyst was initially prepared using the incipient wet impregnation (IWI) method and the superior photocatalytic activity of Ni (over Cu and Co) was observed. After this preliminary screening, the best-performing Ni-based hybrid photocatalyst was prepared using one of the following methodologies: (i) precipitation deposition method (PRDM), (ii) IWI method, and (iii) colloidal deposition method (CM). The effects of the synthesis method on the HER photocatalytic performance were studied with triethanolamine (TEOA) as the sacrificial agent under simulated solar light irradiation using a 300-W xenon lamp with a 395-nm cutoff filter. Moreover, the effects of the catalyst exposure to the reaction medium (immobilization or suspension) were studied for practical applications.

## 2. Materials and Methods

### 2.1. Chemicals

Melamine ( $C_3H_6N_6$ , 99%) and dihydrogen hexachloroplatinate(IV) hydrate, 99.9% (metal basis) ( $H_2PtCl_6 \cdot H_2O$ ) were purchased from Alfa Aesar (Haverhill, MA, USA). Nickel sulfate hexahydrate ( $NiSO_4 \cdot 6H_2O$ ), copper sulfate pentahydrate ( $CuSO_4 \cdot 5H_2O$ ), and cobalt sulfate monohydrate ( $CoSO_4 \cdot H_2O$ ) (Merck, Darmstadt, Germany), sodium hydroxide (NaOH), ethanol ( $C_2H_5OH$ ), methanol ( $CH_3OH$ ), cyclohexane ( $C_6H_{12}$ ), 1-butanol ( $C_4H_{10}O$ ), and ascorbic acid ( $C_6H_8O_6$ ) were obtained from VWR (Radnor, PA, USA). Triton X-100 ( $C_{14}H_{22}O(C_2H_4O)_n$  ( $n = 9-10$ )) was supplied by Sigma-Aldrich (Darmstadt, Germany). TEOA ( $C_6H_{15}NO_3$ ) was acquired from Sigma-Aldrich (Darmstadt, Germany). All chemicals were used as received.

### 2.2. Synthesis of ex-g-CN

Bulk carbon nitride (g-CN) was synthesized with prethermal decomposition of melamine using the procedure established in a previous study [23]. Briefly, a closed crucible with melamine was placed into a muffle furnace (Carbolite Gero, GPC 1200, Derbyshire, UK) for thermal decomposition. The heating program consisted of two steps: heating to 450 °C with a gradient of 2 °C min<sup>-1</sup>, and this temperature was kept for 2 h. The sample was then heated to 550 °C at a rate of 2 °C min<sup>-1</sup>, maintaining this temperature for 4 h. Bulk g-CN was crushed in a mortar and pestle, rinsed with ultrapure water, and dried overnight at 80 °C. Carbon nitride (ex-g-CN) was exfoliated from g-CN by placing g-CN in an open crucible inside a muffle furnace for 2 h at 500 °C using a heating ramp of 2 °C min<sup>-1</sup>. The ex-g-CN was obtained after thermal treatment.

### 2.3. Cocatalyst Loading onto ex-g-CN

#### Incipient Wet Impregnation

The IWI method was used to synthesize Ni, Cu, Co, and Pt-loaded ex-g-CN catalyst (2 wt.% theoretical loadings) for the preliminary screening of hydrogen production. The Ni-based catalyst synthesized using this method was called Ni<sub>IWI</sub>/ex-g-CN [38]. According to stoichiometric calculations, the required amount of a respective salt precursor was added dropwise to the ex-g-CN. The beaker containing the catalyst powder was placed in a sonicator for better dispersion. The material was dried overnight at 80 °C before further use.

### 2.4. Precipitation Deposition Method

Ni<sub>PRDM</sub>/ex-g-CN (2 wt.% theoretical Ni loading) was synthesized using the PRDM [39]. The respective amount of the nickel salt precursor was added to 300 mL of milli-Q water. The solution was maintained at pH 9 using 0.1M NaOH. At a stable pH, ex-g-CN was added with continuous stirring. The deposition-precipitation procedure was conducted at



70 °C at a constant pH for 2 h, and the slurry was stirred and dried overnight at the same temperature. The catalyst was washed and dried at 80 °C under vacuum.

### 2.5. Colloidal Deposition Method

Ni<sub>CM</sub>/ex-g-CN (2 wt.% theoretical Ni loading) was synthesized using the CM. The microemulsion system for synthesizing Ni nanoparticles consists of two phases, e.g., the water and oil phases. The nickel salt precursor, surfactant (Triton X-100), and co-surfactant (1-butanol) were present in the water phase. The oil phase was cyclohexane. Two microemulsions were prepared for the synthesis: (1) with Ni salt and (2) with a reducing agent (ascorbic acid). The synthesis process was conducted in a glass reactor with stirring. Emulsion 2 contained ascorbic acid, cyclohexane, butanol-1, triton X-100, and water. Emulsion 1 contained the nickel salt precursor, cyclohexane, butanol-1, triton X-100, and water. Emulsion 2 was added slowly to the reactor containing emulsion 1. The mixture was stirred at 700 rpm for 30 min at room temperature to form the colloidal stabilized Ni nanoparticles and then stirred for 2 h at room temperature. The ex-g-CN support was then added to the mixture with vigorous stirring to deposit the Ni nanoparticles onto the surface of ex-g-CN. The suspension was stirred further for 2 h at 55 °C. After the process, the reactor was cooled to room temperature. The solid was centrifuged and washed several times with acetone. Finally, the catalyst was dried at 80 °C under vacuum.

### 2.6. Characterization

The Brunauer–Emmett–Teller (BET) surface area was determined from a nitrogen adsorption–desorption experiment at 77 K (quadratorp, Quantachrome, Boynton Beach, FL, USA). The crystalline phases were examined using X-ray diffraction (XRD, Mini Flex 600C, Rigaku, Tokyo, Japan) was conducted using CuK $\alpha$  radiation at a voltage, current, and spin speed of 40 kV, 15 mA, and 80 rpm, respectively, in the range between 3° and 60° 2 $\theta$  with a step size of 0.0075°. Transmission electron microscopy (TEM, JEM-ARM300F2) images were obtained using a probe corrected with a cold FEG emitter (JEOL Ltd., Tokyo, Japan) operated at 300 kV with a camera length of 10 cm. The acquired and evaluated high-angle annular dark-field images represent a detection angle of 54–220 mrad. The image contrasts were formed mainly by Rutherford scattering and were correlated to the atomic number. X-ray photoelectron spectroscopy (XPS, Phoibos 150 analyzer, SPECS GmbH, Berlin, Germany) was conducted under ultra-high vacuum conditions (base pressure  $5 \times 10^{-10}$  mbar) using a monochromatic Al K $\alpha$  X-ray source (1486.74 eV). The energy resolution measured from the FWHM of the Ag 3d<sup>5/2</sup> peak for a sputtered silver foil was 0.62 eV at the Catalan Institute of Nanoscience and Nanotechnology in Barcelona. Ni loading in Ni-loaded ex-g-CN samples was determined using inductively coupled plasma optical emission spectrometry (Perkin-Elmer Optima 4300DV model system) in the Chemical Analyses Service of the Universitat Autònoma de Barcelona.

### 2.7. Photocatalytic Experiments

The photocatalytic experiments were performed in a noncommercial side-irradiated double-walled quartz-glass reactor (shown in a previous work [40]) with a maximum volume of 35 mL. In general, 20 mg of the prepared photocatalyst was placed into the reactor, and 20 mL of an aqueous TEOA solution (10 vol% TEOA) was added. The solution was flushed with Ar for 15 min to remove oxygen, and the reactor was closed with a rubber septum. The reactor was connected to a thermostat (ministat 125, Huber, Germany, T<sub>set</sub> = 19 °C) and placed onto a magnetic stirrer in front of a 300-W Xe lamp equipped with a 395-nm cutoff filter. The distance between the lamp and reactor was 10 cm. The lamp was switched on, and after irradiating the intensively stirred photocatalyst suspension for the desired time, a gas phase sample was taken with a gas-tight syringe. The gas sample was analyzed by gas chromatography (Agilent Technologies 7890 A) equipped with a thermal conductivity detector.

The hydrogen production photocatalytic activity was calculated as follows:

$$H_2 \left( \mu\text{mol g}^{-1}\text{h}^{-1} \right) = \frac{(V_0 - V_L) \cdot H_2(\text{GC})}{m_{\text{cat}} \cdot t_R \cdot V_m} \quad (1)$$

where  $V_0$  is the total volume of the reactor,  $V_L$  is the volume of the solution,  $H_2$  is the amount of  $H_2$  detected using GC,  $m_{\text{cat}}$  is the amount (g) of catalyst,  $t_R$  is the irradiation time, and  $V_m$  is the molar volume of hydrogen.

### 3. Results

#### 3.1. Catalyst Characterization

Before assessing the as-prepared photocatalysts for the HER, they were characterized using the different techniques. Optical properties were characterized using UV-Vis and photoluminescence (PL) spectroscopy (Figures S1 and S2). The bandgap energy for bulk and exfoliated g-CN were 2.42 and 2.62 eV showing light absorption in the visible range. After loading with Co, Ni, and Cu, the bandgap energy was 2.6, 2.5, and 2.4 eV, respectively. The optical properties remained after cocatalyst loading. In the case of different methods to load Ni onto ex-g-CN, bandgap energy was constant at about 2.5 eV. PL spectroscopy showed that g-CN materials absorbed the maximum in the range of 430–460 nm. The chemical composition was studied using FTIR (Figure S3) and spectra are typical for g-CN materials. Peaks at  $806 \text{ cm}^{-1}$  can be attributed to triazine units, whereas the strong bands between  $1636$  and  $1242 \text{ cm}^{-1}$  belong to the C=N and C–N bonds of heterocyclic rings. There were no peak alterations and new peaks after the addition of the cocatalyst.

#### 3.2. X-ray Diffraction

The phase structures of g-CN, ex-g-CN, and Ni-loaded ex-g-CN were examined using XRD and the diffractograms are shown in Figure 1. All samples showed the characteristic peak at  $27.2^\circ 2\theta$  and a weaker peak at  $13^\circ 2\theta$ . The strong peak was indexed to the (002) plane, a characteristic interlayer stacking peak of aromatic g- $\text{C}_3\text{N}_4$  systems. Moreover, the weak peak was assigned to the (100) crystal plane, which was attributed to the repeated tri-s-triazine units. The decrease in intensity and the slight shift in the peaks were attributed to exfoliation and Ni loading. There were no peaks of Ni due to the low Ni content. The XRD patterns of cobalt and copper loaded ex-g-CN showed similar peaks with no visible peak of respective metal (Figure S4).

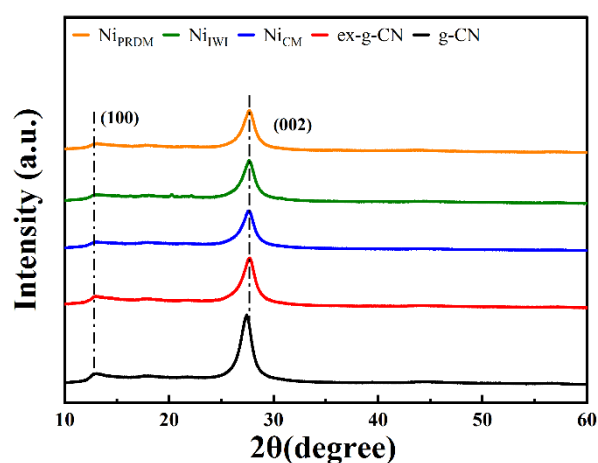


**Figure 1.** XRD patterns of g-CN, ex-g-CN, and Ni-loaded ex-g-CN synthesized using the incipient wet impregnation (IWI) method, colloidal method (CM), and precipitation deposition method (PRDM).

#### 3.3. Brunauer–Emmett–Teller

The specific surface areas were measured to reveal any change in the structural features of carbon nitride before and after exfoliation. The surface area of ex-g-CN, obtained from

the N<sub>2</sub> adsorption-desorption curves (Figure S5), was significantly higher than that of g-CN (169.3 m<sup>2</sup>/g vs. 5.4 m<sup>2</sup>/g, respectively). The surface areas of the Ni-loaded ex-g-CN, Ni<sub>PRDM</sub>, Ni<sub>IWI</sub>, and Ni<sub>CM</sub> were 84.6, 69.8, and 65 m<sup>2</sup>/g, respectively. The reduction in the surface area is probably due to blockage of the pores with the loaded metal particles.

### 3.4. Inductively Coupled Plasma (ICP) Mass Spectrometry (MS)

The theoretical loading of Ni for all samples was 2%. The Ni content of the Ni<sub>PRDM</sub>, Ni<sub>IWI</sub>, and Ni<sub>CM</sub>, determined using ICP-OES, were 1.7, 1.2, and 1.4 wt.%, respectively, corresponding to Ni deposition yields of 85%, 60%, and 70%, respectively. The Ni loading ratio on the surface of g-ex-CN was high compared with that of Pt. The surface charge of Ni was positive, and g-CN was negative, whereas the surface charge of Pt was negative. Because of the negative charge of Pt, the deposition yield for Pt obtained in earlier investigations was consistently lower (below 50%) [41,42]. The copper and cobalt actual loadings were 1.7% and 1.4%, respectively (theoretical loading in both cases was 2%).

### 3.5. X-ray Photoelectron Spectroscopy

XPS measurements were conducted to investigate the composition of the Ni-loaded ex-g-CN photocatalysts. As shown in Figure 2, the XPS survey spectra confirmed the presence of C, N, O, and Ni. Ni was visible in the sample prepared using the CM. Figure 2b presents the high-resolution spectra of Ni 2p. Four significant peaks were observed at 852.3, 857.2, 870.1, and 873.5 eV. The peaks at 852.3 and 870.1 eV correspond to metallic Ni. These peaks were clearly visible in the sample prepared using the CM (Ni<sub>CM</sub>), but they were either reduced in intensity (Ni<sub>PRDM</sub>) or absent (Ni<sub>IWI</sub>) for the other two samples, even if Ni was detected using ICP-MS. The other two peaks at 857.2 and 873.1 eV correspond to Ni<sup>2+</sup>. The two peaks at 862.5 and 876.8 eV are satellite peaks of Ni<sup>2+</sup>. Ni always showed strong satellite peaks approximately 6 eV above the main electronic lines [31,43–47]. The XPS peaks of cobalt and copper loaded ex-g-CN (Figure S6) confirmed the presence of these species in different oxidation states.

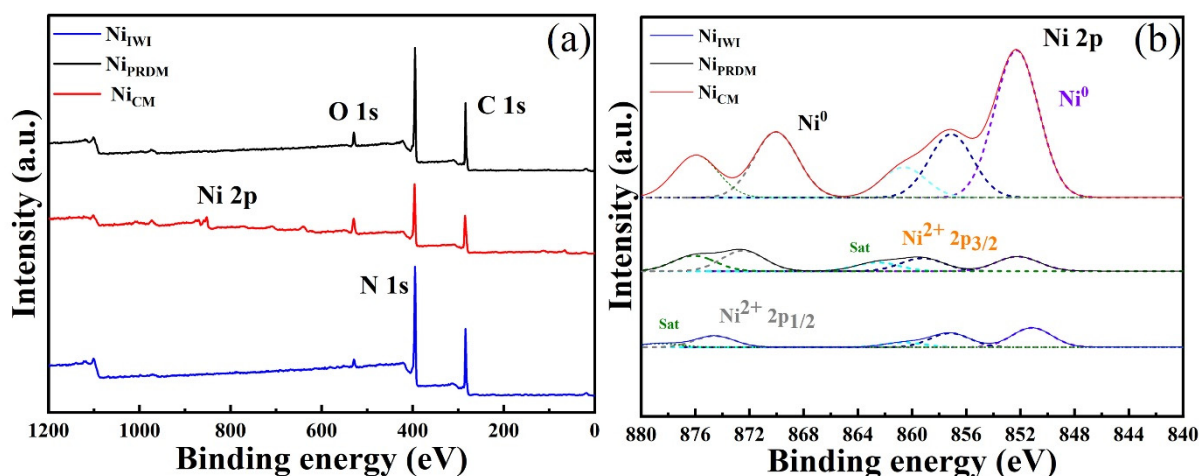
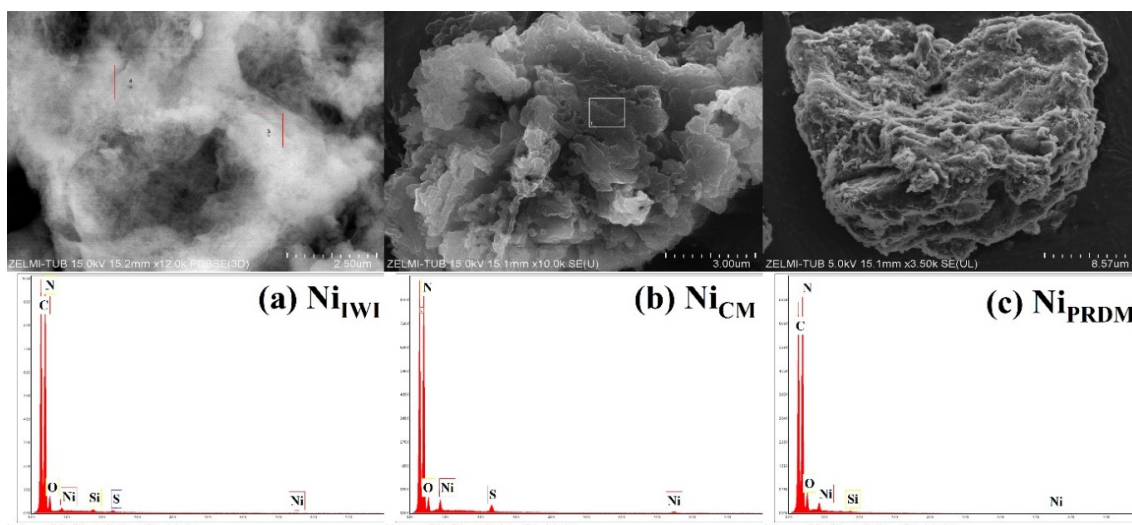


Figure 2. XPS profiles of the obtained samples for (a) survey and (b) Ni 2p scan.

### 3.6. Morphology

The morphology of the Ni-based catalysts synthesized using different methods was investigated using SEM (Figure 3). The catalysts synthesized using the CM were studied further using TEM (Figure 4). All catalysts showed a stacked morphology, and EDX analysis (Figure 3) confirmed the Ni loading. In Figure 4, TEM images of the Ni-based catalyst synthesized using the CM at different magnifications are presented together with the corresponding EDX elemental mapping. A flat-sheet structure with thin layers was observed. EDX mapping showed that the synthesis method yielded Ni species loaded on

the ex-g-CN surface. TEM images and EDX spectra of cobalt and copper loaded ex-g-CN are shown in Figure S7. They do not show nanoparticles on the surface.



**Figure 3.** SEM images and EDX spectra of Ni-loaded ex-g-CN synthesized using the (a) incipient wet impregnation (IWI) method, (b) colloidal method (CM), and (c) precipitation deposition method (PRDM).

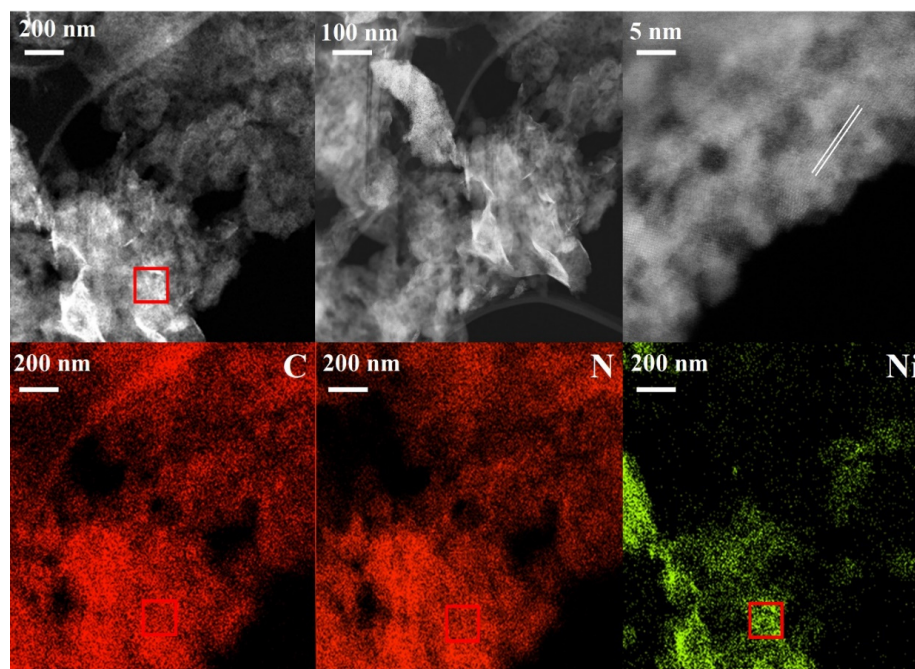


**Figure 4.** TEM images at different resolution and EDX mapping (from top left image) of Ni<sub>CM</sub>.

### 3.7. Photocatalytic H<sub>2</sub> Production Activity

The photocatalytic activity of the synthesized hybrid materials was studied for hydrogen production. First, the metal-loaded ex-g-CN catalysts synthesized using the IWI method were screened. The best-performing non-noble metal was chosen for further study. Second, the best-performing non-noble metal-based catalyst was synthesized with different methods, and the effects of the synthesis method on H<sub>2</sub> production were studied. Furthermore, the effects of the catalyst concentration and catalyst exposure to reaction medium (immobilized or suspended) on hydrogen production were studied. The reactions were



performed in the presence of TEOA as a sacrificial electron donor, and the HER activities were evaluated under visible-light irradiation ( $\lambda > 396$  nm).

### 3.8. Screening Experiments

Screening experiments were performed for the synthesized catalysts; the results are presented in Figure 5a. Almost negligible hydrogen was produced for ex-g-CN without a co-catalyst after 6 h [48]. Ni (2% loading) performed best with  $84.5 \mu\text{mol h}^{-1} \text{g}^{-1}$  hydrogen produced, followed by 2% loading on cobalt ( $12.3 \mu\text{mol h}^{-1} \text{g}^{-1}$ ) and copper ( $0 \mu\text{mol h}^{-1} \text{g}^{-1}$ ). The catalyst performed in the following order: Ni > Co > Cu = ex-g-CN [48–50]. Pt (2% and 0.5% loading) outperformed all non-noble metal-based photocatalysts for hydrogen production (Figure 5a). Further experiments were performed with the best-performing non-noble metal Ni system.

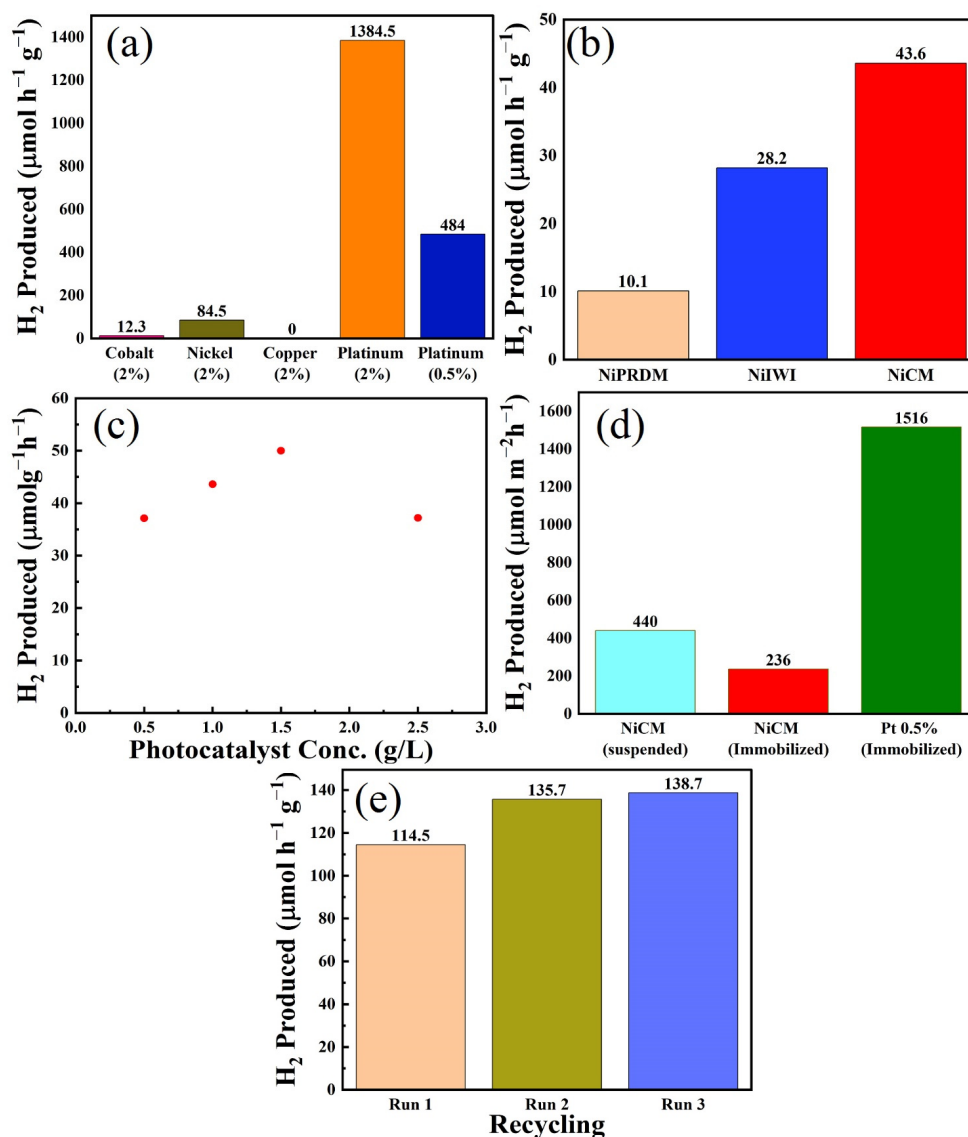


**Figure 5.** (a) Comparison of the photocatalytic H<sub>2</sub> evolution with different noble and non-noble metals; (b) photocatalytic H<sub>2</sub> production activities of different Ni-based samples under visible-light irradiation for 6 h; (c) effect of the catalyst concentration on the hydrogen production; (d) photocatalytic H<sub>2</sub> evolution of suspended and immobilized Ni<sub>CM</sub>-based photocatalysts and analogous immobilized Pt-based photocatalyst; and (e) re-utilization of the catalyst (estimated error 10%).

### 3.9. Effect of the Ni Loading Method on Hydrogen Production

After selecting Ni as a cocatalyst for further investigations, the effects of the loading method on H<sub>2</sub> production were studied, and the results are presented in Figure 5b. Ni-loaded ex-g-CN synthesized using the CM performed best, with a H<sub>2</sub> production rate of 43.6  $\mu\text{mol h}^{-1} \text{g}^{-1}$ . The presence of Ni nanoparticles on the material surface (confirmed by TEM, vide supra) could explain the higher photocatalytic activity of this system. The catalysts synthesized using the impregnation and precipitation methods were less active, with H<sub>2</sub> production rates of 28.2 and 10.1  $\mu\text{mol h}^{-1} \text{g}^{-1}$ , respectively. In addition to XPS, although ICP and EDX verified the presence of Ni, no nanoparticles were observed by TEM, which could explain the lower activity of these catalysts. A plausible explanation could be that the Ni precursor is still present on ex-g-CN after synthesis and was reduced to Ni during irradiation (via photodeposition). Further experiments were performed using the best-performing Ni<sub>CM</sub>.

### 3.10. Effect of Photocatalyst Concentration

The effects of photocatalyst concentration on hydrogen production were examined by varying the mass of Ni<sub>CM</sub> between 10 and 50 mg, keeping the liquid volume (20 mL) constant, resulting in a variation of the photocatalyst concentration between 0.5 and 2.5 g/L. Figure 5c shows the hydrogen produced as a function of photocatalyst concentration. No hydrogen production occurred in the absence of the photocatalyst. Hydrogen production initially increased with increasing photocatalyst concentration but decreased at high photocatalyst concentrations after reaching a maximum of approximately 1.5 g/L. The amount of hydrogen produced was 37.1, 43.6, 50, and 37.2  $\mu\text{mol h}^{-1} \text{g}^{-1}$  for 10 (0.5 g/L), 20 (1 g/L), 30 (1.5 g/L), and 50 (2.5 g/L) mg of catalyst, respectively. Hydrogen production increased with increasing amount of photocatalyst because of the availability of more active sites for reaction until 2.5 g/L of catalyst. Further increases in photocatalyst concentration decreased hydrogen production because of the hindered light absorption and scattering.

### 3.11. Immobilized vs. Suspended Photocatalysts

Photocatalyst immobilization is essential for technical applications. Therefore, its influence on photocatalytic H<sub>2</sub> production was studied. The photocatalyst was immobilized onto a filter paper using the method reported by Schwarze et al. [51], and the hydrogen production from the immobilized and suspended catalysts was compared. The results are presented in Figure 5d and were compared with those for the analogous Pt-based immobilized photocatalyst. The same amount of suspended and immobilized catalysts was used in all cases. The suspended Ni-based photocatalyst (440  $\mu\text{mol m}^{-2} \text{h}^{-1}$  hydrogen) performed better than the immobilized Ni-based photocatalyst (236  $\mu\text{mol m}^{-2} \text{h}^{-1}$  hydrogen). Immobilization led to an approximately 50% loss of photocatalytic hydrogen production activity. This activity loss was expected because not all particles contribute to the reaction when the photocatalyst particles are immobilized as a thin film. The photocatalyst particles deep in the film layer will not be irradiated. Optimizing the film thickness of the catalyst is the key to improving the activity and later use on a larger scale. Furthermore, the immobilized photocatalyst experiments were conducted with a sunlight simulator equipped with an air mass 1.5 global filter with a lower total intensity. The Pt immobilized catalyst produced 1516  $\mu\text{mol m}^{-2} \text{g}^{-1}$  H<sub>2</sub> for only 0.5% loading. Although Pt clearly outperformed Ni as a cocatalyst when combined with ex-g-CN, the use of Ni provides an alternative non-noble metal-based system with good photocatalytic activity.

### 3.12. Recycling of the Catalyst

The recycling of the suspended Ni<sub>CM</sub> system was demonstrated by performing three cycles of hydrogen production after subjecting the photocatalyst to washing and drying. The amount of hydrogen produced by the photocatalyst increased slightly for at least three consecutive cycles (Figure 5e). In the colloidal method, a reducing agent was used to reduce the Ni salt precursor to Ni nanoparticles. Some residual Ni salt precursor might be

adsorbed and reduced during the first irradiation cycle. As a result, more active centers are available for the second run, leading to a higher activity. This assumption was proven by the third run that showed the same activity as the second run. Therefore, the material remained stable, and the slight activation observed potentially arise from changes in the surface composition of the Ni-based cocatalysts under reductive turnover conditions (i.e., changes in the NiO/Ni ratio).

#### 4. Conclusions

Non-noble metals (Ni, Cu, and Co) were evaluated as cocatalysts loaded onto ex-g-CN for hydrogen production. The preliminary study on Ni, Cu, and Co synthesized using the IWI method showed that Ni had seven times higher hydrogen production than Co, whereas Cu had little catalytic activity. The Ni-loaded ex-g-CN synthesized using three different synthesis methods was compared: incipient wetness impregnation, colloidal deposition, and precipitation deposition. The Ni<sub>CM</sub> performed best because of the high loading of nanoparticles on the surface of ex-g-CN confirmed using TEM and XPS. The morphology, structure, and surface properties of the Ni-loaded ex-g-CN photocatalysts were characterized using TEM, XRD, XPS, BET, and ICP, and tested for hydrogen production using a 300 W xenon lamp equipped with a 395 nm cutoff filter. Hydrogen production increased with increasing photocatalyst concentration up to 1.5 g/L. A further increase in the photocatalyst concentration led to lower activity because of hindrance and light scattering. The suspended catalyst performed better than a filter-paper-immobilized counterpart. However, immobilization can be helpful for scale-up and industrial applications. The reduced light penetration onto the film formed upon immobilization leads to the loss of photocatalytic activity because not all particles contribute to the reaction. Furthermore, Ni-loaded ex-g-CN proved to be a stable catalyst that can be recycled and reused without significant loss of activity.

**Supplementary Materials:** The following supporting information can be downloaded at: <https://www.mdpi.com/article/10.3390/nano12224006/s1>, Figure S1: UV-Vis Spectra of synthesized catalysts; inset tauc plots, Figure S2: PL spectra of g-CN and ex-g-CN, Figure S3: FTIR spectra of all synthesized catalysts, Figure S4: XRD patterns of Co- and Cu-loaded ex-g-CN, Figure S5: Adsorption and desorption curves of g-CN and ex-g-CN; inset particle size distribution, Figure S6: XPS profiles of the obtained samples for (a) Co 2p and (b) Cu 2p, Figure S7: TEM and EDX images of Co and Cu-loaded ex-g-CN. References [23,52,53] are cited in Supplementary Materials.

**Author Contributions:** Conceptualization, A.G.R., M.T., M.S. and M.M.; methodology, A.G.R. and M.S.; software, A.G.R. and M.S.; validation, A.G.R.; formal analysis, A.G.R., M.S. and M.T.; investigation, A.G.R., M.T. and M.S.; resources, M.S. and M.M.; writing—original draft preparation, A.G.R.; writing—review and editing, X.S., M.S., J.G.-A. and M.M.; visualization, A.G.R.; supervision, X.S., J.G.-A. and M.M.; funding acquisition, M.S., M.T., J.G.-A., X.S. and M.M. All authors have read and agreed to the published version of the manuscript.

**Funding:** M. Schwarze and M. Tasbihi acknowledge support funded by the Deutsche Forschungsgemeinschaft (DFG, German Research Foundation) under Germany's Excellence Strategy—EXC 2008/1 (UniSysCat)—390540038.

**Institutional Review Board Statement:** Not applicable.

**Informed Consent Statement:** Not applicable.

**Data Availability Statement:** The data presented in this study are available on request from the corresponding author.

**Acknowledgments:** X. Sala and J. García-Antón gratefully acknowledge the Ministerio de Ciencia, Innovación y Universidades, and FEDER (PID2019-104171-RB-I00). X. Sala thanks ICREA for the ICREA Academia award 2020.

**Conflicts of Interest:** The authors declare no conflict of interest.

## References

1. Sun, C.; Zhang, H.; Liu, H.; Zheng, X.; Zou, W.; Dong, L.; Qi, L. Enhanced activity of visible-light photocatalytic H<sub>2</sub> evolution of sulfur-doped g-C<sub>3</sub>N<sub>4</sub> photocatalyst via nanoparticle metal Ni as cocatalyst. *Appl. Catal. B Environ.* **2018**, *235*, 66–74. [[CrossRef](#)]
2. Sordello, F.; Minero, C. Photocatalytic hydrogen production on Pt-loaded TiO<sub>2</sub> inverse opals. *Appl. Catal. B Environ.* **2015**, *163*, 452–458. [[CrossRef](#)]
3. Bi, G.; Wen, J.; Li, X.; Liu, W.; Xie, J.; Fang, Y.; Zhang, W. Efficient visible-light photocatalytic H<sub>2</sub> evolution over metal-free g-C<sub>3</sub>N<sub>4</sub> co-modified with robust acetylene black and Ni(OH)<sub>2</sub> as dual co-catalysts. *RSC Adv.* **2016**, *6*, 31497–31506. [[CrossRef](#)]
4. Nasir, M.S.; Yang, G.; Ayub, I.; Wang, S.; Wang, L.; Wang, X.; Yan, W.; Peng, S.; Ramakarishna, S. Recent development in graphitic carbon nitride based photocatalysis for hydrogen generation. *Appl. Catal. B Environ.* **2019**, *257*, 117855.
5. Liu, J.; Cao, G.; Yang, Z.; Wang, D.; Dubois, D.; Zhou, X.; Graff, G.L.; Pederson, L.R.; Zhang, J.-G. Oriented nanostructures for energy conversion and storage. *ChemSusChem* **2008**, *1*, 676–697. [[CrossRef](#)]
6. Dong, J.; Shi, Y.; Huang, C.; Wu, Q.; Zeng, T.; Yao, W. A New and stable Mo-Mo<sub>2</sub>C modified g-C<sub>3</sub>N<sub>4</sub> photocatalyst for efficient visible light photocatalytic H<sub>2</sub> production. *Appl. Catal. B Environ.* **2019**, *243*, 27–35. [[CrossRef](#)]
7. Zheng, Y.; Lin, L.; Wang, B.; Wang, X. Graphitic Carbon Nitride Polymers toward Sustainable Photoredox Catalysis. *Angew. Chem. Int. Ed. Engl.* **2015**, *54*, 12868–12884. [[CrossRef](#)]
8. Kudo, A.; Miseki, Y. Heterogeneous photocatalyst materials for water splitting. *Chem. Soc. Rev.* **2009**, *38*, 253–278. [[CrossRef](#)]
9. Chen, C.; Ma, W.; Zhao, J. Semiconductor-mediated photodegradation of pollutants under visible-light irradiation. *Chem. Soc. Rev.* **2010**, *39*, 4206–4219. [[CrossRef](#)]
10. Mekhilef, S.; Saidur, R.; Safari, A. A review on solar energy use in industries. *Renew. Sustain. Energy Rev.* **2011**, *15*, 1777–1790. [[CrossRef](#)]
11. Ayub, I.; Munir, A.; Amjad, W.; Ghafoor, A.; Nasir, M.S. Energy- and exergy-based thermal analyses of a solar bakery unit. *J. Therm. Anal. Calorim.* **2018**, *133*, 1001–1013. [[CrossRef](#)]
12. Kumar, P.; Boukherroub, R.; Shankar, K. Sunlight-driven water-splitting using two-dimensional carbon based semiconductors. *J. Mater. Chem. A* **2018**, *6*, 12876–12931. [[CrossRef](#)]
13. Han, X.; Xu, D.; An, L.; Hou, C.; Li, Y.; Zhang, Q.; Wang, H. Ni-Mo nanoparticles as co-catalyst for drastically enhanced photocatalytic hydrogen production activity over g-C<sub>3</sub>N<sub>4</sub>. *Appl. Catal. B Environ.* **2019**, *243*, 136–144. [[CrossRef](#)]
14. Xu, J.; Fujitsuka, M.; Kim, S.; Wang, Z.; Majima, T. Unprecedented effect of CO<sub>2</sub> calcination atmosphere on photocatalytic H<sub>2</sub> production activity from water using g-C<sub>3</sub>N<sub>4</sub> synthesized from triazole polymerization. *Appl. Catal. B Environ.* **2019**, *241*, 141–148. [[CrossRef](#)]
15. Rana, A.G.; Ahmad, W.; Al-Matar, A.; Shawabkeh, R.; Aslam, Z. Synthesis and characterization of Cu-Zn/TiO<sub>2</sub> for the photocatalytic conversion of CO<sub>2</sub> to methane. *Environ. Technol.* **2017**, *38*, 1085–1092. [[CrossRef](#)] [[PubMed](#)]
16. Zhao, X.; Feng, J.; Liu, J.; Lu, J.; Shi, W.; Yang, G.; Wang, G.; Feng, P.; Cheng, P. Metal-Organic Framework-Derived ZnO/ZnS Heteronanostructures for Efficient Visible-Light-Driven Photocatalytic Hydrogen Production. *Adv. Sci.* **2018**, *5*, 1700590. [[CrossRef](#)] [[PubMed](#)]
17. Yuan, Y.-J.; Chen, D.; Zhong, J.; Yang, L.X.; Wang, J.; Liu, M.J.; Tu, W.-G.; Yu, Z.-T.; Zou, Z.-G. Interface engineering of a noble-metal-free 2D-2D MoS<sub>2</sub>/Cu-ZnIn<sub>2</sub>S<sub>4</sub> photocatalyst for enhanced photocatalytic H<sub>2</sub> production. *J. Mater. Chem. A* **2017**, *5*, 15771–15779. [[CrossRef](#)]
18. Chen, Q.; Cheng, X.; Long, H.; Rao, Y. A short review on recent progress of Bi/semiconductor photocatalysts: The role of Bi metal. *Chin. Chem. Lett.* **2020**, *31*, 2583–2590. [[CrossRef](#)]
19. Zhao, L.; Jia, J.; Yang, Z.; Yu, J.; Wang, A.; Sang, Y.; Zhou, W.; Liu, H. One-step synthesis of CdS nanoparticles/MoS<sub>2</sub> nanosheets heterostructure on porous molybdenum sheet for enhanced photocatalytic H<sub>2</sub> evolution. *Appl. Catal. B Environ.* **2017**, *210*, 290–296. [[CrossRef](#)]
20. Xu, J.; Qi, Y.; Wang, C.; Wang, L. NH<sub>2</sub>-MIL-101(Fe)/Ni(OH)<sub>2</sub>-derived C,N-codoped Fe<sub>2</sub>P/Ni<sub>2</sub>P cocatalyst modified g-C<sub>3</sub>N<sub>4</sub> for enhanced photocatalytic hydrogen evolution from water splitting. *Appl. Catal. B Environ.* **2019**, *241*, 178–186. [[CrossRef](#)]
21. Li, H.; Wang, M.; Wei, Y.; Long, F. Noble metal-free NiS<sub>2</sub> with rich active sites loaded g-C<sub>3</sub>N<sub>4</sub> for highly efficient photocatalytic H<sub>2</sub> evolution under visible light irradiation. *J. Colloid Interface Sci.* **2019**, *534*, 343–349. [[CrossRef](#)] [[PubMed](#)]
22. Ong, W.J.; Tan, L.L.; Ng, Y.H.; Yong, S.T.; Chai, S.P. Graphitic Carbon Nitride (g-C<sub>3</sub>N<sub>4</sub>)-Based Photocatalysts for Artificial Photosynthesis and Environmental Remediation: Are We a Step Closer to Achieving Sustainability? *Chem. Rev.* **2016**, *116*, 7159–7329. [[CrossRef](#)]
23. Rana, A.; Tasbihi, M.; Schwarze, M.; Minceva, M. Efficient Advanced Oxidation Process (AOP) for Photocatalytic Contaminant Degradation Using Exfoliated Metal-Free Graphitic Carbon Nitride and Visible Light-Emitting Diodes. *Catalysts* **2021**, *11*, 662. [[CrossRef](#)]
24. Wang, X.; Maeda, K.; Thomas, A.; Takanabe, K.; Xin, G.; Carlsson, J.M.; Domen, K.; Antonietti, M. A metal-free polymeric photocatalyst for hydrogen production from water under visible light. *Nat. Mater.* **2009**, *8*, 76–80. [[CrossRef](#)] [[PubMed](#)]
25. Yu, J.; Wang, K.; Xiao, W.; Cheng, B. Photocatalytic reduction of CO<sub>2</sub> into hydrocarbon solar fuels over g-C<sub>3</sub>N<sub>4</sub>-Pt nanocomposite photocatalysts. *Phys. Chem. Chem. Phys.* **2014**, *16*, 11492–11501. [[CrossRef](#)]
26. Zhang, W.; Bariotaki, A.; Smonou, I.; Hollmann, F. Visible-light-driven photooxidation of alcohols using surface-doped graphitic carbon nitride. *Green Chem.* **2017**, *19*, 2096–2100. [[CrossRef](#)]



27. Maeda, K.; Wang, X.; Nishihara, Y.; Lu, D.; Antonietti, M.; Domen, K. Photocatalytic Activities of Graphitic Carbon Nitride Powder for Water Reduction and Oxidation under Visible Light. *J. Phys. Chem. C* **2009**, *113*, 4940–4947. [[CrossRef](#)]
28. Rana, A.; Minceva, M. Analysis of Photocatalytic Degradation of Phenol with Exfoliated Graphitic Carbon Nitride and Light-Emitting Diodes Using Response Surface Methodology. *Catalysts* **2021**, *11*, 898. [[CrossRef](#)]
29. Li, L.; Yi, J.; Zhu, X.; Pan, L.; Chen, Z.; Hua, Y.; Yang, W.; Liu, J.; Zhu, X.; Li, H.; et al. Solar driven high efficiency hydrogen evolution catalyzed by surface engineered ultrathin carbon nitride. *New J. Chem.* **2020**, *44*, 19314–19322. [[CrossRef](#)]
30. Chen, P.-W.; Li, K.; Yu, Y.-X.; Zhang, W.-D. Cobalt-doped graphitic carbon nitride photocatalysts with high activity for hydrogen evolution. *Appl. Surf. Sci.* **2017**, *392*, 608–615. [[CrossRef](#)]
31. Zhang, S.; Qian, X.; Yan, J.; Chen, K.; Huang, J. Nickel-decorated g-C<sub>3</sub>N<sub>4</sub> hollow spheres as an efficient photocatalyst for hydrogen evolution and oxidation of amines to imines. *New J. Chem.* **2020**, *44*, 11710–11719. [[CrossRef](#)]
32. Shiraishi, Y.; Kofuji, Y.; Kanazawa, S.; Sakamoto, H.; Ichikawa, S.; Tanaka, S.; Hirai, T. Platinum nanoparticles strongly associated with graphitic carbon nitride as efficient co-catalysts for photocatalytic hydrogen evolution under visible light. *Chem. Commun.* **2014**, *50*, 15255–15258. [[CrossRef](#)] [[PubMed](#)]
33. Samanta, S.; Martha, S.; Parida, K. Facile Synthesis of Au/g-C<sub>3</sub>N<sub>4</sub> Nanocomposites: An Inorganic/Organic Hybrid Plasmonic Photocatalyst with Enhanced Hydrogen Gas Evolution Under Visible-Light Irradiation. *ChemCatChem* **2014**, *6*, 1453–1462. [[CrossRef](#)]
34. Álvarez-Prada, I.; Nguyen, A.D.; Romero, N.; Hou, H.; Benazzi, E.; Escriche, L.; Acharjya, A.; Thomas, A.; Schwarze, M.; Scholmacker, R.; et al. Insights into the light-driven hydrogen evolution reaction of mesoporous graphitic carbon nitride decorated with Pt or Ru nanoparticles. *Dalton Trans.* **2022**, *51*, 731–740. [[CrossRef](#)] [[PubMed](#)]
35. Bu, Y.; Chen, Z.; Li, W. Using electrochemical methods to study the promotion mechanism of the photoelectric conversion performance of Ag-modified mesoporous g-C<sub>3</sub>N<sub>4</sub> heterojunction material. *Appl. Catal. B Environ.* **2014**, *144*, 622–630. [[CrossRef](#)]
36. Cao, S.; Li, Y.; Zhu, B.; Jaroniec, M.; Yu, J. Facet effect of Pd cocatalyst on photocatalytic CO<sub>2</sub> reduction over g-C<sub>3</sub>N<sub>4</sub>. *J. Catalysis* **2017**, *349*, 208–217. [[CrossRef](#)]
37. Daş, E.; Gürsel, S.A.; Şanlı, L.I.; Yurtcan, A.B. Comparison of two different catalyst preparation methods for graphene nanoplatelets supported platinum catalysts. *Int. J. Hydrogen Energy* **2016**, *41*, 9755–9761. [[CrossRef](#)]
38. Ahmad, W.; Mehmood, U.; Al-Ahmed, A.; Al-Sulaiman, F.A.; Aslam, M.Z.; Kamal, M.S.; Shawabkeh, R. Synthesis of zinc oxide/titanium dioxide (ZnO/TiO<sub>2</sub>) nanocomposites by wet incipient wetness impregnation method and preparation of ZnO/TiO<sub>2</sub> paste using poly(vinylpyrrolidone) for efficient dye-sensitized solar cells. *Electrochim. Acta* **2016**, *222*, 473–480. [[CrossRef](#)]
39. Tasbihi, M.; Fresno, F.; Simon, U.; Villar-García, I.J.; Pérez-Dieste, V.; Escudero, C.; O’Shea, V.A.D.L.P. On the selectivity of CO<sub>2</sub> photoreduction towards CH<sub>4</sub> using Pt/TiO<sub>2</sub> catalysts supported on mesoporous silica. *Appl. Catal. B Environ.* **2018**, *239*, 68–76. [[CrossRef](#)]
40. Yang, J.; Acharjya, A.; Ye, M.; Rabeah, J.; Li, S.; Kochovski, Z.; Youk, S.; Roeser, J.; Grüneberg, J.; Penschke, C.; et al. Protonated Imine-Linked Covalent Organic Frameworks for Photocatalytic Hydrogen Evolution. *Angew. Chem. Int. Ed.* **2021**, *60*, 19797–19803. [[CrossRef](#)]
41. Schröder, M.; Kailasam, K.; Rudi, S.; Fündling, K.; Rieß, J.; Lublow, M.; Thomas, A.; Schomäcker, R.; Schwarze, M. Applying thermo-destabilization of microemulsions as a new method for co-catalyst loading on mesoporous polymeric carbon nitride-towards large scale applications. *RSC Adv.* **2014**, *4*, 50017–50026. [[CrossRef](#)]
42. Parapat, R.Y.; Saputra, O.H.I.; Ang, A.P.; Schwarze, M.; Schomäcker, R. Support effect in the preparation of supported metal catalysts via microemulsion. *RSC Adv.* **2014**, *4*, 50955–50963. [[CrossRef](#)]
43. Deng, P.; Hong, W.; Cheng, Z.; Zhang, L.; Hou, Y. Facile fabrication of nickel/porous g-C<sub>3</sub>N<sub>4</sub> by using carbon dot as template for enhanced photocatalytic hydrogen production. *Int. J. Hydrogen Energy* **2020**, *45*, 33543–33551. [[CrossRef](#)]
44. Deng, P.; Xiong, J.; Lei, S.; Wang, W.; Ou, X.; Xu, Y.; Xiao, Y.; Cheng, B. Nickel formate induced high-level in situ Ni-doping of g-C<sub>3</sub>N<sub>4</sub> for a tunable band structure and enhanced photocatalytic performance. *J. Mater. Chem. A* **2019**, *7*, 22385–22397. [[CrossRef](#)]
45. Deng, P.; Gan, M.; Zhang, X.; Li, Z.; Hou, Y. Non-noble-metal Ni nanoparticles modified N-doped g-C<sub>3</sub>N<sub>4</sub> for efficient photocatalytic hydrogen evolution. *Int. J. Hydrogen Energy* **2019**, *44*, 30084–30092. [[CrossRef](#)]
46. Reddy, I.N.; Jayashree, N.; Manjunath, V.; Kim, D.; Shim, J. Photoelectrochemical Studies on Metal-Doped Graphitic Carbon Nitride Nanostructures under Visible-Light Illumination. *Catalysts* **2020**, *10*, 983. [[CrossRef](#)]
47. Öztürk, S.; Xiao, Y.-X.; Dietrich, D.; Giesen, B.; Barthel, J.; Ying, J.; Yang, X.-Y.; Janiak, C. Nickel nanoparticles supported on a covalent triazine framework as electrocatalyst for oxygen evolution reaction and oxygen reduction reactions. *Beilstein J. Nanotechnol.* **2020**, *11*, 770–781. [[CrossRef](#)]
48. Zhao, H.; Jiang, Z.; Xiao, K.; Sun, H.; Chan, H.S.; Tsang, T.H.; Yang, S.; Wong, P.K. Photo-assisted separation of noble-metal-free oxidation and reduction cocatalysts for graphitic carbon nitride nanosheets with efficient photocatalytic hydrogen evolution. *Appl. Catal. B Environ.* **2021**, *280*, 119456. [[CrossRef](#)]
49. Schubert, J.S.; Popovic, J.; Haselmann, G.M.; Nandan, S.P.; Wang, J.; Giesriegl, A.; Cherevan, A.S.; Eder, D. Immobilization of Co, Mn, Ni and Fe oxide co-catalysts on TiO<sub>2</sub> for photocatalytic water splitting reactions. *J. Mater. Chem. A* **2019**, *7*, 18568–18579. [[CrossRef](#)]
50. Zhang, G.; Lan, Z.A.; Lin, L.; Lin, S.; Wang, X. Overall water splitting by Pt/g-C<sub>3</sub>N<sub>4</sub> photocatalysts without using sacrificial agents. *Chem. Sci.* **2016**, *7*, 3062–3066. [[CrossRef](#)]

51. Schwarze, M.; Thiel, T.A.; Tasbihi, M.; Schroeter, M.; Menezes, P.W.; Walter, C.; Driess, M.; Schomäcker, R. Use of Cellulose for the Production of Photocatalytic Films for Hydrogen Evolution Along the Lines of Paper Production. *Energy Technol.* **2022**, *10*, 2100525. [[CrossRef](#)]
52. Huang, J.; Qian, W.; Ma, H.; Zhang, H.; Ying, W. Highly selective production of heavy hydrocarbons over cobalt–graphene–silica nanocomposite catalysts. *RSC Adv.* **2017**, *7*, 33441–33449. [[CrossRef](#)]
53. Wang, X.; Zhang, B.; Zhang, W.; Yu, M.; Cui, L.; Cao, X.; Liu, J. Super-light Cu@Ni nanowires/graphene oxide composites for significantly enhanced microwave absorption performance. *Sci. Rep.* **2017**, *7*, 1584. [[CrossRef](#)] [[PubMed](#)]

#### **4.4 Paper IV: Analysis of photocatalytic degradation of phenol with exfoliated Graphitic Carbon Nitride and Light-Emitting Diodes Using Response Surface Methodology**

Adeem Ghaffar Rana, Mirjana Minceva

Catalysts 2021 11 (8), 898 (<https://doi.org/10.3390/catal11080898>)

**Author contribution:** The thesis author conceptualized the paper's idea and characterized the catalysts. He evaluated and interpreted the experimental results and wrote the manuscript draft.

##### **Summary**

Response surface methodology (RSM) can be employed to maximize the response variable by optimization of operational factors. The RSM has been extensively used to effectively design experiments. In contrast to the traditional ways of designing the experiments, the interactions among process variables can be determined by statistical techniques. Paper I showed that phenol degraded efficiently using g-C<sub>3</sub>N<sub>4</sub>, and a visible light LED lamp. Optimization can be ensured by tuning the operating parameters affecting the removal efficiency of phenol from water. Paper IV aims to model the phenol degradation process using RSM. In this study, three operating parameters were considered, and Box–Benken design (BBD) was used for the design of experiment (DoE). RSM was applied to determine the mathematical relationship between the operating parameters and phenol degradation.

In this work, already synthesized exfoliated g-C<sub>3</sub>N<sub>4</sub> (paper I) was used under the influence of visible light LED lamp, for phenol degradation. While the operating parameters significantly affect the efficiency of the process, the phenol degradation process can be modeled using RSM, to derive an empirical equation predicting the degradation efficiency of phenol. This work chose three parameters: catalyst concentration, pollutant concentration, and solution pH. Experiments were conducted according to a three-variable BBD experimental design for RSM. The upper and lower limits of the parameter were catalyst concentration (0.25-0.75 g/L), phenol initial concentration (20-100 ppm), and pH (3-10). The systematic approach for the experimental design gives the advantage of fewer experiments, thus reducing the time required, apart from being more economical. Phenol degradation experimental data were fitted with four models: two-factor interaction (2FI), linear, quadratic, and cubic models, to obtain the regression equations. An empirical regression quadratic model produced the best fit, and an equation was developed to relate the phenol degradation efficiency with the three aforementioned operating parameters. Analysis of variance (ANOVA) showed that the model is significant with an R<sup>2</sup> of 0.96. The statistical analysis demonstrated that phenol concentration in the studied range majorly affected phenol degradation. The quadratic model showed a significant correlation between the predicted and experimental values of photocatalytic

degradation of phenol. The predictions of the quadratic model were validated for 50 ppm of phenol under optimal conditions, involving a catalyst concentration of 0.4 g/L, and a solution pH of 6.5. The model predicted a degradation efficiency of 88.62%, whereas the experimentally achieved efficiency was 83.75%, which is less than a 5% error from the predicted value. It is concluded that the response surface methodology can be used to obtain a decent prediction for the photocatalytic application.

## Article

# Analysis of Photocatalytic Degradation of Phenol with Exfoliated Graphitic Carbon Nitride and Light-Emitting Diodes Using Response Surface Methodology

Adeem Ghaffar Rana <sup>1,2</sup>  and Mirjana Minceva <sup>1,\*</sup> 

<sup>1</sup> Biothermodynamics, TUM School of Life Sciences, Technical University of Munich, Maximus-von-Imhof-Forum 2, 85354 Freising, Germany; adeem.rana@tum.de

<sup>2</sup> Department of Chemical, Polymer, and Composite Materials Engineering, University of Engineering and Technology (UET), Lahore 39161, Pakistan

\* Correspondence: mirjana.minceva@tum.de; Tel.: +49-8161716170

**Abstract:** Response surface methodology (RSM) involving a Box–Benken design (BBD) was employed to analyze the photocatalytic degradation of phenol using exfoliated graphitic carbon nitride (g-C<sub>3</sub>N<sub>4</sub>) and light-emitting diodes (wavelength = 430 nm). The interaction between three parameters, namely, catalyst concentration (0.25–0.75 g/L), pollutant concentration (20–100 ppm), and pH of the solution (3–10), was examined and modeled. An empirical regression quadratic model was developed to relate the phenol degradation efficiency with these three parameters. Analysis of variance (ANOVA) was then applied to examine the significance of the model; this showed that the model is significant with an insignificant lack of fit and an R<sup>2</sup> of 0.96. The statistical analysis demonstrated that, in the studied range, phenol concentration considerably affected phenol degradation. The RSM model shows a significant correlation between predicted and experimental values of photocatalytic degradation of phenol. The model's accuracy was tested for 50 ppm of phenol under optimal conditions involving a catalyst concentration of 0.4 g/L catalysts and a solution pH of 6.5. The model predicted a degradation efficiency of 88.62%, whereas the experimentally achieved efficiency was 83.75%.

**Keywords:** g-C<sub>3</sub>N<sub>4</sub>; photocatalysis; response surface methodology; wastewater treatment; phenol



**Citation:** Rana, A.G.; Minceva, M. Analysis of Photocatalytic Degradation of Phenol with Exfoliated Graphitic Carbon Nitride and Light-Emitting Diodes Using Response Surface Methodology. *Catalysts* **2021**, *11*, 898. <https://doi.org/10.3390/catal11080898>

Academic Editor: Annalisa Vacca

Received: 2 July 2021

Accepted: 23 July 2021

Published: 25 July 2021

**Publisher's Note:** MDPI stays neutral with regard to jurisdictional claims in published maps and institutional affiliations.



**Copyright:** © 2021 by the authors. Licensee MDPI, Basel, Switzerland. This article is an open access article distributed under the terms and conditions of the Creative Commons Attribution (CC BY) license (<https://creativecommons.org/licenses/by/4.0/>).

## 1. Introduction

For all living beings, water is considered to be the most important resource. Easy access to clean water is one of the biggest challenges for mankind. In the last few decades, advancements in science, technology, and industrialization have led to considerable benefits to mankind but at the cost of a more polluted environment, particularly water [1]. There are multiple categories of pollutants in water, such as heavy metals, dyes, pesticides, pharmaceuticals, and other organic pollutants. Amongst organic pollutants, phenolic compounds, with ~3 million tons of global production, are an emerging contaminant detected in water [1–4].

Phenols or phenolics are essential because of their wide range of applications in the processing and manufacturing industry. However, the ecosystem's contamination by phenolics is concerning because of the adverse implications on human health such as their endocrine-disrupting abilities and carcinogenic behavior [1,5,6]. Moreover, these chemicals cause environmental issues such as water hardness, pH change, and a decrease in dissolved oxygen level. Furthermore, the Environmental Protection Agency (EPA) and the European Union (EU) have included a few phenols in their priority pollutants list. It is necessary to make this polluted water containing phenols and other pollutants suitable for human use and aquatic life using certain techniques to minimize the usage of these chemicals [5].

The removal of phenolic compounds from wastewater has attracted considerable attention from researchers [5]. Many biological, chemical, and physical techniques such

as membrane filtration, coagulation–flocculation, adsorption [7,8], ion exchange, bacterial and fungal biosorption [9], aerobic and anaerobic processes [10] are used for phenol removal. In these processes, there are many constraints such as high cost, and low efficiency; furthermore, these methods do not completely remove phenol from wastewater [11,12]. Moreover, using these techniques, phenol is transferred from wastewater to a solid phase that requires treatment for safe disposal, which leads to additional cost for the whole process. Thus, it is necessary to develop an alternative effective and cost-efficient method for phenol removal from wastewater.

Advanced oxidative processes (AOP) are successful for achieving the complete removal of pollutants [13]. The degradation process using AOP can be performed in several ways, such as using only oxidizing agents, light irradiance in addition with oxidizing agents, and photocatalysis [14]. For all these processes, the degradation process is conducted using  $\text{OH}^-$  radicals that are generated during the oxidation reaction. Among these processes, photocatalysis has attracted considerable interest because it can harvest solar light with the help of semiconductor materials (catalysts). The catalysts can help solve environmental issues related to water contaminations; these semiconductor materials are nontoxic and efficient. Note that different semiconductor materials such as ZnO [15],  $\text{TiO}_2$  [16],  $\text{SiO}_2$ ,  $\text{Al}_2\text{O}_3$  [8], and  $\text{g-C}_3\text{N}_4$  [17,18], are used for environmental applications in photocatalysis; these have considerable advantages because of the large surface areas, adsorption capacities, and better absorption of light. Among these materials,  $\text{g-C}_3\text{N}_4$  offers improved visible light absorption [17,19–21].

$\text{g-C}_3\text{N}_4$ , a polymeric semiconductor, composed of C, N, and H, has gained considerable interest from researchers for novel generation of photocatalysts because of its widespread catalytic uses in oxidation and reduction processes, such as pollutant degradation, water splitting, and  $\text{CO}_2$  reduction. These materials have been extensively used for environmental remediation because they are easy to synthesize, metal-free, inexpensive, and easily available [22–24]. Furthermore,  $\text{g-C}_3\text{N}_4$  possesses higher thermal and chemical stability because of  $\pi$ -conjugated frameworks connecting the 2D layered structure of tri-s-triazine building blocks.  $\text{g-C}_3\text{N}_4$  can be activated by visible light of 420–460 nm because of its low bandgap energy (2.7 eV) [25,26]. There are, however, certain challenges associated with the application of  $\text{g-C}_3\text{N}_4$  in phenol removal such as low surface area, fast recombination rate, and low conductivity, thus resulting in lower efficiency. To overcome these limitations, multiple strategies have been used to improve the surface electronic structures and activity of the bulk  $\text{g-C}_3\text{N}_4$  in visible light. To improve the activity of pristine  $\text{g-C}_3\text{N}_4$ , strategies such as metal and non-metal doping, exfoliation, hard and soft templating, and metal oxide heterojunctions have been used [27–31].

Factors affecting the removal efficiency can be tuned by the morphology and/or chemistry of the catalyst and by optimizing the operating parameters. Multiple operating parameters play an important role in the photocatalytic degradation process, thus making their optimization important for achieving good photocatalytic degradation of the target pollutant. Response surface methodology (RSM) is one of the most commonly applied optimization techniques; it is a powerful optimization tool for an experimental design that efficiently helps in systemic analysis [5,11,14]. RSM uses mathematics and statistics to analyze the relative significance of influencing factors on the response of the studied system. RSM is suitable for predicting the effect of individual experimental operating parameters, in addition to locating interactions between parameters and their impact on a response variable. RSM uses a systematic technique to simultaneously vary all parameters and evaluate the influence of these parameters on photocatalytic degradation [32,33]. The greatest advantage of RSM lies in the systematic approach for the experimental design, which mostly requires fewer experiments, thus reducing the time required and thereby being more economical. For designing these experiments, a central composite design (CCD) [3] and Box–Benken design (BBD) [11,12] are most commonly used. For the same number of parameters, BBD requires fewer experiments than CCD [3]; therefore, in this study, BBD is selected as a preferred design approach.

The objective of this study was to analyze the photocatalytic degradation of phenol with metal-free g-C<sub>3</sub>N<sub>4</sub> and visible LED light and to model the process using RSM. In this study, the operating parameters considered were catalyst concentration, phenol concentration, and pH of the solution. BBD was used for the experimental design and RSM was applied to determine the mathematical relationship between operating parameters and phenol degradation. Finally, the correlation determined by RSM was experimentally validated.

## 2. Materials and Methods

### 2.1. Chemicals and Materials

Melamine (C<sub>3</sub>H<sub>6</sub>N<sub>6</sub>, 99%) was purchased from Alfa Aesar. Phenol (C<sub>6</sub>H<sub>5</sub>OH, 99%) was purchased from Merck. Acetonitrile (C<sub>2</sub>H<sub>3</sub>N, 99.99%) and ultra-pure water for high-performance liquid chromatography (HPLC) were purchased from Sigma Aldrich. NaOH and HCl were purchased from VWR chemicals. All chemicals used were of analytical grade and used as-received without any further purification.

### 2.2. Photocatalyst Synthesis

Photocatalyst was prepared as per the procedure used in our previous study [18]; the synthesis process is briefly reported here. Melamine was placed in a muffle furnace (Carbolite Gero, GPC 1200, Derbyshire, UK) in a closed crucible to prepare bulk g-C<sub>3</sub>N<sub>4</sub> using thermal decomposition. The synthesis process comprised two steps: A heating ramp rate of 2 °C min<sup>-1</sup> was programmed up to 450 °C; this temperature was maintained for 2 h. Then, the temperature was increased to 550 °C using a heating ramp rate of 2 °C min<sup>-1</sup> and then maintained for 4 h. The material synthesized was crushed in mortar after cooling, then rinsed with ultrapure water, and dried overnight at 80 °C. The exfoliation process was conducted in an open crucible at 500 °C for 2 h at a heating ramp rate of 2 °C min<sup>-1</sup> in a muffle furnace.

### 2.3. Characterization of the Photocatalyst

Fourier transform infrared (FTIR) measurements (4000–400 cm<sup>-1</sup>) were performed on a Spectrum Two FT-IR Spectrometer (PerkinElmer, Switzerland) with a universal ATR (UATR Two) cell equipped with a ZnSe single crystal. The acquisition performed using 60 scans and the resolution was set to 4 cm<sup>-1</sup>. Zetasizer Nano ZEN5600 (Malvern, UK) was used to measure the zeta potential of the synthesized material. SU8030 (Hitachi, Japan) SEM-type microscope operated at an acceleration voltage of 10 kV and a probe current of 15 pA was used to examine the morphology of the material with scanning electron microscopy (SEM).

### 2.4. RSM with Box–Behnken Experimental Design

The influence of three independent operating parameters, i.e., catalyst concentration (A), phenol initial concentration (B), and pH of the solution (C), was considered in RSM. The remaining reaction conditions, namely, the airflow rate (50 mL/min) and reaction time (3 h), was kept constant in the experiment based on previous study [18]. The degradation efficiency of phenol (Equation (1)) was set as a response variable. Note that a previous study [18] was conducted to obtain the upper and lower limits of the parameters. Table 1 shows the ranges and levels of independent parameters A, B, and C. BBD was used to examine the combined effect of these three variables. Section 3.3 lists the set of experiments in table; it includes a replication of experiments at the central point. Regression analysis was performed using OriginPro 2021 9.8.0.200 (OriginLab Corporation, Northampton, MA, USA) software. The suggested model's data were analyzed for significance and suitability using analysis of variance (ANOVA).



**Table 1.** Independent parameters and their ranges and levels.

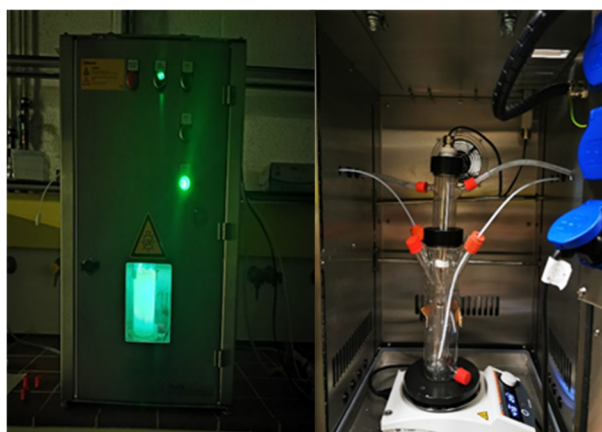
Independent Parameters	Symbol	Range and Level		
		Low (−1)	Middle (0)	High (+1)
Catalyst concentration (g/L)	A	0.25	0.5	0.75
Phenol initial concentration (ppm)	B	20	60	100
pH	C	3	6.5	10

### 2.5. Photocatalytic Experiments

Figure 1 shows the photocatalytic experiments that were conducted in a jacketed glass reactor (working volume 225 mL) (Peschl Ultraviolet GmbH, Mainz, Germany) with a safety cabinet. The reactor was irradiated from inside using a custom-made LED immersion lamp; the LED has maximum emission at 430 nm. Glass reactor was then sonicated with a reaction mixture for uniform dispersion, followed by stirring with continuous airflow to maintain adsorption–desorption equilibrium for 30 min. Subsequently, lights were turned on, which is considered as zero time ( $t_0$ ). Nine to ten samples (1 mL) were periodically collected from the reaction mixture. After centrifugation and filtration, the samples were analyzed using HPLC. For acidic and basic reaction conditions, the pH of the mixture was adjusted using 0.1 M HCl and NaOH. The phenol degradation efficiency was determined using the following Equation:

$$\text{Degradation efficiency (\%)} = \frac{C_0 - C}{C_0} \times 100 \quad (1)$$

where  $C_0$  is the initial phenol concentration and  $C$  is the residual phenol concentration in the solution at an irradiation time  $t$ .

**Figure 1.** Photocatalytic reactor setup.

The reduction of the reaction mixture volume due to the sampling was less than 5% at the end of the experiments and was therefore not considered in the calculation of the phenol degradation efficiency.

### 2.6. Analytical Techniques

A prominence HPLC system from Shimadzu (Kyoto, Japan) was used for analyzing the samples obtained from the reactor. The system is equipped with a binary pump (Model LC-20AB), an autosampler (Model SIL-20A), a degasser (Model DGU-20A3,) and a diode-array detector (Model SPD-M20A). Phenomenex (C18, 150 × 4.6 mm, 3 μm) column was used with a fixed flow rate of 0.8 mL/min, with the mobile phase gradient of water (A) and acetonitrile (B): starts with 15% B, followed by 60% B in 7 min and back to 15% B in 8 min;



injection of 5  $\mu\text{L}$ ; UV light of 254 nm. Phenol was analyzed at a maximum absorption wavelength ( $\lambda_{\text{max}}$ ) of 270 nm.

### 3. Results and Discussion

#### 3.1. Photocatalyst Characterization

The metal-free  $\text{g-C}_3\text{N}_4$  used in this study was synthesized and characterized in our previous study [18] using transmission electron microscopy (TEM), Brunauer–Emmett–Teller isotherms (BET), X-ray diffraction (XRD), X-ray photoelectron spectroscopy (XPS), photoluminescence (PL), and UV-Vis spectroscopy. In this study, scanning electron microscopy (SEM), Fourier transform infrared spectroscopy (FTIR), and zeta potential analyses were performed. Table 2 lists the physical properties of metal-free  $\text{g-C}_3\text{N}_4$  before and after its exfoliation.

**Table 2.** Summary of characterization results [18].

Characterization	Bulk $\text{g-C}_3\text{N}_4$		Exfoliated $\text{g-C}_3\text{N}_4$	
BET	Surface area 11 $\text{m}^2/\text{g}$	Pore size 1.91 $\text{\AA}$	Surface area 170 $\text{m}^2/\text{g}$	Pore size 1.96 $\text{\AA}$
XRD	Weak peaks ( $2\theta$ ) 13.0°	Strong peaks ( $2\theta$ ) 27.2°	Weak peaks ( $2\theta$ ) 13.1°	Strong peaks ( $2\theta$ ) 27.4°
PL/UV-Vis	Max. absorption 458 nm	Bandgap 2.58 eV	Max. absorption 436 nm	Bandgap 2.68 eV
XPS	C1s peaks 288.2, 284.6, 286.2 and 292.9 eV	N1s peaks 398.5, 399.8, 400.8, 404.1 eV	C1s peaks 287.8, 284.7, 286.2 and 293.5 eV	N1s peaks 397.8, 399.1, 400.1, 403.5 eV

The exfoliated material has a significantly higher surface area than the bulk material, while the average pore size of both materials is almost the same (Table 2 and Figure S1). Using XRD, the material shows two characteristic peaks of  $\text{g-C}_3\text{N}_4$  (Figure S4) [34,35]. The strong and weak peaks of N1s and C1s observed in XPS confirm the chemical state of  $\text{g-C}_3\text{N}_4$  (Figure S3) [17,36–41]. Table 2 lists the maximum absorption wavelength and bandgap of the material, which are presented in Figure S2 [42,43].

In Figure 2, the selected SEM images of bulk and exfoliated  $\text{g-C}_3\text{N}_4$  are presented. The thermal exfoliation transformed the stacked and aggregated structure of bulk  $\text{g-C}_3\text{N}_4$  in a porous nanosheet structure. The reduction in layer thickness (Figure 2b) leads to an increase in the specific surface area of  $\text{g-C}_3\text{N}_4$  [17,44–46].

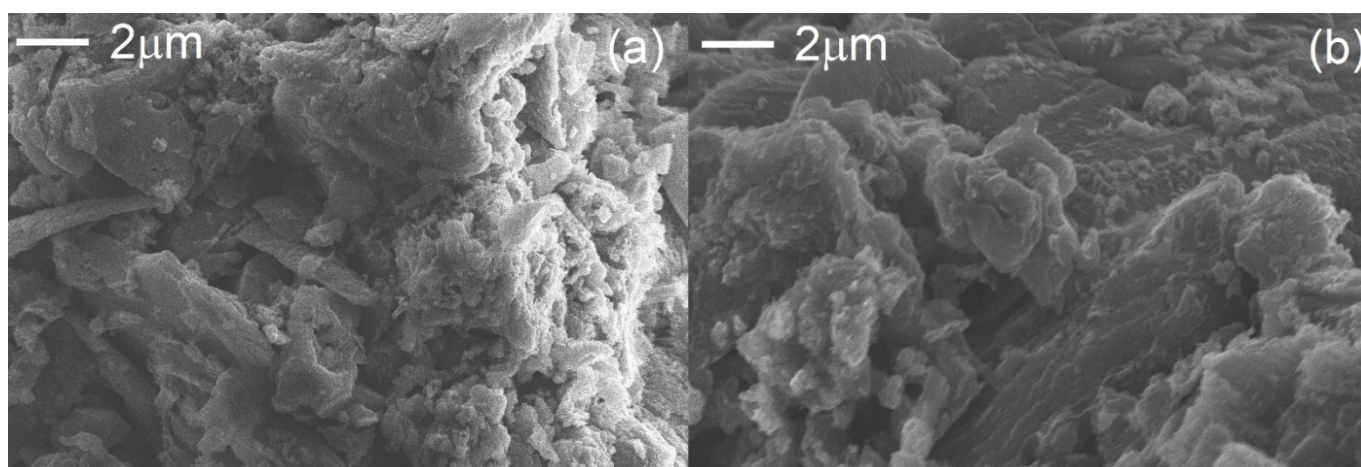


**Figure 2.** SEM images of the bulk (a) and exfoliated (b)  $\text{g-C}_3\text{N}_4$ .

Figure 3 shows the catalysts' FTIR spectra. A broad peak is observed between 3200 and 3000  $\text{cm}^{-1}$ , which can be attributed to the stretching vibrations of N–H bonds from

residual amino groups and adsorbed  $\text{H}_2\text{O}$ . The sharp peak that appears at  $806\text{ cm}^{-1}$  can be attributed to the breathing mode of triazine units [47,48], whereas the strong bands between  $1636$  and  $1242\text{ cm}^{-1}$  belong to the  $\text{C}=\text{N}$  and  $\text{C}-\text{N}$  bonds of heterocyclic rings. Because the spectra of both materials show the same absorption bands, the chemical structure remained unaltered after treatment.

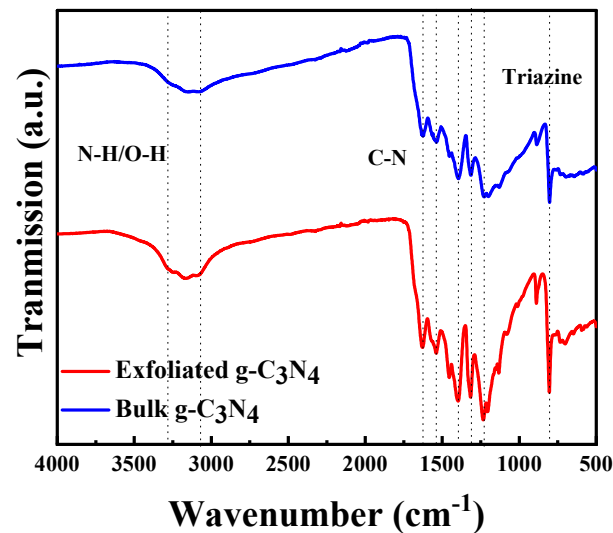


Figure 3. Fourier transform infrared spectra of bulk and exfoliated  $\text{g-C}_3\text{N}_4$ .

Figure 4 shows the effect of pH on the zeta potential of the exfoliated  $\text{g-C}_3\text{N}_4$ . The catalyst surface is positively charged at acidic pH (3) and negatively charged at natural (6) and basic pH (10).

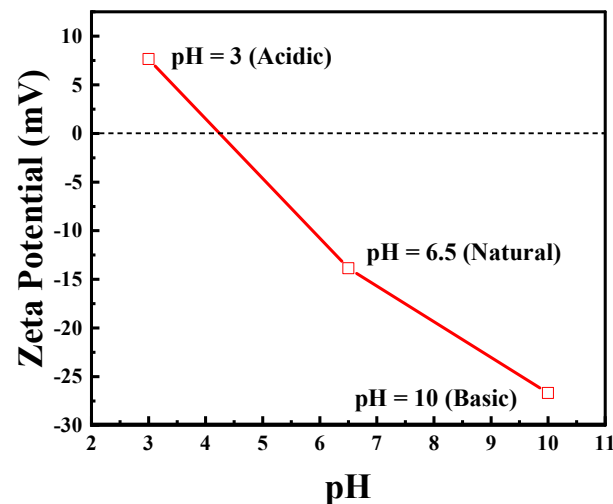


Figure 4. Zeta potential at different pH of the synthesized exfoliated  $\text{g-C}_3\text{N}_4$ . Reproduced with permission from [18].

The optical properties (PL/UV-Vis) and surface area (BET) of the material have changed with exfoliation; however, the chemical state (XPS), phase (XRD), and the chemical structure (FTIR) remained the same after exfoliation.

### 3.2. Photodegradation Studies

The photodegradation efficiency of exfoliated  $\text{g-C}_3\text{N}_4$  photocatalyst was evaluated under visible light irradiation using  $430\text{ nm}$  wavelength LEDs. The influence of individual

operation parameters, catalyst concentration, phenol concentration, and pH of the solution, in their preselected ranges (Table 1), was examined. For all experiments, an adsorption time of 30 min was used before the light irradiation was started. Moreover, the photolysis experiment was performed to verify the removal of phenol in the absence of the catalyst. Phenol removal with adsorption in the dark and photolysis is insignificant compared to the removal of phenol obtained in the presence of light (Figure 5a). Figure 5a shows the effect of g-C<sub>3</sub>N<sub>4</sub> photocatalyst concentration in the range of 0.1–0.75 g/L on phenol degradation, which increased with the increase in catalyst concentration up to 0.75 g/L because of an increased number of active sites available for the reaction to occur. However, there is no significant increase at >0.5 g/L because an additional increase of the catalyst concentration might cause light scattering and hindrance in light absorption. The effect of phenol concentration on the performance of the catalyst on phenol degradation was examined for three concentrations between 20 and 100 ppm and is shown in Figure 5b. The phenol degradation efficiency decreased as the concentration increased because of the higher number of molecules for adsorption on the available active sites, which hinders the absorption of light. Figure 5c shows the effect of different pH on phenol degradation. Increasing the pH decreases the degradation efficiency of exfoliated g-C<sub>3</sub>N<sub>4</sub>. Note that acidic pH is most favorable for phenol degradation because as per the zeta potential (Figure 3) and the surface charge of the catalyst is positive at an acidic pH, which helps attract OH<sup>-</sup> ions produced in the solution due to dissociation of H<sub>2</sub>O<sub>2</sub> to the surface and improves the degradation efficiency.

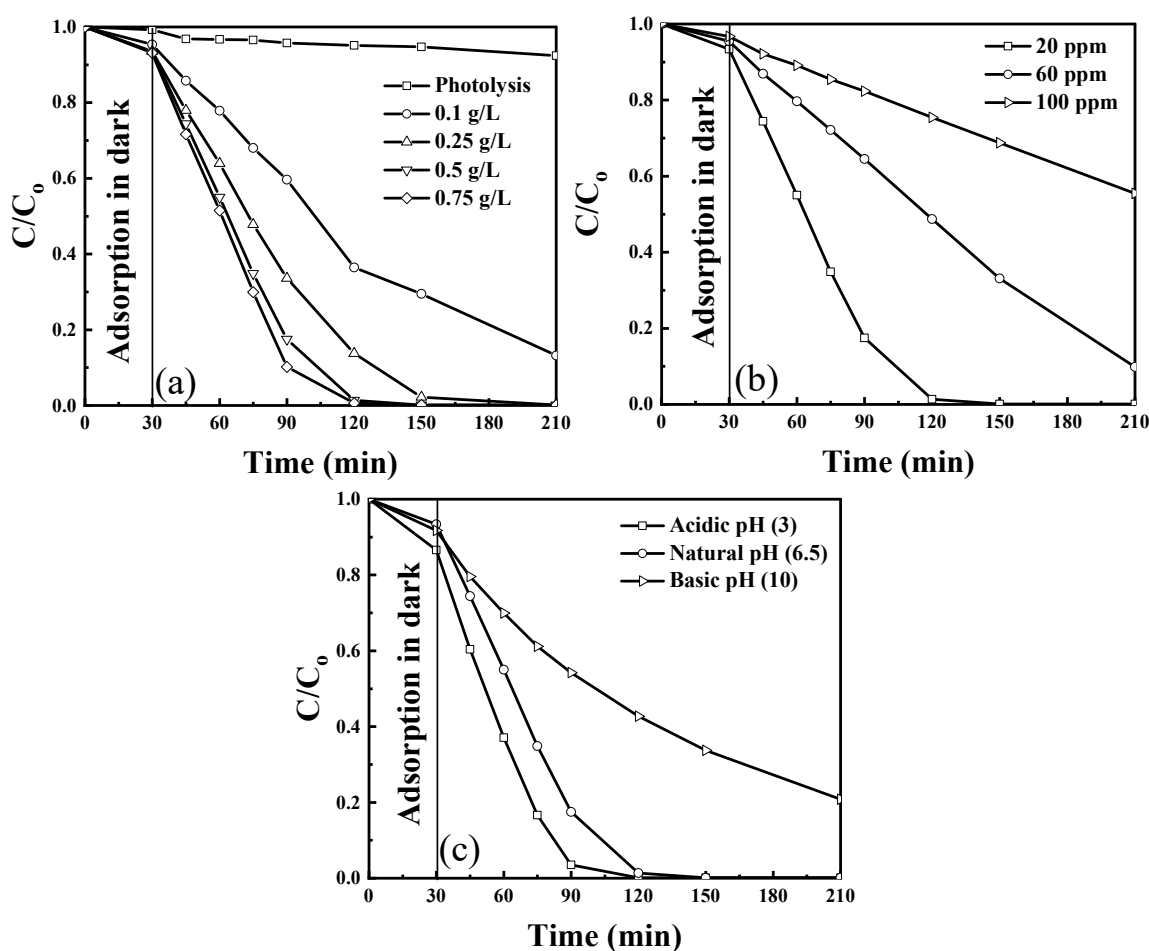


**Figure 5.** Phenol degradation at preselected (a) catalyst concentration (at 20 ppm and natural pH) (b) pollutant concentration (at 0.5 g/L and natural pH), and (c) pH of the solution (at 0.5 g/L and 20 ppm); airflow = 50 mL/min. Reproduced with permission from [18].

### 3.3. Response Surface Methodology

#### 3.3.1. Model Equation

To analyze the combined effect of three variables: catalyst concentration (A), phenol concentration (B), and pH of the solution (C) on the degradation efficiency of phenol (Equation (1)), a three-variable BBD was used in the experimental design for RSM. Table 3 lists the set of performed experiments and the obtained phenol degradation (in 3 h and under an airflow of 50 mL/min).

**Table 3.** Box–Behnken design with experimental and predicted phenol degradation efficiency values with Equation (2).

Run	Experimental Conditions			Phenol Degradation Efficiency (%)	
	Catalyst Concentration (g/L)	Phenol Initial Concentration (ppm)	pH	Experimental	Predicted
1	0.25	100	6.5	43.49	44.23
2	0.50	60	6.5	82.25	85.72
3	0.25	20	6.5	100	93.95
4	0.75	60	3.0	94.09	86.18
5	0.75	20	6.5	100.00	100.00
6	0.50	20	10.0	79.18	74.07
7	0.50	20	3.0	100.00	100.00
8	0.50	60	6.5	84.93	85.72
9	0.25	60	10.0	40.77	43.02
10	0.50	60	6.5	85.94	85.72
11	0.50	100	10.0	24.09	24.35
12	0.50	100	3.0	54.43	54.79
13	0.75	60	10.0	53.15	55.74
14	0.25	60	3.0	70.39	73.46
15	0.50	60	6.5	88.37	85.72
16	0.75	100	6.5	58.31	56.95
17	0.50	60	6.5	87.12	85.72

Experimental data were fitted with four different models: two-factor interaction (2FI), linear, quadratic, and cubic model to obtain regression equations. Three different tests, namely, the sequential model sum of squares, lack of fit, and model summary statistics, were conducted to determine the adequacy of various models; the results are presented in Table 4. The response surface model is then used to select the best model based on the following criterion: the highest-order polynomial with additional significant terms and the model is not aliased (Table 4). The cubic model has the highest polynomial model because there are no sufficient unique design points to independently estimate all terms for that model. The aliased model results in unstable and inaccurate coefficients and graphs. Thus, the aliased model cannot be selected [49,50]. The criteria used in the lack of fit test is the non-significant lack of fit ( $p$ -value > 0.05) based on which a quadratic model is selected. Moreover, multiple summary statistics are calculated to compare models or to confirm the adequacy of the model. These statistics include adjusted  $R^2$ , predicted  $R^2$ , and prediction error sum of squares (PRESS). A good model will have a largely predicted  $r^2$ , and a low PRESS. According to the aforementioned criteria, adjusted  $R^2$  (0.967) and predicted  $R^2$  (0.805) are in reasonable agreement with each other and have a low PRESS. Thus, the quadratic model is finally selected to build the response surface.

**Table 4.** Adequacy of the models tested.

Source	Sum of Squares	Degree of Freedom	Mean Square	F Value	p-Value	Remark
Sequential model sum of squares						
Linear	7118.98	3	2372.99	18.77	<0.0001	-
2FI	109.60	3	36.53	0.238	0.8678	-
Quadratic	1407.83	3	469.27	26.07	0.0004	Suggested
Cubic	104.30	3	34.76	6.41	0.0523	Aliased
Lack of fit tests						
Linear	1621.73	9	180.19	33.22	<0.0021	-
2FI	1512.13	6	252.02	46.46	<0.0012	-
Quadratic	104.29	3	34.76	6.41	0.0523	Suggested
Cubic	0	0	-	-	-	Aliased
Source	Standard deviation	R <sup>2</sup>	Adjusted R <sup>2</sup>	Predicted R <sup>2</sup>	PRESS	-
Model summary statistic						
Linear	11.24	0.8124	0.769	0.694	2678.06	-
2FI	12.38	0.8250	0.720	0.462	4712.53	-
Quadratic	4.24	0.9856	0.967	0.805	1702.70	Suggested
Cubic	2.33	0.9975	0.999	-	-	Aliased

Based on regression coefficients from Table 5, the following empirical second-order polynomial equation was obtained:

$$\begin{aligned} \text{Degradation Efficiency (\%)} &= 85.72 + 6.36 A - 24.86 B - 15.22 C + 3.71 AB - 2.83 AC - 2.38 BC - 5.05 A^2 - 5.22 B^2 \\ &\quad - 16.07 C^2 \end{aligned} \quad (2)$$

where, A, B, and C are the catalyst concentration, phenol concentration, and pH of the solution, respectively.

**Table 5.** Coefficients of the second-order polynomial (quadratic) equation.

Factor	Coefficient Estimate	Degree of Freedom	Standard Error	95% Confidence Interval Low	95% Confidence Interval Low	F Value	p-Value
Intercept	85.72	1	1.90	81.24	90.21	-	-
A	6.36	1	1.50	2.82	9.91	17.99	0.0038
B	-24.86	1	1.50	-28.40	-21.31	274.63	<0.0001
C	-15.22	1	1.50	-18.76	-11.67	102.89	<0.0001
AB	3.71	1	2.12	-1.31	8.72	3.05	0.1242
AC	-2.83	1	2.12	-7.85	2.19	1.78	0.2239
BC	-2.38	1	2.12	-7.40	2.64	1.26	0.2989
A <sup>2</sup>	-5.05	1	2.07	-9.94	-0.16	5.96	0.0446
B <sup>2</sup>	-5.22	1	2.07	-10.11	-0.33	6.38	0.0394
C <sup>2</sup>	-16.07	1	2.07	-20.96	-11.18	60.44	0.0001

The influence of model terms on the degradation of phenol as per p-values (Table 5) is in the following order B < C < C<sup>2</sup> < A < B<sup>2</sup> < A<sup>2</sup> < AB < AC < BC. The mixed interaction terms AB, AC, and BC are not significant because their p-value is > 0.05 and may be removed from Equation (2).

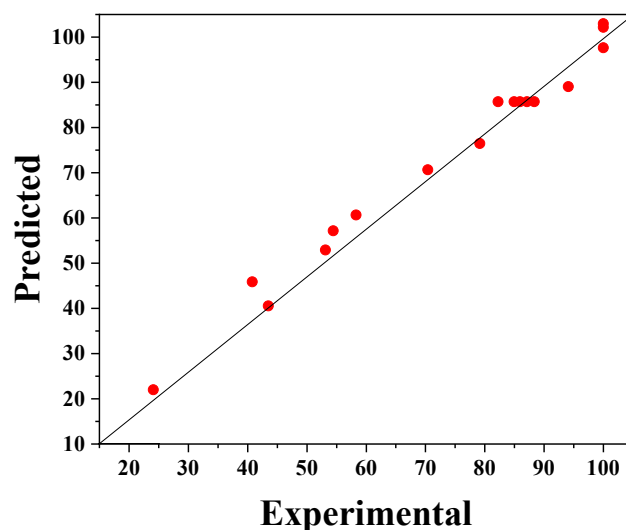
An ANOVA of the second-order polynomial (Equation (2)) for phenol degradation was conducted; the results are shown in Table 6. In statistics, the significance of the model can be confirmed by a large F-value (53.31) and a small p-value (<0.0001). Furthermore, the significance of the model can be confirmed by the lack of fit test. In this study, the lack of fit is not significant because its p-value is >0.05. The accuracy of the model is confirmed by the low coefficient of variation (CV) value of 5.79%. The results showed that the signal-to-noise ratio of 24.89 is adequate.

**Table 6.** Analysis of variance ANOVA of the second-order polynomial (Equation (2)).

Source	Sum of Squares	Degree of Freedom	Mean Square	F Value	p-Value	Remark
Model	8636.42	9	959.60	53.31	<0.0001	Significant
Residual	126.00	7	18.00	-	-	-
Lack of fit	104.30	3	34.77	6.41	0.0523	Not Significant
Pure error	21.70	4	5.42	-	-	-
-	Adjusted $R^2 = 0.967$	Predicted $R^2 = 0.810$	Model precision = 24.89		-	-
-	Std. dev. = 4.24	Mean = 73.32	C.V. % = 5.79	-	-	-

Furthermore, the coefficient of determination  $R^2$  confirmed the fit of the model. For the used model, the value of the predicted  $R^2 = 0.810$  (Table 6) is in agreement with adjusted  $R^2 = 0.967$ , which indicates that the obtained model is significant.

Equation (2) provides a suitable relationship ( $R^2 = 0.810$ ) between the response (degradation efficiency) and the parameters, which can be seen in Figure 6. In this figure, the experimental values of phenol degradation are plotted against the predicted values obtained from the RSM model; these values of the percentage phenol degradation fit well.

**Figure 6.** The experimental phenol degradation efficiency (%) plotted against the predicted values from the RSM model.

### 3.3.2. Interaction Effects of Independent Operating Parameters

Three dimensional (3D) response surface and contour plots were generated using the regression model (Equation (2)) to visualize the influence of the independent operating parameters on phenol degradation; they are presented in Figures 7–9. In surface and contour plots, one parameter is maintained constant at its zero levels, whereas the other two are varied in the studied range reported in Table 1.



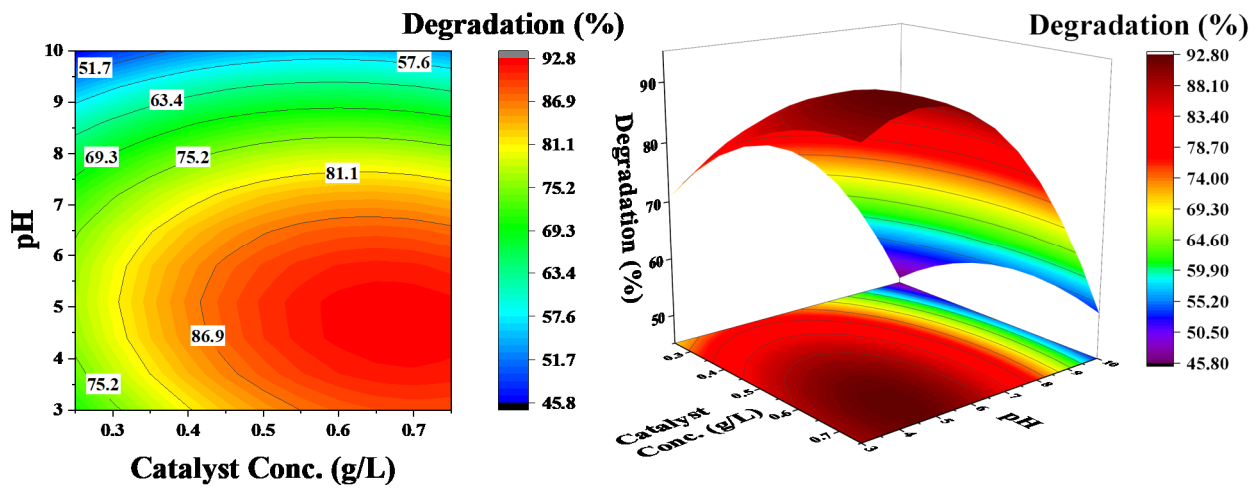


Figure 7. Effect of catalyst concentration and pH on the degradation of phenol: pollutant concentration was kept constant at 60 ppm.

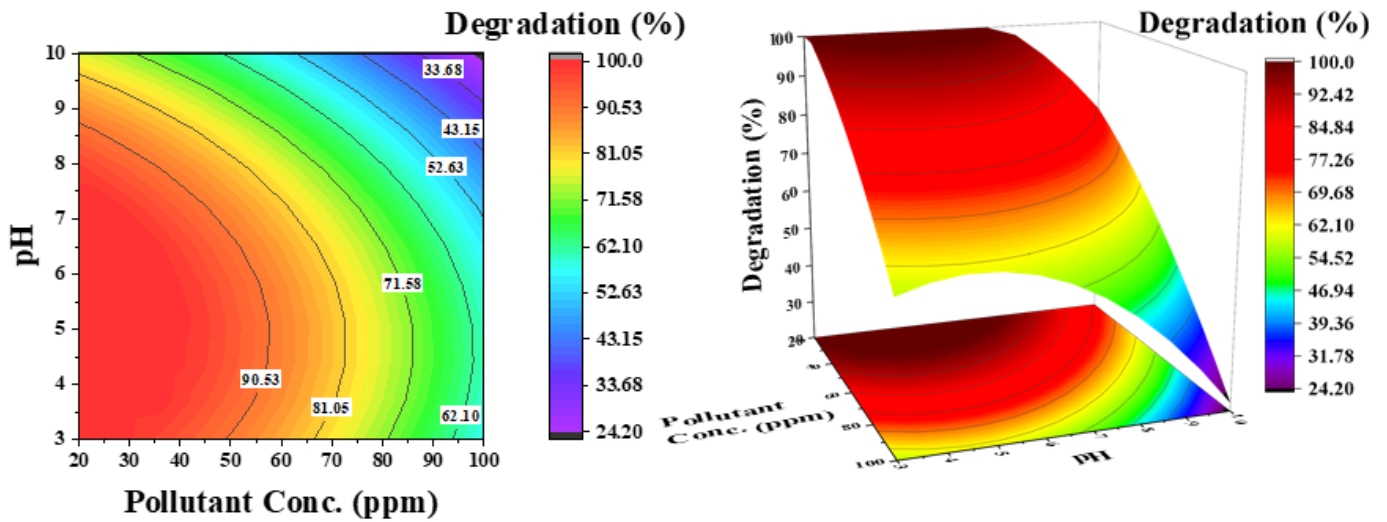


Figure 8. Effect of pollutant concentration and pH on the degradation of phenol: catalyst concentration was kept constant at 0.5 g/L.

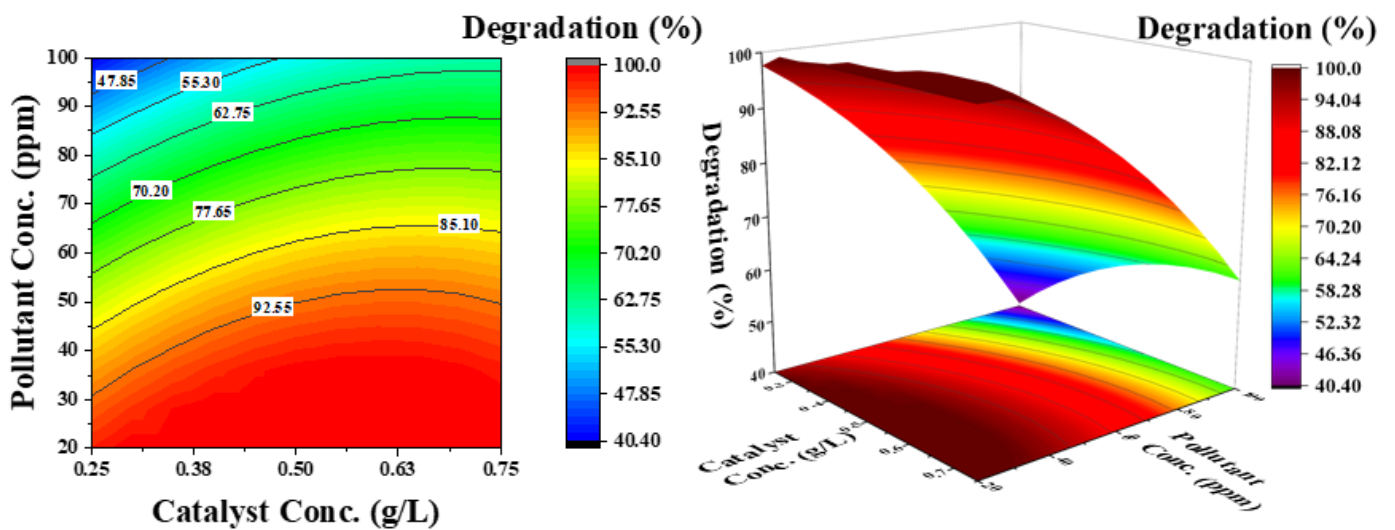


Figure 9. Effect of catalyst concentration and pollutant concentration on the degradation of phenol: pH was kept constant at 6.5.

Figure 7 shows the influence of pH and catalyst concentration on the degradation efficiency of phenol at a constant phenol concentration of 60 ppm. The contour lines show a decrease in the degradation efficiency with an increase in pH; there is no considerable increase in efficiency, even at higher catalyst concentrations. However, an increase in degradation efficiency with a decrease in pH is observed. These results demonstrate that pH has a significant effect on phenol degradation and a low pH favors the degradation process. This phenomenon is linked with the zeta potential of the catalyst surface [18]. There is a positive charge at the surface of the catalyst at an acidic pH (Figure 2), which attracts the  $\text{OH}^-$  ions produced in the solution due to dissociation of  $\text{H}_2\text{O}_2$  and significantly increases the degradation process. However, at a basic pH, the surface charge is negative and there could be electrostatic repulsion that reduces the efficiency of the degradation process.

Figure 8 shows the influence of pH and pollutant concentration on phenol degradation at a constant catalyst concentration of 0.5 g/L. For selecting the catalyst concentration, the effect of initial pollutant concentration is important. The contour lines demonstrate that simultaneously increasing both parameters (pH and phenol concentration) considerably decreases the degradation efficiency of phenol (33%), which is 62% at a low pH. As shown in Figure 5b, at low pH and low pollutant concentration, 100% degradation is achieved in a considered reaction time of 3 h. An increase in degradation efficiency from high to low pH can then be associated with catalyst surface charge. However, a decrease in efficiency at low pH from low to high phenol concentration is attributed to the increased number of pollutant molecules compared with the available active sites.

Figure 9 shows the effect of catalyst concentration and pollutant concentration at a constant pH of 6.5. The contour lines demonstrate that both parameters independently affect the degradation efficiency. By increasing the catalyst concentration at a lower pollutant concentration, phenol degradation increases; however, at a higher pollutant concentration, the degradation efficiency decreases. This can be attributed to the availability of active sites on the catalyst surface for  $\text{OH}^-$  radicals, as well as phenol molecules. The electron-hole pair generated from the catalyst surface improves the degradation rate.

### 3.3.3. Experimental Validation of RSM Model

To demonstrate the applicability of the model, a hypothetical case study for water with a phenol concentration of 50 ppm was considered. The model equation was used to identify the optimum catalyst concentration and pH, leading to maximal phenol degradation in 3 h under an airflow rate of 50 mL/min. According to the model prediction, maximal phenol degradation of 88.62% is achievable using 0.4 g/L of catalyst concentration and operating at a pH of 6.5. To examine the accuracy of the model prediction, an experiment was conducted under these conditions. The experimentally obtained phenol degradation was 83.75%, which is less than a 5% deviation from the predicted value. Thus, the optimum operating point obtained by RSM was successfully confirmed; this suggests that RSM can be a useful tool for optimizing photocatalytic processes. Similarly, the model developed can be used for minimizing the catalyst amount or for maximizing the degradation efficiency of phenols for any set of parameters in range.

## 4. Conclusions

Metal-free  $\text{g-C}_3\text{N}_4$  was used for the photocatalytic degradation of phenol from an aqueous solution. The morphology of the catalyst was confirmed by SEM, and the surface charge was confirmed using zeta potential. Based on zeta potential, the catalyst surface was confirmed to have a positive surface charge under acidic conditions and a negative surface charge under basic conditions; therefore, acidic pH favors the degradation process. A RSM based on the BBD was used to analyze the degradation efficiency of phenol. The influence of experimental parameters, namely, catalyst concentration, pollutant concentration, and pH of the solution, and their interaction at a different level was examined for phenol degradation. An empirical regression quadratic model was developed for the response variable. Analysis of variance (ANOVA) demonstrated that the model is significant with



an insignificant lack of fit and a high coefficient of determination ( $R^2$ ) of 0.96, which can be helpful to navigate the design space. Furthermore, an optimized degradation efficiency of 83.75% was achieved for phenol concentration of 50 ppm, catalyst concentration of 0.4 g/L, and a solution pH of 6.5 pH (in 3 h and under an airflow of 50 mL/min). Thus, the results suggest that the RSM can be used for the optimization of parameters for maximizing the photocatalytic degradation of phenol using g-C<sub>3</sub>N<sub>4</sub> and LEDs.

**Supplementary Materials:** The following are available online at <https://www.mdpi.com/article/10.3390/catal11080898/s1>, Figure S1 N<sub>2</sub> adsorption-desorption isotherms of bulk and exfoliated g-C<sub>3</sub>N<sub>4</sub>. The inset shows the corresponding BJH pore size distribution curves of the sample, Figure S2 (a) UV-Vis absorption spectra and (b) PL spectra of bulk and exfoliated g-C<sub>3</sub>N<sub>4</sub>; insets of (a) showing the Tauc plots, Figure S3 XPS spectra of bulk and exfoliated g-C<sub>3</sub>N<sub>4</sub> C1s, N1s, Figure S4 X-ray diffraction patterns of bulk and exfoliated g-C<sub>3</sub>N<sub>4</sub>.

**Author Contributions:** Conceptualization, A.G.R.; Formal analysis, A.G.R.; Investigation, A.G.R.; Methodology, A.G.R.; Resources, M.M.; Supervision, M.M.; Writing—original draft, A.G.R.; Writing—review and editing, M.M. All authors have read and agreed to the published version of the manuscript.

**Funding:** This research received no external funding.

**Acknowledgments:** A.G.R. acknowledges the financial support from the Higher Education Commission, Pakistan, and Deutscher Akademischer Austauschdienst (DAAD), Germany.

**Conflicts of Interest:** The authors declare no conflict of interest.

## References

1. Zulfiqar, M.; Samsudin, M.F.R.; Sufian, S. Modelling and optimization of photocatalytic degradation of phenol via TiO<sub>2</sub> nanoparticles: An insight into response surface methodology and artificial neural network. *J. Photochem. Photobiol. A Chem.* **2019**, *384*, 112039. [CrossRef]
2. Jourshabani, M.; Shariatnia, Z.; Badiei, A. Facile one-pot synthesis of cerium oxide/sulfur-doped graphitic carbon nitride (g-C<sub>3</sub>N<sub>4</sub>) as efficient nanophotocatalysts under visible light irradiation. *J. Colloid Interface Sci.* **2017**, *507*, 59–73. [CrossRef] [PubMed]
3. Hassani, A.; Eghbali, P.; Metin, O. Sonocatalytic removal of methylene blue from water solution by cobalt ferrite/mesoporous graphitic carbon nitride (CoFe<sub>2</sub>O<sub>4</sub>/mpg-C<sub>3</sub>N<sub>4</sub>) nanocomposites: Response surface methodology approach. *Environ. Sci. Pollut. Res. Int.* **2018**, *25*, 32140–32155. [CrossRef] [PubMed]
4. Mirzaei, A.; Yerushalmi, L.; Chen, Z.; Haghghat, F. Photocatalytic degradation of sulfamethoxazole by hierarchical magnetic ZnO@g-C<sub>3</sub>N<sub>4</sub>: RSM optimization, kinetic study, reaction pathway and toxicity evaluation. *J. Hazard. Mater.* **2018**, *359*, 516–526. [CrossRef]
5. Choquette-Labbé, M.; Shewa, W.; Lalman, J.; Shanmugam, S. Photocatalytic Degradation of Phenol and Phenol Derivatives Using a Nano-TiO<sub>2</sub> Catalyst: Integrating Quantitative and Qualitative Factors Using Response Surface Methodology. *Water* **2014**, *6*, 1785–1806. [CrossRef]
6. Yasar Arafath, K.A.; Baskaralingam, P.; Gopinath, S.; Nilavunesan, D.; Sivanesan, S. Degradation of phenol from retting-pond wastewater using anaerobic sludge reactor integrated with photo catalytic treatment. *Chem. Phys. Lett.* **2019**, *734*, 136727. [CrossRef]
7. Hararah, M.A.; Ibrahim, K.A.; Al-Muhtaseb, A.a.H.; Yousef, R.I.; Abu-Surrah, A.; Qatatsheh, A.a. Removal of phenol from aqueous solutions by adsorption onto polymeric adsorbents. *J. Appl. Polym. Sci.* **2010**, *117*, 1908–1913. [CrossRef]
8. Aslam, Z.; Qaiser, M.; Ali, R.; Abbas, A.; Ihsanullah; Zarin, S. Al<sub>2</sub>O<sub>3</sub>/MnO<sub>2</sub>/CNTs nanocomposite: Synthesis, characterization and phenol adsorption. *Fuller. Nanotub. Carbon Nanostruct.* **2019**, *27*, 591–600. [CrossRef]
9. Huang, C.H.; Liou, R.M.; Chen, S.H.; Hung, M.Y.; Lai, C.L.; Lai, J.Y. Microbial degradation of phenol in a modified three-stage airlift packing-bed reactor. *Water Environ. Res.* **2010**, *82*, 249–258. [CrossRef]
10. Yavuz, Y.; Savas Koparal, A.; Bakir Ögütveren, Ü. Phenol Removal through Chemical Oxidation using Fenton Reagent. *Chem. Eng. Technol.* **2007**, *30*, 583–586. [CrossRef]
11. Asanjarani, N.; Bagtash, M.; Zolgharnein, J. A comparison between Box–Behnken design and artificial neural network: Modeling of removal of Phenol Red from water solutions by nanocobalt hydroxide. *J. Chemom.* **2020**, *34*, e3283. [CrossRef]
12. Peng, H.; Zou, C.; Wang, C.; Tang, W.; Zhou, J. The effective removal of phenol from aqueous solution via adsorption on CS/beta-CD/CTA multicomponent adsorbent and its application for COD degradation of drilling wastewater. *Environ. Sci. Pollut. Res. Int.* **2020**, *27*, 33668–33680. [CrossRef] [PubMed]
13. Chowdhury, P.; Nag, S.; Ray, A.K. Degradation of Phenolic Compounds through UV and Visible-Light-Driven Photocatalysis: Technical and Economic Aspects. In *Phenolic Compounds—Natural Sources, Importance and Applications*; IntechOpen: London, UK, 2017. [CrossRef]

14. Tetteh, E.K.; Rathilal, S.; Naidoo, D.B. Photocatalytic degradation of oily waste and phenol from a local South Africa oil refinery wastewater using response methodology. *Sci. Rep.* **2020**, *10*, 8850. [[CrossRef](#)] [[PubMed](#)]
15. Md Rosli, N.I.; Lam, S.-M.; Sin, J.-C.; Satoshi, I.; Mohamed, A.R. Photocatalytic Performance of ZnO/g-C<sub>3</sub>N<sub>4</sub> for Removal of Phenol under Simulated Sunlight Irradiation. *J. Environ. Eng.* **2018**, *144*, 04017091. [[CrossRef](#)]
16. Rana, A.G.; Ahmad, W.; Al-Matar, A.; Shawabkeh, R.; Aslam, Z. Synthesis and characterization of Cu-Zn/TiO<sub>2</sub> for the photocatalytic conversion of CO<sub>2</sub> to methane. *Environ. Technol.* **2017**, *38*, 1085–1092. [[CrossRef](#)]
17. Lima, M.J.; Silva, A.M.T.; Silva, C.G.; Faria, J.L. Graphitic carbon nitride modified by thermal, chemical and mechanical processes as metal-free photocatalyst for the selective synthesis of benzaldehyde from benzyl alcohol. *J. Catal.* **2017**, *353*, 44–53. [[CrossRef](#)]
18. Rana, A.G.; Tasbihi, M.; Schwarze, M.; Minceva, M. Efficient Advanced Oxidation Process (AOP) for Photocatalytic Contaminant Degradation Using Exfoliated Metal-Free Graphitic Carbon Nitride and Visible Light-Emitting Diodes. *Catalysts* **2021**, *11*, 662. [[CrossRef](#)]
19. Al-Kandari, H.; Abdullah, A.M.; Ahmad, Y.H.; Al-Kandari, S.; AlQaradawi, S.Y.; Mohamed, A.M. An efficient eco advanced oxidation process for phenol mineralization using a 2D/3D nanocomposite photocatalyst and visible light irradiations. *Sci. Rep.* **2017**, *7*, 9898. [[CrossRef](#)] [[PubMed](#)]
20. Moradi, V.; Ahmed, F.; Jun, M.B.G.; Blackburn, A.; Herring, R.A. Acid-treated Fe-doped TiO<sub>2</sub> as a high performance photocatalyst used for degradation of phenol under visible light irradiation. *J. Environ. Sci.* **2019**, *83*, 183–194. [[CrossRef](#)] [[PubMed](#)]
21. Nobijari, L.A.; Schwarze, M.; Tasbihi, M. Photocatalytic Degradation of Phenol Using Photodeposited Pt Nanoparticles on Titania. *J. Nanosci. Nanotechnol.* **2020**, *20*, 1056–1065. [[CrossRef](#)] [[PubMed](#)]
22. Jourshabani, M.; Shariatnia, Z.; Badiie, A. In situ fabrication of SnO<sub>2</sub>/S-doped g-C<sub>3</sub>N<sub>4</sub> nanocomposites and improved visible light driven photodegradation of methylene blue. *J. Mol. Liq.* **2017**, *248*, 688–702. [[CrossRef](#)]
23. Jourshabani, M.; Shariatnia, Z.; Badiie, A. Sulfur-Doped Mesoporous Carbon Nitride Decorated with Cu Particles for Efficient Photocatalytic Degradation under Visible-Light Irradiation. *J. Phys. Chem. C* **2017**, *121*, 19239–19253. [[CrossRef](#)]
24. Jourshabani, M.; Shariatnia, Z.; Badiie, A. Controllable Synthesis of Mesoporous Sulfur-Doped Carbon Nitride Materials for Enhanced Visible Light Photocatalytic Degradation. *Langmuir* **2017**, *33*, 7062–7078. [[CrossRef](#)]
25. Lee, S.C.; Lintang, H.O.; Yuliati, L. A urea precursor to synthesize carbon nitride with mesoporosity for enhanced activity in the photocatalytic removal of phenol. *Chem. Asian J.* **2012**, *7*, 2139–2144. [[CrossRef](#)] [[PubMed](#)]
26. Ren, H.-T.; Jia, S.-Y.; Wu, Y.; Wu, S.-H.; Zhang, T.-H.; Han, X. Improved Photochemical Reactivities of Ag<sub>2</sub>O/g-C<sub>3</sub>N<sub>4</sub> in Phenol Degradation under UV and Visible Light. *Ind. Eng. Chem. Res.* **2014**, *53*, 17645–17653. [[CrossRef](#)]
27. Deng, P.; Gan, M.; Zhang, X.; Li, Z.; Hou, Y. Non-noble-metal Ni nanoparticles modified N-doped g-C<sub>3</sub>N<sub>4</sub> for efficient photocatalytic hydrogen evolution. *Int. J. Hydrogen Energy* **2019**, *44*, 30084–30092. [[CrossRef](#)]
28. Hu, J.Y.; Tian, K.; Jiang, H. Improvement of phenol photodegradation efficiency by a combined g-C<sub>3</sub>N<sub>4</sub>/Fe(III)/persulfate system. *Chemosphere* **2016**, *148*, 34–40. [[CrossRef](#)] [[PubMed](#)]
29. Huang, Z.; Li, F.; Chen, B.; Lu, T.; Yuan, Y.; Yuan, G. Well-dispersed g-C<sub>3</sub>N<sub>4</sub> nanophases in mesoporous silica channels and their catalytic activity for carbon dioxide activation and conversion. *Appl. Catal. B Environ.* **2013**, *136–137*, 269–277. [[CrossRef](#)]
30. Sharma, M.; Vaidya, S.; Ganguli, A.K. Enhanced photocatalytic activity of g-C<sub>3</sub>N<sub>4</sub>-TiO<sub>2</sub> nanocomposites for degradation of Rhodamine B dye. *J. Photochem. Photobiol. A Chem.* **2017**, *335*, 287–293. [[CrossRef](#)]
31. Hernández-Uresti, D.B.; Vázquez, A.; Sanchez-Martinez, D.; Obregón, S. Performance of the polymeric g-C<sub>3</sub>N<sub>4</sub> photocatalyst through the degradation of pharmaceutical pollutants under UV-vis irradiation. *J. Photochem. Photobiol. A Chem.* **2016**, *324*, 47–52. [[CrossRef](#)]
32. Abdullah, A.H.; Moey, H.J.M.; Yusof, N.A. Response surface methodology analysis of the photocatalytic removal of Methylene Blue using bismuth vanadate prepared via polyol route. *J. Environ. Sci.* **2012**, *24*, 1694–1701. [[CrossRef](#)]
33. Song, C.; Li, X.; Wang, L.; Shi, W. Fabrication, Characterization and Response Surface Method (RSM) Optimization for Tetracycline Photodegradation by Bi<sub>3</sub>.84W<sub>0.16</sub>O<sub>6.24</sub>-graphene oxide (BWO-GO). *Sci. Rep.* **2016**, *6*, 37466. [[CrossRef](#)]
34. Wang, J.; Guo, P.; Dou, M.; Wang, J.; Cheng, Y.; Jönsson, P.G.; Zhao, Z. Visible light-driven g-C<sub>3</sub>N<sub>4</sub>/m-Ag<sub>2</sub>Mo<sub>2</sub>O<sub>7</sub> composite photocatalysts: Synthesis, enhanced activity and photocatalytic mechanism. *RSC Adv.* **2014**, *4*, 51008–51015. [[CrossRef](#)]
35. Wang, Y.; Yang, W.; Chen, X.; Wang, J.; Zhu, Y. Photocatalytic activity enhancement of core-shell structure g-C<sub>3</sub>N<sub>4</sub>@TiO<sub>2</sub> via controlled ultrathin g-C<sub>3</sub>N<sub>4</sub> layer. *Appl. Catal. B Environ.* **2018**, *220*, 337–347. [[CrossRef](#)]
36. Yuan, Y.-J.; Shen, Z.; Wu, S.; Su, Y.; Pei, L.; Ji, Z.; Ding, M.; Bai, W.; Chen, Y.; Yu, Z.-T.; et al. Liquid exfoliation of g-C<sub>3</sub>N<sub>4</sub> nanosheets to construct 2D-2D MoS<sub>2</sub>/g-C<sub>3</sub>N<sub>4</sub> photocatalyst for enhanced photocatalytic H<sub>2</sub> production activity. *Appl. Catal. B Environ.* **2019**, *246*, 120–128. [[CrossRef](#)]
37. Muñoz-Batista, M.J.; Rodríguez-Padrón, D.; Puente-Santiago, A.R.; Kubacka, A.; Luque, R.; Fernández-García, M. Sunlight-Driven Hydrogen Production Using an Annular Flow Photoreactor and g-C<sub>3</sub>N<sub>4</sub>-Based Catalysts. *ChemPhotoChem* **2018**, *2*, 870–877. [[CrossRef](#)]
38. Yuan, X.; Zhou, C.; Jin, Y.; Jing, Q.; Yang, Y.; Shen, X.; Tang, Q.; Mu, Y.; Du, A.K. Facile synthesis of 3D porous thermally exfoliated g-C<sub>3</sub>N<sub>4</sub> nanosheet with enhanced photocatalytic degradation of organic dye. *J. Colloid Interface Sci.* **2016**, *468*, 211–219. [[CrossRef](#)]
39. Xu, J.; Zhang, L.; Shi, R.; Zhu, Y. Chemical exfoliation of graphitic carbon nitride for efficient heterogeneous photocatalysis. *J. Mater. Chem. A* **2013**, *1*, 14766–14772. [[CrossRef](#)]
40. Li, Y.; Wang, M.-Q.; Bao, S.-J.; Lu, S.; Xu, M.; Long, D.; Pu, S. Tuning and thermal exfoliation graphene-like carbon nitride nanosheets for superior photocatalytic activity. *Ceram. Int.* **2016**, *42*, 18521–18528. [[CrossRef](#)]

41. Yang, L.; Liu, X.; Liu, Z.; Wang, C.; Liu, G.; Li, Q.; Feng, X. Enhanced photocatalytic activity of g-C<sub>3</sub>N<sub>4</sub> 2D nanosheets through thermal exfoliation using dicyandiamide as precursor. *Ceram. Int.* **2018**, *44*, 20613–20619. [[CrossRef](#)]
42. Papailias, I.; Giannakopoulou, T.; Todorova, N.; Demotikali, D.; Vaimakis, T.; Trapalis, C. Effect of processing temperature on structure and photocatalytic properties of g-C<sub>3</sub>N<sub>4</sub>. *Appl. Surf. Sci.* **2015**, *358*, 278–286. [[CrossRef](#)]
43. Yu, B.; Meng, F.; Khan, M.W.; Qin, R.; Liu, X. Facile synthesis of AgNPs modified TiO<sub>2</sub>@g-C<sub>3</sub>N<sub>4</sub> heterojunction composites with enhanced photocatalytic activity under simulated sunlight. *Mater. Res. Bull.* **2020**, *121*, 110641. [[CrossRef](#)]
44. Yang, Y.; Lei, W.; Xu, Y.; Zhou, T.; Xia, M.; Hao, Q. Determination of trace uric acid in serum using porous graphitic carbon nitride (g-C<sub>3</sub>N<sub>4</sub>) as a fluorescent probe. *Microchim. Acta* **2017**, *185*, 39. [[CrossRef](#)] [[PubMed](#)]
45. Dong, F.; Wang, Z.; Sun, Y.; Ho, W.K.; Zhang, H. Engineering the nanoarchitecture and texture of polymeric carbon nitride semiconductor for enhanced visible light photocatalytic activity. *J. Colloid Interface Sci.* **2013**, *401*, 70–79. [[CrossRef](#)] [[PubMed](#)]
46. Sturini, M.; Speltini, A.; Maraschi, F.; Vinci, G.; Profumo, A.; Pretali, L.; Albini, A.; Malavasi, L. g-C<sub>3</sub>N<sub>4</sub>-promoted degradation of ofloxacin antibiotic in natural waters under simulated sunlight. *Environ. Sci. Pollut. Res. Int.* **2017**, *24*, 4153–4161. [[CrossRef](#)] [[PubMed](#)]
47. Zhu, B.; Xia, P.; Ho, W.; Yu, J. Isoelectric point and adsorption activity of porous g-C<sub>3</sub>N<sub>4</sub>. *Appl. Surf. Sci.* **2015**, *344*, 188–195. [[CrossRef](#)]
48. Praus, P.; Svoboda, L.; Dvorský, R.; Reli, M. Nanocomposites of SnO<sub>2</sub> and g-C<sub>3</sub>N<sub>4</sub>: Preparation, characterization and photocatalysis under visible LED irradiation. *Ceram. Int.* **2018**, *44*, 3837–3846. [[CrossRef](#)]
49. Kumar, M.; Ponselvan, F.I.; Malviya, J.R.; Srivastava, V.C.; Mall, I.D. Treatment of bio-digester effluent by electrocoagulation using iron electrodes. *J. Hazard. Mater.* **2009**, *165*, 345–352. [[CrossRef](#)] [[PubMed](#)]
50. Liu, J.; Wang, J.; Leung, C.; Gao, F. A Multi-Parameter Optimization Model for the Evaluation of Shale Gas Recovery Enhancement. *Energies* **2018**, *11*, 654. [[CrossRef](#)]

## 5 Overall discussion

This thesis fulfills three objectives: (1) to study the effects of various physical and chemical modifications on the properties (structural, optical, surface, morphological) and efficiency of the semiconductor g-C<sub>3</sub>N<sub>4</sub> in catalyzing redox reactions, i.e., pollutant degradation (oxidation reaction) and hydrogen production from water (reduction reaction); (2) to understand the effect of the light source on the photocatalytic efficiency of the g-C<sub>3</sub>N<sub>4</sub>; and (3) to investigate and analyze a photocatalytic reaction using the response surface methodology. The results of four papers, as summarized in section 4, are discussed below. The discussion is focused on the selection of g-C<sub>3</sub>N<sub>4</sub>, and the impact of modifications on the catalytic activity of g-C<sub>3</sub>N<sub>4</sub>. Additionally, the photocatalytic efficiency is explained under different operating conditions (for instance, catalyst concentration, pollutant concentration, oxygen, pH). The re-usability of the catalyst is discussed, along with the applications for which the catalyst can be used. Optimization and modeling of the photocatalytic process, using the response surface methodology, are presented.

### 5.1 Impact of g-C<sub>3</sub>N<sub>4</sub> modifications on its photocatalytic activity

Photocatalysis is the acceleration of a photoreaction in the presence of a catalyst that can absorb light. The photocatalytic activity depends on the ability of the catalyst to create electron-hole pairs and generate free radicals, such as, the hydroxyl radical, which can undergo secondary reactions. The current thesis used photocatalysis to perform two applications: degradation of various pollutants (oxidation reaction), and hydrogen production from water splitting (reduction reaction). In general, photocatalysts should have specific properties to efficiently carry out different reactions, and the photocatalyst should be catalytically active via light irradiation. Photoinduced reactions are, in principle, initiated via the absorption of photons that lead to excitation of electrons in the material, followed by an electron transfer from/to a reaction substrate. The catalytic activity of the photocatalyst depends on several material properties, such as light absorption, crystallinity, porosity, and the presence of additional components acting as co-catalysts. Concerning light harvesting, the optimal photocatalyst should efficiently absorb over the entire wavelength range of the solar spectrum. However, this property has not yet been achieved. In fact, TiO<sub>2</sub> and other common semiconductors only absorb a negligible amount of solar energy directly.

g-C<sub>3</sub>N<sub>4</sub> is a photocatalytic material with a graphite-like layered structure with excellent electron/hole transporting ability, high thermal and chemical stability, and a relatively low bandgap (2.7–2.8 eV). The bandgap of g-C<sub>3</sub>N<sub>4</sub> permits a strong light absorption in the visible light region (400–450 nm). Furthermore, the structure and properties of g-C<sub>3</sub>N<sub>4</sub> are easy to control. Different precursors, such as dicyandiamide, melamine, urea, and thiourea, can be used to synthesize the g-C<sub>3</sub>N<sub>4</sub>. In this work, g-C<sub>3</sub>N<sub>4</sub> was chosen due to its photocatalytic activity

in the visible light range, and melamine was utilized as the precursor. This is since, during the synthesis process, the melamine precursor yield was 50% compared to urea (5%), as reported in the literature.

Photocatalysis has the advantages of mild reaction conditions, high efficiency, and a wide application range. However, photocatalytic reactions also suffer certain drawbacks in practical applications, due to several properties of the photocatalysts, such as narrow absorption spectra, low surface area, low photon quantum efficiency, and easy recombination of electrons and holes. Bulk g-C<sub>3</sub>N<sub>4</sub> has similar limitations that result in the low activity for photocatalytic reactions. Different modification techniques, i.e., exfoliation, co-catalyst addition, and doping of metal and non-metals, can overcome and minimize these limitations, as well as enhance the catalytic efficiency of the g-C<sub>3</sub>N<sub>4</sub>.

Exfoliation is a process that comprises various methods for delaminating layered materials into nanosheets. A classic example is graphene synthesis, a single layer of graphite. Exfoliation can be carried out thermally, ultrasonically, mechanically, and in the liquid phase. In this thesis (papers I, III, and IV), thermal exfoliation was used as it provided a convenient way to enhance the surface area, introduce pores, and tune the texture of the material. Exfoliation of bulk g-C<sub>3</sub>N<sub>4</sub> produced from melamine increased the surface area of g-C<sub>3</sub>N<sub>4</sub> from 10 m<sup>2</sup>/g to 170 m<sup>2</sup>/g. Compared to the past studies, thermal exfoliation showed a higher yield than ultrasonic exfoliation [77]. Thermal exfoliation also provided a rapid and straightforward way to delaminate the material from 3D to 2D nanosheets g-C<sub>3</sub>N<sub>4</sub>. Compared to bulk g-C<sub>3</sub>N<sub>4</sub>, the obtained nanosheets demonstrated improved electron migration, surface area, morphology, a higher lifetime of charge carriers, and a decreased recombination rate of the photo-generated electrons and holes. All these changes enhanced the photocatalytic performance of exfoliated g-C<sub>3</sub>N<sub>4</sub> compared to the bulk material. In paper I, for the identical operating conditions, phenol degradation was improved from 40% in 180 min for bulk g-C<sub>3</sub>N<sub>4</sub> to 100% in just 90 min for the exfoliated g-C<sub>3</sub>N<sub>4</sub>. Exfoliated g-C<sub>3</sub>N<sub>4</sub> increased the efficiency of the process, and reduced the time required to degrade phenol completely.

Introducing either metal or non-metal impurities via doping is one of the most common and effective methods for improving the semiconductor performance. Doping can help increase the concentration of semiconductor carriers, reduce the recombination of electron-hole pairs, and generate traps to capture electrons and holes. In addition, it causes redshift, extending the photo response of the photocatalyst to a longer wavelength region. According to the types of dopants, doping can be classified into either metal-, non-metal-, and metal/non-metal simultaneous doping.

Several research groups have focused on non-metal doping that generates covalent bonds. The non-metal doping has an advantage over metal doping, since it is cost-effective,

environmentally friendly, and does not act as a recombination center. In paper II, S, P, and O were doped on bulk g-C<sub>3</sub>N<sub>4</sub> using acid-functionalization of the melamine. When heated for synthesis, the sulfur functionalized melamine produced a porous g-C<sub>3</sub>N<sub>4</sub>, since sulfur evaporates and leaves pores in the structure, while phosphorus is not removed rapidly. XPS also confirmed this hypothesis, which shows a high amount of phosphorus compared to sulfur with the same initial amount. Acid-functionalization gave a rapid, single-step protocol, compared to the literature, for doping non-metal on the surface of g-C<sub>3</sub>N<sub>4</sub>. The non-metal doping facilitated an increase in the surface area and narrowed down the bandgap of the g-C<sub>3</sub>N<sub>4</sub>, which led to increased activity of the g-C<sub>3</sub>N<sub>4</sub> towards hormone removal (paper II).

The metal doping method dopes metal in the catalyst by high temperature firing or via auxiliary deposition. Metal doping usually suppresses the recombination rate of electrons and holes and expands the response spectrum range of the photocatalyst. However, the incorporated metals sometimes evolve to act as recombination centers of electrons and holes, affecting the photocatalytic effect. The doping and dopant concentration can influence the photocatalysis experiment to diverse extents. In paper III, distinct metals (Ni, Co, and Cu) were loaded on the surface of the exfoliated g-C<sub>3</sub>N<sub>4</sub>. It was shown that doping increased the hydrogen production rate by multiple folds. In addition, metal loading decreased the surface area of the material due to the pore blockage of the exfoliated g-C<sub>3</sub>N<sub>4</sub>. The influence on the catalytic efficiency of the material was largely dependent on the particular metal. For instance, Ni-loaded exfoliated g-C<sub>3</sub>N<sub>4</sub> performed the best among other materials for hydrogen production.

Several strategies for doping metals and non-metals on the surface of g-C<sub>3</sub>N<sub>4</sub> have been reported by past studies. The synthesis method can affect the surface, optical, morphological, and chemical properties, including the catalytic efficiency of the material. In paper III, Ni-doped exfoliated g-C<sub>3</sub>N<sub>4</sub> was synthesized using incipient wet impregnation, precipitation deposition, and colloidal methods. For this type of catalyst, the catalyst synthesized using the colloidal method, performed best for hydrogen production. The colloidal method has an *in-situ* reduction mechanism that helps to reduce the metal salt and produce metal nanoparticles on the surface of the exfoliated g-C<sub>3</sub>N<sub>4</sub>. TEM and XPS characterizations confirmed this hypothesis since these characterizations confirmed the presence of the nanoparticle on the surface of the material. Nanoparticle synthesis can be achieved via several reduction methods that can reduce the metal on the surface of the catalyst, for instance, thermal treatment in H<sub>2</sub>. The thermal treatment can decompose the carbon base catalyst and supplement an additional heating step to the process post-synthesis, thereby increasing the process-related expenses.

## **5.2 Influence of operating conditions on the performance of g-C<sub>3</sub>N<sub>4</sub>**

The operating conditions, i.e., catalyst and pollutant concentration, pH of the reaction medium, oxygen concentration, and light source, are some of the key parameters that affect the

performance of g-C<sub>3</sub>N<sub>4</sub> during reactions. Paper I studied the effects of different parameters on the reaction kinetics and catalytic efficiency of the exfoliated g-C<sub>3</sub>N<sub>4</sub>. In general, an increase in catalyst concentration increases the performance of the catalytic process. Nevertheless, after a threshold catalyst concentration, a subsequent increase may downgrade the catalyst performance via hindrance and scattering of the light. Increasing the pollutant concentration decreases the performance of the catalytic process, attributing to the presence of more pollutant molecules towards the accessible active sites. The pH of the reaction medium also affects the process. For instance, while for an oxidation application, acidic pH favors the catalytic efficiency of g-C<sub>3</sub>N<sub>4</sub> due to the positive surface charge, the acidic pH might be counterproductive for a reduction application. In addition, light sources significantly affect the process efficiency. For instance, for g-C<sub>3</sub>N<sub>4</sub>, two lamps (xenon lamp and LED lamp) were tested. The single wavelength LED lamp at 430 nm showed a better degradation efficiency relative to a xenon full spectrum lamp. As confirmed via PL spectroscopy, g-C<sub>3</sub>N<sub>4</sub> demonstrated the maximum absorption at the same wavelength (430 nm), at which the single wavelength LED lamp irradiated the light. Even though the xenon lamp irradiated light at 430 nm, the irradiation intensity at 430 nm showed a lower magnitude compared to the LED lamp. Therefore, the LED lamps achieved a better degradation efficiency of g-C<sub>3</sub>N<sub>4</sub> than the xenon lamp. Practically, phenol was degraded only by 20% for the xenon lamp in 180 minutes, compared to a total degradation with an LED lamp in 90 minutes. For oxidation applications, oxygen plays an essential role in forming ROS, which are used in the reactions to degrade pollutants. Additionally, the presence and absence of oxygen in the reaction medium, were also studied in paper I. It was shown that phenol degraded only by 50% without external oxygen in 180 min, compared to a total degradation in the presence of oxygen in 90 min.

In Paper III, the effect of catalyst exposure to the reaction medium was investigated for hydrogen production from water. The catalyst was exposed to the reaction medium in suspension and was immobilized. It was observed that the suspended catalyst produced a better efficiency than the immobilized catalyst on the surface of the filter paper. The catalyst surface was lost with immobilization on the surface of the filter paper, due to which, less hydrogen was produced. The suspended catalyst (440  $\mu\text{mol m}^{-2} \text{g}^{-1}$  hydrogen) performed better than the immobilized catalyst (236  $\mu\text{mol m}^{-2} \text{g}^{-1}$  hydrogen), with around 50% of activity loss. However, immobilization can be beneficial towards scale-up and industrial applications.

In papers I, II, and III, the stability of the catalyst was investigated. The catalysts used in photocatalytic experiments can also be reused, considering that these catalysts are stable. It was shown that g-C<sub>3</sub>N<sub>4</sub> is in fact a very stable catalyst that can be reused after washing for at least 3 cycles. The reused catalyst demonstrated an identical efficiency, while the structure of the material remained unaltered. In all cycles, the reused g-C<sub>3</sub>N<sub>4</sub> showed the same activity in papers I and II. The catalytic activity of the reused catalyst increased slightly with each cycle

in paper III via *in situ* photoreduction of the catalyst during the reaction. Due to photoreduction, the metal on the surface of the catalyst gets reduced to the nanoparticle, which helps achieve higher hydrogen production.

Exfoliated g-C<sub>3</sub>N<sub>4</sub> has been used recently for many oxidation and reduction applications. The current thesis used exfoliated and modified g-C<sub>3</sub>N<sub>4</sub> for water pollutant degradation (oxidation process) and hydrogen production from water splitting (reduction process). Both these processes were characterized by different reaction conditions and were affected by the surface charge of g-C<sub>3</sub>N<sub>4</sub>. In paper I, the photooxidation of phenol was carried out, and exfoliated g-C<sub>3</sub>N<sub>4</sub> successfully degraded the phenol. The oxidation reactions were carried out due to ROS produced during the reaction, and g-C<sub>3</sub>N<sub>4</sub>, due to its positive charge, offered a favorable condition towards organic pollutant degradation. In paper II, the non-metallic doped g-C<sub>3</sub>N<sub>4</sub> was used to remove and degrade the hormones. The removal of hormones from the water was achieved via adsorption and photodegradation. The high surface area of the catalyst and hydrophobicity of the pollutant facilitated a rapid elimination via adsorption. Additionally, the surface area was an assisting factor during photodegradation, along with a narrow bandgap. Oxygen facilitated ROS generation, which enhanced the oxidative degradation of the organic pollutants. In paper III, the metal-doped g-C<sub>3</sub>N<sub>4</sub> was used for the photoreduction of water to produce hydrogen. The water splitting experiments were conducted without oxygen, in order to avoid the oxidation of the generated hydrogen back into the water. Since holes are suitable for oxidation, hole scavengers are indispensable during water splitting. While g-C<sub>3</sub>N<sub>4</sub> could not reduce the water into hydrogen, non-noble metal doping successfully reduced water with g-C<sub>3</sub>N<sub>4</sub>.

### **5.3 Selection of photocatalytic reaction operating parameters by response surface methodology**

Numerous operating parameters affect photocatalytic reactions. If the experiments are designed systematically, the influence of these operating parameters on the response variable can be better studied. The systematic design approach can help reduce the experiments with the maximum interaction of the operating parameters, saving time and catalyst compared to a simple trial and error approach. In paper IV, the RSM, combined with the DoE, was used to model phenol degradation with g-C<sub>3</sub>N<sub>4</sub>. CCD and BBD are commonly used methods for designing experiments. For the same number of parameters, BBD requires fewer experiments than CCD.

Consequently, BBD was selected as the preferred design approach in paper IV. Three parameters, namely the catalyst- and pollutant concentration, and the surface pH, affecting the photocatalytic degradation of phenol, were selected, including the degradation efficiency as the response variable. An empirical regression quadratic model was derived to relate the



phenol degradation efficiency with these three parameters. ANOVA demonstrated that the model is significant with an insignificant lack of fit and a high coefficient of determination ( $R^2$ ). The statistical analysis showed that the pollutant concentration is a major factor affecting phenol degradation, within the studied range of the operating parameters. RSM showed a significant correlation between the predicted and experimental values of phenol degradation. The model predicted a 88.62% degradation efficiency for 50 ppm phenol solution, 0.4 g L<sup>-1</sup> catalyst concentration, and a solution pH of 6.5. The model proved accurate with a 5% deviation, while achieving 83.75% of phenol degradation.

## 6 Conclusion

The current thesis focused on and explored g-C<sub>3</sub>N<sub>4</sub> modifications, and the principal outcomes of the investigations are published in 4 peer-reviewed papers. In this section, the conclusions of these papers are summarized.

In paper I, to the best of knowledge, a comparative study of two lamps was presented for g-C<sub>3</sub>N<sub>4</sub> catalyzed phenol degradation, for the first time. A parametric study was carried out to investigate the effects of operating parameters on the degradation of phenol using g-C<sub>3</sub>N<sub>4</sub>. It was concluded that the exfoliation improved the properties of the material and assisted in the degradation of phenol. The positive surface charge of g-C<sub>3</sub>N<sub>4</sub> during acidic pH facilitated the degradation process, while enhancing the catalytic efficiency. Oxygen concentration in the system was observed to be necessary for the degradation process, as oxygen produces ROS that take part in the reaction. The comparative study of two lamps showed that g-C<sub>3</sub>N<sub>4</sub> performed much better using a single wavelength LED than a xenon lamp.

Paper II studied the effects of non-metal (oxygen, sulfur, and phosphorous) doping on the activity of g-C<sub>3</sub>N<sub>4</sub>. The modified g-C<sub>3</sub>N<sub>4</sub> was studied for the photodegradation of endocrine-disrupting hormones (17 $\beta$ -estradiol and 17 $\alpha$ -ethinylestradiol). This work used a rapid, one-step protocol for the non-metallic doping of g-C<sub>3</sub>N<sub>4</sub> using acid-functionalized melamine for sulfur, oxygen, and phosphorous doped g-C<sub>3</sub>N<sub>4</sub>. It was concluded that non-metal doping of g-C<sub>3</sub>N<sub>4</sub> modified its energy bandgap and increased the surface area. Sulfur-doped g-C<sub>3</sub>N<sub>4</sub> performed better than the phosphorous and oxygen-doped g-C<sub>3</sub>N<sub>4</sub>. Sulfur-doped g-C<sub>3</sub>N<sub>4</sub> exhibited the highest photocatalytic activity toward the studied hormones, due to its higher BET surface area and lower energy bandgap.

Paper III studied the effects of non-noble metal loading on g-C<sub>3</sub>N<sub>4</sub> for hydrogen production using water splitting. Nickel, cobalt, and copper were loaded on exfoliated g-C<sub>3</sub>N<sub>4</sub>, and used for hydrogen production from water splitting. It was concluded that nickel-loaded g-C<sub>3</sub>N<sub>4</sub> produced more hydrogen than other exfoliated g-C<sub>3</sub>N<sub>4</sub>. In addition, three synthesis methods, i.e., incipient wet impregnation, precipitation deposition, and colloidal, were used for loading Ni on the surface of g-C<sub>3</sub>N<sub>4</sub>. For hydrogen production, nickel-loaded exfoliated g-C<sub>3</sub>N<sub>4</sub> synthesized using the colloidal method, was observed to be the best. The *in-situ* reduction in the colloidal method assisted the reduction of nickel, and this hypothesis was confirmed by TEM and XPS. For hydrogen production, the nickel nanoparticle formation during the colloidal method, was inferred to be the reason for the best photoactivity.

In paper IV, a study was conducted to model the photocatalytic degradation reaction, using the DoE combined with the RSM. An empirical regression quadratic model was developed, which can be used to select the suitable operating parameters for the desired degradation. Three experimental parameters, namely, catalyst concentration, pollutant concentration, and solution

pH, were considered for the phenol degradation efficiency, which was the response variable. The results suggest that the RSM can be used to optimize the operating parameters, for maximizing the photocatalytic degradation of phenol, using g-C<sub>3</sub>N<sub>4</sub> and LEDs. Similarly, the developed model can minimize the catalyst amount, or maximize the degradation efficiency of phenol, for any set of in-range parameters.

In conclusion, the physical and chemical modifications of g-C<sub>3</sub>N<sub>4</sub> improved its structural, surface, optical, and morphological properties, resulting in an enhanced catalytic performance for redox applications. Furthermore, g-C<sub>3</sub>N<sub>4</sub> performed better under the influence of the single wavelength visible light LED lamp, in relation to the full spectrum xenon lamp. Finally, DoE combined with RSM can be used to select the suitable operating parameter for the desired degradation.

## 7 Outlook

Based on 4 years of experimental work on this topic, and the obtained experimental results, the following suggestions can be proposed for further work:

1. The current thesis employed the batch glass reactor for photocatalytic degradation experiments. Micro- and continuous reactors possess an extraordinary potential for experimentation purposes. The micro-reactors can facilitate the high-throughput screening of the catalyst. However, there are chances of air entrapment during the immobilization of the catalyst at the reactor surface, which may affect the catalytic activity. The continuous reactors can help process a large quantity of wastewater at industrial scales.
2. The metal-free exfoliated g-C<sub>3</sub>N<sub>4</sub> was synthesized from bulk g-C<sub>3</sub>N<sub>4</sub> derived from melamine via thermal exfoliation. It effectively removed the phenol from the wastewater to a level below the safe limit for potable water. Other precursors, such as a mixture of urea and melamine, can be investigated to explore their effects on the morphology, surface area, and absorption of g-C<sub>3</sub>N<sub>4</sub>. Since both these precursors produce different yields and properties of the final product, combining both precursors might reveal a novel characteristic of g-C<sub>3</sub>N<sub>4</sub>. Combining two or more exfoliation techniques can be tested for better and enhanced exfoliation and catalytic performances. The metal-free g-C<sub>3</sub>N<sub>4</sub> may be tested for degradation of other toxic, emerging pollutants from the pharmaceutical industry or volatile organic compounds (VOCs).
3. The g-C<sub>3</sub>N<sub>4</sub> was modified using the doping method. However, synthesizing composites of metal-organic frameworks (MOFs), covalent organic frameworks (COFs), and perovskites with undoped and doped g-C<sub>3</sub>N<sub>4</sub> can subsequently be explored. Attributing to the fact that MOFs/COFs are relatively new materials with higher surface areas, the catalytic activity may be enhanced if nanocomposites are fabricated with g-C<sub>3</sub>N<sub>4</sub>.
4. The photocatalytic system was successfully modeled using RSM, and an empirical equation was derived from the experimental data. This methodology should be used more often to save catalysts and experimental time.
5. The non-noble metals (Ni, Cu, Co) were doped on g-C<sub>3</sub>N<sub>4</sub> for hydrogen production. The doping of non-transition metals should be explored to help resource inexpensive and hole scavenger-free alternatives for hydrogen production.
6. Different *in situ* spectroscopic techniques (FTIR, TGA, XAS, TRPL) can be used to understand the synthesis process of g-C<sub>3</sub>N<sub>4</sub>, and its effects on the properties of the final product. These investigations may disclose novel features to comprehend and interpret the structure and properties (surface and chemical) of the material, and its impact on the catalytic performance. Consequently, it may also facilitate the design and development of high-performance metal-free and metal-doped novel photocatalysts.

## 8 References

1. Bi, G., et al., *Efficient visible-light photocatalytic H<sub>2</sub> evolution over metal-free g-C<sub>3</sub>N<sub>4</sub> co-modified with robust acetylene black and Ni(OH)<sub>2</sub> as dual co-catalysts*. RSC Advances, 2016. **6**(37): p. 31497-31506.
2. Sordello, F. and C. Minero, *Photocatalytic hydrogen production on Pt-loaded TiO<sub>2</sub> inverse opals*. Applied Catalysis B: Environmental, 2015. **163**: p. 452-458.
3. Sun, C., et al., *Enhanced activity of visible-light photocatalytic H<sub>2</sub> evolution of sulfur-doped g-C<sub>3</sub>N<sub>4</sub> photocatalyst via nanoparticle metal Ni as cocatalyst*. Applied Catalysis B: Environmental, 2018. **235**: p. 66-74.
4. Liu, J., et al., *Oriented nanostructures for energy conversion and storage*. ChemSusChem, 2008. **1**(8-9): p. 676-97.
5. Nasir, M.S., et al., *Recent development in graphitic carbon nitride based photocatalysis for hydrogen generation*. Applied Catalysis B: Environmental, 2019. **257**.
6. Ameta, R., et al., *Chapter 6 - Photocatalysis*, in *Advanced Oxidation Processes for Waste Water Treatment*, S.C. Ameta and R. Ameta, Editors. 2018, Academic Press. p. 135-175.
7. KwarciaK-Kozłowska, A., *7 - Removal of pharmaceuticals and personal care products by ozonation, advance oxidation processes, and membrane separation*, in *Pharmaceuticals and Personal Care Products: Waste Management and Treatment Technology*, M.N.V. Prasad, M. Vithanage, and A. Kapley, Editors. 2019, Butterworth-Heinemann. p. 151-171.
8. Yang, X. and D. Wang, *Photocatalysis: From Fundamental Principles to Materials and Applications*. ACS Applied Energy Materials, 2018. **1**(12): p. 6657-6693.
9. Xu, Y.-J., *Promises and Challenges in Photocatalysis*. Frontiers in Catalysis, 2021. **1**.
10. Zhu, S. and D. Wang, *Photocatalysis: Basic Principles, Diverse Forms of Implementations and Emerging Scientific Opportunities*. Advanced Energy Materials, 2017. **7**(23): p. 1700841.
11. Gusain, R., et al., *Adsorptive removal and photocatalytic degradation of organic pollutants using metal oxides and their composites: A comprehensive review*. Advances in Colloid and Interface Science, 2019. **272**: p. 102009.

12. Das, S. and A. Chowdhury, *Recent advancements of g-C<sub>3</sub>N<sub>4</sub>-based magnetic photocatalysts towards the degradation of organic pollutants: a review*. *Nanotechnology*, 2021. **33**(7).
13. Bhatnagar, A. and A.K. Jain, *A comparative adsorption study with different industrial wastes as adsorbents for the removal of cationic dyes from water*. *Journal of Colloid and Interface Science*, 2005. **281**(1): p. 49-55.
14. Fawzi Suleiman Khasawneh, O. and P. Palaniandy, *Removal of organic pollutants from water by Fe<sub>2</sub>O<sub>3</sub>/TiO<sub>2</sub> based photocatalytic degradation: A review*. *Environmental Technology & Innovation*, 2021. **21**.
15. Isik, Z., et al., *Entrapment of TiO<sub>2</sub> and ZnO powders in alginate beads: Photocatalytic and reuse efficiencies for dye solutions and toxicity effect for DNA damage*. *Environmental Technology & Innovation*, 2019. **14**: p. 100358.
16. Han, F., et al., *Photocatalytic degradation of azo dye acid orange 7 using different light sources over Fe<sup>3+</sup>-doped TiO<sub>2</sub> nanocatalysts*. *Environmental Technology & Innovation*, 2018. **12**: p. 27-42.
17. da S. Pereira, W., et al., *Investigation on the photocatalytic performance of Ag<sub>4</sub>P<sub>2</sub>O<sub>7</sub> microcrystals for the degradation of organic pollutants*. *Applied Surface Science*, 2019. **493**: p. 1195-1204.
18. Shaban, M., et al., *Photocatalytic removal of Congo red dye using MCM-48/Ni<sub>2</sub>O<sub>3</sub> composite synthesized based on silica gel extracted from rice husk ash; fabrication and application*. *Journal of Environmental Management*, 2017. **204**: p. 189-199.
19. Mandal, S., et al., *Interactive Fe<sub>2</sub>O<sub>3</sub>/porous SiO<sub>2</sub> nanospheres for photocatalytic degradation of organic pollutants: Kinetic and mechanistic approach*. *Chemosphere*, 2019. **234**: p. 596-607.
20. Nickheslat, A., et al., *Phenol photocatalytic degradation by advanced oxidation process under ultraviolet radiation using titanium dioxide*. *J Environ Public Health*, 2013. **2013**: p. 815310.
21. De Zuane, J., *Handbook of Drinking Water Quality*. 1996.
22. Richardson, S.D. and S.Y. Kimura, *Emerging environmental contaminants: Challenges facing our next generation and potential engineering solutions*. *Environmental Technology & Innovation*, 2017. **8**: p. 40-56.
23. Ukić, Š., et al., *Toxicity of pharmaceuticals in binary mixtures: Assessment by additive and non-additive toxicity models*. *Ecotoxicology and Environmental Safety*, 2019. **185**: p. 109696.

24. Quesada, H.B., et al., *Surface water pollution by pharmaceuticals and an alternative of removal by low-cost adsorbents: A review*. Chemosphere, 2019. **222**: p. 766-780.
25. Praveena, S.M., et al., *Pharmaceuticals residues in selected tropical surface water bodies from Selangor (Malaysia): Occurrence and potential risk assessments*. Science of The Total Environment, 2018. **642**: p. 230-240.
26. Matongo, S., et al., *Pharmaceutical residues in water and sediment of Msunduzi River, KwaZulu-Natal, South Africa*. Chemosphere, 2015. **134**: p. 133-140.
27. Burns, E.E., et al., *Temporal and spatial variation in pharmaceutical concentrations in an urban river system*. Water Research, 2018. **137**: p. 72-85.
28. Raizada, P., et al., *Fabrication of dual Z-scheme photocatalyst via coupling of BiOBr/Ag/AgCl heterojunction with P and S co-doped g-C<sub>3</sub>N<sub>4</sub> for efficient phenol degradation*. Arabian Journal of Chemistry, 2020. **13**(3): p. 4538-4552.
29. Hasija, V., et al., *Recent advances in noble metal free doped graphitic carbon nitride based nanohybrids for photocatalysis of organic contaminants in water: A review*. Applied Materials Today, 2019. **15**: p. 494-524.
30. Rattan Paul, D. and S.P. Nehra, *Graphitic carbon nitride: a sustainable photocatalyst for organic pollutant degradation and antibacterial applications*. Environmental Science and Pollution Research, 2021. **28**(4): p. 3888-3896.
31. Sudhaik, A., et al., *Review on fabrication of graphitic carbon nitride based efficient nanocomposites for photodegradation of aqueous phase organic pollutants*. Journal of Industrial and Engineering Chemistry, 2018. **67**: p. 28-51.
32. Mousavi, M., A. Habibi-Yangjeh, and S.R. Pouran, *Review on magnetically separable graphitic carbon nitride-based nanocomposites as promising visible-light-driven photocatalysts*. Journal of Materials Science: Materials in Electronics, 2018. **29**(3): p. 1719-1747.
33. Behera, A., et al., *Constructive Interfacial Charge Carrier Separation of a p-CaFe<sub>2</sub>O<sub>4</sub>@n-ZnFe<sub>2</sub>O<sub>4</sub> Heterojunction Architect Photocatalyst toward Photodegradation of Antibiotics*. Inorganic Chemistry, 2019. **58**(24): p. 16592-16608.
34. Hamza, R.A., O.T. Iorhemen, and J.H. Tay, *Occurrence, impacts and removal of emerging substances of concern from wastewater*. Environmental Technology & Innovation, 2016. **5**: p. 161-175.
35. Luo, Y., et al., *A review on the occurrence of micropollutants in the aquatic environment and their fate and removal during wastewater treatment*. Science of The Total Environment, 2014. **473-474**: p. 619-641.

36. Rosman, N., et al., *Hybrid membrane filtration-advanced oxidation processes for removal of pharmaceutical residue*. Journal of Colloid and Interface Science, 2018. **532**: p. 236-260.
37. Kanakaraju, D., B.D. Glass, and M. Oelgemöller, *Advanced oxidation process-mediated removal of pharmaceuticals from water: A review*. Journal of Environmental Management, 2018. **219**: p. 189-207.
38. Martins, F., et al., *Analysis of Fossil Fuel Energy Consumption and Environmental Impacts in European Countries*. Energies, 2019. **12**(6): p. 964.
39. Chen, X., et al., *Recent advances in photocatalytic renewable energy production*. Energy Mater, 2022. **2**(200001): p. 10.
40. Hisatomi, T., J. Kubota, and K. Domen, *Recent advances in semiconductors for photocatalytic and photoelectrochemical water splitting*. Chemical Society Reviews, 2014. **43**(22): p. 7520-7535.
41. Wen, M., et al., *Design and architecture of metal organic frameworks for visible light enhanced hydrogen production*. Applied Catalysis B: Environmental, 2017. **218**: p. 555-569.
42. Fuku, K., et al., *The Synthesis of Size- and Color-Controlled Silver Nanoparticles by Using Microwave Heating and their Enhanced Catalytic Activity by Localized Surface Plasmon Resonance*. Angewandte Chemie International Edition, 2013. **52**(29): p. 7446-7450.
43. Bhatkhande, D.S., V.G. Pangarkar, and A.A.C.M. Beenackers, *Photocatalytic degradation for environmental applications – a review*. Journal of Chemical Technology & Biotechnology, 2002. **77**(1): p. 102-116.
44. Cheng, H., et al., *Hydrogen Doped Metal Oxide Semiconductors with Exceptional and Tunable Localized Surface Plasmon Resonances*. Journal of the American Chemical Society, 2016. **138**(29): p. 9316-9324.
45. Fujishima, A. and K. Honda, *Electrochemical Photolysis of Water at a Semiconductor Electrode*. Nature, 1972. **238**(5358): p. 37-38.
46. Kamegawa, T., Y. Shimizu, and H. Yamashita, *Superhydrophobic Surfaces with Photocatalytic Self-Cleaning Properties by Nanocomposite Coating of TiO<sub>2</sub> and Polytetrafluoroethylene*. Advanced Materials, 2012. **24**(27): p. 3697-3700.
47. Cheng, H., et al., *A Plasmonic Molybdenum Oxide Hybrid with Reversible Tunability for Visible-Light-Enhanced Catalytic Reactions*. Advanced Materials, 2015. **27**(31): p. 4616-4621.



48. Hoffmann, M.R., et al., *Environmental Applications of Semiconductor Photocatalysis*. Chemical Reviews, 1995. **95**(1): p. 69-96.
49. Ahmad, H., et al., *Hydrogen from photo-catalytic water splitting process: A review*. Renewable and Sustainable Energy Reviews, 2015. **43**: p. 599-610.
50. Maeda, K. and K. Domen, *Photocatalytic Water Splitting: Recent Progress and Future Challenges*. The Journal of Physical Chemistry Letters, 2010. **1**(18): p. 2655-2661.
51. Takata, T., et al., *Photocatalytic water splitting with a quantum efficiency of almost unity*. Nature, 2020. **581**(7809): p. 411-414.
52. Nadeem, M.A., et al., *An Overview of the Photocatalytic Water Splitting over Suspended Particles*. Catalysts, 2021. **11**(1).
53. Burton, P.D., et al., *Synthesis of High Surface Area ZnO(0001) Plates as Novel Oxide Supports for Heterogeneous Catalysts*. Catalysis Letters, 2010. **139**(1): p. 26-32.
54. Ba-Abbad, M.M., et al., *Visible light photocatalytic activity of Fe<sup>3+</sup>-doped ZnO nanoparticle prepared via sol-gel technique*. Chemosphere, 2013. **91**(11): p. 1604-1611.
55. Rana, A.G., et al., *Efficient Advanced Oxidation Process (AOP) for Photocatalytic Contaminant Degradation Using Exfoliated Metal-Free Graphitic Carbon Nitride and Visible Light-Emitting Diodes*. Catalysts, 2021. **11**(6).
56. Rana, A.G. and M. Minceva, *Analysis of Photocatalytic Degradation of Phenol with Exfoliated Graphitic Carbon Nitride and Light-Emitting Diodes Using Response Surface Methodology*. Catalysts, 2021. **11**(8).
57. Bignozzi, C.A., et al., *Nanostructured photoelectrodes based on WO<sub>3</sub>: applications to photooxidation of aqueous electrolytes*. Chemical Society Reviews, 2013. **42**(6): p. 2228-2246.
58. Tian, L., et al., *Solvothermal synthesis of CNTs-WO<sub>3</sub> hybrid nanostructures with high photocatalytic activity under visible light*. Catalysis Communications, 2012. **17**: p. 99-103.
59. Franking, R., et al., *Facile post-growth doping of nanostructured hematite photoanodes for enhanced photoelectrochemical water oxidation*. Energy & Environmental Science, 2013. **6**(2): p. 500-512.
60. Bang, J.U., et al., *Geometric Effect of Single or Double Metal-Tipped CdSe Nanorods on Photocatalytic H<sub>2</sub> Generation*. The Journal of Physical Chemistry Letters, 2012. **3**(24): p. 3781-3785.

61. Jinshu, W., et al., *Mechanochemical Synthesis of Fluorine-Doped SrTiO<sub>3</sub> and Its Photo-oxidation Properties*. Chemistry Letters, 2003. **32**(6): p. 540-541.
62. Kumar, S., S. Karthikeyan, and A. Lee, *g-C<sub>3</sub>N<sub>4</sub>-Based Nanomaterials for Visible Light-Driven Photocatalysis*. Catalysts, 2018. **8**(2).
63. Ren, H.-T., et al., *Improved Photochemical Reactivities of Ag<sub>2</sub>O/g-C<sub>3</sub>N<sub>4</sub> in Phenol Degradation under UV and Visible Light*. Industrial & Engineering Chemistry Research, 2014. **53**(45): p. 17645-17653.
64. Lee, S.C., H.O. Lintang, and L. Yuliati, *A urea precursor to synthesize carbon nitride with mesoporosity for enhanced activity in the photocatalytic removal of phenol*. Chem Asian J, 2012. **7**(9): p. 2139-44.
65. Hu, J.Y., K. Tian, and H. Jiang, *Improvement of phenol photodegradation efficiency by a combined g-C<sub>3</sub>N<sub>4</sub>/Fe(III)/persulfate system*. Chemosphere, 2016. **148**: p. 34-40.
66. Deng, P., et al., *Non-noble-metal Ni nanoparticles modified N-doped g-C<sub>3</sub>N<sub>4</sub> for efficient photocatalytic hydrogen evolution*. International Journal of Hydrogen Energy, 2019. **44**(57): p. 30084-30092.
67. Huang, Z., et al., *Well-dispersed g-C<sub>3</sub>N<sub>4</sub> nanophases in mesoporous silica channels and their catalytic activity for carbon dioxide activation and conversion*. Applied Catalysis B: Environmental, 2013. **136-137**: p. 269-277.
68. Sharma, M., S. Vaidya, and A.K. Ganguli, *Enhanced photocatalytic activity of g-C<sub>3</sub>N<sub>4</sub>-TiO<sub>2</sub> nanocomposites for degradation of Rhodamine B dye*. Journal of Photochemistry and Photobiology A: Chemistry, 2017. **335**: p. 287-293.
69. Hernández-Uresti, D.B., et al., *Performance of the polymeric g-C<sub>3</sub>N<sub>4</sub> photocatalyst through the degradation of pharmaceutical pollutants under UV-vis irradiation*. Journal of Photochemistry and Photobiology A: Chemistry, 2016. **324**: p. 47-52.
70. Idriss, H., *Hydrogen production from water: past and present*. Current Opinion in Chemical Engineering, 2020. **29**: p. 74-82.
71. Dincer, I. and H. Ishaq, *Chapter 3 - Solar Energy-Based Hydrogen Production*, in *Renewable Hydrogen Production*, I. Dincer and H. Ishaq, Editors. 2022, Elsevier. p. 91-122.
72. Pei, S., X. Ge, and L. Sun, *Metal Ions Doping for Boosting Luminescence of Lanthanide-Doped Nanocrystals*. Frontiers in Chemistry, 2020. **8**.
73. Patnaik, S., D.P. Sahoo, and K. Parida, *Recent advances in anion doped g-C<sub>3</sub>N<sub>4</sub> photocatalysts: A review*. Carbon, 2021. **172**: p. 682-711.

74. Zong, X., G. Lu, and L. Wang, *Nonmetal Doping in TiO<sub>2</sub> Toward Visible-Light-Induced Photocatalysis*, in *Environmental Photochemistry Part III*, D.W. Bahnemann and P.K.J. Robertson, Editors. 2015, Springer Berlin Heidelberg: Berlin, Heidelberg. p. 87-113.
75. Starukh, H. and P. Praus, *Doping of Graphitic Carbon Nitride with Non-Metal Elements and Its Applications in Photocatalysis*. *Catalysts*, 2020. **10**(10): p. 1119.
76. Geim, A.K. and K.S. Novoselov, *The rise of graphene*. *Nature Materials*, 2007. **6**(3): p. 183-191.
77. Dong, X. and F. Cheng, *Recent development in exfoliated two-dimensional g-C<sub>3</sub>N<sub>4</sub> nanosheets for photocatalytic applications*. *Journal of Materials Chemistry A*, 2015. **3**(47): p. 23642-23652.
78. Boschloo, G., T. Edvinsson, and A. Hagfeldt, *Chapter 8 - Dye-Sensitized Nanostructured ZnO Electrodes for Solar Cell Applications*, in *Nanostructured Materials for Solar Energy Conversion*, T. Soga, Editor. 2006, Elsevier: Amsterdam. p. 227-254.
79. Védrine, J.C., *Heterogeneous Catalysis on Metal Oxides*. *Catalysts*, 2017. **7**(11): p. 341.
80. Kozuch, S. and J.M.L. Martin, *"Turning Over" Definitions in Catalytic Cycles*. *ACS Catalysis*, 2012. **2**(12): p. 2787-2794.
81. Ameta, R., et al., *Photocatalysis*, in *Advanced Oxidation Processes for Waste Water Treatment*. 2018. p. 135-175.
82. Ameta, S.C. and R. Ameta, *Advanced Oxidation Processes for Waste Water Treatment; Emerging Green Chemical Technology*. 2018.
83. Kumar, S., S. Karthikeyan, and A.F. Lee, *g-C<sub>3</sub>N<sub>4</sub>-Based Nanomaterials for Visible Light-Driven Photocatalysis*. *Catalysts*, 2018. **8**(2): p. 74.
84. Kisch, H., *Semiconductor Photocatalysis*. *Semiconductor Photocatalysis*. 2014. 1-8.
85. Linsebigler, A.L., G. Lu, and J.T. Yates, *Photocatalysis on TiO<sub>2</sub> Surfaces: Principles, Mechanisms, and Selected Results*. *Chemical Reviews*, 1995. **95**(3): p. 735-758.
86. Herrmann, J.-M., *Heterogeneous photocatalysis: fundamentals and applications to the removal of various types of aqueous pollutants*. *Catalysis Today*, 1999. **53**(1): p. 115-129.
87. Rueda-Marquez, J.J., et al., *A critical review on application of photocatalysis for toxicity reduction of real wastewaters*. *Journal of Cleaner Production*, 2020. **258**.

88. Ohtani, B., *Titania Photocatalysis beyond Recombination: A Critical Review*. Catalysts, 2013. **3**(4): p. 942-953.
89. Gaya, U.I. and A.H. Abdullah, *Heterogeneous photocatalytic degradation of organic contaminants over titanium dioxide: a review of fundamentals, progress and problems*. Journal of photochemistry and photobiology C: Photochemistry reviews, 2008. **9**(1): p. 1-12.
90. Schneider, J., et al., *Understanding TiO<sub>2</sub> photocatalysis: mechanisms and materials*. Chemical reviews, 2014. **114**(19): p. 9919-9986.
91. Karamian, E. and S. Sharifnia, *On the general mechanism of photocatalytic reduction of CO<sub>2</sub>*. Journal of CO<sub>2</sub> Utilization, 2016. **16**: p. 194-203.
92. White, J.L., et al., *Light-driven heterogeneous reduction of carbon dioxide: photocatalysts and photoelectrodes*. Chemical reviews, 2015. **115**(23): p. 12888-12935.
93. Kubacka, A., M. Fernandez-Garcia, and G. Colon, *Advanced nanoarchitectures for solar photocatalytic applications*. Chemical reviews, 2012. **112**(3): p. 1555-1614.
94. Daghrir, R., P. Drogui, and D. Robert, *Modified TiO<sub>2</sub> for environmental photocatalytic applications: a review*. Industrial & Engineering Chemistry Research, 2013. **52**(10): p. 3581-3599.
95. Sankar, M., et al., *The benzaldehyde oxidation paradox explained by the interception of peroxy radical by benzyl alcohol*. Nature Communications, 2014. **5**(1): p. 3332.
96. Rana, A.G., et al., *Synthesis and characterization of Cu-Zn/TiO<sub>2</sub> for the photocatalytic conversion of CO<sub>2</sub> to methane*. Environmental Technology, 2017. **38**(9): p. 1085-1092.
97. Gao, X. and X. Meng, *Photocatalysis for Heavy Metal Treatment: A Review*. Processes, 2021. **9**(10): p. 1729.
98. Ollis, D.F., E. Pelizzetti, and N. Serpone, *Photocatalyzed destruction of water contaminants*. Environmental Science & Technology, 1991. **25**(9): p. 1522-1529.
99. Mills, A., R.H. Davies, and D. Worsley, *Water purification by semiconductor photocatalysis*. Chemical Society Reviews, 1993. **22**(6): p. 417-425.
100. Styring, S., *Artificial photosynthesis for solar fuels*. Faraday Discuss, 2012. **155**: p. 357-76.
101. Hernández-Alonso, M.D., et al., *Development of alternative photocatalysts to TiO<sub>2</sub>: Challenges and opportunities*. Energy & Environmental Science, 2009. **2**(12).

102. Maeda, K., *Photocatalytic water splitting using semiconductor particles: history and recent developments*. Journal of Photochemistry and Photobiology C: Photochemistry Reviews, 2011. **12**(4): p. 237-268.
103. Ahmad, H., et al., *Hydrogen from photo-catalytic water splitting process: A review*. Renewable and Sustainable Energy Reviews, 2015. **43**: p. 599-610.
104. Xiao, N., et al., *The roles and mechanism of cocatalysts in photocatalytic water splitting to produce hydrogen*. Chinese Journal of Catalysis, 2020. **41**(4): p. 642-671.
105. Neațu, Ș., J.A. Maciá-Agulló, and H. Garcia, *Solar Light Photocatalytic CO<sub>2</sub> Reduction: General Considerations and Selected Bench-Mark Photocatalysts*. International Journal of Molecular Sciences, 2014. **15**(4): p. 5246-5262.
106. Zheng, Q., et al., *Visible-Light-Responsive Graphitic Carbon Nitride: Rational Design and Photocatalytic Applications for Water Treatment*. Environmental Science & Technology, 2016. **50**(23): p. 12938-12948.
107. Md Rosli, N.I., et al., *Photocatalytic Performance of ZnO/g-C<sub>3</sub>N<sub>4</sub> for Removal of Phenol under Simulated Sunlight Irradiation*. Journal of Environmental Engineering, 2018. **144**(2).
108. Lima, M.J., et al., *Graphitic carbon nitride modified by thermal, chemical and mechanical processes as metal-free photocatalyst for the selective synthesis of benzaldehyde from benzyl alcohol*. Journal of Catalysis, 2017. **353**: p. 44-53.
109. Nobijari, L.A., M. Schwarze, and M. Tasbihi, *Photocatalytic Degradation of Phenol Using Photodeposited Pt Nanoparticles on Titania*. Journal of Nanoscience and Nanotechnology, 2020. **20**(2): p. 1056-1065.
110. Al-Kandari, H., et al., *An efficient eco advanced oxidation process for phenol mineralization using a 2D/3D nanocomposite photocatalyst and visible light irradiations*. Scientific Reports, 2017. **7**(1): p. 9898.
111. Moradi, V., et al., *Acid-treated Fe-doped TiO<sub>2</sub> as a high performance photocatalyst used for degradation of phenol under visible light irradiation*. Journal of Environmental Sciences, 2019. **83**: p. 183-194.
112. Daniel, M.C. and D. Astruc, *Gold nanoparticles: assembly, supramolecular chemistry, quantum-size-related properties, and applications toward biology, catalysis, and nanotechnology*. Chem Rev, 2004. **104**(1): p. 293-346.
113. McLaren, A., et al., *Shape and size effects of ZnO nanocrystals on photocatalytic activity*. Journal of the American Chemical Society, 2009. **131**(35): p. 12540-12541.

114. Li, Y.-F. and Z.-P. Liu, *Particle size, shape and activity for photocatalysis on titania anatase nanoparticles in aqueous surroundings*. Journal of the American Chemical Society, 2011. **133**(39): p. 15743-15752.
115. Ong, W.-J., et al., *Graphitic carbon nitride (g-C<sub>3</sub>N<sub>4</sub>)-based photocatalysts for artificial photosynthesis and environmental remediation: are we a step closer to achieving sustainability?* Chemical reviews, 2016. **116**(12): p. 7159-7329.
116. Wang, J. and S. Wang, *A critical review on graphitic carbon nitride (g-C<sub>3</sub>N<sub>4</sub>)-based materials: Preparation, modification and environmental application*. Coordination Chemistry Reviews, 2022. **453**.
117. Zhang, W., et al., *Micro-interfacial mechanisms on sludge dewaterability enhancement using cerium chloride for preparation of carbon-based functional material*. Journal of Hazardous Materials, 2020. **386**: p. 121930.
118. Wu, J., et al., *Bidirectional Photochromism via Anchoring of Carbon Dots to TiO<sub>2</sub> Porous Films*. ACS Applied Materials & Interfaces, 2020. **12**(5): p. 6262-6267.
119. Bi, Z., et al., *Biomass-derived porous carbon materials with different dimensions for supercapacitor electrodes: a review*. Journal of Materials Chemistry A, 2019. **7**(27): p. 16028-16045.
120. Weiss, E.A., *Designing the Surfaces of Semiconductor Quantum Dots for Colloidal Photocatalysis*. ACS Energy Letters, 2017. **2**(5): p. 1005-1013.
121. Yuan, B., et al., *Water-soluble ribbon-like graphitic carbon nitride (g-C<sub>3</sub>N<sub>4</sub>): green synthesis, self-assembly and unique optical properties*. J. Mater. Chem. C, 2014. **2**(39): p. 8212-8215.
122. Wang, S., et al., *Controllable synthesis of nanotube-type graphitic C<sub>3</sub>N<sub>4</sub> and their visible-light photocatalytic and fluorescent properties*. Journal of Materials Chemistry A, 2014. **2**(9).
123. He, B., et al., *Multidimensional (0D-3D) functional nanocarbon: Promising material to strengthen the photocatalytic activity of graphitic carbon nitride*. Green Energy & Environment, 2021. **6**(6): p. 823-845.
124. Tian, J., et al., *Recent progress in design, synthesis, and applications of one-dimensional TiO<sub>2</sub> nanostructured surface heterostructures: a review*. Chem Soc Rev, 2014. **43**(20): p. 6920-37.
125. Weng, B., et al., *One-dimensional nanostructure based materials for versatile photocatalytic applications*. RSC Advances, 2014. **4**(25).

126. Bai, X., et al., *Photocatalytic Activity Enhanced via g-C<sub>3</sub>N<sub>4</sub> Nanoplates to Nanorods*. The Journal of Physical Chemistry C, 2013. **117**(19): p. 9952-9961.
127. Zhang, Z., et al., *High-pressure bulk synthesis of crystalline C(6)N(9)H(3).HCl: a novel c(3)n(4) graphitic derivative*. J Am Chem Soc, 2001. **123**(32): p. 7788-96.
128. Niu, P., et al., *Graphene-Like Carbon Nitride Nanosheets for Improved Photocatalytic Activities*. Advanced Functional Materials, 2012. **22**(22): p. 4763-4770.
129. Luo, B., G. Liu, and L. Wang, *Recent advances in 2D materials for photocatalysis*. Nanoscale, 2016. **8**(13): p. 6904-20.
130. Alivisatos, A.P., *Semiconductor Clusters, Nanocrystals, and Quantum Dots*. Science, 1996. **271**(5251): p. 933-937.
131. Gu, Q., et al., *Template-free synthesis of porous graphitic carbon nitride microspheres for enhanced photocatalytic hydrogen generation with high stability*. Applied Catalysis B: Environmental, 2015. **165**: p. 503-510.
132. Fattakhova-Rohlfing, D., A. Zaleska, and T. Bein, *Three-dimensional titanium dioxide nanomaterials*. Chem Rev, 2014. **114**(19): p. 9487-558.
133. Lukatskaya, M.R., B. Dunn, and Y. Gogotsi, *Multidimensional materials and device architectures for future hybrid energy storage*. Nature Communications, 2016. **7**(1): p. 12647.
134. Griffiths, P.R. and J.A. de Haseth, *Fourier Transform Infrared Spectrometry*. 2007.
135. Jenkin, J.G., R.C.G. Leckey, and J. Liesegang, *The development of x-ray photoelectron spectroscopy: 1900–1960*. Journal of Electron Spectroscopy and Related Phenomena, 1977. **12**(1): p. 1-35.
136. John F. Watts, J.W., *An Introduction To Surface Analysis By XPS And AES*. 2003.
137. Williams, D.B. and C.B. Carter, *The Transmission Electron Microscope*, in *Transmission Electron Microscopy*. 2009. p. 3-22.
138. Mast, J., et al., *Characterization of nanomaterials by transmission electron microscopy: Measurement procedures*, in *Characterization of Nanoparticles*. 2020. p. 29-48.
139. Yoshida, A., Y. Kaburagi, and Y. Hishiyama, *Scanning Electron Microscopy*, in *Materials Science and Engineering of Carbon*. 2016. p. 71-93.
140. Erdman, N., D.C. Bell, and R. Reichelt, *Scanning Electron Microscopy*, in *Springer Handbook of Microscopy*. 2019. p. 229-318.



141. Choquette-Labbé, M., et al., *Photocatalytic Degradation of Phenol and Phenol Derivatives Using a Nano-TiO<sub>2</sub> Catalyst: Integrating Quantitative and Qualitative Factors Using Response Surface Methodology*. *Water*, 2014. **6**(6): p. 1785-1806.
142. Asanjarani, N., M. Bagtash, and J. Zolgharnein, *A comparison between Box–Behnken design and artificial neural network: Modeling of removal of Phenol Red from water solutions by nanocobalt hydroxide*. *Journal of Chemometrics*, 2020. **34**(9).
143. Peng, H., et al., *The effective removal of phenol from aqueous solution via adsorption on CS/beta-CD/CTA multicomponent adsorbent and its application for COD degradation of drilling wastewater*. *Environ Sci Pollut Res Int*, 2020. **27**(27): p. 33668-33680.
144. Abdullah, A.H., H.J.M. Moey, and N.A. Yusof, *Response surface methodology analysis of the photocatalytic removal of Methylene Blue using bismuth vanadate prepared via polyol route*. *Journal of Environmental Sciences*, 2012. **24**(9): p. 1694-1701.
145. Song, C., et al., *Fabrication, Characterization and Response Surface Method (RSM) Optimization for Tetracycline Photodegradation by Bi<sub>3.84</sub>W<sub>0.16</sub>O<sub>6.24</sub>-graphene oxide (BWO-GO)*. *Sci Rep*, 2016. **6**: p. 37466.
146. Hassani, A., P. Eghbali, and O. Metin, *Sonocatalytic removal of methylene blue from water solution by cobalt ferrite/mesoporous graphitic carbon nitride (CoFe<sub>2</sub>O<sub>4</sub>/mpg-C<sub>3</sub>N<sub>4</sub>) nanocomposites: response surface methodology approach*. *Environ Sci Pollut Res Int*, 2018. **25**(32): p. 32140-32155.

# Appendix

**Supplementary Information of all papers**

## Supporting Information

# Efficient advanced oxidation process (AOP) for photocatalytic contaminant degradation using exfoliated metal-free graphitic carbon nitride and visible light-emitting diodes

Adeem Ghaffar Rana <sup>1,2</sup>, Minoo Tasbihi <sup>3</sup>, Michael Schwarze <sup>3</sup>, and Mirjana Minceva <sup>1, \*</sup>

<sup>1</sup> Biothermodynamics, TUM School of Life Sciences Weihenstephan, Technical University of Munich, Maximus-von-Imhof-Forum 2, 85354, Freising, Germany; adeem.rana@tum.de; mirjana.minceva@tum.de

<sup>2</sup> Department of Chemical, Polymer and Composite Materials Engineering, University of Engineering and Technology (UET), Lahore, Pakistan; adeem.rana@tum.de

<sup>3</sup> Department of Chemistry, Technische Universität Berlin, Str. des 17. Juni 124, D-10623 Berlin, Germany; minoo.tasbihi@tu-berlin.de; michael.schwarze@tu-berlin.de

\* Correspondence: Mirjana.minceva@tum.de; Tel.: (+498161716170)

The photocatalytic experiments were conducted in a jacketed glass reactor (Peschl Ultraviolet GmbH) with a maximum working capacity of 225 mL, under a custom-made LED immersion lamp comprising 6 LEDs (each of 10 W) with maximum emission at 430 nm and UV-visible light irradiation using a 150 W full-spectrum xenon lamp. The reactor was placed in a safety cabinet. The light source is immersed in the reaction medium and is 1 cm away from the medium with jacket and coolant in between. There are four ports at the reactor and these are used to introduce air and take samples. The safety cabinet has a fan to keep the environment cool in case of heating.

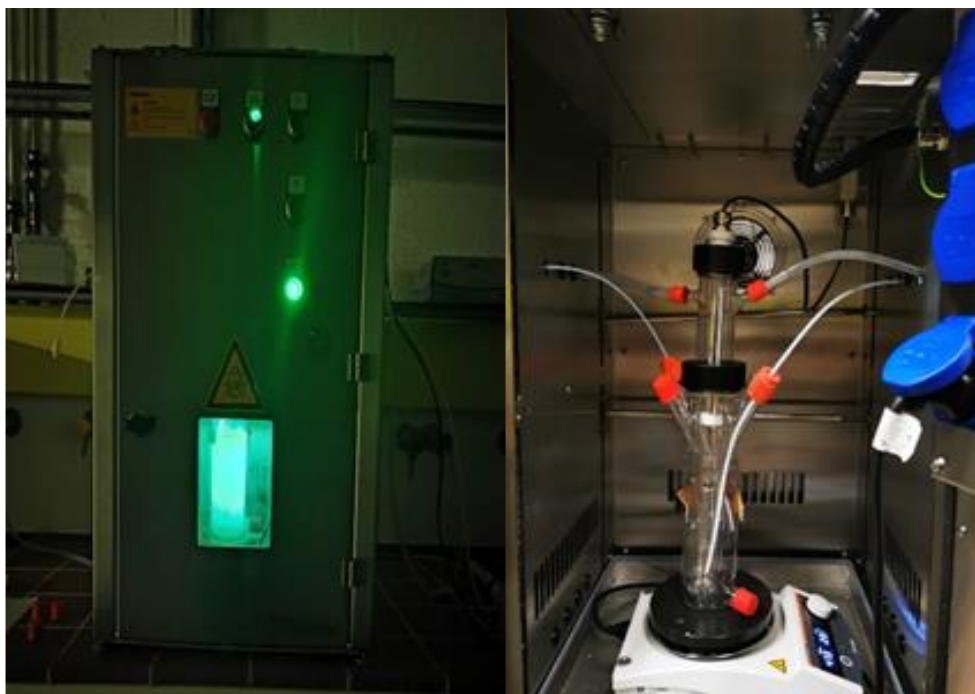


**Figure S1** Photocatalytic reactor setup

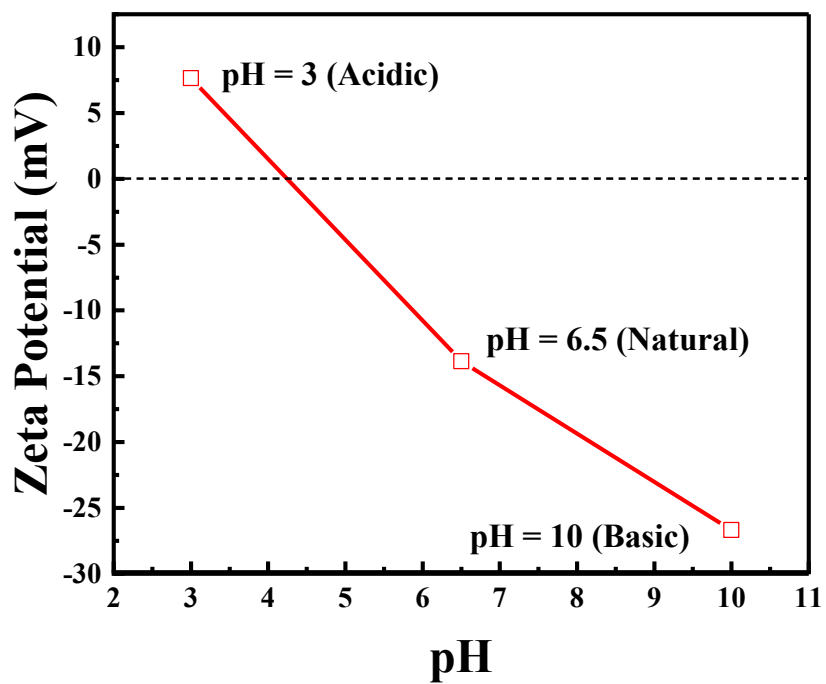


Figure S2 Zeta potential of exfoliated g-C<sub>3</sub>N<sub>4</sub> as a function of the pH value of the suspension

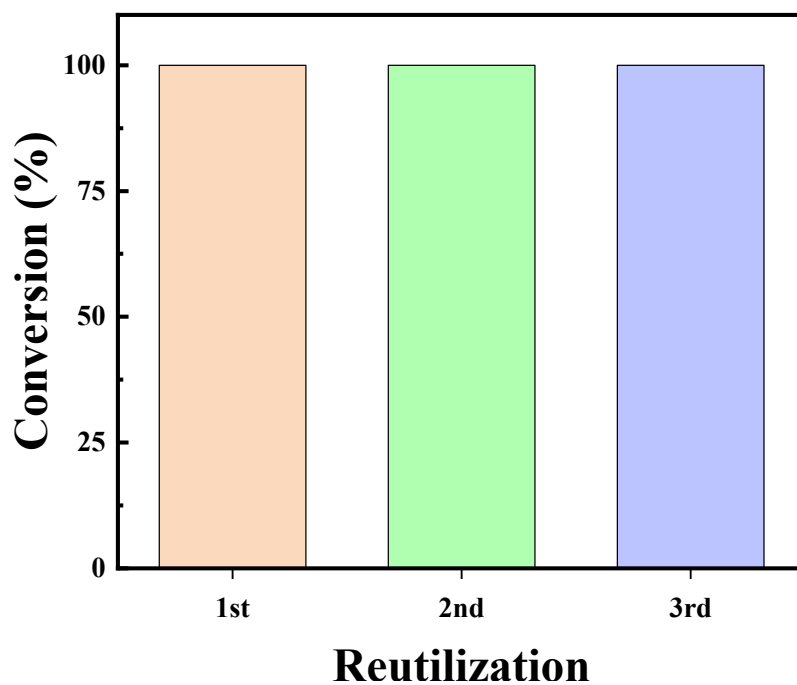
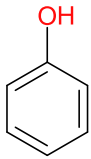
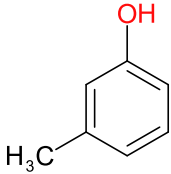
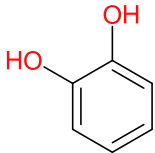
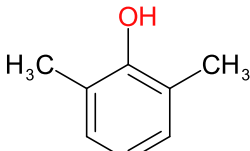
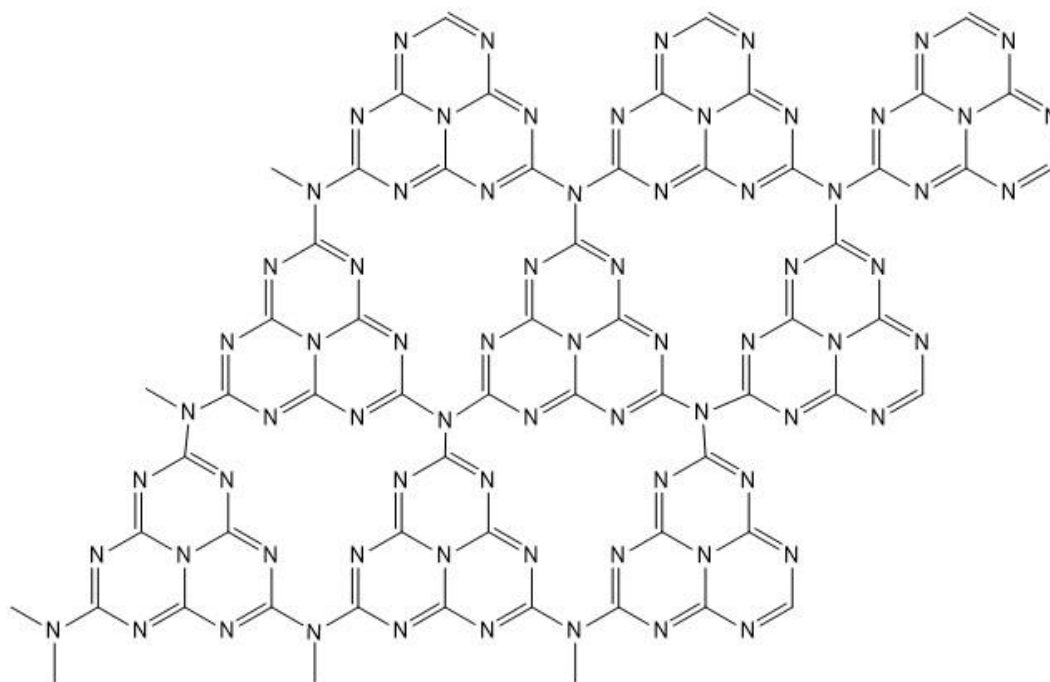


Figure S3 Phenol degradation conversion for the reutilized catalyst;  $C_0 = 20$  ppm, airflow = 50 mL/min, catalyst = 0.5 g/L, pH = natural

**Table S1** Chemical structures of the pollutants used

phenol	
<i>m</i> -cresol	
catechol	
xyleneol	



**Figure S4** tri-s- triazine as unit structures of g-C<sub>3</sub>N<sub>4</sub>

# ChemistrySelect

Supporting Information

## **Synthesis of Highly Active Doped Graphitic Carbon Nitride using Acid-Functionalized Precursors for Efficient Adsorption and Photodegradation of Endocrine-Disrupting Compounds**

Adeem Ghaffar Rana, Mian Zahid Hussain, Nikki Hammond, Simon Vlad Luca, Roland A. Fischer, and Mirjana Minceva\*



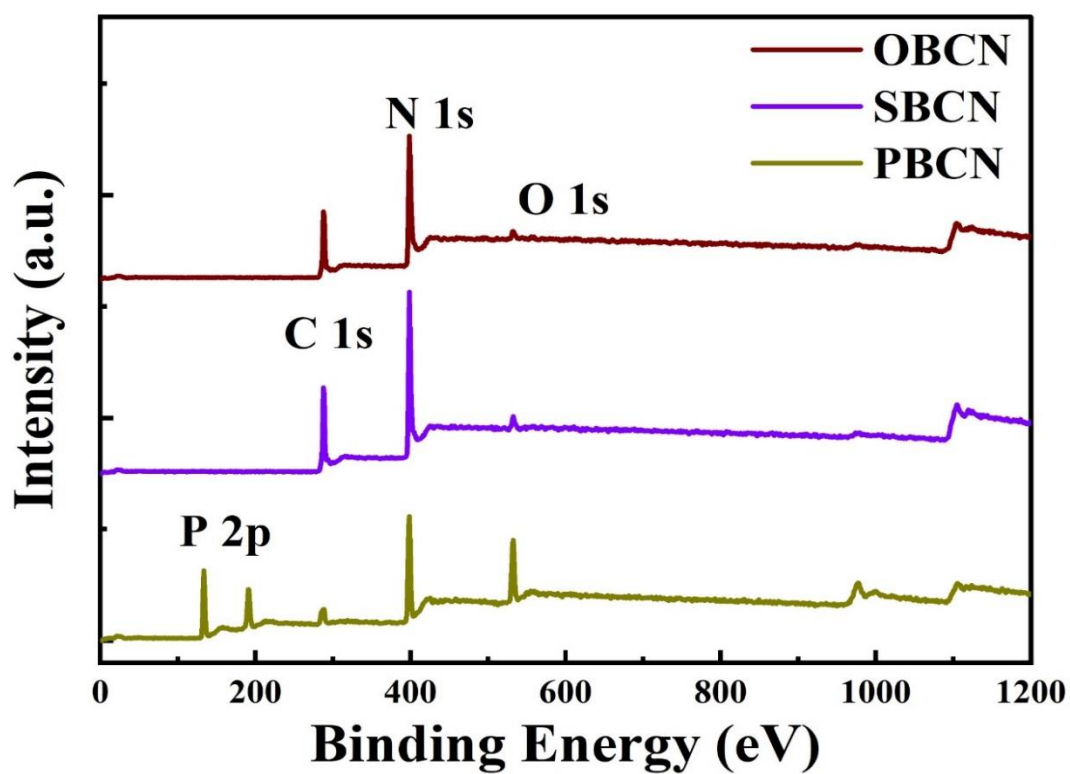


Figure S1 XPS survey spectra of the synthesized materials

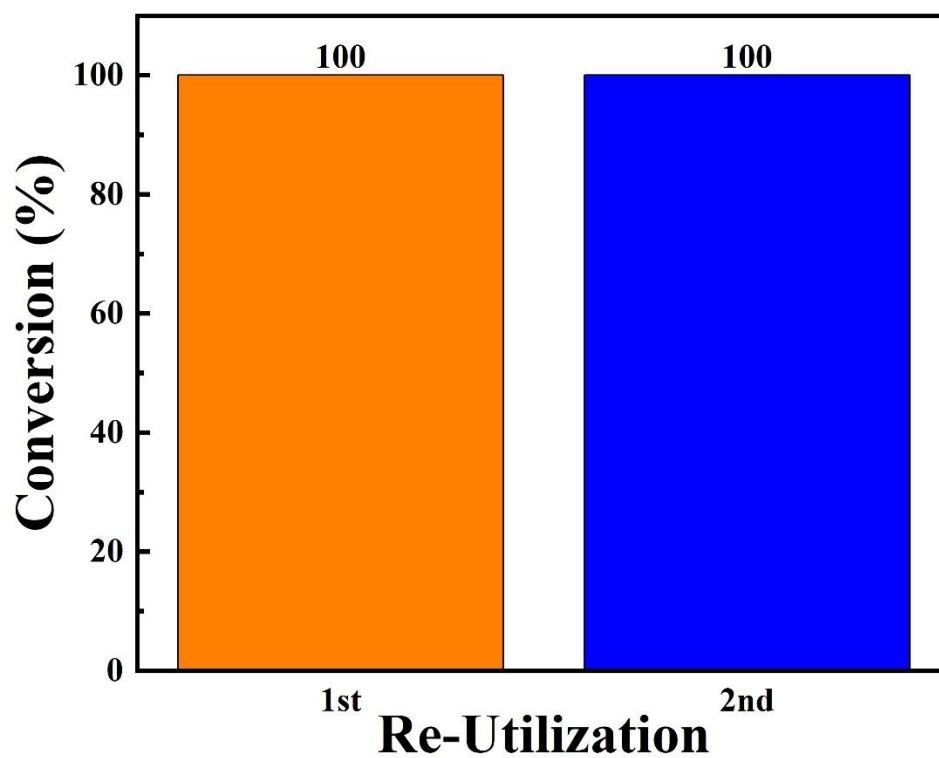


Figure S2 17  $\beta$  Estradiol (E2) degradation conversion for the reutilized catalyst;  $C_0 = 5$  mg/L, airflow = 50 mL/min, catalyst = 0.1 g/L, pH = natural

## Experimental Setup

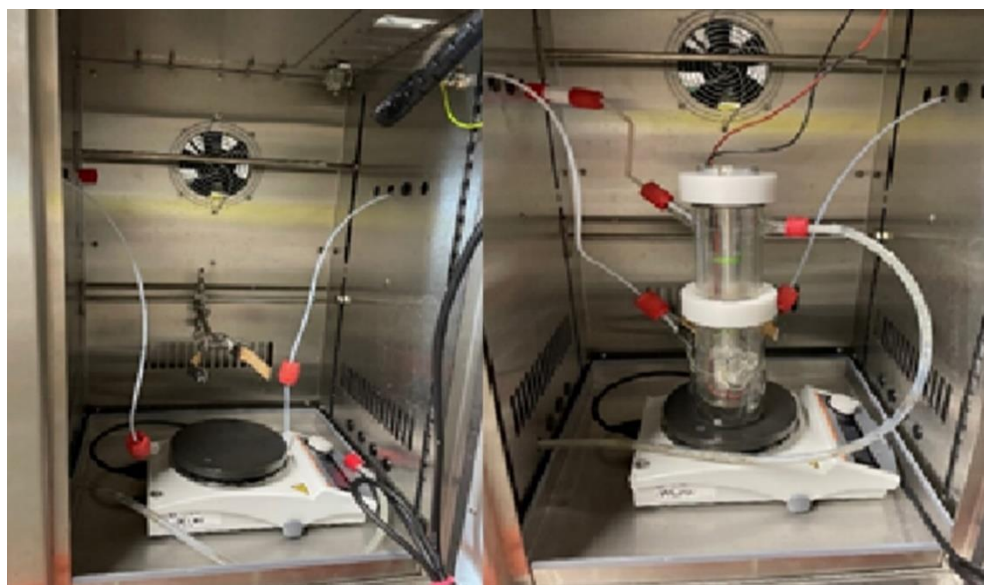


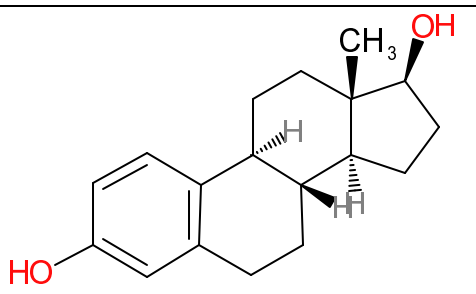
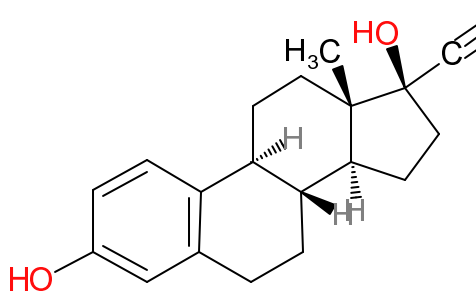
Figure S3 Photocatalytic reactor setup

The photocatalytic experiments were conducted in a jacketed glass reactor (custom-made) with a maximum working capacity of 120 mL under a custom-made LED immersion lamp comprising 6 LEDs (each of 10 W) with maximum emission at 430 nm. The reactor was placed in a safety cabinet. The light source is immersed in the reaction medium and is 1 cm away from the medium with a jacket and coolant in between. There are three ports of the reactor, and these are used to introduce air and take samples. The safety cabinet has a fan to keep the environment cool in case of heating.

Table S1 Parameters of adsorption models

Pseudo-first-order parameters		Pseudo-second-order parameters			Elovich parameters		
$(\text{min}^{-1}) k_1$	$R^2$	$q_e(\text{mg/g})$	$(\text{g}/(\text{mg}\cdot\text{min})) k_2$	$R^2$	$\alpha (\text{mg/g}\cdot\text{min})$	$\beta (\text{g/mg})$	$R^2$
0.01875	0.471	33.38	0.0198	0.999	6.55E+16	1.3347	0.9043

Table S2 Chemical structures of hormone pollutants

17 $\beta$ estradiol	 <p>The chemical structure of 17<math>\beta</math> estradiol is a steroid nucleus with a phenolic A ring (hydroxyl group at C3), a ketone at C4, and hydroxyl groups at C17 and C13. A methyl group is attached at C13.</p>
17 $\alpha$ ethinylestradiol	 <p>The chemical structure of 17<math>\alpha</math> ethinylestradiol is a steroid nucleus with a phenolic A ring (hydroxyl group at C3), a ketone at C4, a methyl group at C13, and a hydroxyl group at C17. An ethynyl group (-C≡CH) is attached at C17.</p>

# Influence of Cocatalysts (Ni, Co, and Cu) and Synthesis Method on the Photocatalytic Activity of Exfoliated Graphitic Carbon Nitride for Hydrogen Production

The optical properties of pristine and modified g-CN were studied using UV-Vis (Figure S1) and PL spectroscopy (Figure 2). All materials show absorption in the visible range, and the bandgap of the materials change only slightly with modification. Exfoliation leads to a blue shift in the absorption, and its bandgap increases from 2.42 to 2.61 eV. With the addition of metal co-catalysts, the bandgap changes slightly and remains in the same range, absorbing visible light. In the case of Ni, the deposition process had no influence. The PL spectrum shows maximum absorption wavelengths of 458 nm and 436 nm for g-CN and ex-g-CN, respectively. The blue shift is also confirmed by PL spectroscopy.

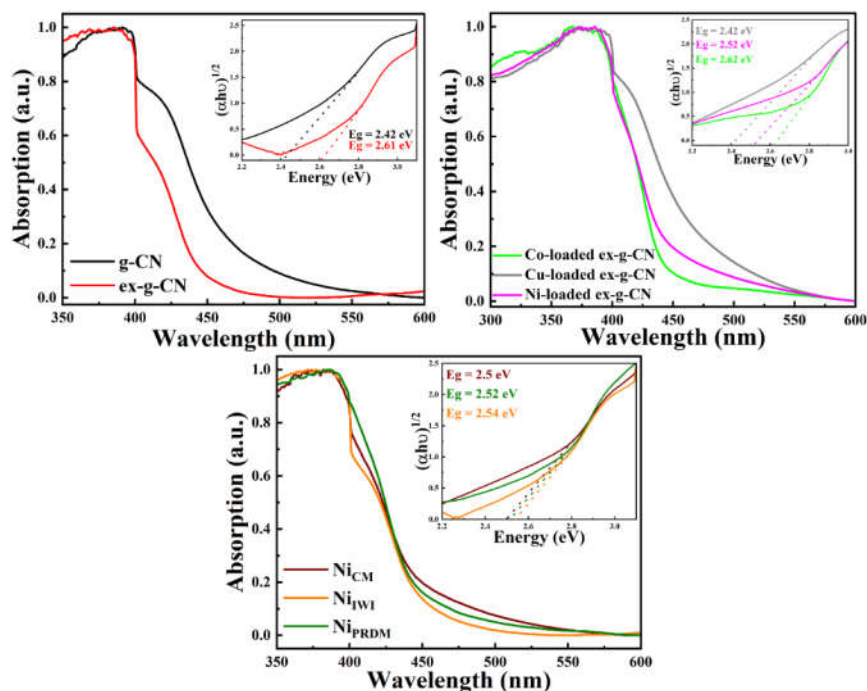


Figure S1. UV-Vis Spectra of synthesized catalysts; inset tauc plots.

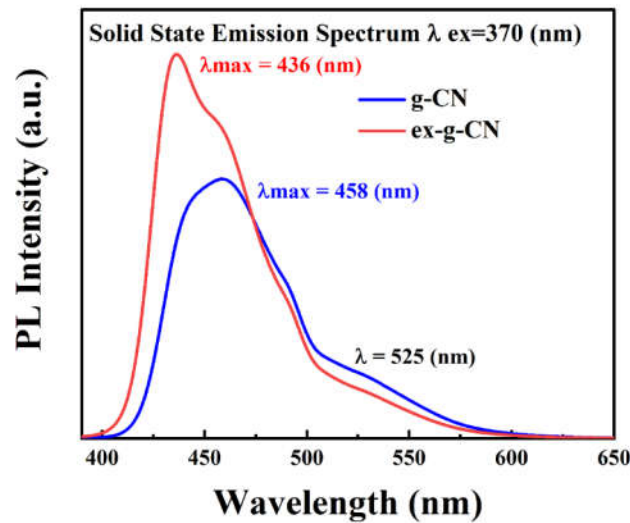


Figure S2. PL spectra of g-CN and ex-g-CN [1].

The chemical composition and the functional groups are studied using FTIR (Figure S3). A broad peak is observed between  $3200$  and  $3000$   $\text{cm}^{-1}$ , which can be attributed to the stretching vibrations of N–H bonds from residual amino groups and adsorbed H<sub>2</sub>O. The sharp peak at  $806$   $\text{cm}^{-1}$  can be attributed to the breathing mode of triazine units, whereas the strong bands between  $1636$  and  $1242$   $\text{cm}^{-1}$  belong to the C=N and C–N bonds of heterocyclic rings. The spectra of all materials show the same absorption bands, the chemical structure remained unaltered after modification, and due to the low content of co-catalysts, there are no peaks of the respective metals.

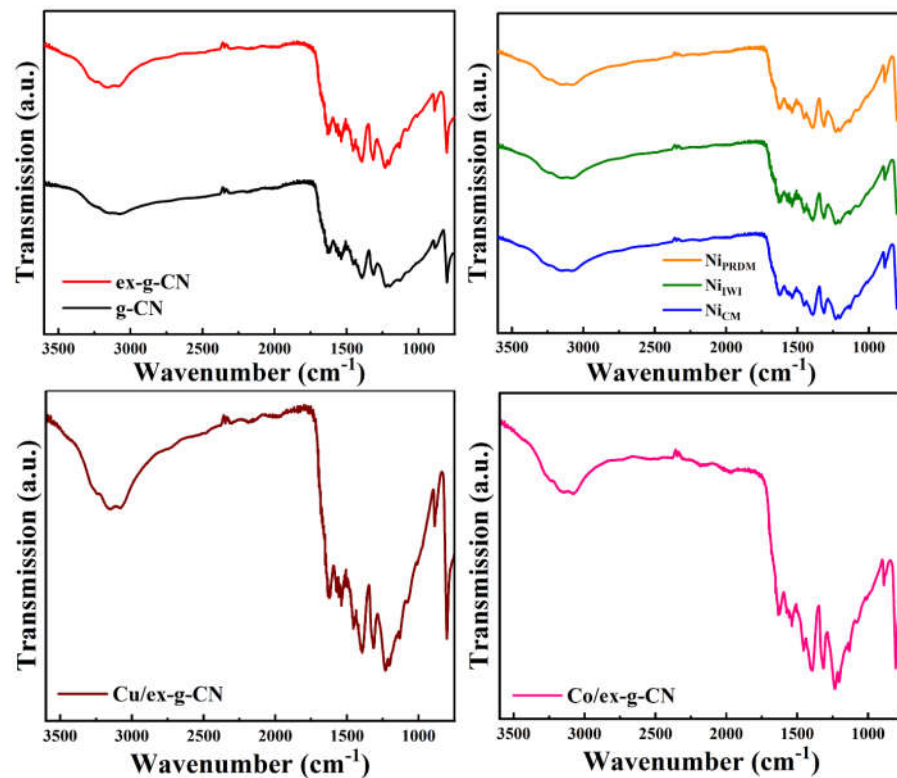


Figure S3. FTIR spectra of all synthesized catalysts.

The XRD patterns of cobalt- and copper-loaded ex-g-CN are shown in Figure S4. It shows typical  $2\theta$  peaks of g-C<sub>3</sub>N<sub>4</sub> at 13.1° and 27°. Due to the low cocatalyst loading, there are no visible peaks of cobalt or copper.

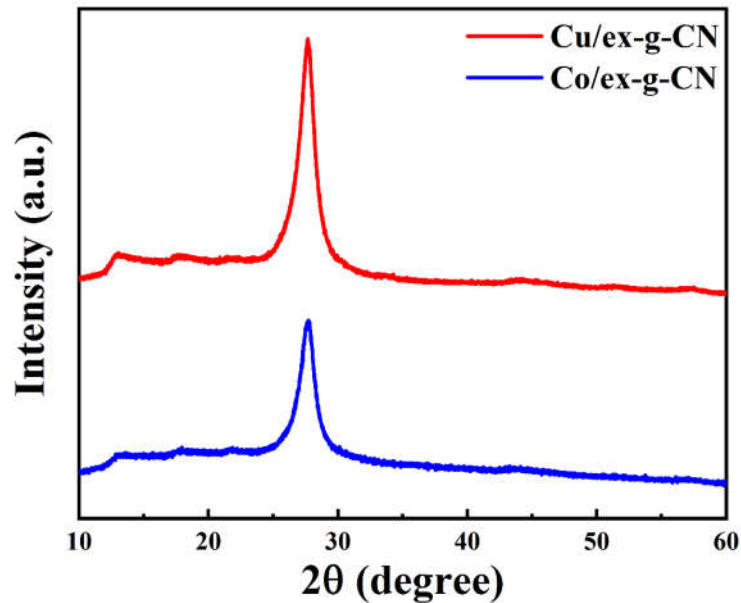


Figure S4. XRD patterns of Co- and Cu-loaded ex-g-CN.

Figure S5 shows the N<sub>2</sub> adsorption-desorption isotherms and BJH pore size distributions of g-CN and ex-g-CN. Both samples show a hysteresis loop of type IV, suggesting the existence of a large number of pores. The pore size distribution curves of both materials show a maximum at a radius of 1.9 nm, which means that the materials were mesoporous [1].

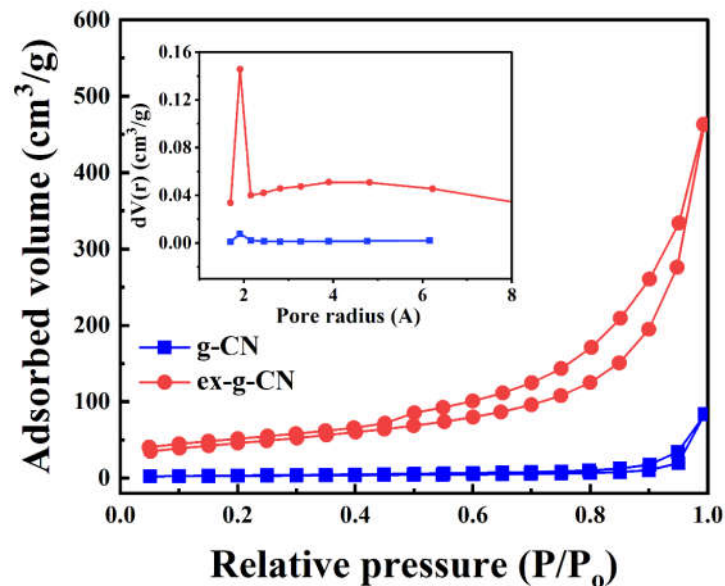


Figure S5. Adsorption and desorption curves of g-CN and ex-g-CN; inset particle size distribution.

The chemical states of cobalt and copper are studied using the XPS and shown in Figure S6. Cobalt is present majorly in oxide or unreduced form in  $2p_{3/2}$  and  $2p_{1/2}$  states [2]. Copper is also present in the +2 and +1 oxidized states [3].

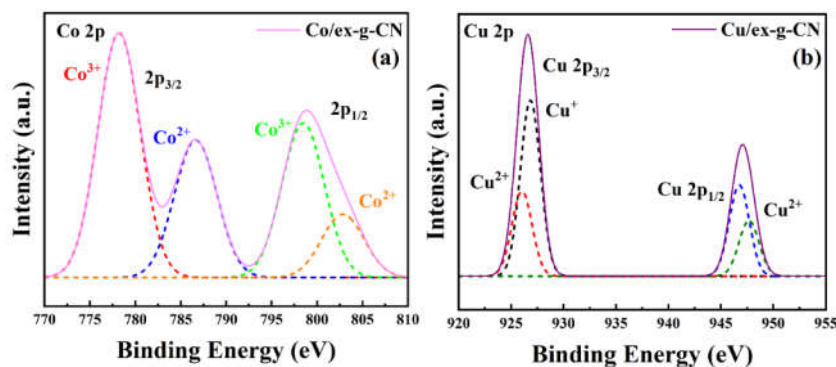


Figure S6. XPS profiles of the obtained samples for (a) Co 2p and (b) Cu 2p.

TEM and EDX of cobalt- and copper-loaded ex-g-CN are shown in Figure S7. EDX confirmed the presence of copper and cobalt on the surface of ex-g-CN. TEM confirmed the nanosheet structure of ex-g-CN, but Co and Cu are not shown in the form of metal nanoparticles.

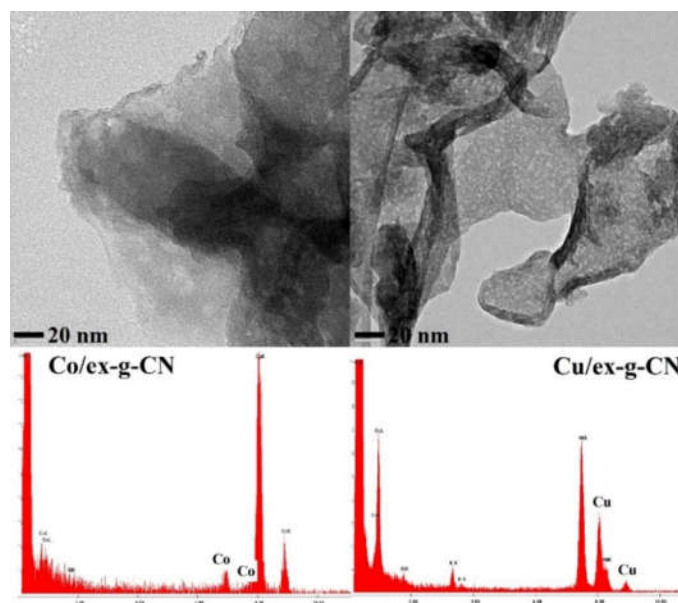


Figure S7. TEM and EDX images of Co and Cu-loaded ex-g-CN.

## References

1. Rana, A.; Tasbihi, M.; Schwarze, M.; Minceva, M. Efficient Advanced Oxidation Process (AOP) for Photocatalytic Contaminant Degradation Using Exfoliated Metal-Free Graphitic Carbon Nitride and Visible Light-Emitting Diodes. *Catalysts* **2021**, *11*, 662.
2. Huang, J.; Qian, W.; Ma, H.; Zhang, H.; Ying, W. Highly selective production of heavy hydrocarbons over cobalt-graphene-silica nanocomposite catalysts. *RSC Adv.* **2017**, *7*, 33441–33449.
3. Wang, X.; Zhang, B.; Zhang, W.; Yu, M.; Cui, L.; Cao, X.; Liu, J. Super-light Cu@Ni nanowires/graphene oxide composites for significantly enhanced microwave absorption performance. *Sci. Rep.* **2017**, *7*, 1584.



# Analysis of Photocatalytic Degradation of Phenol with Exfoliated Graphitic Carbon Nitride and Light-Emitting Diodes using Response Surface Methodology (RSM)

Adeem Ghaffar Rana <sup>1,2</sup>, and Mirjana Minceva <sup>1,\*</sup>

<sup>1</sup> Biothermodynamics, TUM School of Life Sciences, Technical University of Munich, Maximus-von-Imhof-Forum 2, 85354, Freising, Germany; adeem.rana@tum.de; mirjana.minceva@tum.de;

<sup>2</sup> Department of Chemical, Polymer and Composite Materials Engineering, University of Engineering and Technology (UET), Lahore, Pakistan; adeem.rana@tum.de

\* Correspondence: mirjana.minceva@tum.de; Tel.: (+498161716170)

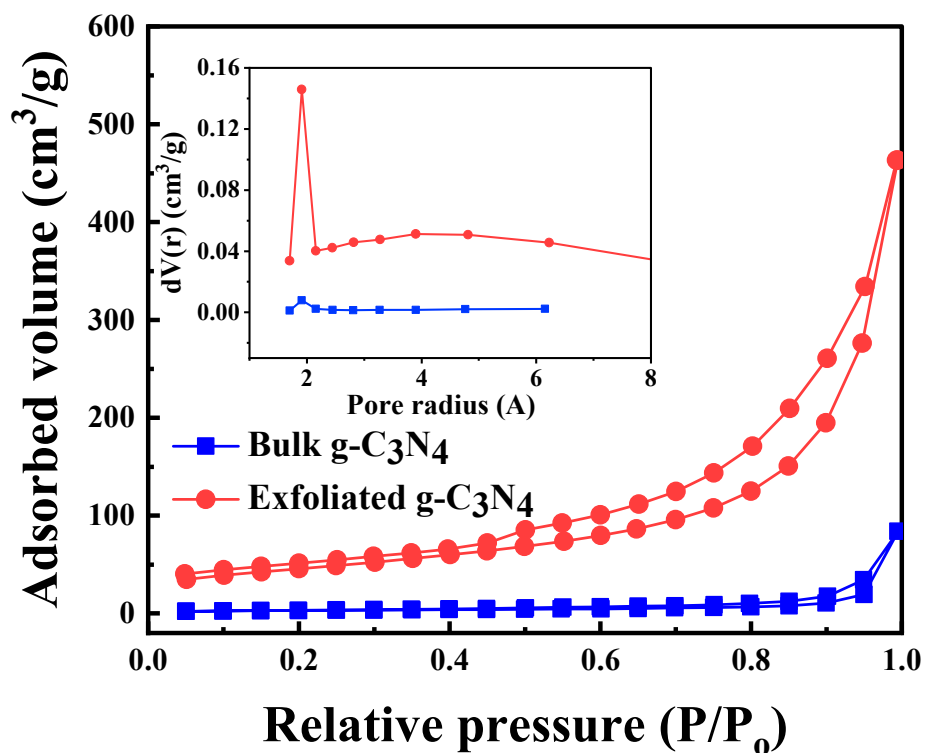


Figure S1 N<sub>2</sub> adsorption-desorption isotherms of bulk and exfoliated g-C<sub>3</sub>N<sub>4</sub>. The inset shows the corresponding BJH pore size distribution curves of the sample



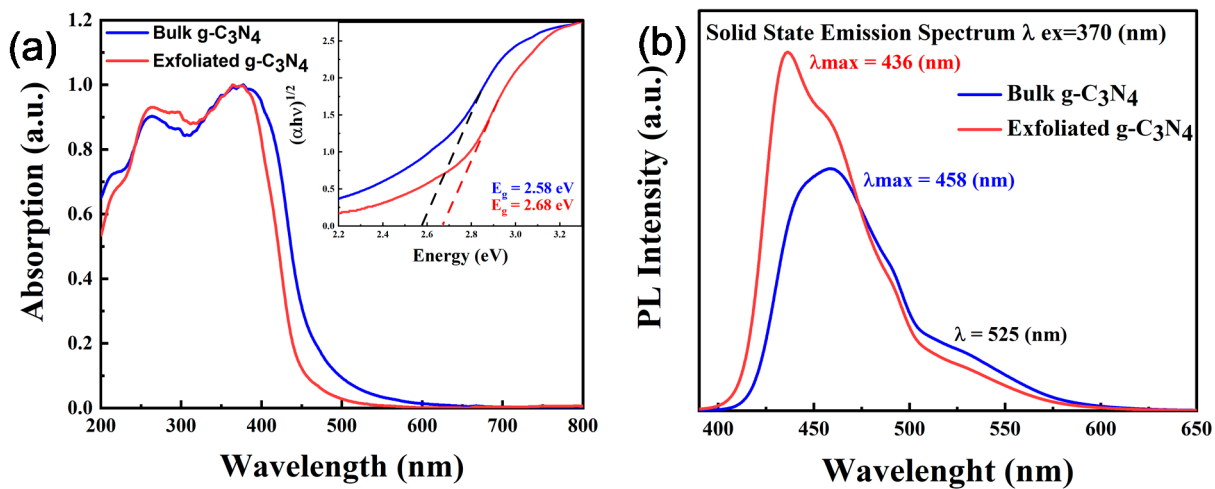


Figure S2 (a) UV-Vis absorption spectra and (b) PL spectra of bulk and exfoliated g-C<sub>3</sub>N<sub>4</sub>; insets of (a) showing the Tauc plots

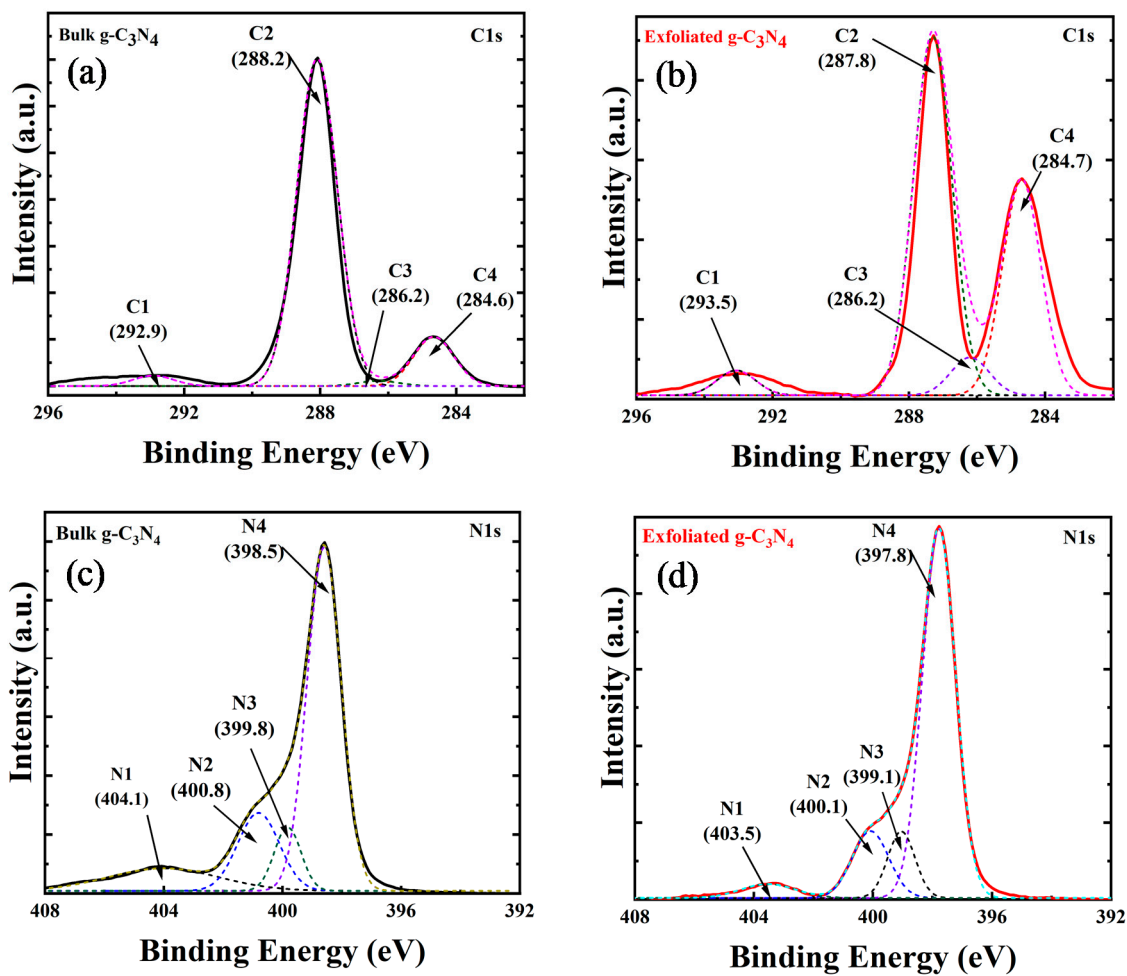


Figure S3 XPS spectra of bulk and exfoliated g-C<sub>3</sub>N<sub>4</sub> C1s, N1s

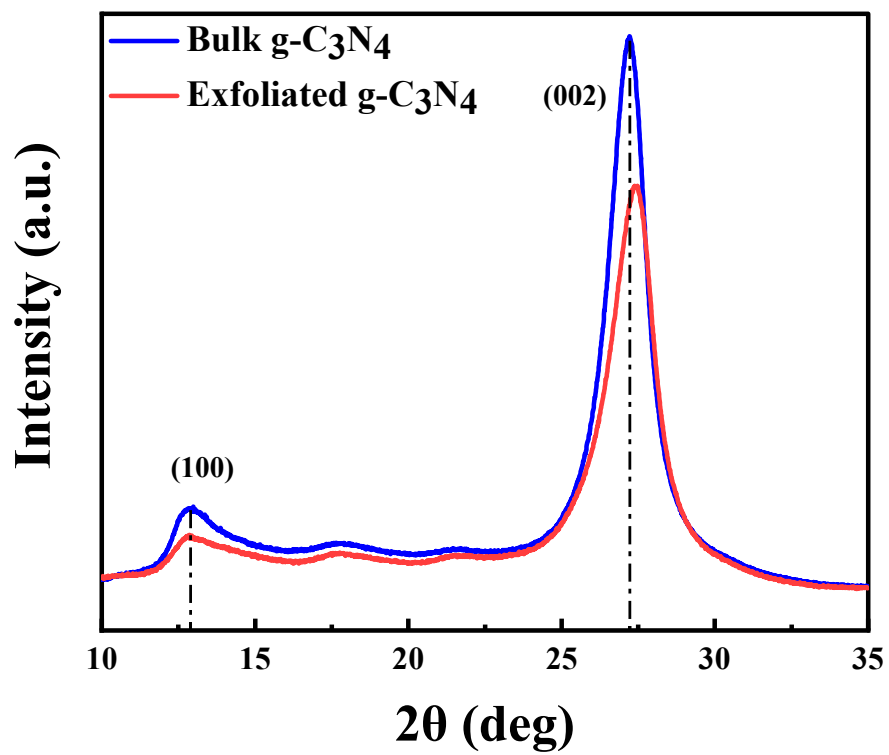


Figure S4 X-ray diffraction patterns of bulk and exfoliated g-C<sub>3</sub>N<sub>4</sub>

## List of abbreviations and symbols

g-C <sub>3</sub> N <sub>4</sub>	Graphitic carbon nitride
ex-g-CN	Exfoliated graphitic carbon nitride
XRD	X-ray powder diffraction
XPS	X-ray photoelectron spectroscopy
PL	Photoluminescence spectroscopy
FTIR	Fourier transform infrared spectroscopy
BET	Brunauer–Emmett–Teller
TEM	Transmission electron microscopy
SEM	Scanning electron microscopy
LED	Light-emitting diodes
RSM	Response surface methodology
BBD	Box–Benkhen design
E2	17 $\beta$ -estradiol
EE2	17 $\alpha$ -ethinylestradiol
TEOA	Triethanolamine
WWTPs	Wastewater treatment plants
CB	Conduction band
VB	Valence band
NHE	Normal Hydrogen Electrode
IUPAC	International Union of Pure and Applied Chemistry
TON	Turnover number
ROS	Reactive oxygen species
CNT	Carbon nanotubes
CNF	Carbon nanofibers
UV-Vis	Ultraviolet-visible spectroscopy
HPLC	High-performance liquid chromatography
DoE	Design of experiment
CCD	Central composite design
EDCs	Endocrine-disrupting compounds
HER	Hydrogen evolution reaction

2FI	Two-factor interaction
ANOVA	Analysis of variance
VOCs	Volatile organic compounds
MOFs	Metal-organic frameworks
COFs	Covalent organic frameworks
XAS	X-ray absorption spectroscopy
TRPL	Time-Resolved Photoluminescence
TGA	Thermogravimetric analysis